Chair of Physical Metallurgy

Doctoral Thesis

Atomistic approaches for investigating planar defects in compositionally complex alloys

Dipl.-Ing. Dominik Franz Josef Gehringer, BSc

June 2023

MONTANUNIVERSITÄT LEOBEN
www.unileoben.ac.at

AFFIDAVIT

I declare on oath that I wrote this thesis independently, did not use other than the specified sources and aids, and did not otherwise use any unauthorized aids.

I declare that I have read, understood, and complied with the guidelines of the senate of the Montanuniversität Leoben for "Good Scientific Practice".

Furthermore, I declare that the electronic and printed version of the submitted thesis are identical, both, formally and with regard to content.

Date 27.06.2023

Signature Author
Dominik Franz Josef Gehringer

Acknowledgements

During the path to my thesis, there had been a lot of smaller and larger hurdles to overcome as well as extra work beyond what is presented on the following pages. Therefore I want to mention those persons, from which I had the chance to learn:

My greatest thanks go to my supervisor David Holec, who has read every single line of text I have ever written. He taught me all the necessary skills from interpreting results to making graphs up to article writing. I also greatly appreciate his support, which often went beyond what would be asked from a supervisor. Finally, besides what I have learned for "*work*" he also set an example to me on how to treat people. While I am excited about the future, there is certainly a sad eye to leave the group after such a long time.

I would like to extend my sincere thanks to my collaborators, Dr. Liam Huber and Prof. Jörg Neugebauer. Firstly, for the hospitality, secondly for the insight I was able to gain during my stays at MPIE, and finally for their patience in correcting my manuscript drafts. The stays in Düsseldorf at a different research facility were truly inspiring in many ways.

Thanks should also go to Martin Friák for his hospitality and the fruitful discussions during my stays in Brno.

I am also grateful for the DOC scholarship granted by the Austrian Academy of Sciences.

To my girls ...

Contents

Abstract

A huge fraction of engineering materials, ranging from steels to ceramics, are composed of crystals. These constituent crystals exhibit a wide variety of defects, which modern materials science exploits to use for tuning of specific material properties. However, for knowledge-driven materials design it is of utmost importance to understand the fundamental mechanisms, how such defects impacts materials. Atomistic modeling combined with first-principles methods is able to provide unique insight into properties such as e.g., local atomic structures.

The microstructural complexity of modern materials requires increasingly demanding and sophisticated atomistic models. The standard tools for modelling such complex models however have several shortcomings. Density functional theory (DFT), which gives insight into the electronic structure, is limited to small models. These are small in terms of atoms present and hence fail to describe structurally complex defects. In contrast, molecular dynamics (MD) can handle large models, however falls short in describing the chemical complexity of modern materials such as, e.g. alloys.

In the present thesis we have implemented a hybrid approach coupling DFT and MD, to overcome these limitations. We have applied the approach to study interfaces (planar defects) in TiAl intermetallic alloys. Thereby, we study the impact of alloying elements on interfacial mechanical properties.

In a second part we tackle the challenge of modeling disordered alloys with finite atomistic models. We provide the theory and a corresponding implementation to generate atomistic models of disordered system. Using the developed tools we create models to study a grain boundary in a (disordered) Ni-base alloy. Besides giving the theoretical prerequisites, we focus on the impact of chemical disorder on solute segregation of alloying elements. Finally, we compare predictions from thermodynamic models between a standard single-species-matrix and the realistic chemically complex matrix.

Kurzfassung

Ein beträchtlicher Anteil der technisch relevanten Werkstoffe, von Stählen bis hin zu Keramiken, ist aus Kristallen aufgebaut. Jene Kristalle sind mit verschiedenen Defekten versehen, welche die moderne Werkstoffwissenschaft nutzt, um gewisse Materialeigenschaften zu verbessern. Um jedoch wissensbasiertes Werkstoffdesign betreiben zu können, ist es wichtig die fundamentalen Mechanismen zu kennen, um den Einfluss der Defekte auf das Material zu verstehen. Atomistische Modellierung in Kombination mit *ab-initio* Berechnungen können hier einzigartige Einsichten, wie z.B. die lokale atomare Struktur, in die Werkstoffe bringen.

Die mikrostrukturelle Komplexität moderner Materialien verlangt jedoch nach immer größeren und dementsprechend komplexeren atomaren Modellen. Die Standardmethoden, um solche Modelle zu untersuchen, weisen jedoch einige Defizite auf. Die Dichtefunktionaltheorie (DFT), mit der die elektronische Struktur untersucht werden kann, ist auf kleine Modelle limitiert. Die, hinsichtlich der Anzahl der vorhandenen Atome, kleinen Modelle versagen, wenn strukturell komplexe Defekte beschrieben werden müssen. Im Gegensatz dazu können mit Molekulardynamik (MD) große Systeme modelliert werden. Hier ist jedoch der einschränkende Faktor die chemische Komplexität, wie sie z.B. bei Legierungen auftritt.

In dieser Arbeit wurde ein hybrider Ansatz implementiert, wobei DFT und MD gekoppelt werden, um die vorhin beschriebenen Probleme zu lösen. Der Ansatz wurde verwendet, um Phasengrenzflächen (ebene Defekte) in intermetallischen TiAl Legierungen zu untersuchen. Dabei wurden weiters der Einfluss von Legierungselementen auf die mechanischen Eigenschaften dieser Grenzflächen untersucht. Der zweite Teil dieser Arbeit widmet sich der atomistischen Modellierung von Lösungen in Festkörpern, zur Beschreibung von Legierungen mit einer endlichen Anzahl von Atomen. Wir präsentieren dafür die theoretischen Grundlagen, sowohl als auch eine Implementierung dieser, für die Generierung eben jener Modelle. Mit den entwickelten Werkzeugen untersuchen wir eine Korngrenze in einer (ungeordneten) Nickelbasislegierung. Neben den theoretischen Grundlagen zeigen wir den Einfluss von chemischer Unordnung, auf das Verhalten von Segregationselementen. Abschließend vergleichen wir Vorhersagen von thermodynamischen Modellen, zwischen einem vereinfachten Reinelementsystem und dem realistischen ungeordneten System.

Chapter 1

Introduction

1.1 Interfaces in materials

In the past decades, materials science was tremendously successful in pushing properties of materials systems to their limits. A very impressive example of this material tuning can be observed if one has a look at the mechanical properties of the third generation of Advanced High Strength Steels (AHSS). Although a typical alloy still consists of nearly pure iron (Fe) with only a few per cent of alloying elements, ultimate tensile strengths of more than $\approx$ 1200 MPa are achievable, while pure *bcc*-Fe is soft and weak with a strength of $\approx$ 450 MPa. Only slight changes in chemistry induce this tremendous improvement (nearly three times), which can be attributed to microstructural differences, involving the presence of vast amounts of crystal defects such as grain boundaries, stacking faults, or dislocations. However, it is crucial to point out that extended two-dimensional planar crystal defects, such as interfaces and grain boundaries are by far one of the most important tools material scientists have at hand when it comes to designing novel materials (not only steels or metals). Furthermore, because of their significance, there is a huge demand for understanding these defects from a fundamental point of view and in various different classes of materials such as but not limited to steels, non-ferrous alloys (e.g. aluminum), protective coatings, refractory metals or ceramics, to name just a few. Atomistic investigations of these defects push the current tools to their limits or sometimes even beyond. The huge demand for fundamental understanding, in combination with the limitation of the standard tools, provides the main motivation for the present thesis.

As a consequence of the defects' importance for materials performance, much experimental effort has been invested to study them already for decades. Experiments in general, and investigations at the atomic scale in particular, however, come with great efforts in terms of technical equipment, research staff, and financial means. Here, atomistic simulations proved to be a complementary tool to help to understand experimentally observed phenomena

at only a fraction of the costs of an experimental investigation. Some physical quantities are sometimes hardly or not at all accessible experimentally (e.g. activation energies for diffusion processes). In such cases, theoretical methods can give insight and a qualitative and increasingly more often also quantitaive feeling for the physical quantities under investigation and thus guide experiments.

To be able to design such interfaces in a controlled manner, it is of utmost importance to understand how alloying elements interact with such interfaces. Consequently, understanding solute segregation and the impact of those on interfacial properties is a key aspect when designing novel materials. Due to the complexity (chemical or structural) of modern materials, this turns out to be very hard on the atomistic level. Here the present thesis aims at making two small steps forward which will be explained in greater detail in the next section. Hence we try to improve the current understanding of solute segregation phenomena, to planar defects in metallic systems.

1.2 Outline

In the following section, we will give a short written outline of the present thesis. The thesis is divided into three parts, each consisting of two chapters.

In the first part, we point out the challenges and summarize the suggested solutions. Therefore, we start in Chap. 2 with the theoretical foundations of the standard tools namely molecular dynamics (MD) and density functional theory (DFT). Those will be needed to understand their limitations. In Chap. 3 we give an overview of alternative or adapted methods that try to overcome the shortcomings. Therein, we discuss density-based methods intended to improve DFT (in certain aspects), while we put a major focus on the recent development of machine-learned force fields (ML-FF). These ML-FFs are intended to speed up DFT calculations or to make MD applicable to a wider range of materials. We conclude the chapter, with an overview of hybrid methods trying to combine the best of both worlds.

The second part of the thesis tackles the challenge of structurally complex planar defects. Therefore, Chap. 4 starts with an introduction to a coupled quantum-mechanical and molecular-mechanical (QM/MM) scheme [1]. Within the scope of this thesis we have implemented this approach and therefore provide details on the implementation. The QM/MM approach requires a system decomposition into a QM and MM part, however, not all properties (e.g. pressure) are known in both parts. Hence, Chapter 4 continues by suggesting how volume relaxations might be incorporated which itself requires to know the pressure for the whole QM/MM system. The final part of the Chap. 4 provides a guide on how to carry out the methodologically rather involved QM/MM calculations. In Chap. 5 we apply the approach implemented in Chap. 4 to study solute segregation to interfaces in TiAl alloys.

Beyond studying and elucidating energetics of segregation, we present the impact of solute on the mechanical properties of the interfaces.

The third part of the thesis tackles the challenge of chemical complexity in real alloys. Therefore, in Chap. 6 we present a method to generate finite sized-cells of disordered alloys optimizing pair correlations. We furthermore suggest a way to include triplet interactions and present our implementation. In the last chapter, we apply our computer program to generate models of disordered bulk and grain boundary structures (GB). We use these models to study solute segregation to a grain boundary in a specific Ni-base superalloy. We adapt an existing thermodynamic model for GB segregation to be applicable for disordered systems. Finally, we provide a simple method on how to extract the necessary model parameters from DFT calculations.

Chapter 2

Standard tools of atomistic modeling

In modern atomistic modeling, there are a lot of methods out there. While some are specific, and suitable only for a small range of problems (e.g. special class of material systems), we will give an introduction to the two most-widespread methods. Namely, to Kohn-Sham density functional theory (KS-DFT) that operates on the electronic level, and to Molecular Dynamics (MD) that treats systems on the atomistic level. The by far larger part of this chapter is dedicated to DFT, as we try to give the reader an overview of the assumptions and approximations which are at its heart. In a very condensed fashion, we go from the N-electron problem over Hartree and Hartree-Fock approximation to KS-DFT. We then shortly outline the main idea of MD. Finally, we discuss the shortcomings of the methods in light of their suitability to model planar defects in metallic systems.

2.1 Quantum mechanical descriptions

Upon investigation of condensed matter one usually thinks of an atom, as a core surrounded by electrons. As those electrons form bonds, their spatial distribution determines nearly all subsequent material properties. Consequently, methods able to compute properties of electrons can give a unique insight into materials and are therefore called electronic structure methods. Since they often require no empirical data, they are often termed first-principles methods. Secondly, in practice they reveal additional insights only at a high computational costs. The present section shall give the reader an overview of the most important parts of the underlying theory and the most important approximations made. Therefore the following text is structured as follows. Firstly, we introduce the theoretical foundations, as well as the first attempts to solve the underlying problem. The second part introduces the workhorse of modern QM calculations, namely DFT. Finally, the last section introduces alternative, less popular methods which proved to be successful in materials science problems.

2.1.1 N-electron problem and wave function-based methods

To know how electrons behave around a core, one has to solve the fundamental equation of quantum mechanics, the Schrödinger equation. The equation describes the evolution of a system of N quantum particles at positions $\vec{r}_i, \ldots, \vec{r}_N$ over time and reads

$$-i\hbar\frac{\partial}{\partial t}\Psi = \hat{H}\Psi \tag{2.1}$$

where $\hat{H}$ is the Hamilton operator. The solution is called the many-body wave function Ψ. For most applications, it is sufficient to know only stationary (time-independent) solutions, which modifies the above equation to

$$\hat{H}\Psi = E\Psi \tag{2.2}$$

and drastically reduces the efforts to solve the equation. Although Eq. (2.2) is compact in its notation, putting it into the context of atoms and electrons reveals the underlying complexity. We can do so by having a closer look at the two main constituents Φ and $\hat{H}$. Consider a simulation box with M atoms located in space at $\{\vec{R}_i\}$ where $\vec{R}_i \in \mathbb{R}^3$, which are surrounded by N electrons at $\{\vec{r}_i\}$ where $\vec{r}_i \in \mathbb{R}^3$. As a matter of fact the many-body wave function Ψ depends on all these coordinates $\Psi(\{\vec{r}_i\}, \{\vec{R}_i\})$. The difficulty in solving the equation becomes even more obvious when looking at $\hat{H}$. As the Hamiltonian "*measures*" the energy in the system we can write it simply as the sum of kinetic energies and electrostatic interactions occurring in the box

$$\hat{H} = \hat{T}_n + \hat{T}_e + \hat{V}_{n-n} + \hat{V}_{e-e} + \hat{V}_{n-e} \tag{2.3}$$

where

$\hat{T}_n$ is the kinetic energy (operator) of the nuclei (note that n means nuclei in this context)

$\hat{T}_e$ is the kinetic energy (operator) of the electrons

$\hat{V}_{n-n}$ the electrostatic repulsion of the positively charged munclei

$\hat{V}_{e-e}$ the electrostatic repulsion of the negatively charged electrons

$\hat{V}_{n-e}$ the electrostatic attraction between electrons and nuclei

and may be expanded to (in atomic units)

$$\hat{H} = \underbrace{-\frac{1}{2}\sum_{i}^{M}\frac{\Delta_{\vec{R}_i}}{M_i}}_{\hat{T}_n} \underbrace{-\frac{1}{2}\sum_{j}^{N}\Delta_{\vec{r}_j}}_{\hat{T}_e} + \underbrace{\sum_{i,i'\neq i}^{M,M}\frac{Z_i Z_{i'}}{\left|\vec{R}_i - \vec{R}_{i'}\right|}}_{\hat{V}_{n-n}} + \underbrace{\sum_{j,j'\neq j}^{N,N}\frac{1}{|\vec{r}_j - \vec{r}_{j'}|}}_{\hat{V}_{e-e}} \underbrace{-\sum_{i,j}^{M,N}\frac{Z_i}{\left|\vec{R}_i - \vec{r}_j\right|}}_{\hat{V}_{n-e}} \tag{2.4}$$

where Z_i is the nuclear charge and M_i the mass of the i^{th}'s atoms core. Note that finding Ψ is a $3(N+M)$ dimensional problem and is infeasible to solve for any practical application.

Born-Oppenheimer (BO) approximation

The mass of a single proton is three orders of magnitude larger than that of electrons, and hence one expects the nuclei to react only slowly to external changes. Consequently $\hat{T}_n \ll \hat{T}_e$, and it is legit to think of our system as electrons orbiting around the "*static*" cores [2]. In other words, we solve Eq. (2.4) for fixed values of $\vec{R}_1, \ldots, \vec{R}_M$. Instead of the wave function being dependent on the nuclear coordinates, those become parameters of the same $\Psi(\{\vec{r}_i\}, \{\vec{R}_i\}) \rightarrow \Psi(\{\vec{r}_i\}; \{\vec{R}_i\})$. Note the semi-colon to indicate that the nuclei positions are no dependent variables but rather parameters. Thus, to fully explore a system one has to sample the whole $3M$ dimensional space of the nuclei coordinates. This hyper-dimensional surface spanned by $\vec{R}_1, \ldots, \vec{R}_M$) is therefore called the Born-Oppenheimer surface. For brevity, we will omit the nuclear coordinates in the following and refer to Ψ as $\Psi(\{\vec{r}_i\})$. This approximation with fixed the nuclei coordinates, however, has four positive consequences on the problem. Firstly the problem is reduced from $3(N+M)$ to $3N$ dimensions. Secondly $\hat{V}_{n-n}$ becomes a constant. Thirdly the electron-nucleus interaction $\hat{V}_{n-e}$ can be seen as the interaction of an electron with an external (coulombic) potential of ions. Hence in the following $\hat{V}_{n-e}$ becomes $\hat{V}_{\text{ext}}$. Lastly, the kinetic energy of the nuclei can be omitted. Consequently, Eq. (2.4) reduces under the BO approximation to

$$\hat{H} = \underbrace{-\frac{1}{2}\sum_{j}^{N}\Delta_{\vec{r}_j}}_{\hat{T}_e} + \underbrace{\frac{1}{2}\sum_{i,i'\neq i}^{N,N}\frac{1}{|\vec{r}_i - \vec{r}_{i'}|}}_{\hat{V}_{e-e}} \underbrace{-\hat{V}_{\text{ext}}}_{\hat{V}_{n-e}}. \tag{2.5}$$

Ground state approximation

Although the BO approximation is sensible, intuitive, and extraordinarily helpful towards solving the problem, it is yet still too complex for practical applications. One reason is that there is not only one function Ψ that would satisfy Schrödinger equation with the many-body Hamiltonian, but rather infinitely many. Each solution is called "*eigenfunction*" of the Hamiltonian $\hat{H}$ where the energy is the corresponding "*eigenvalue*". A step forward is to search only for the solution with the lowest eigenvalue E_0. Again the problem becomes

more trackable, as it becomes an optimization (minimization) problem. As the object to minimize is a function, one can apply variational calculus to find the ground state solution. The *Rayleigh-Ritz* principle states that for any trial wave function $|\Psi\rangle$ the following relation must hold [3]

$$\mathcal{E}[\Psi] = \frac{\left\langle \Psi \middle| \hat{H} \middle| \Psi \right\rangle}{\langle \Psi | \Psi \rangle} \geq E_0 \ . \tag{2.6}$$

Consequently, only the ground state solution Ψ_0 will satisfy $\Psi_0 > E_0$. Hence when searching for the ground state energy, the Schrödinger equation with the many-body Hamiltonian can be reformulated as a minimization problem. Searching for the ground state makes solving the equation actually feasible at all, however, comes at a cost. The ground state of a system corresponds to the state the system will have at 0 K. Whenever we search for a solution to the Schrödinger equation using variational methods, we demand the system to be at 0 K implicitly. Note, that any theory which puts the many-body problem in a variational framework, is inherently a ground state theory.

Finally, restricting ourselves to the ground state also reduces the complexity of the BO surface. The BO surface for the ground state is parameterized by the ionic positions $\{\vec{R}_i\}$ and reads

$$E(\{\vec{R}_i\}) = \left\langle \Psi_0(\{\vec{r}_i\};\{\vec{R}_i\}) \middle| \hat{H} \middle| \Psi_0(\{\vec{r}_i\};\{\vec{R}_i\}) \right\rangle \ . \tag{2.7}$$

Moreover, Eq. (2.7) is referred to as the potential energy surface (PES). The PES becomes the central quantity when bringing machine learning to materials science, see Sec. 3.2.

Hartree approximation

As we have restricted the domain of solutions, some actual wave functions might be inserted. Hartree suggested to approximating the many-body wave function as the product of single particle wave functions [4], such that

$$\Psi(\{\vec{r}_i\}) = \prod_i^N \varphi(\vec{r}_i) \tag{2.8}$$

Hence by plugging Eq. (2.8) into the *Rayleigh-Ritz* principle it follows that the energy functional $\mathcal{E}$ depends on the single particle wave function $\mathcal{E}[\varphi_1, \ldots, \varphi_N]$. The functional is minimized when all functional derivatives with respect to the single particle orbitals vanish. Hence, instead of one we arrive at N simpler single particle Schrödinger equations, we can be obtained by computing the functional derivatives with respect to the single particle wave function φ_i

$$\begin{aligned}\frac{\delta\mathcal{E}[\varphi_1,\ldots,\varphi_N]}{\delta\varphi_i} &= \frac{\delta}{\delta\varphi_i}\left[\left\langle\Psi\middle|\hat{H}\middle|\Psi\right\rangle - \sum_i^N \varepsilon_i \int \varphi_i^*(\vec{r}_i)\varphi_i(\vec{r}_i)\mathrm{d}\vec{r}_i\right] \\ = \frac{\delta}{\delta\varphi_i}\Bigg[\int \prod_i^N \varphi_i^*(\vec{r}_i)\left\{-\frac{1}{2}\sum_i^N \Delta_{\vec{r}_i} + \frac{1}{2}\sum_{i,i'\neq i}^{N,N}\frac{1}{|\vec{r}_i-\vec{r}_{i'}|}\right\}\prod_i^N \varphi_i(\vec{r}_i)\mathrm{d}\vec{r}_1\cdots\mathrm{d}\vec{r}_N \\ - \sum_i^N \varepsilon_i \int \varphi_i^*(\vec{r}_i)\varphi_i(\vec{r}_i)\mathrm{d}\vec{r}_i\Bigg]\end{aligned} \tag{2.9}$$

where ε_i are the corresponding Lagrange multipliers. By demanding that every variation of φ_i vanishes we arrive at the Hartree equations, which therefore read

$$\left[-\frac{1}{2}\Delta_{\vec{r}_i} + \underbrace{\sum_{j\neq i}^N \int \frac{\varphi_j^*(\vec{r}')\varphi_j(\vec{r}')}{|\vec{r}-\vec{r}'|}\mathrm{d}\vec{r}'}_{v_{H,i}} + V_{\mathrm{ext}}(\vec{r})\right]\varphi_i(\vec{r}) = \varepsilon_i\varphi_i(\vec{r}). \tag{2.10}$$

After splitting the equation into the N single particle equations in Eq. (2.10), one should note that all φ_i enters all N equations. Hence, these equations must be solved self-consistently. To give a more intuitive interpretation of the Hartree term we can use the fact that, one can compute the total charge density as the sum of the single particle's charge density.

$$n(\vec{r}) = \sum_i^N \varphi_i^*(\vec{r})\varphi_i(\vec{r}) = \sum_i^N |\varphi_i(\vec{r})|^2 \tag{2.11}$$

Therefore we can rewrite and simplify Eq. (2.10) even more by

$$V_{H,i}(\vec{r}) = \sum_{j\neq i}^N \int \frac{\varphi_j^*(\vec{r}')\varphi_j(\vec{r}')}{|\vec{r}-\vec{r}'|}\mathrm{d}\vec{r}' = \int \frac{\overbrace{\sum_{j\neq i}^N |\varphi_j(\vec{r}')|^2}^{\approx n(\vec{r})}}{|\vec{r}-\vec{r}'|}\mathrm{d}\vec{r}' \approx \int \frac{n(\vec{r})}{|\vec{r}-\vec{r}'|}\mathrm{d}\vec{r}' = V_H(\vec{r}) \tag{2.12}$$

where v_H is usually referred to as the *Hartree potential*. Note that by substituting $\sum_{j\neq i}^N |\varphi_j(\vec{r}')|^2$ with the $n(\vec{r})$, one introduces an artificial term which is the interaction of the i^{th} particle with itself. Hence this spurious interaction is referred to as the *self-interaction*. The Hartree potential, however, has an intuitive physical interpretation. It represents the coulombic repulsion caused by the charge density $n(\vec{r})$.

Hartree–Fock approximation

The Hartree-Fock (HF) approximation [5] tries to overcome an important shortcoming of the Hartree approximation. Namely, Pauli exclusion principle which is not taken into account. Upon exchanging any two particles, Ψ must change its sign. In other words

$$\Psi(\vec{r}_1, \ldots, \vec{r}_i, \ldots, \vec{r}_j, \ldots, \vec{r}_N) = -\Psi(\vec{r}_1, \ldots, \vec{r}_j, \ldots, \vec{r}_i, \ldots, \vec{r}_N) \tag{2.13}$$

must hold true for any indices i and j. A clever way to construct a wave function satisfying this property and still being made of single particle wave functions is to use a *Slater-determinant* [6]

$$\Psi(\vec{r}_1, \ldots, \vec{r}_N) = \frac{1}{\sqrt{N!}} \begin{vmatrix} \varphi_1(\vec{r}_1) & \varphi_2(\vec{r}_1) & \cdots & \varphi_N(\vec{r}_1) \\ \varphi_1(\vec{r}_2) & \varphi_2(\vec{r}_2) & \cdots & \varphi_N(\vec{r}_2) \\ \vdots & \vdots & \ddots & \vdots \\ \varphi_1(\vec{r}_N) & \varphi_2(\vec{r}_N) & \cdots & \varphi_N(\vec{r}_N) \end{vmatrix}. \tag{2.14}$$

Similarly to Eq. (2.9), one can now plug Eq. (2.14) into the variational calculus apparatus. The derivation is more cumbersome than it was for the Hartree equation, hence we only provide the resulting *Hartree-Fock* equations which read

$$\left[\Delta_{\vec{r}_i} + \underbrace{\int \frac{n(\vec{r'})}{|\vec{r} - \vec{r}'|} \mathrm{d}\vec{r}'}_{v_H(\vec{r})} - \sum_j^N \underbrace{\int \frac{\varphi_j^*(\vec{r}')\varphi_j(\vec{r})\varphi_i(\vec{r}')}{\varphi_i(\vec{r})|\vec{r} - \vec{r}'|} \mathrm{d}\vec{r}}_{V_F^i(\vec{r})}\right] \varphi_i(\vec{r}) = \varepsilon_i \varphi_i(\vec{r}) \tag{2.15}$$

where $V_H(\vec{r})$ is the Hartree potential as introduced in Eq. (2.12). $V_F^i(\vec{r})$ is the Fock-exchange potential for the i^{th} particle to account for the Pauli exchange. However, in contrast to the Hartree potential, the Fock exchange potential has no classical analogous physical interpretation. It is caused by the purely quantum-mechanical exchange phenomena. Similarly to the Hartree-equations (Eq. (2.10)) the Hartree-Fock equations need to be solved self-consistently.

Although the HF method fully accounts for electron exchange, it does not exactly describe the coulombic correlation. Stating $\sum_i^N |\varphi_i(\vec{r})|^2 \approx \sum_i^N |\varphi_{j\neq i}(\vec{r})|^2$ in Eq. (2.12) is a so called *mean-field* assumption, and any deviations will not be captured properly. Due to this latter approximation, there are several limitations to the HF method. Firstly, even for an infinitely large basis set, one will never reach the exact energy. This limit is called *Hartree-Fock* limit. Secondly, solutions of the HF equations for real molecules usually provide an approximate electronic structure. Thirdly, especially in strongly-correlated materials, this approximation can lead to large deviations from experimental values.

2.1.2 Density-based methods – Density Functional Theory (DFT)

Wave-function-based methods suffer from a major drawback, preventing their use in a broad field of materials science: The problem needs to be solved still in a $3N$ dimensional function space. Already in the early 1930s, Thomas and Fermi tried to solve this problem. By using the charge density $n(\vec{r})$ as the central variable. Such an approach would of course reduce the problem to the three dimensions only.

Hohenberg–Kohn theorems

Such a reduction raises the question if a quantum-mechanical system is fully described by a single quantity $n(\vec{r})$ at all, compared to e.g. N single particle functions in the Hartree approximation. It is, indeed surprisingly easy to prove it. In the 1960s, Hohenberg and Kohn proved two theorems in their paper [7]:

Firstly, that for any external potential $V_{\text{ext}}(\vec{r})$ (as defined in Eq. 2.5) there exists exactly one ground state charge density $n(\vec{r})$ or vice versa. In other words, there exists a unique mapping (up to a constant), between an external potential $V_{\text{ext}}(\vec{r})$ and the ground state electron density $n(\vec{r})$. Furthermore, as the many-body wave function Ψ itself is a functional of the charge density, it follows that the external potential hence uniquely determines Ψ. Thus the system is fully determined by the charge density only. The theorem is simply proven by a *reductio ad absurdum*, by comparing two Hamiltonians that only differ by V_{ext}.

Secondly, they rigorously proved that there exists a universal functional, that yields the ground state energy. In other words, they proved, that the ground state approximation (Section 2.1.1) can be applied to the density directly, assuming the energy functional is known. Nevertheless, up to this day, there has not been found a functional that would express the total energy of the many-body Hamiltonian as a function of the electron density.

While the functionals for the electron-electron repulsion (Eq. 2.12) and the electron-ion attraction are straightforward to write down, other contributions are not. Those include:

Kinetic energy A functional for the kinetic energy is only known of the homogeneous electron gas [8]. For any general electron distribution, this is not known. Finding approximate kinetic energy density functionals (KEDF) is the central subject of investigation for all research in the field of orbital free DFT (OF-DFT, see Sec. 3.1.1). However, the contribution of the kinetic energy is very large compared to other terms. Hence, in practice methods minimizing the total energy functional, often suffer from convergence troubles, upon employing approximate kinetic energy density functionals.

Exchange energy is the energy increase due to Pauli's repulsion of fermions. Similar to the kinetic energy, an expression has been found for the homogeneous electron gas, by Dirac [9]. For general distributions of the electron density, no expression has been found.

Correlation turned out to be more difficult than computing the exchange energy. To treat correlation effects in the homogeneous electron gas an approximation for low electron densities [10] and a limit form for very high electron densities were found [11].

Kohn-Sham method

Only a few years later, fully aware of the shortcomings described before (Sec. 2.1.2), they proposed a different method to obtain the round state density. Therein, they suggest using a fictitious system non-interacting particles. This set of non interacting particles is chosen such that it yields the same ground state density as the interacting system. The Kohn-Sham (KS) equations

$$\left\{-\frac{1}{2}\nabla^2 + V_{\text{eff}}\right\}\phi_i(\vec{r}) = \epsilon_i\phi_i(\vec{r})\ . \tag{2.16}$$

where $\phi_i(\vec{r})$ are called Kohn-Sham (KS) orbitals and ϵ_i the corresponding eigenvalues, and v_{eff} is the so called "*effective*" of KS-potential. Again computing the sum of the density of all KS orbitals would yield the electron density, similarly to Eq. (2.11). There are, however, a few things to note about this scheme.

Firstly, the real system is replaced with a set of fictitious non-interacting particles. Consequently, the energies of the KS-orbitals ϵ_i have no physical correspondence except for the highest occupied one [12]. There were many approaches how to interpret the eigenvalues [13–15]. The actual physics in the above equations is hidden in the effective or Kohn-Sham potential which reads

$$V_{\text{eff}} = V_{\text{ext}} + V_H + V_{XC} \tag{2.17}$$

where V_{XC} is the so-called exchange correlation potential. Therefore only the last term contains "*unknown*" contributions, which are subject to approximations. Note that the KS approach is exact in case V_{XC} would be known. As this exchange-correlation term is usually a rather small part of the total energy, the KS approach was definitely a major breakthrough. Nevertheless, the major challenge, namely finding accurate and efficient approximations to the exchange-correlation energy remained.

We note that from the definition of the universal energy functional a definition for v_{XC} might be obtained, and show which quantum-mechanical effects one needs to take into account. However, for brevity, we omit this derivation.

It was Kohn and Sham themselves in their original work, who provided the first approximation for v_{XC}. As it was of particular interest to compute the electronic structure of metallic materials, where the valence electrons are spatially delocalized, it is fair to assume that the electron density in the interstitial regions is close to a homogeneous electron gas. Thus, the idea was to approximate the exchange and correlation effects with a homogeneous electron gas

$$V_{XC} = V_X^{\text{hom}} + V_C^{\text{hom}} \tag{2.18}$$

where v_X^{hom} and v_C^{hom} are the exchange and correlation potentials of the homogeneous electron gas. While V_X^{hom} is known in closed form, Perdew and Zunger [16] suggested using an interpolation between the aforementioned high and low-density form of V_C^{hom}. This approach, as both V_X^{hom} and V_C^{hom} are local functionals, was named local density approximation (LDA). Although LDA is a rather crude approximation, it turned out to be a real success due to the cancellation of errors. LDA tends to overestimate E_X and underestimate E_C. However, for metallic systems where fluctuations in the electron density are usually small, LDA yields good results.

Eq. (2.17) moreover reveals that also the KS-equations have to be solved self-consistently, as the effective potential is a functional of the electron density.

KS-DFT became the workhorse of modern atomistic DFT calculations. There are many different implementations available, and the KS method became the de-facto standard in DFT. Therefore, in the following we review its shortcomings which exist until the present day.

Wave-function method Strictly, spoken, KS-DFT is not within the original spirit of DFT, as it considers an orbital for each particle. Treating each particle separately leads to enormous computational demand. Hence, further approximations, namely e.g. pseudopotentials, are needed to apply DFT to practically relevant systems. We note that accurate density-based methods remain elusive until the present day.

Exchange-correlation energy Over the past decades, there have been many of different exchange-correlations functionals suggested by the scientific community. Those vary in the physics they include as well as in their computational demand. While some of them became popular (e.g. PBE [17], B3LYP [18], PW91 [19] or SCAN [20, 21]) and turned out to be universally applicable, many of them were fitted to special use cases. One must note that the improved exchange-correlation functionals, especially PBE, led to the real breakthrough of DFT. Despite all improvements in functional design, major DFT-codes use the HF method to compute Fock exchange energy from the KS-orbitals, when "*exact*" exchange is needed.

2.2 Molecular dynamics/statics

In MD, one shifts the focus from electrons to atoms. Instead of electrons treated using quantum mechanics, in MD the motion of atoms is governed by classical mechanics. Therefore, MD is inherently suited to study larger systems than DFT. Therefore, for a system of atoms located at positions $\vec{R}_i$ the equations of motions in a Hamiltonian formalism read

$$\frac{\partial \vec{p}_i}{\partial t} = \frac{\partial \hat{H}}{\partial \vec{R}_i} \tag{2.19}$$

$$\frac{\partial \vec{R}_i}{\partial t} = \frac{\partial \hat{H}}{\partial \vec{p}_i} \tag{2.20}$$

where $\vec{p}_i$ is the momentum vector of the i^{th} atom. In practice, the equations of motion are solved numerically, by introducing a time discretization and integrating to obtain the new positions and velocities. We note that within this thesis we applied only molecular statics. In molecular statics, the Hamiltonian is evaluated for a set of atoms and are moved to find the lowest energy configuration. In contrast in MD they move due thermal vibrations. Consequently, within this section, we will neglect to provide details about integration algorithms and thermostats. The Hamiltonian of a system of M interacting particles is given by the kinetic energy and the particle interaction energies

$$\hat{H} = \sum_{i}^{M} \frac{|\vec{p}_i|^2}{2m_i} + \sum_{i,j>i}^{M,M} V^{(2)}(\vec{R}_i, \vec{R}_j) + \sum_{i,j>i,k>j}^{M,M,M} V^{(3)}(\vec{R}_i, \vec{R}_j, \vec{R}_k) + \dots \tag{2.21}$$

where the first term refers to the kinetic energy and will be zero in molecular statics. The second and third terms include pair and three-body interactions consequently. In principle the above sum continues to clusters of size N, in practice, two and three-body potentials are used. Prominent examples of pair potentials are the Lennard-Jones or the Morse potential. Tersoff [22] potentials and a reformulated version of them named analytic bond-order potentials (ABOP) [23] or the Stillinger-Weber [24] are examples of three-body potentials. The latter (three-body) potentials were all developed as improved descriptions for covalent bonding in C and Si. In contrast, the semi-empirical embedded-atom-method (EAM) [25, 26] and derived models such as the Finnis-Sinclair [27] or the modified-EAM [28] became popular choices for metallic systems. In contrast to first-principles methods such as DFT, the potentials have to be parameterized, which in itself is a highly non-trivial task. The predictive power of such a potential strongly depends on the parameterization during which the potential is tuned to reproduce pre-defined properties. The forces on the atoms are computed by the gradient of the internal energy $\vec{F}_i = \nabla_i U$. More recently, huge efforts were made to

parameterize interatomic potentials from DFT data using machine learning. We will review this technique in detail in Sec. 3.2

2.3 Limits of the methods

Although the combination of experimental and theoretical investigations can bring unique insights into the basic mechanisms of materials, there are limits to the standard tools available in computational materials science. The two main tools presented for investigations at the atomic length scale, namely DFT and MD each exhibit different types of limitations, which are discussed in the following section.

	DFT	MD
underlying physics	quantum mechanics	classical mechanics
basic equations	$\hat{H}\psi = E\psi$	$\vec{F} = m\vec{a}$
scaling (N = number of atoms)	$\mathcal{O}(N^3)$	$\mathcal{O}(N)$
accuracy	best available	depends on potential
maximum system size	$\approx$ 1000 atoms	$\approx 10^6 - 10^9$ atoms [29]
resolution	electrons	atoms

Table 2.1: A short comparison of the basic principles and properties of DFT and MD.

2.3.1 Pracatical limitations of DFT

As the interest in has DFT exploded in the last two decades, it also became the tool of choice for a lot of material scientists. The computational efficiency of DFT increased dramatically, due to groundbreaking developments such as pseudo potentials (PPs) [30–33] or the projector augmented wave (PAW) method [34], resulting in ever-larger system sizes and shorted computational times, which in turn allowed investigations of a wide range of complex materials and problems. Nevertheless, modeling spatially extended defects remains still a highly non-trivial task. Modern efficient DFT codes use periodic boundary conditions, thus large enough simulation boxes have to be built to screen off interactions of defects with their periodic images. This, in turn, leads to large numbers of atoms needed to model those scenarios. As a consequence of being an *ab-inito* electronic structure method, DFT allows the calculation of systems with nearly arbitrary chemistry, since PPs are available for nearly all elements of the periodic table. Furthermore, there is no other tool available that would outperform DFT in terms of the accuracy of its predictions, not to speak of unparalleled computational efficiency, stability, and reproducibility of the results. Nevertheless, there are some drawbacks if one wants to employ DFT tools for modeling spatially extended defects.

system size Although (as mentioned in the paragraph before) incredible progress has been made, and more powerful computer hardware and computing concepts (GPU computing) push the limits of possible constantly year by year, the matrix inversions at the heart of every DFT code remain and scale badly. When accurately modeling planar defects, the number of atoms remains the main limiting factor. Of course, clever structural models can mimic a defect with a limited number of atoms, however, as materials (e.g. alloying concepts) become more complex, it becomes more and more necessary to have accurate atomistic models, and thus larger simulation boxes. In the end, the tractable system size is the prohibitive factor for creating accurate atomistic models.

calculated quantities A full DFT calculation requires the calculation of all (non-interacting [35]) (valence) electron wave functions, which is computationally demanding. For many materials science problems, the knowledge of electronic structure is not necessary and many simple quantities such as energies and forces on atoms suffice. Consequently (hand-wavy spoken), more than 99% of the data produced by a DFT code is not needed and thus discarded in many of the evaluations.

ground state-theory The theoretical framework behind DFT [7, 35] is a so-called "*ground state-theory*", thus all calculated quantities describe the quantum-mechanical ground state of a system. Consequently, finite temperatures are not treatable since the theory only holds, strictly speaking, at zero Kelvin. Extensions to finite temperatures (phonon thermodynamics, *ab-initio* MD) are often computationally prohibitive.

2.3.2 Pracatical limitations of MD

Instead of calculating each (valence) electron's wave function, MD treats whole atoms. The total information about the electronic structure, which is calculated by same *ab-initio* method such as DFT, is "*packed*" into an effective interaction between two (or more atoms), the potential. This approach brings numerous advantages, and at first glance seems to overcome all the problems of DFT, from a materials science point of view. First, by employing modern algorithms, MD scales linearly with the number of atoms $\mathcal{O}(N)$, thus tens of thousands of atoms which is more than what is needed to model 2D defects can be computed on a desktop workstation. Also finite temperature studies are possible. Lastly, because of classical mechanics, only forces and energies are calculated in order to evolve the system over time. Therefore MD calculates only data that is mostly needed for further post-processing. However, there are still prohibitive challenges in applying solely MD within the scope of the proposed project.

chemistry To carry out MD simulations, an interatomic potential (IP) is needed for the system under investigation. Although there are many potentials out there and also a

database exists, e.g. the NIST's Interatomic Potential Repository[1], most of them are fitted to properly describe simple single species of binary systems. Hence complex alloys or compounds cannot be studied, since creating potentials requires a lot of experience, a vast amount of DFT/experimental data, and knowledge about the system to be described.

transferability Usually the potentials are fitted to accurately reproduce certain quantities (e.g. mechanical properties, surface properties). Most often the potentials are fitted to bulk properties. When carrying out an MD simulation, one can rely on the potential is very good at describing bulk regions, while for defect regions no information is at hand. Consequently, one has to benchmark the potential against an electronic-structure method in order to ensure that it can reproduce the atomic structure also in the defective region. Therefore, even if an IP might be available for a special system, its computed properties may not be transferable to a special case of interest.

[1] `https://www.ctcms.nist.gov/potentials/`

Chapter 3

Overcoming the limits

We have concluded the previous chapter by summarizing the shortcomings of DFT and MD. For DFT the small model sizes heavily constrain their applicability for planar defects. In contrast for MD, the limited complexity of the chemistry is problematic. The following chapter starts by introducing derivatives of KS-DFT which have the potential to overcome the size limitations, but also points out still existing challenges also with respect to practical usability. The second part is meant as an introduction and concise summary of machine-learned force fields (ML-FF). Those ML-FFs can create potentials for MD from DFT data and hence greatly improve the number of materials systems that can be studied. Furthermore, although more computationally expensive than traditional MD potentials, they allow for MD calculations with close to DFT accuracy. The final part of this chapter is dedicated to hybrid methods. Hybrid methods try to either couple or augment DFT with other methods, its overcome the size limitation.

3.1 DFT-based methods

3.1.1 Orbital-Free DFT

Suppose the kinetic energy is known as a functional of the electron density. Consequently, the energy functional from the second HK theorem is known. For a system with N particles, the dimension of the problem is reduced from $3N$ to 3, compared to a KS-DFT approach. Instead, of solving N single particle equations, the ground state is the solution of a minimization problem which reads [36, 37],

$$E_{\min} = \min_{n \geq 0} \left\{ E[n] - \mu \left(\int_{\Omega} n(\vec{r}) \mathrm{d}\vec{r} - N \right) \right\} \tag{3.1}$$

where μ, the Lagrange multiplier, as well as the second integral term is to enforce a constant number of electrons N. Ω denotes the cell volume. $E[n]$ is the total energy functional, and

reads in the OF framework,

$$E_{\mathrm{OF}} = T[n] + \int_{\Omega} \{V_{ext}(\vec{r}) + V_H(\vec{r}) + V_{XC}(\vec{r})\}\, \mathrm{d}\vec{r} \tag{3.2}$$

where $T[n]$ is the kinetic energy functional, V_{ext} is the external potential from the BO-many-body Hamiltonian (Eq. 2.5), V_H – the Hartree potential (Eq. 2.17) and V_{XC} the exchange-correlation potential as discussed in the previous section (Eq. 2.18). The minimization of Eq. (3.2) can be carried out in two different ways.

Reusing a KS-calculator

As KS-DFT became very popular, and software was available already many (=four) decades ago, Levy, Perdew, and Sahni [38] showed how to recast the OF problem such, that it can be used with any KS-DFT calculator [39, 40]. Therefore, KS-equations are reduced to a single orbital, representing the square root of the many-body wave function, such that Eq. (2.16) becomes

$$\left\{-\frac{\nabla^2}{2} + v_{\mathrm{eff}}(\vec{r})\right\} n^{\frac{1}{2}}(\vec{r}) = \lambda n^{\frac{1}{2}}(\vec{r})\,, \tag{3.3}$$

where λ corresponds to the negative ionization energy [38]. However, in practice, it is known that the approach suffers from convergence issues [41]. Although, Chan, Cohen, and Handy [42] and more recently Karasiev and Trickey [43] tried to understand the convergence problems, the reasons remain unclear to the present day. Hence, this approach is limited to small molecules, which is unfavorable as OF-DFT is expected to be particularly strong for large-scale simulation, due to its inherent linear scaling.

Direct minimization

Due to the aforementioned drawbacks, most implementations directly minimize the energy functional (Eq. (3.2)). Therefore, investigations of large-scale problems using OF-DFT, which would be inaccessible by KS-DFT, are possible.

The most challenging part, however, is to come up with the kinetic energy density functional (KEDF). The main difficulty is that the contribution of the kinetic energy is a substantial part of the system's total energy, roughly one or even more orders larger than the XC. Hence even small inaccuracies in the description have a large impact on the simulations' overall accuracy and performance. KEDFs can be separated into local $T[n]$, and non-local $T[n, n']$ functionals, where the latter ones allow for a more accurate description, but therefore break the linear scaling. The most popular KEDFs were suggested by Wang, Govind, and Carter [44] (WGC, local), and Huang and Carter [45] (HC, non-local), however with a specific material system in mind. The need for a KEDF to accurately describe a system makes them inevitably non-transferable, which has hindered the application of OF-DFT for many decades.

The strong dependency on the quality of an OF-DFT calculation with respect to the employed KEDF makes the method not suitable for all types of materials systems. A few successful applications of the OF-DFT approach include investigations of Al-nanowires [46], dislocations in Mg [47], or melting of Li [48] with up to 10^6 atoms [49].

Advances in OF-DFT theory

Research in OF-DFT, which inherently scales better than KS-DFT, gained a new momentum with the advent of multi-core architectures. Therefore, the following section is separated into two parts. The first one shows theoretical improvements, while the latter one focuses on recent implementations. All of the research in OF-DFT is focused on finding (if possible transferable) KEDFs. While Burke and co-workers [50] suggested already in 2012 to use ML to KEDFs, several research groups [51, 52] for a more detailed review we refer the reader to Ref. [53].

The second approach is to add a kinetic potential to the Levy, Perdew, and Sahni [38] formulation, discussed in Sec. 3.1.1, to come up with an accurate description [54]. Such a potential can then be exactly constructed from KS-orbitals or HF-wave functions [55]. Both ML and potential construction approaches are far more data-efficient (only one or a few QM calculations) compared to ML-FF approaches, moreover providing access to the electronic structure. Yet the methods are still under vivid research, and yet reference implementations are missing.

Recent OF-DFT implementations

As best to our knowledge, there exists only one implementation, by Lehtomäki *et al.* [56] that reuses a KS code (GPAW [57, 58]), as this approach suffers from convergence problems. What VASP is in the KS-DFT community, PROFESS [37, 59, 60] is the corresponding popular counterpart in the OF-DFT, written by the Carter group.

More recently three new OF-DFT implementations appeared, namely ATLAS [61], CONUNDrum [62], and DFTpy [63], all utilizing direct minimization and designed with large-scale simulations in mind. While an OF-DFT approach is much simpler to implement than the KS approach, one should bear in mind that the scientific community is orders of magnitude smaller. Therefore, a review of the source code of the latter two codes (CONUNDrum [64] and DFTpy) reveals that the code quality is far behind those of well-established KS-DFT codes written in the same languages e.g comparing DFTpy [65] with GPAW (Python) or CONUNDrum [64] with S/PHI/nX [66] (C++). For the ATLAS code, sources are not available. Moreover, the implementations are far less feature-complete.

3.1.2 Linear scaling methods

Mostly "*linear-scaling*" or "$\mathcal{O}(N)$" methods became a synonym for approaches that do not use wave functions as the central quantity but rather use the "*density matrix*". For the sake of brevity in this section, we omit, how to recast the many-body Hamiltonian into a density-matrix formalism. In KS-DFT the density can be expressed as

$$n(\vec{r},\vec{r}') = \sum_i \phi_i^{KS}(\vec{r})\phi_i^{*,KS}(\vec{r}') \tag{3.4}$$

where ϕ^{KS} refers to the KS-orbitals, and the sum runs over all occupied states. Similarly, the density matrix is then defined as

$$n(\vec{r},\vec{r}') = \sum_{i,\alpha}\sum_{j,\beta} \phi_{i,\alpha}(\vec{r})K_{i\alpha j\beta}\phi_{j,\beta}(\vec{r}') \tag{3.5}$$

where K is referred to as the "density kernel". $\phi_{i,\alpha}$ are called the "*support functions*" [67, 68]. Imposing a locality assumption makes the kernel, and matrix, sparse and banded, and hence leads to a linear scaling of implementations. Note, that nearsightedness of electronic interactions [69] is also the key assumption beneath ML-FF force-fields (Sec. 3.2). Indeed it can be shown that the matrix elements decay exponentially in size with the distance $|\vec{r}-\vec{r}'|$ for metals, semiconductors, and insulators [70]. Note that the basic concept of the density matrix is even older than DFT [71].

The calculation itself is usually carried out by an iterative optimization of the matrix elements of the density matrix $K_{i\alpha j\beta}$, while two constraints must be met

1. **Conservation of the total number of electrons:** During an iterative process no electrons may be lost or created. In a density-matrix framework, the total number of electrons is given by
$$N = 2\mathrm{Tr}\left[K \cdot S\right] \tag{3.6}$$
where K is the density kernel from Eq. (3.5) and $S_{i\alpha j\beta} = \langle\phi_{i,\alpha}|\phi_{j,\beta}\rangle$ is called the overlap matrix.

2. **Idempotency:** While the above constrained is relatively easy to satisfy, driving the matrix elements such that
$$n(\vec{r},\vec{r}') = \int n(\vec{r},\vec{r}'')n(\vec{r}'',\vec{r}')\mathrm{d}\vec{r}'' \tag{3.7}$$
holds, is not. In fact, as Eq. (3.7) is hard to satisfy, many practical implementations rely on a weaker formulation of idempotency.

Note that in some implementations such as CONQUEST [72] the support functions are modeled as atom-centered functions, that also depend on their neighboring atoms' positions [72]. Such a construction is very similar to the ML-FF, with the difference that the charge density rather than the total energy is the central quantity. For a review of linear-scaling methods, we refer the reader to Ref. [73].

Although being successfully applied to large systems [74], the *localized* nature of the support functions makes the method suitable primarily for covalently bonded systems. The assumption of near sighted electronic interactions (similar to ML-FFs), makes them a bad choice for the description of the delocalized electrons in metallic systems.

As mentioned in Sec. 3.1.2, the nearsightedness of the electronic interactions, makes linear-scaling methods not a universal tool as KS-DFT, but rather limits its use to systems with ionic or covalent bonding. While for such systems linear-scaling methods were successfully employed for over two decades, the application to metals is still ongoing research [75]. Currently, many electronic structure codes implement linear-scaling methods, therefore, we focus here on recent advances in computing metallic systems. For a more detailed review of the implementations, we refer the reader to Ref. [76].

OpenMx implements a linear-scaling method, that is applicable even for metals [77]. Due to the pseudo atomic orbitals (PAO) used in OpenMx, it is highly non-trivial and requires careful tuning, to construct such a basis set suitable for large-scale calculations. Moreover, using more PAOs strongly increases memory requirements. Direct minimization is used to reduce the computational demand by the implementation in Onetep by Ruiz-Serrano and Skylaris [78]. More recently, BigDFT's[79] basis (Daubechies wavelets) were shown to be suited for an efficient linear-scaling approach [80], and was used to calculate $E-V$ curve and DOS of bulk tungsten tungsten employing 3456 atoms [81]. Nevertheless, the work of Mohr *et al.* [81], reveals that the cross-over point between standard KS-DFT and linear-scaling approach (for the tungsten bulk) is at a system size of around 500 atoms. Although, the above methods still scale linearly for metals, they come with huge prefactor, and should be therefore viewed as a proof of concept.

3.1.3 Extended-electron formalism

Within this approach, the authors try to overcome, the problem of finding a general KEDF of OF-DFT. A setback to the OF-DFT endeavors was when Seidl, Perdew, and Kurth [82] showed that the construction of such a general KEDF using perturbation theory would diverge. Therefore, the authors of this method took a more fundamental approach and suggested treating electrons as extended objects in space [83]. It took them nearly a decade to include spin [84] such that the model satisfies empirical observations. In their approach, the wave function of a many-body electron system might be written as a sum of mass and

spin density

$$\Psi(\vec{r}) = \sqrt{\rho(\vec{r})} + \vec{ie}_S\sqrt{S(\vec{r})} \tag{3.8}$$

where ρ is the mass and S the spin density. The total wave function consists of a scalar (mass) and a vectorial part (spin) which has three components in the most general case. $\vec{ie}_S$ denotes a bivector in a geometric algebra. Even before they came up with such an idea it was shown that geometric algebra can reproduce the results of the Pauli (standard) matrix approach of treating spin [85, 86]. Over the last decade, they proved that such a formulation can successfully explain observations made in the Stern-Gerlach [83, 87] or Aspect-type experiments [88, 89]. By restricting the spin to a scalar variable, they reformulated the many-body problem as OF-DFT-like two-density and proved that it yields results extremely close to KS-DFT [90] for small molecules. Therein, they reused the CASTEP code and experienced convergence troubles[1], which might be attributed to issues generally typical for OF-DFT [43]. More recently, they generalized their approach (=find an expression for the bivector potential) for vectorial spin components. We note that this approach has actually raised no attention in the scientific community. However, if such a description is suitable, it will be, firstly be truly linear scaling, secondly, inherently treating magnetism, thirdly, accounting for exact exchange, and finally pushing the boundaries in terms of system size by at least three orders of magnitude. Nevertheless, reference implementations are missing, as reusing a KS-code is probably not a good idea [43] and the vectorial spin component is hard to integrate into an existing OF-DFT code. Finally, due to the fully local nature of the appearing terms, implementation of this model is inherently very well suited to paralleling on modern many-core architectures.

3.2 Machine Learned Force Fields (ML-FF)

The task of creating an ML-FF is to construct a functional form of the PES (Eq. (2.7)) of a system from a small number of reference calculations. The calculations, often carried out using DFT or post-HF methods provide sample points on the PES. The ML-FF is then fitted/trained and used to predict the energy/forces of new configurations. Many different flavors of machine-learned inter-atomic potentials popped up recently and are applied to study various phenomena. While we restrict ourselves to flavors used to study thermodynamics in bulk systems, to demonstrate the broader applicability of ML-FFs, we list a few recent examples. Sauceda *et al.* [91, 92], Chmiela *et al.* [93] studied electronic effects in small molecules using CCSDT (coupled-cluster-singlets-doublets-triplets), reference data. Chemical reactions were studied using both CCSDT [94] and MP2 references [95, 96]. There exist

[1] Private communication with T. Pope

many ML-FFs, and they differ mainly in two points. Firstly, the method they use to encode atomic environments (the descriptors) and consequently the basis functions in which they expand the PES. Secondly, the machine-learning method (regressor), which is used to train the potential.

3.2.1 Common ingredients and concepts of ML-FF

No matter, which flavor of ML-FFs is chosen, all of them try to solve the same problem. Namely, to break up a non-local quantity e.g., the energy into a sum of local contributions. Therefore, in a system with N atoms, the property is rewritten as a sum of local "*environments*". These local environments are usually defined as the set of atoms within a cut-off sphere of size r_{cut}, often chosen to be between 5 and at most 10 Å [97, 98]. Thus, given M_i neighboring atomic positions $\vec{R}'_j$ within the cut-off sphere of the i^{th} atom , the problem reads

$$E = \sum_{i}^{N} U_i(\mathcal{D}(\vec{R}'_1, \ldots, \vec{R}'_{M_i})) \; . \tag{3.9}$$

U_i is the energy contribution of the environment centered around the i^{th}. As the Cartesian coordinates are a bad choice for the parameterization of U_i, the "*descriptor*" function $\mathcal{D}$ is introduced. $\mathcal{D}$ extracts a representation of the local atomic environment – the "*descriptors*" – from the local atomic environment. Given such an environment, an arbitrary number K of descriptors $\vec{d} = (d_1, \ldots, d_K)$ are computed, such that $\mathcal{D}(\vec{R}'^{,i}_1, \ldots, \vec{R}'^{,i}_M) \to \vec{d}$. Note that each descriptor $d_i \in \vec{d}$, (in general) is not necessarily a scalar (as the notation may suggest), but also might be a vector, matrix, or even a function. Consequently, $\mathcal{D}$ actually represents "*family*" of functions, yet for simplicity we refer to it as *function*. We recapitulate: For each atom i, the descriptors $\vec{d}$ of its surrounding environment are computed by feeding it (the positions of the neighboring atoms) into $\mathcal{D}$. Those descriptors are used to parameterize U_i and hence again fed into the representation of $U_i(\vec{d})$.

These observations yield the two key steps of creating any ML-FF:

1. Find a set of descriptors $(d_1, \ldots, d_K)$, often called the *structure representation* (Sec. 3.2.2).
2. Find a representation of U_i in terms of the descriptors.

It is int these two points where ML-FFs differ from each other.

3.2.2 Structure representations

Properties of structure representations

One of the main goals in mind when creating an ML-FF is to accelerate (or replace to a certain degree) computationally demanding electronic-structure calculations. Hence, to

keep the computational acceptable, the descriptors should fulfill several properties. Firstly, a lower number of descriptors reduces the computational demand, however, in turn, reduces the degrees of freedom in parameterizing U_i. Secondly, the set of descriptors should be complete. In other words, each possible atomic environment should be mapped to a unique set of descriptors. Thirdly, the descriptors should be "*cheap*" to compute from the input structure. Moreover, there are further properties the descriptors have to fulfill, namely:

Translational invariantness Translating the nuclei, given an arbitrary translation vector $\vec{T}$ must not change the potential energy

$$\mathcal{D}(\vec{R}_i) = \mathcal{D}(\vec{R}_i + \vec{T}) \; \forall \; i \in 1, \ldots, M_i \, . \tag{3.10}$$

A natural way to construct a representation that satisfies translational invariantness is to use pair-wise distances, as they are used in Moment-Tensor-Potentials (MTP) [99]. Pair-distances $\vec{R}_{ij} = \vec{R}_j - \vec{R}_i$ is an efficient and robust choice for e.g. bulk systems, as phenomena such as bond-stretching are described accurately. However, in organic molecules, slight angular changes of functional groups can affect many pair distances simultaneously, in which such a description is not the optimal choice [97] as it is hard to learn.

Rotational invariantness Similarly to translation, the potential energy has to be invariant under any rotation Q in the orthogonal group of $\mathbb{R}^3$

$$\mathcal{D}(\vec{R}_i) = \mathcal{D}(\{Q \cdot \vec{R}_j^i\}) \; \forall \; i \in 1, \ldots, M_i \, . \tag{3.11}$$

A potential that does not satisfy the rotational property would potentially cause angular momenta to arise on molecules in dynamical simulations and hence is not practically usable [97].

Invariance to atomic permutations The potential energy surface is defined within the Born-Oppenheimer approximation (Sec. 2.1.1). Thus the ions are assumed to be indistinguishable. Hence, the energy must be invariant to any permutation of atoms of the same species.

Smoothness when an atom leaves or enters the interaction neighborhood While the cut-off sphere is an artificial restriction to be able to perform practical calculations efficiently, nature does not know about it. Therefore, if another atom is leaving or entering the sphere, the PES must not exhibit any discontinuities.

3.2.3 Representation of the atomic contribution

After having found proper descriptors $\vec{d}$, reference data can be collected to construct the PES. Therefore, suppose, we have computed N structures with DFT to sample the PES

and computed their descriptor vectors (= training set). Note that in the previous section N referred to the number of atoms. Then, the atomic contributions of the PES for an unknown configuration $\vec{d}$ are computed

$$U_i(\vec{d}) = \sum_j^N \alpha_j K(\vec{d}, \vec{d}^{(j)}) \,. \tag{3.12}$$

The training configurations are indexed by j. α_j refers to the elements of the coefficient vector, determined during the regression process. K refers to the *kernel* and measures the similarity between a training configuration $\vec{d}^{(j)}$ and the unknown $\vec{d}$. It is usually, but not necessarily linear, function and must be symmetric ($K(\vec{d}, \vec{d}') = K(\vec{d}', \vec{d})$) and positive definite. Eq. (3.12) has one import consequence: To obtain a good quality PES [100], in addition to the descriptors, a good measure of the distance in feature space (=kernel) $K(\vec{d}, \vec{d}')$ is essential. The representation (Eq. (3.12)) of the local atomic energy contribution, more precisely, the kernel function is determined by the regression method. This is the point where "*machine-learning*" enters the game.

3.2.4 Commonly used potentials by their descriptors

The research area is very vivid and therefore it is hard to give a complete overview. Nevertheless, recently, Drautz [101] as well as Musil *et al.* [102] showed that nearly all descriptors described below, including more recent developments (PIP [103], or NICE[104]) are related to each other. For an in-depth review of structural representations, we refer the reader to Ref. [102].

Steinhardt parameters Describing local atomic environments was necessary already before the ML era. Steinhardt, Nelson, and Ronchetti [105] proposed bond order parameters, which found many different applications over the last decades. Specific subsets of Steinhardt's parameters are used to accomplish, e.g., solid/liquid [106] or lattice classification, or identification of defects. Being computed by a sum of spherical harmonics over all neighboring atoms, they are already inherently translation and rotation invariant. They have been used already as a basis for the empirical interatomic-potentials [107]. Note, that the bispectrum descriptor (discussed below) is a generalization of Steinhardt's parameters [108].

Atom-centered symmetry functions (ACSF) In 2011 Behler suggested ACSFs [109]. He proposed three two-body (=functions of the pair-distances) functions to encode the radial part of the environment and two three-body functions to encode the angular part. Those functions consist of an *ad-hoc* chosen analytic part multiplied by a cut-off function, inspired

by Tersoff [110] potentials. ACSFs were designed for and are still a popular choice in neural netword (NN)-based FFs [109].

Gaussian Approximation Potentials (GAP) was the first non NN approach. The main novelty of Bartók *et al.* [111] is the usage of the so-called *bispectrum* many-body descriptor [112]. It is a three-point correlation function, allowing nearly a one-to-one representation of the atomic neighborhood (completeness), and is computed by projecting the atomic density function on a four-dimensional unit-sphere. Represented by a series expansion of 4D spherical harmonics it satisfies all the properties discussed in Sec. 3.2.2. The potential gets its name from the fact that the bispectrum coefficients are computed using Gaussian process regression (kernel in Eq. (3.12) is a generalized multivariate Gaussian). The representation of the atomic structure as a bispectrum brought superior accuracy to GAPs, compared to the NN potentials at the time they were developed.

Smooth overlap of atomic positions (SOAP) representation improves a shortcoming of ACSF in combination with NN. Namely, no matter how good the descriptors are, in a NN approach the kernel function – Eq. (3.12) – might not necessarily be a good choice for the PES prediction. Using NNs, the kernel depends on the setup (number of hidden layers and activation function). Using the bispectrum descriptors from the GAPs approach, Bartók, Kondor, and Csányi [100] derived a closed form for a kernel (SOAP kernel) yet with a slightly different definition of the atomic density function (sum of Gaussian's centered at the neighboring atoms). The advantage of a known kernel function is three-fold. Firstly, adjusting the similarity measure during the fitting process allows for more control during the fitting process. Secondly, results become more reproducible compared to NN approaches. Thirdly, the kernel allows for a better representation of the atomic contributions (Eq. (3.12)). Finally, we note that SOAP is not a representation of atoms, but rather a definition for a kernel. Summarizing, the SOAP kernel improves the representation of U_i (Eq. (3.12)) for the descriptors used in GAP.

Spectral neighbor analysis potential (SNAP) uses the same (bispectrum) descriptors as proposed by the early version of GAP [111]. The major difference to GAP is it uses a different representation of the atomic contribution. SNAP [113] expresses the atomic contribution, by adding a linear term of selected bispectrum components to a reference potential. Having a linear kernel allows an efficient calculation of the forces [113] as a closed form is known. Recently, it was found that SNAPs can be improved by adding an additional quadratic term [114].

Moment Tensor Potential (MTP) use a cleverly chosen set of basis functions, of which the atomic energy is a linear expansion of, and which satisfy all the properties discussed in

Sec. 3.2.2. The basic building blocks of the basis functions are so-called moment-tensors, consisting, similarly to the bispectrum, of a radial and an angular part. The angular part is encoded in "*powers*" of the pair-distance vectors of the neighborhood. The "*powers*" are constructed, such that they yield multi-dimensional tensors, representing moments of the pair-distances. While ACSFs contain only two and three body terms, the bispectrum and the moment-tensor approach can approximate any arbitrary multibody interaction. Their accuracy, similarly as for GAPs, is systematically improvable [99], and consequently they can be efficiently evaluated [115] and therefore cut the computational demand.

Atomic cluster expansion (ACE) is based on an earlier work [116] showing a close relation between multibody-potentials and cluster expansion (CE) formalism. Drautz [101] expands the local atomic energy in a CE style, as a sum of multi-body contributions that read

$$U_i = U_i^{(1)}(\vec{R}_i) + \frac{1}{2!}\sum_j U_i^{(2)}(\vec{R}_i, \vec{R}_j) + \frac{1}{3!}\sum_{j,k} U_i^{(3)}(\vec{R}_i, \vec{R}_j, \vec{R}_k) + \dots \,. \tag{3.13}$$

However, CE expansions suffer from two major drawbacks. Firstly, the CE sum converges slowly, such that multi-body contributions of order > 15 are required to describe properties of metals [116]. Secondly, the number of individual contributions $U^{(k)}$ scales exponentially, and thus is prohibitively expensive. By expanding the multi-body-terms $U^{(k)}$ as a product of orthogonal basis functions, one can rewrite Eq. (3.13) by exploiting coefficient symmetries. Doing so the CE energy becomes polynomial with respect to the basis, and therefore can be evaluated in linear time [101]. Moreover, Steinhardt's bond-order parameters, bispectra, as well as the moment-tensor description can be cast into the ACE formalism [101].

3.2.5 Concluding note on what potential to use

While all of the above-presented potentials are designed for general usage, there are a few considerations to make when applying such ML-FF. Under the perspective of data efficiency – how much data is needed to train such a potential – GAP, MTP, and ACE outperform [98] NN approaches. The flexibility of NNs (adjustable, yet intransparent kernel) has to be accounted for with more data. Furthermore, they are also superior in both accuracy and computational efficiency, as the underlying energy representation is physically informed. In contrast to NNs, all approaches utilizing a series of basis functions (GAP, MTP, ACE), are systematically improvable. Adding more basis functions will improve the accuracy at the cost of computational efficiency. While larger NNs will achieve the same, one can not do that in a systematic way. The newer development (MTP and ACE) allow for more efficient evaluation, compared to GAPs and SNAPs, without, sacrificing (at least for showcases) accuracy. While at this time (spring 2023), ACE's implementation – PACE – allows for the fastest

evaluation per MD time step [117]. Nevertheless, even PACE increases the computational cost, compared to an empirical potential, by roughly two orders of magnitude [117]. We note that for quantum-chemistry applications different types of potentials, then those described here are used [93, 118]. For an overview of available potential flavours we refer the reader to Tab. 3.1.

3.3 Hybrid methods

Hybrid methods exploit, that in a system with a crystal defect, only a small region is of interest. Only within this region, "*high accuracy*" of electronic structure methods is necessary, while the bulk-like surroundings might be treated with a computationally cheaper methodology. Hence, such hybrid approaches are inherently not as universal as electronic structure methods, as they assume a bulk-like material around the defect. However, they can greatly improve computational efficiency compared to using electronic structure methods solely.

3.3.1 Lattice Green's functions

A very elegant and computationally efficient approach is to couple the QM region with the bulk via lattice Green's functions (LGFs), developed by Sinclair *et al.* [133]. Woodward and Rao [134] were able to study the long-ranged strain field of dislocations [135]. Therefore, the surrounding region is coupled via LGF

$$u(\vec{R}') = -\sum_{\vec{R}'} G^L(\vec{R}, \vec{R}') f(\vec{R}')\,. \tag{3.14}$$

G^L, the lattice Green function provides an approximation to the displacements u near a defect due the forces f in the harmonic limit [136]. The forces on an atom can be expressed in turn via the force constant matrix $D(\vec{R}, \vec{R}')$. In other words, G^L denotes the lattice's response to the forces around the defect. Such a coupling allows very accurate coupling by eliminating the mismatch between QM and classical molecular mechanical (MM) potentials. There, are a few reasons why the method is limited to selected applications (mostly dislocations).

Firstly, while LGFs for points are known for a long time in a closed form [137, 138], one has to note that the response is different for each crystal structure. Although Ghazisaeidi and Trinkle [139] proposed an approach for general Bravais lattices, it remained unsuitable for multi-atom-basis geometries. Yasi and Trinkle [140] came up with a method to compute the LGF for bulk cells with multiple atoms in the unit cell. Note, that all of these developments refer to a point (line) defect in a bulk crystal, which immediately shows up the next shortcoming in terms of applicability. QM/LGF coupling becomes a highly non-trivial task once

Table 3.1: Summary of popular ML-FFs. The first column contains the name, the second the names and the publication where the FF has been suggested. The third column refers to the regression method (KRR = kernel ridge regression, GPR = gaussian process regression), while the last columns, states the name and a reference to an implementation. For a more flavours of ML-FFs we refer the reader to Refs. [97, 98].

FF Type	Author(s)	Regression method	Implementation
Artificial neural networks	Behler and Parrinello [119]	NN	RuNNer [120] (LAMMPS)
aenet	Artrith and Urban [121]	NN	aenet
amp	Khorshidi and Peterson [122]	NN	amp [122] (ASE)
DeePMD	Chmiela *et al.* [123]	NN	DeePMD-kit (LAMMPS)
PhysNet	Unke and Meuwly [118]	NN	
symmetric gradient domain machine learning (sGDML)	Chmiela *et al.* [93]	KRR	sGDML [124]
adaptive, generalizable, and neighborhood informed (AGNI)	Botu and Ramprasad [125] [126, 127]	KRR	LAMMPS
Gaussian approximation potentials (GAP)	Bartók *et al.* [111]	GPR	GAP [128]
Modified GAP + tree body angular terms	Jinnouchi, Karsai, and Kresse [129],[130]	KRR	VASP [131]
Moment tensor potentials (MTP)	Shapeev [99]	linear	mlip [115] (LAMMPS)
Spectral neighbor analysis potential (SNAP)	Thompson *et al.* [113]	linear	FitSNAP (LAMMPS) [132]
Atomic cluster expansion (ACE)	Drautz [101]	non-linear	PACE [117] (LAMMPS)

a planar defect (grain-boundary, interface) crosses the QM domain. Ghazisaeidi and Trinkle [141] proposed a method how to compute LGF for planar defects, however to the best of our knowledge, the method has never been applied to a real use case. Furthermore, all the aforementioned developments, came from a single group (Trinkle at Illinois), consequently only a very limited set of tools are available to implement such QM/LGF coupling with a boundary inside the QM region. Finally, the main setback of the QM/LGF coupling is that there is no universal approach. Consequently, a change in the bulk material or defect type (e.g. interface, vacancy, or dislocation) would implicitly lead to methodological changes. Lastly, with real material becoming chemically more complex, it will be hard — if not impossible — to couple a disordered QM region (discrete picture), with an LGF for a disordered bulk (continuous picture).

3.3.2 Constrained DFT

Another, elegant way of coupling a QM region to a bulk MM region is by introducing boundary conditions. The charge density at a sufficient distance from a defect is again similar to those found in the bulk region. Such a coupling proposed by Zhang, Lu, and Curtin [142], works by partitioning the total system into three, a *core* (I), *buffer* (II) and a bulk-like region (III), according to Fig. 3.1. Regions I and II are placed into a vacuum, which will introduce forces, due to undulations in electrostatic potential (see Fig. 3.1d)

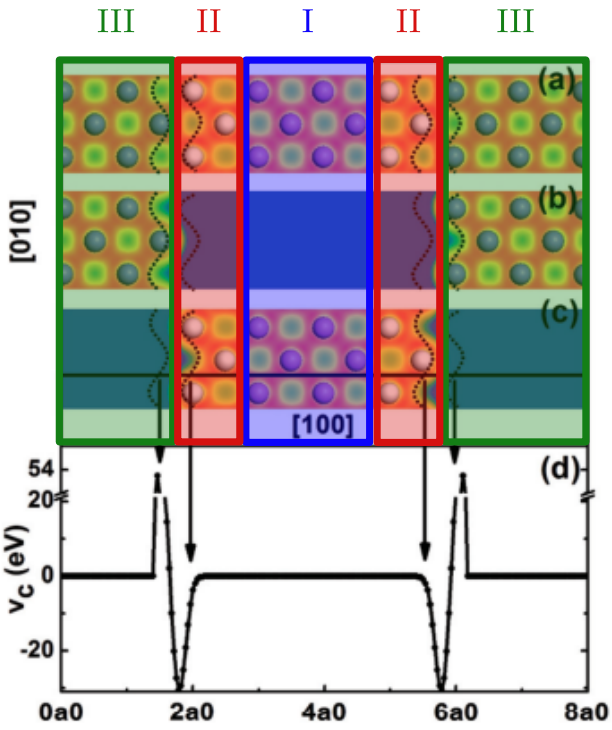

Figure 3.1: System decomposition into *core* (I, blue), *buffer* (II, red) and bulk-like region (III, green) [142]. The lower panel shows the compensation potential from Eq. (3.15).

Hence, the main concept is to drive the charge density $n(\vec{r})$ towards a bulk-like density, to eliminate the artificial forces. Practically, this is achieved by introducing a penalty term to the KS-Hamiltonian, and introducing an external potential in an overlap (=constrained) region Ω_C between II and III (dashed lines in Fig. 3.1c). The external potential, driving the charge density to be a bulk-like reads

$$\tilde{v}_c^{\lambda}(\vec{r}) = \lambda \int_{\Omega} \frac{n_{\mathrm{QM}}(\vec{r}') - n_{\mathrm{target}}(\vec{r}')}{|\vec{r} - \vec{r}'|} \mathrm{d}\vec{r}' \tag{3.15}$$

The constraint potential $\tilde{v}_c^{\lambda}$ constraint is a penalty term associated with the total electrostatic potential generated by any differences between the target and actual electron densities [142]. λ is the weight of the penalty term. Consequently, introducing such a potential requires a modification of the KS-Hamiltonian, such that Eq. (2.16) becomes

$$\left\{ -\frac{\nabla^2}{2} + v_{\mathrm{eff}} + \overbrace{w\tilde{v}_c^{\lambda}}^{v_c^{\lambda}} \right\} \phi_i^{\lambda}(\vec{r}) = \varepsilon_i^{\lambda} \phi_i^{\lambda}(\vec{r})\,. \tag{3.16}$$

$w(\vec{r})$ is a cutoff function, to spatially confine within Ω_c and thus to make the coupling numerically stable. Note, that in addition to the constraint potential Eq. (3.16), λ was introduced as a parameter. The solution is then found for $\lambda \to \infty$ [143], which refers to perfect coupling. Therefore, the only source of methodological error is introduced from λ not being infinity. Hence, the "*error*", arising from a finite λ can be measured using

$$C(\lambda) = \frac{1}{2\lambda} \int_{\Omega_c} \left(n_{\mathrm{QM}}(\vec{r}) - n_{\mathrm{target}}(\vec{r})\right) v_c^{\lambda}(\vec{r}) \mathrm{d}\vec{r}\,. \tag{3.17}$$

Consequently, there is a single knob to turn to improve coupling. In practice, the λ parameter space is sampled with a few numbers, and the solution $\lambda \to \infty$ is extrapolated. While coupling QM and MM on a charge density level, is without a doubt extremely elegant, the approach does not come without shortcomings.

Firstly, keeping the QM buffer regions, and, consequently, system sizes small, is traded against the sampling of the penalty parameter λ. Thus at least a few SC-loops are needed to get a converged KS-DFT. For calculations, where ionic relaxations take place, the sampling becomes a major bottleneck. Unfortunately, this is often the case for defects. Secondly, the construction of the bulk-like charge-density n_{target}, which is an elaborated process, and requires again a DFT calculation in advance. Zhang, Lu, and Curtin [142], broke the total density apart into atomic contributions and parameterized the atomic charge densities using Gaussian-type orbitals. Thirdly, modifying a KS-Hamiltonian requires also changing the underlying code, which is a nontrivial task. Lastly, also the convergence of the constrained charge density as a function of λ varies from system to system and needs investigation.

Chapter 4

QM/MM for metals

The main challenge in studying crystal defects is that many (hundreds) of atoms are needed to model them, while still, a very accurate description is necessary. The reasons for large models are manifold. Some defects, such as dislocations exhibit long-ranged stress fields. Consequently, the dislocation core needs to be padded with matrix material resulting in large simulation cells. Another reason is that in practice many implementations of DFT utilize periodic boundary conditions to solve Eq. (2.16) efficiently. Thus structural motifs for low-symmetry (planar) defects require to incorporate hundreds of atoms. The grains in Fig. 4.1 are separated by a highly symmetric boundary, which allows to create small atomistic models. This is however, not the case for grain boundaries in general. However, a closer look at the underlying atomistic models reveals that the majority of the atoms are constituents of a matrix region, marked red in Fig. 4.1 in which the defect is embedded.

Thus the simple idea of QM/MM is to treat the matrix-like regions (red in Fig. 4.1) by classical approach (=MM), and the region of interest with modified chemistry (blue) using

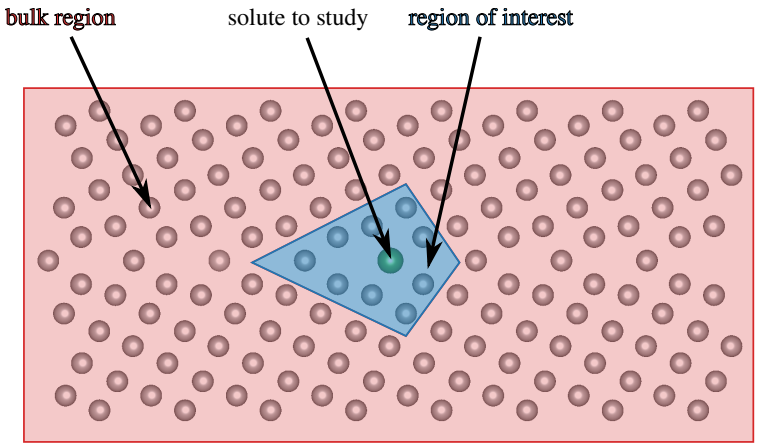

Figure 4.1: Atomistic model of a Σ5(210) grain boundary in fcc-Al with a solute atom. The blue region represents the chemically interesting region.

an accurate quantum-mechanical treatment (=QM). Both methods are coupled by a property that is accessible to QM and MM treatments. In most QM/MM schemes the regions are coupled by the atomic forces. This makes QM/MM schemes a very universal tool since any method capable of computing forces on atoms is a potential candidate for the QM region. Similar arguments hold for the MM region. In practice, most of the schemes couple KS-DFT with MD [1, 144, 145]. If not specified otherwise, in the following we will assume exactly such coupling. Of course, such an approach also exhibits downsides. Firstly, some system properties (e.g. electronic structure, pressure) are not accessible throughout the whole system as they might not be defined or representative. Secondly, the method exhibits a computational overhead in terms of additional atoms resulting in large(r) DFT cells which needs to be taken into account.

The present section gives an introduction to the QM/MM scheme suggested by Huber *et al.* [1]. Therefore, the notation and the order of presentation for Secstions 4.1 and 4.2 are taken from Ref. [1]. We then continue with a short section presenting some technical details of our implementation. The next section suggests a method on how volume relaxations might be incorporated into the QM/MM scheme if the system can be modeled with reduced dimensions as presented in Sec. 4.5.1.

4.1 System decomposition/partitioning

Consider a large system — similar to Fig. 4.1 — with a small region of interest (I, blue) surrounded by matrix material (II, red). In the following, we will refer to Region I as "QM" and Region II as "MM" region. Moreover, following the notation of [1], superscripts denote the description of the method the region is treated with. As already suggested in the 1990s [146, 147], the total energy for such a system can be written as

$$E_{I+II} = E_I^{\mathrm{QM}} + E_{II}^{\mathrm{MM}} + E_{\mathrm{int}} \tag{4.1}$$

where E_{int} is the interaction energy between the systems. If E_{int} is known exactly, the decomposition would be ideal (Fig. 4.3a). Upon partitioning a system into a QM and a MM region, the applicability of a scheme strongly depends on how accurately the interactions between the systems, E_{int}, are described. In molecular systems, due to covalent bonding, the electrons are confined within those bonds. Thus, the QM part is "*cut*" out from the whole system upon partitioning, and the broken bonds are saturated with so-called "*link*" atoms. In organic chemistry, well-established and mature QM/MM schemes such as ONOIM [148–150] are available. However, cutting the QM region out of a metal bulk will create vacuum surfaces, which themselves introduce large perturbations of the charge density. Moreover,

Fig. 4.2 reveals that those are long-ranged, thus leading to incorrect forces also far away from the surface, which in turn makes the force-based coupling more difficult.

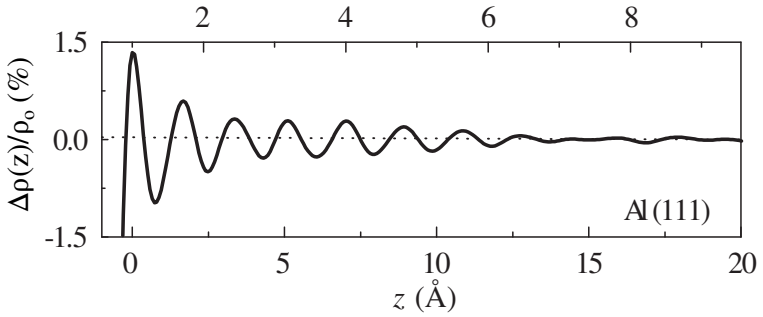

Figure 4.2: Friedel oscillations on Al (111) surface. The bottom axes are the distance from the surface and the top axis is the index of the atomic layers [151].

In practice E_{int} has to be approximated. Following the work of Choly *et al.* [144] and [1] we employ a classical approximation.

$$E_{\text{int}} \approx E_{\text{int}}^{\text{MM}} = E_{I+II}^{\text{MM}} + E_{I}^{\text{MM}} - E_{II}^{\text{MM}} \tag{4.2}$$

Note that, it is hypothetically possible to compute E_{int} using QM methods, the additional computational demand would outweigh the gain in accuracy by far [152]. Hence, a classical approximation was found to be a good compromise between accuracy and computational cost [144]. Now, substituting Eq. 4.2 into Eq. 4.1 leaves us with an expression for the total QM/MM energy

$$E_{I+II} \approx E_{I+II}^{\text{QM/MM}} = E_{I+II}^{\text{MM}} - E_{I}^{\text{QM}} - E_{I}^{\text{MM}}. \tag{4.3}$$

This scheme was first presented by Choly *et al.* [144]. They cut region I from the bulk material, and impose 3D-periodic boundary conditions on the QM cell. Moreover, they employed OF-DFT in the QM region to investigate the core of a screw dislocation. As the dislocation core is embedded in pure bulk, there are no discontinuities at the edges of the QM cell, which is specific to the dislocation model. Consequently, Choly's scheme cannot be straightforwardly applied to grain boundaries. Liu *et al.* [153] refined Choly's approach and suggested to subdivide region I into a "*core*" and "*buffer*" zone (Fig. 4.3b). For the *core* region, the corresponding energies of the MM representations $E_{I+II}^{\text{MM}} - E_{I}^{\text{MM}}$ cancel each other such that only E_{I}^{QM} is left. The positions of the *buffer* atoms are determined by the MM forces. Consequently, they do not suffer from the vacuum surface and protect the *core* atoms from begin exposed to the artificial interface [153]. To obtain accurate energies for the total system, again the QM and MM energy contributions of the buffer-vacuum surface need to cancel. However, as a consequence of Eq. (4.2), this cancellation is rather poor. Nevertheless,

upon comparing the energy differences between two systems (e.g. formation energies), also this cancels unless the two systems yield very different buffer-vacuum interfaces. However, this is not expected, at least not for practical applications.

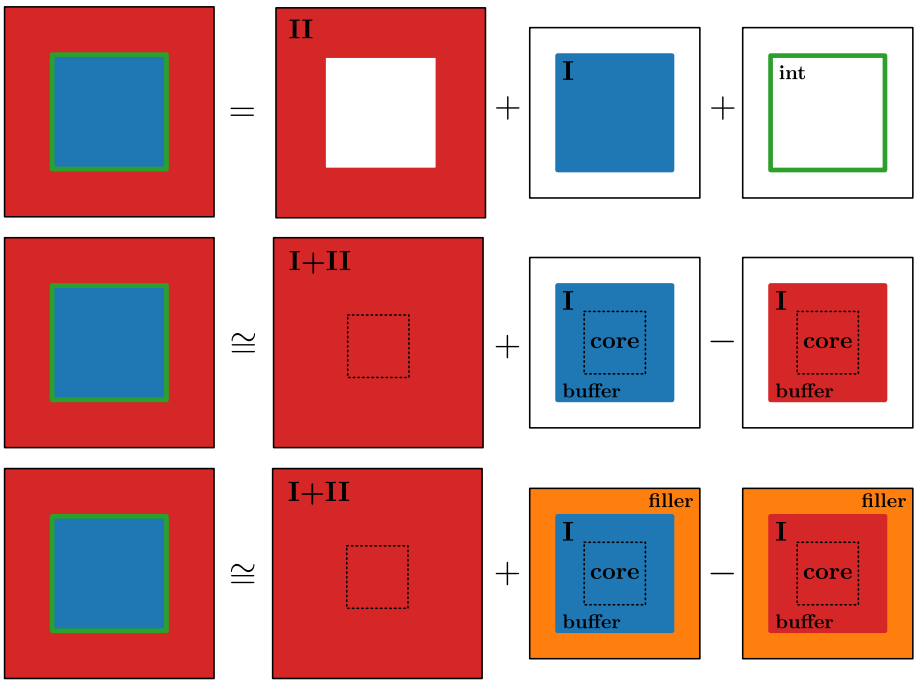

Figure 4.3: Schematic of the system partitioning into (a) ideal decomposition, (b) approximating classically and subdividing region I into *core* and *buffer* zones [153], and (c) the method proposed by Huber *et al.* [1], with filler region shown in gray.

4.2 Ionic relaxation

While the Eqs. (4.1)–(4.3) allow to carry out single point calculations, bear in mind that applying hybrid methods in metallic systems was mostly driven to capture long-range, e.g. elastic effects. Hence, it is desirable to relax the coupled system's ionic positions. Therefore, one needs to compute the forces on the ions for both regions, I and II. For the *core* region, we obtain contributions from all three energy terms of Eq. (4.3), hence the forces on the ions read

$$\mathbf{F}_{I+II}^{\mathrm{QM/MM}}(\mathbf{R}_I^{\mathrm{core}}) = -\nabla_{\mathbf{R}_I^{\mathrm{core}}} E_{I+II}^{\mathrm{QM/MM}} = \mathbf{F}_I^{\mathrm{QM}}(\mathbf{R}_I^{\mathrm{core}}) + \underbrace{\mathbf{F}_{I+II}^{\mathrm{MM}}(\mathbf{R}_I^{\mathrm{core}}) - \mathbf{F}_I^{\mathrm{MM}}(\mathbf{R}_I^{\mathrm{core}})}_{\approx 0}. \tag{4.4}$$

In the *core* region we want to have QM forces only, it turns out that the latter two terms cancel out nearly perfectly. Note, that if the buffer size is larger than the MM potential's cutoff radius, both terms equate exactly to zero [1]. Furthermore, to close the cutoff, the

MM potential must go to zero, thus this term is small anyhow. Nevertheless, to make sure that region I is exclusively described by QM, a correction force $\mathbf{F}^{\text{corr}}_{I_{\text{core}}} = -\mathbf{F}^{\text{MM}}_{I+II}(\mathbf{R}^{\text{core}}_I) + \mathbf{F}^{\text{MM}}_I(\mathbf{R}^{\text{core}}_I)$, such that Eq. (4.4) reads

$$\mathbf{F}^{\text{QM/MM}}_{I+II}(\mathbf{R}^{\text{core}}_I) = \mathbf{F}^{\text{QM}}_I(\mathbf{R}^{\text{core}}_I) \; . \tag{4.5}$$

Similarly to Eq. (4.4) for the *core* region, we obtain all three contributions also for the *buffer* region:

$$\mathbf{F}^{\text{QM/MM}}_{I+II}(\mathbf{R}^{\text{buffer}}_I) = -\nabla_{\mathbf{R}^{\text{buffer}}_I} E^{\text{QM/MM}}_{I+II} = \mathbf{F}^{\text{QM}}_I(\mathbf{R}^{\text{buffer}}_I) + \mathbf{F}^{\text{MM}}_{I+II}(\mathbf{R}^{\text{buffer}}_I) - \mathbf{F}^{\text{MM}}_I(\mathbf{R}^{\text{buffer}}_I) \; . \tag{4.6}$$

There is however, a substantial difference compared to Eq. (4.6), namely that $\mathbf{F}^{\text{QM}}_I(\mathbf{R}^{\text{buffer}}_I)$ and $\mathbf{F}^{\text{MM}}_I(\mathbf{R}^{\text{buffer}}_I)$ are strongly influenced by the artificial vacuum surface introduced due to the decomposition. Those forces are not sensible from a physical point of view, and similarly to the energies there is no reason to expect that they cancel out. Thus, as suggested by Liu *et al.* [153], a reasonable correction is to take the forces from the MM descriptions of the system. Hence, similarly as before, by introducing a correction force that reads $\mathbf{F}^{\text{corr}}_{I_{\text{buffer}}} = -\mathbf{F}^{\text{QM}}_I(\mathbf{R}^{\text{buffer}}_I) + \mathbf{F}^{\text{MM}}_I(\mathbf{R}^{\text{buffer}}_I)$, Eq. (4.6) will simplify to the MM forces of the whole system and hence become

$$\mathbf{F}^{\text{QM/MM}}_{I+II}(\mathbf{R}^{\text{buffer}}_I) = \mathbf{F}^{\text{MM}}_{I+II}(\mathbf{R}^{\text{buffer}}_I) \; . \tag{4.7}$$

Finally, for Region II there is only the MM description available such that the forces there are taken from the MM calculation of the whole system

$$\mathbf{F}^{\text{QM/MM}}_{I+II}(\mathbf{R}_{II}) = \mathbf{F}^{\text{MM}}_{I+II}(\mathbf{R}_{II}) \tag{4.8}$$

4.3 Filler-filler interface

Huber *et al.* [1] addressed the influence of the artificial vacuum surface on $\mathbf{F}^{\text{QM}}_I(\mathbf{R}^{\text{buffer}}_I)$ and $\mathbf{F}^{\text{MM}}_I(\mathbf{R}^{\text{buffer}}_I)$. Thus, as shown in Fig. 4.3c, they suggest substituting the vacuum surface, by a metal-metal interface. Atoms making up this interface are called "*filler*" atoms and are kept fixed during an ionic relaxation process. By imposing PBCs, the *filler-filler* interface electronically is much less perturbative compared to the vacuum surface, however, comes at the cost of additional atoms in the QM region. One may take the view, that the filler atoms lead very quickly to bulk-like charge density in the buffer zone. Consequently, Huber's

filler atoms work similarly as the coupling to a bulk-like charge density via-constrained DFT (Sec. 3.3.2) proposed by Zhang, Lu, and Curtin [142].

By keeping the *filler-filler* interface static throughout most of the calculations, those energy contributions will largely cancel upon taking the difference. The drawback of keeping the *filler* atoms fixed is, that since the *buffer* atoms are allowed to relax, also a *buffer-filler* interface is introduced. Those contributions do not necessarily cancel as those from the *filler-filer* interface do. Nevertheless, by increasing the *buffer* thickness the *buffer* atoms bordering the *filler* zone will exhibit smaller displacements. In other words, the methodological error introduced by the *buffer-filler* interface can be tackled with larger *buffer* zones. Nevertheless, note that this (probably) incomplete canceling is a concern also for schemes using a vacuum surface.

Huber's QM/MM scheme is similar to the QM/LGF coupling suggested earlier by Woodward and Rao [134]. If instead of the *filler* atoms, the *buffer* zone was to extend to the edge of the periodic domain, one would reproduce Woodward's method. However, the QM and MM contributions of the *buffer-filler* interface cancel better than for a *buffer-buffer* interface. Despite reported successful applications of Woodward's approach [135, 154–156], note that all applications require accurate forces and geometries only. In this point the *filler* augmented QM/MM scheme excels as it additionally to forces allows to compute also accurate energies of a system [1], e.g. segregation energies [157].

The errors of a QM/MM scheme with fictious *filler* atoms are comparable to the constrained DFT approach. The QM/MM scheme is however, preferable from a practical point of view. We have summarized arguments for this decision in Sec. 3.3.2.

4.4 Implementation

4.4.1 Basic infrastructure and algorithm representation

Since the QM/MM workflow requires coupling to different simulation codes to interact, in addition to structural partitioning, ionic relaxation, etc. it is desirable, to code such a workflow at a high level of abstraction. We note, that common workflows — assuming they are simple enough — can be encoded as a directed graph. A directed graph representation of a general workflow consists only of two types of nodes. Command nodes, shown in blue in Fig. 4.4, and branching nodes for a flow control. Each of the command nodes can be seen as a function taking several input values (possibly generated by a different command node) and producing several output values itself. Hence, in addition to the black lines (Fig. 4.4) denoting the execution flow, a "*data-flow*" exists in parallel. In practice the visualization of such yields extensive diagrams which is the reason why we omit them here.

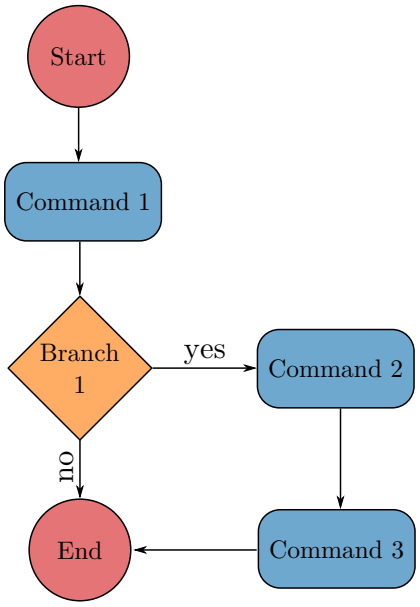

Figure 4.4: A directed graph, to represent a general workflow. The execution flow is denoted by the arrows. Blue rounded rectangles are operations, and yellow diamonds refer to branching blocks

Deferred execution of data flow We quickly want to focus on a the practical challenge encountered during encoding such directed graphs in a computer language. Consider the simple example of computing $2x^2$. Therefore, we link two command nodes, namely "*square*" having one (named "x"), and "*mul*", having two number(s) ("a" and "b") input values and one output value. Figure 4.5 shows how a corresponding directed graph might look like. Therefore consider the following listing to set up the data flow (blue arrows) in for the workflow shown in Fig. 4.5:

```
def setup_data_flow(g: Graph) -> NoReturn:
    g.square.input.x = g.input
    g.mul.input.a = g.power.output
    g.mul.input.b = 2
    g.result = g.mul.output
```

Listing 1: Setup of the dataflow for simple directed graph

Especially focus on the last line. Any computer program (independent of language) will execute the right-hand side and try to evaluate the corresponding value, which results in constant values being set upon the graph construction. Consequently, the correct behavior would be that `g.power.output` is evaluated at each time the command node is encountered during the execution. We have solved the problem by allowing "*Pointer*" to be set as values, which themselves represent a recipe on how to obtain the proper input value from another node. If such a pointer is encountered it is in-directed at run-time and the corresponding value is loaded. This is an elegant way to delay the execution with only minor changes to

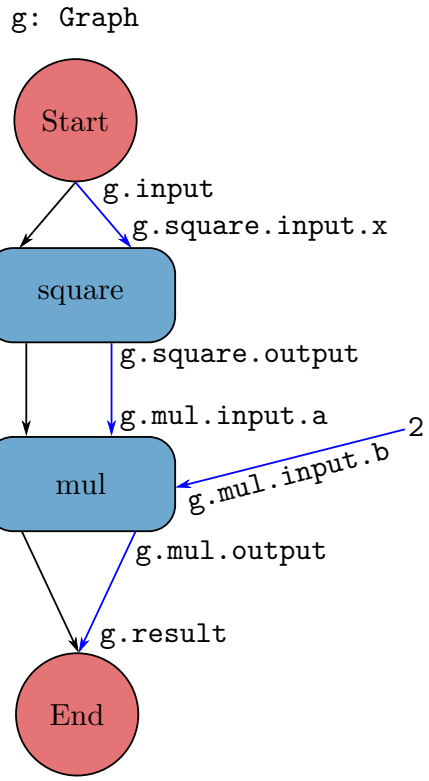

Figure 4.5: A directed graph, to represent the $2x^2$ workflow. The execution flow is denoted by the black arrows. Blue arrows represent the data flow. Each arrow corresponds to a input or output value of a node. The descriptions at the arrows refer to Lst. 1.

the code and maintain expressiveness. Hence, the only modification such that the above example works in our framework would be changing the last line from `g.power.output` to `Pointer(g).power.output`.

We have implemented such a directed graph infrastructure as a sub-part in an open-source package named `pyiron_contrib` [158], which itself implements community additions to the `pyiron` [159]. The present work focuses on the QM/MM workflow implementation, however, note, that using this directed graph infrastructure also other simulation workflows such as nudged-elastic-band method [160], general structural relaxation, finite-temperature-string method [161] and thermodynamic integration have been implemented.

4.4.2 System partitioning

The system partitioning step is the most important step of the QM/MM setup as it will strongly influence the quality of the results. However, there is no general way to construct the *core*, *buffer*, and *filler* zones. Consequently, our implementation features two different modes to decompose the system and set up the QM cell. The first one is to manually assign the atoms (through their id) to the individual QM domains, and manually specify the box size. The second, semi-automated approach was suggested by Huber *et al.* [1], where a

number of seed atoms (usually only a few around the defect) are chosen.

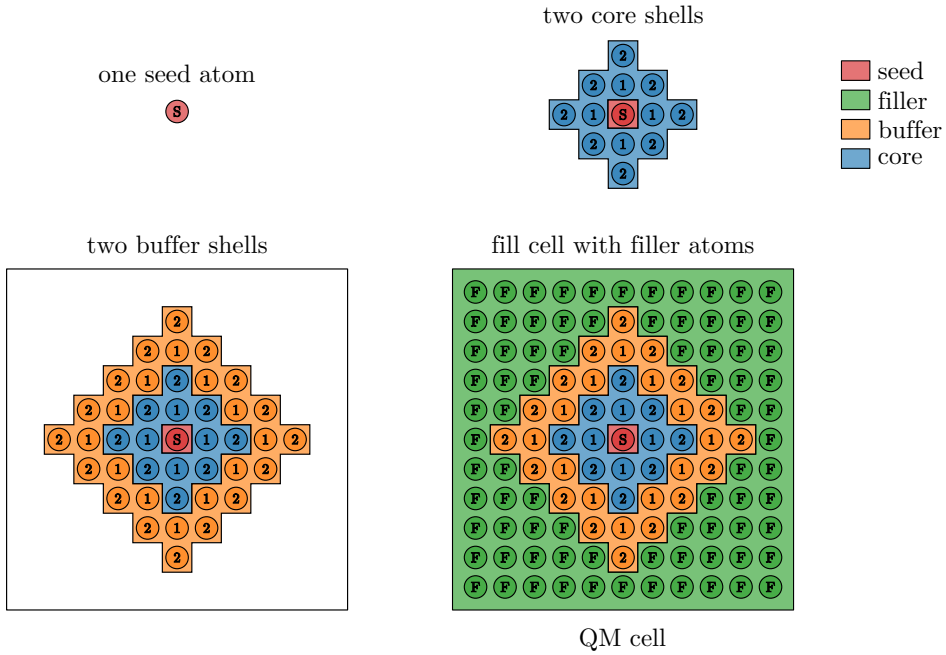

Figure 4.6: Illustration of the semi-automatic QM cell construction in our implementation. The schematic figure start from one seed atom, and adds two *core* and two *buffer* shells. The numbers within the atoms denote the shell index. For example, 2 in a blue circle indicates that these atoms belong to the second *core* shell.

Instead of manually assigning the atoms, the number of shells is specified for both *core* and *buffer* regions. As a "*shell*" we refer to the set nearest neighboring atoms. Fig. 4.6 illustrates such a schematic construction for two *core* and two *buffer* shells. After the construction of *core* and *buffer* domain, the cluster is padded with a user-specified *filler* spacing (see lower left figure in Fig. 4.6). This filler spacing might differ in different coordinate directions in practice. Finally, our algorithm fills up the cell with filler atoms marked in green in Fig. 4.6. Note, however, that even this semi-automated approach needs human intervention as atoms might get too close and eventually require manual deletion, depending on the system. Furthermore, this approach will not work, or at least not yield the most computationally efficient cells, under all circumstances.

4.4.3 Structural minimizers

Most of the implementation efforts within this work were dedicated to providing calculation framework, that allows coupled QM/MM relaxation. Therefore, we have implemented two different minimizers. A simple gradient descent and a (limited memory) Broyden-Fletcher-Goldfarb-Shanno (L) [162]-BFGS [163–166] algorithm. Internal tests revealed that the gradient descent algorithm led to more robust calculations at the cost of slower convergence. The gradient descent implementation exhibits an adaptive weight feature, which itself was found

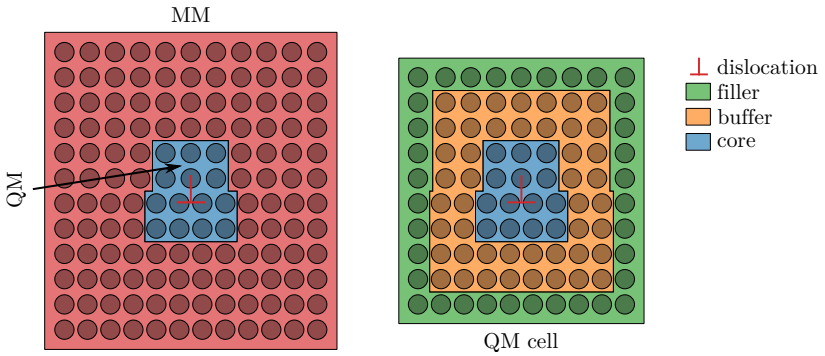

(a) Schematic system decomposition for an edge dislocation. The QM cell is built using *filler* atoms according to Huber *et al.* [1].

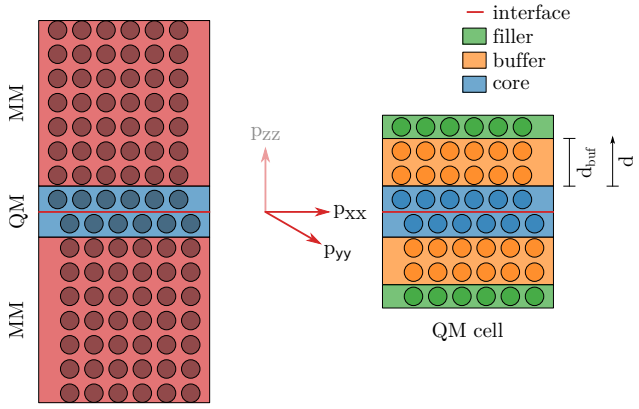

(b) Schematic system decomposition for a stacking fault.

Figure 4.7: Possible QM/MM decompositions and QM cells for a) a dislocation and b) a stacking fault.

(again by internal tests) to slow down the convergence overall. If not mentioned otherwise, results within this thesis were obtained using the gradient descent algorithm.

4.5 Properties across both systems

4.5.1 Volume relaxation in with reduced dimensions

As previously mentioned not all system quantities are available both to classical and electronic structure methods. Furthermore, due to the artificial coupling artifacts, e.g., *filler* atoms due to PBCs, some properties such as, e.g., pressure in the QM cell have no physical meaning. The consequence is that volume relaxation cannot be taken into account for the QM region. Usually, the stress on a simulation box is defined in DFT codes as

$$\sigma_{\alpha\beta} = \frac{1}{V}\frac{\partial^2 E}{\partial\varepsilon_\alpha \partial\varepsilon_\beta}\,, \tag{4.9}$$

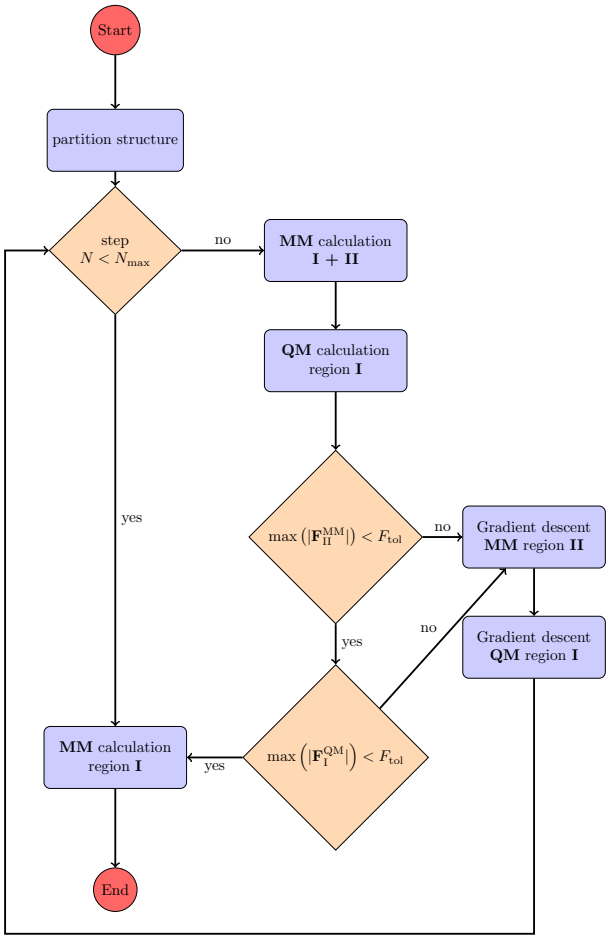

Figure 4.8: Execution diagram of the QM/MM scheme proposed by Huber *et al.* [1] for an ionic relaxation calculation. Blue rectangles refer to execution blocks, whereas orange denotes branching blocks

where the greek subscript letter denote the coordinate axes. While in a plane-wave expansion, for instance, the components of $\sigma_{\alpha\beta}$ can be calculated analytically for each term of the Hamiltonian, the above equation does not apply to the MD approach. In the classical simulation approaches, the pressure is computed via the virial theorem and reads

$$\sigma_{\alpha\beta} = \frac{1}{V}\left[\sum_{k}^{N} \underbrace{M_k v_\alpha^k v_\beta^k}_{\text{at 0 K=0}} + \sum_{k}^{N} R_\alpha^k f_\beta^k\right] \tag{4.10}$$

where M_k is the atomic mass, v_α^k the velocity of the k^{th} atom into the α direction. R_α^k is the α component of the k^{th} atom position vector, and f_β^k the β component of the corresponding force vector.

Note that, all presented QM/MM schemes (presented above) are centered around calculating accurate forces, which are then used to couple both methods. As the forces $\mathbf{f}^k$ are accessible to

both DFT and MD, we suggest that the virial stress (Eq. (4.10)) can be used to relax (a subset of) the lattice parameters of the simulation cell. However, for point defects where the QM cell is padded with *filler* atoms in all three dimensions (e.g. Fig 4.7a), the pressure of the system has no meaning as the filler atoms are kept fixed artificially. Moreover, it would be hard to model shearing of the *core* (and *buffer*) region as that leads to a deformation of the QM cell and hence possibly to non-constant *filler-filler* interactions throughout a single calculation. Nevertheless, consider a system that can be modeled with reduced dimensionality such as the stacking-fault shown in Fig. 4.7b, where the *core* region is spanning the whole QM cell in two dimensions and is padded with *buffer* and *filler* atoms only in the direction perpendicular to the interface. In such scenario, the stress components σ_{xx} and σ_{yy} can be computed for the QM cell, from the forces obtained from the QM methodology. Note, that Eq. (4.10) will need an adaption since the QM forces for the *buffer* atoms at the *buffer-filler* interface have again no physical meaning. To circumvent this we suggest a linear force-mixing in the *buffer* region, such that Eq. (4.10) becomes

$$\sigma_{\alpha\beta} = \sum_{k\in\{\mathbf{R}_I^{\text{core}}\}}^{N} R_\alpha^k f_\beta^k + \sum_{k\in\{\mathbf{R}_I^{\text{buffer}}\}}^{N} R_\alpha^k \left[\chi f_\beta^{k,\text{QM}} - (1-\chi) f_\beta^{k,\text{MM}}\right] . \tag{4.11}$$

Hence for the *buffer* atoms we mix the QM and MM forces such that at the *core-buffer* interface we use QM and at the *buffer-filler* interface pure MM forces. Consequently, those atoms (at the *buffer-filler* interface) exhibit a "*bulk*"-like force rather than artificial ones induced by the *filler* atoms. Therefore, χ is a function of distance from the core region having the value one at the *core-buffer* and zero at the *buffer-filler* interface. For Fig. 4.7b with a buffer thickness of d_{buff} and d as the distance from the *core* region one obtains

$$\chi = 1 - \frac{d}{d_{\text{buff}}} \tag{4.12}$$

Finally, we note that the presented approach is not implemented in the current version of the QM/MM scheme, as it is only suitable for a subset of the problems.

4.5.2 Local atomic strain

Furthermore, it is possible to derive the virial strain also for an atom i, which at 0K is computed from by a tensor product of the interatomic forces and the distance vectors to the neighboring atoms within a sphere of volume Ω as [167]

$$\sigma_{\alpha\beta}^i = \frac{1}{2\Omega} \sum_{j\in\Omega} (R_\alpha^i - R_\alpha^j) \otimes f_\beta^{ij} . \tag{4.13}$$

Similary to Eq. (4.10) the greek subscripts correspond to the individual components. The summation includes all neighbors within a volume Ω and is usually truncated using a cutoff radius. To compute the local atomic strain throughout the whole QM/MM cell one must recall that the β component of the pair force between atom i and the neighboring atom j, f_β^{ij} and is easily accessible in MM. For the QM we have to reconstruct this property manually.

Reconstruction of the pair-forces via charge density

In a DFT framework where the spatial distribution of all electrons $n(\vec{r})$ is known, the forces on the ions are calculated using Hellman-Feynman theorem as the derivatives of the Hamiltonian with respect to the i^{th} nucleic coordinate component in a direction α

$$f_\alpha^i = -\left\langle \Psi \left| \frac{\partial \hat{H}}{\partial R_\alpha^i} \right| \Psi \right\rangle . \tag{4.14}$$

Carrying out the differentiation for the many-body Hamiltonian one obtains [168]

$$f_\alpha^i = -Z_i \sum_{j \neq i}^{N} Z_j \frac{R_\alpha^i - R_\alpha^i}{|\vec{R}_j - \vec{R}_i|^3} + Z_i \int \frac{n(\vec{r})(r_\alpha - R_\alpha^i)}{|\vec{r} - \vec{R}_i|^3} \mathrm{d}\vec{r} . \tag{4.15}$$

Note that in the above equation, the (first) electrostatic contribution excludes the self-interaction using the $j \neq i$ condition. However, the latter (second) term accounts for the electron-nuclei interaction with atoms "*own*" electrons. To resolve this part of self-interaction, when reconstructing pair forces in a DFT calculation, it is desirable, to re-write the total charge density as a sum of atomic contributions.

$$n(\vec{r}) = \sum_{i}^{N} n_i(\vec{r}) \tag{4.16}$$

Technically, such a decomposition is achieved by assigning spatial regions of the charge density to individual atoms using charge partitioning schemes. By plugging Eq. (4.16) into Eq. (4.15) and exchanging the sum and integral of the second term we can rewrite as

$$f_\alpha^i = -Z_i \sum_{j \neq i}^{N} Z_j \frac{R_\alpha^i - R_\alpha^i}{|\vec{R}_j - \vec{R}_i|^3} + Z_i \sum_{j \neq i}^{N} \int \frac{n_j(\vec{r})(r_\alpha - R_\alpha^i)}{|\vec{r} - \vec{R}_i|^3} \mathrm{d}\vec{r} . \tag{4.17}$$

Finally, we can decompose the sums and pull out just the contributions of the j^{th} atom and hence arrive at a definition of pair force which reads:

$$f_\alpha^{ij} = -Z_i Z_j \frac{R_\alpha^i - R_\alpha^i}{|\vec{R}_j - \vec{R}_i|^3} + Z_i \int \frac{n_j(\vec{r})(r_\alpha - R_\alpha^i)}{|\vec{r} - \vec{R}_i|^3} \mathrm{d}\vec{r} . \tag{4.18}$$

The definition, however, exhibits one major shortcoming, namely it is not invariant to the permutation of the atoms. However, pair forces must be symmetric such that

$$f_\alpha^{ij} = -f_\alpha^{ji} \tag{4.19}$$

exchanging indices only changes the sign. The definition in Eq. (4.18) however will satisfy Eq. (4.19) only in the case that $n_i(\vec{r}) = n_j(\vec{r})$, which cannot be assumed. Therefore, propose adapting Eq. (4.18) to

$$f_\alpha^{ij} = -Z_i Z_j \left[\frac{R_\alpha^i - R_\alpha^i}{|\vec{R}_j - \vec{R}_i|^3} + \frac{1}{2Z_j} \int \frac{n_j(\vec{r})(r_\alpha - R_\alpha^i)}{|\vec{r} - \vec{R}_i|^3} \mathrm{d}\vec{r} - \frac{1}{2Z_i} \int \frac{n_i(\vec{r})(r_\alpha - R_\alpha^j)}{|\vec{r} - \vec{R}_j|^3} \mathrm{d}\vec{r} \right] \tag{4.20}$$

As $\vec{f}^{ij}$ and $\vec{f}^{ji}$ must add up to zero, the (first) electrostatic term of the nuclei in Eq. (4.20) cancels by changing the indices as well as the latter two terms. Note that this was not the case for Eq. (4.18). Furthermore, consider a conventional *fcc* Al cell, where all four atoms of the cell have to be assigned the same charge density distribution, due to symmetry reasons, the electron-nuclei interaction will also vanish. In other words, Eq. (4.20) measures the net Coulomb force on the ions which arises from the deformation of the atomic charge density contributions, due to the formation of the atomic bonds.

Implementation of pair-force reconstruction via charge density composition We have implemented the above-presented formalism, to study the local atomic strain for a TiN/AlN multilayer system. However, instead of Eq. (4.20) we used Eq. (4.18) to compute the pair forces and symmetrized $\tilde{f^{ij}} = \frac{1}{2}\left(\vec{f}^{ij} + \vec{f}^{ji}\right)$ them manually afterwards. For the charge density decomposition (Eq. (4.16)) we have tested Hirshfeld [169], Bader [170] and Voronoi charge partitioning. For Hirshfeld charge partitioning, a custom implementation was created, while for Bader- and Voronoi-partitioning we employed tools from the Henkelman group [171–173]. However, during applying the reconstruction a lot of technical issues appeared, which in the end made the process impractical. Firstly, charge partitioning algorithms are grid-based algorithms, thus $n(\vec{r})$ must be known on a sufficiently dense grid. Besides convergence tests to estimate proper FFT grid sizes (for the employed plane-wave code), dense-enough grids are impractical for a DFT-based geometry optimization (due to a vast computational overhead). Hence, obtaining $n(\vec{r})$ at a dense grid is outsourced into a separate DFT calculation. This is a major drawback as calculation results cannot be used directly. In addition all the partitioning algorithms are intended to be used using the all-electron charge density, which must be reconstructed manually if frozen-core approximation (such as projector-augmented-wave [34] PAW) is used. Furthermore, for the employed wurzite w-AlN and cubic c-TiN multilayer (w-AlN/c-TiN) model containing 288 atoms in total,

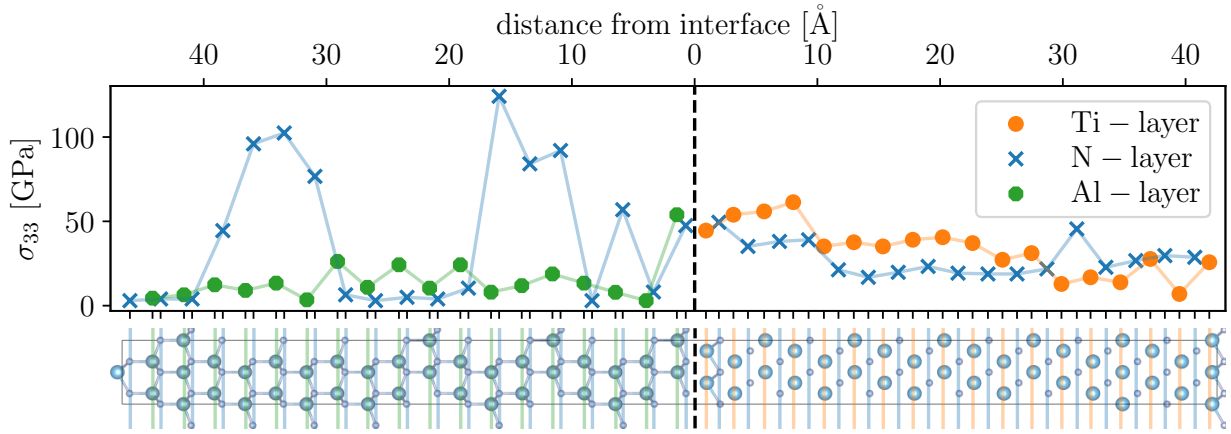

Figure 4.9: Out of (interface) plane atomic stress component σ_{33} for each layer of a w-AlN/c-TiN multilayer system. The atomic stress tensor was averaged over all atoms in one place. Blue crosses refer to the nitrogen layer, while orange correspond to Ti and green to Al layers.

the partial charges $n_i(\vec{r})$ must be known on the dense grid, resulting in vast amounts of data ($\approx$ 1 TB for the presented case).

Nevertheless, Fig. 4.9 shows the local atomic stress, for each layer in the w-AlN/c-TiN multilayer. The forces to required to calculate the local atomic stress tenors were computed according to Eq. (4.20), while a cutoff radius of $r_c = 12.5$ Å($\Omega = \frac{3}{4} r_c^3 \pi$) was used in the summation of Eq. (4.13).

The main message of Fig. 4.9 is that due to the stress peaks in the nitrogen layers (orange circles), the multilayer is expected to fail in the w-AlN region. More precisely, the weakest link is not the interface, but rather a region $\approx 10 - 15$ Åaway from it in the AlN bulk material. Interestingly, Koutná *et al.* [174], Löfler [175] recently showed using MD that such multilayer systems fracture in w-AlN region, slightly away from the interface.

Although we have shown that the above proposed workflow to is able to reconstruct pair forces, there are a few caveats that limit the applicability of the proposed approach. Firstly, the DFT charge density needs to be partitioned into atomic contributions, which is a data intensive task. Consequently, also when computing the pair forces one has to sum of the atomic contributions, which is is again a data intensive task. Moreover, it might be necessary to carry out a convergence test with respect to the FFT grid to ensure that the results are converged. In summary, while the approach might be able to bring useful insight, the practical applicability is difficult due to technical details.

Reconstruction of the pair-forces via atom-removal

Another, much simpler method, inspired by beam theory from classical mechanical engineering was suggested by Cui and Chew [176]. To calculate local atomic stresses at a grain

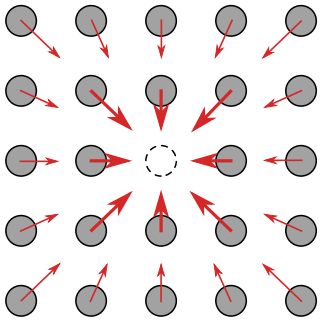

Figure 4.10: Removing an atom from a bulk system, will exert forces on all other atoms in the system. This is a consequence of the atomic force being a variable charge density

boundary, they reconstructed the pair forces by removing an atom from the system. Figure 4.10 illustrates their method. After removing an atom from the system, a DFT calculation is carried out with fixed atomic positions to find the forces on all other atoms. Thus, when removing an atom i from the structure, one will obtain the forces for all atoms $j \neq i$. In other words, one (DFT) calculation is needed to compute one row (or column) of the pair-force matrix f^{ij}. While this approach circumvents all the technical difficulties as it is inherently not a grid-based algorithm — compared to the previously presented one — it comes at the cost that N single-point DFT calculations are needed to fill the pair-force matrix fully.

While Cui tried to recover local atomic stresses at a copper grain boundary we have applied, the method to recover pair forces in an amorphous WBC system. Thus, for the $W_{120}B_{45}C_{135}$, 300 additional calculations were carried out to obtain $\vec{f}^{ij}$ as a proof-of-concept. Fig. 4.11 shows the norm of the reconstructed (pair) forces as a function of the neighbor distance.

By plotting the forces per pair-type as a function of distance, we recover the interaction of the individual species with each other. Finally we note that it would be interesting to compare the forces from Fig. 4.11, with the predictions of a ML-FF in order to validate the presented approach.

During the course of this thesis, we did neither develop/implement the pair-force reconstruction via charge density (Sec. 4.5.2) nor atom removal (Sec. 4.5.2) beyond a proof-of-concept studies (see Fig. 4.11). The main reason for not following the ideas is, that recently, machine-learned force fields (see Sec. 3.2) became routinely available for the major codes, such as VASP or LAMMPS (see Tab. 3.1). Upon training of these force fields, energies and forces are correlated with ionic environments. Hence, these properties are broken up into a sum of local contributions. Using such ML-FF allows us to extract the desired pair-forces $\vec{f}^{ij}$ more elegantly, and most importantly with only minimal computational overhead once the ML-FF is trained.

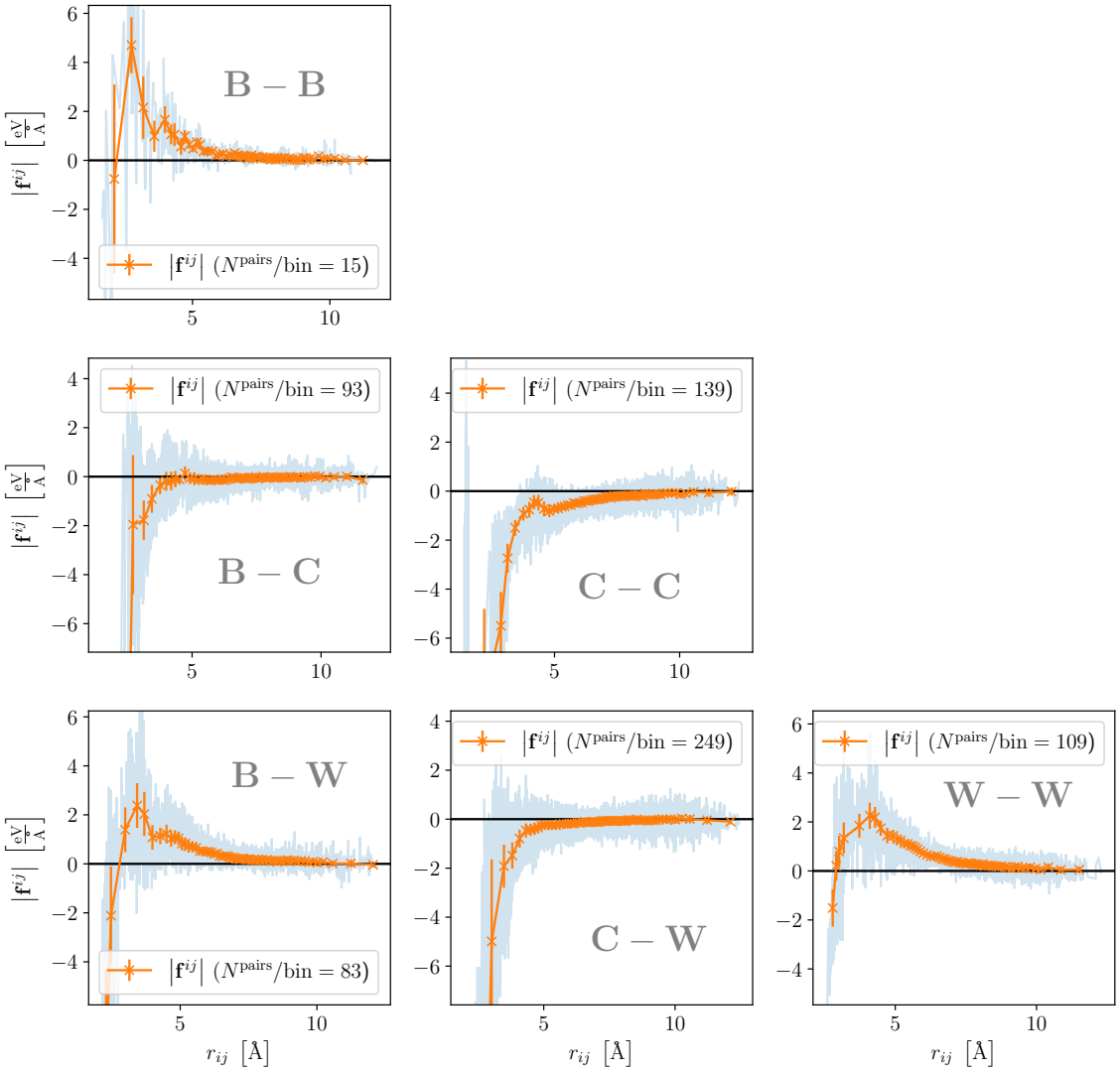

Figure 4.11: Norms of the recovered pair forces for an amorphous $W_{120}B_{45}C_{135}$ cell ($14.55 \times 14.55 \times 14.55$ Å). The force-norms are plotted against the neighbor distance, and grouped by the bond type.

4.6 Caveats and practical guide to QM/MM for metals

The following section will deal with practical considerations when applying QM/MM to metallic systems. Such include tips with respect to system choice, and parameter tuning as well as a step-by-step guide to carry out production QM/MM calculations.

4.6.1 Strengths and weaknesses

It is inevitable to understand the strengths and weaknesses of a QM/MM approach compared to a DFT, MD, or ML-FF treatment before, choosing a system to study. QM/MM is – as any other hybrid approach – fundamentally limited where only a small part of the system (*core* region) is of special interest, such as boundary planes or defects. Especially when systems

are fundamentally inaccessible to a DFT treatment QM/MM turns out to be superior for practical reasons. Hence, we will discuss only such use cases in the following if not specified otherwise.

Chemical versatility

Compared to MD and ML-FF, DFT (or KS-DFT or QM) allows to investigate complex chemistries within the *core* region leveraging its computational demands. In this regard, MD is severely limited in terms of chemistry due to the potential available. Furthermore, even if an interatomic potential existed, it is non-trivial to verify that it would model the defect accurately if it was not fitted for such a specific purpose. The same argument holds when comparing ML-FF approaches. Due to the data-driven approach, the local atomic environments similar to those around the defect need to be amongst the training data to allow for confident predictions. Hence, a benchmark is necessary to prove that defect geometries and energies are predicted correctly. In contrast, we [177] and Huber *et al.* [157] have extensively proven that a proper QM/MM scheme can reproduce DFT results extremely accurately. Moreover, an ML-FF is usually fitted for a limited chemical compositional range, hence to screen the periodic table a multitude of those is needed.

Efficiency

ML-FFs come at the cost of input data generation and fitting, where the cost of a QM/MM calculation is usually comparable to one heavy single-point DFT calculation. That is because the MM part is negligible in terms of computational demand compared to the MM region. While an ML-FF, once it is fitted, is superior in terms of computational demand, to generate sufficient input data for training a ML can still be a resource-intensive process. Nevertheless, when many structurally different defects are investigated, an ML based approach will outperform QM/MM.

Transparency and simplicity

Compared to other methods, described in Chapter 3, which overcome the size limitation, the presented QM/MM approach is transparent in a twofold manner. Firstly, all the approximations made are rather simple and do not require changes to DFT or MD formalism and hence the underlying codes. Secondly, the coupling does not require computing of complex properties but rather solely relies on forces. This leads to two major advantages, yet not for the user. Although our QM/MM approach is not as general as the $\mathcal{O}(N)$-DFT approach, it took two individuals almost a year to implement the underlying infrastructure and the QM/MM scheme. In contrast, developing a modern DFT/MD package can take whole research groups many years if not decades. The algorithmic simplicity, furthermore,

allows one to easily prove the correctness of the implementation. This is manifested in our implementation having not more than a few hundred lines of code.

Here, we note a nice property of our coupled approach, which we will illustrate with an example. Suppose, the QM/MM approach predicts wrong formation energies for a solute atom at a dislocation. There are only three points where things can go wrong. Firstly, the DFT part does not converge. Such a problem is easy to track down, and, more importantly, to fix. Secondly, the MD calculation exhibits problems. However, when choosing and rescaling a proper potential this is very unlikely to happen. Thirdly, one or more of the coupling parameters are not properly set. Again, such errors are easily tracked down by visually inspecting the QM cell, or looking at the output of the coupled programs. Most importantly, those problems are very easy to solve in practice.

Methodological overhead

Although the QM/MM approach can efficiently treat systems that are inaccessible to QM methods, while maintaining their accuracy, this comes at a cost of a methodological overhead. Those additional steps include potential rescaling and manual system partitioning. Furthermore, convergence tests with respect to the coupling parameters (number of buffer and core shells) and as well for the structure minimizer settings need to be carried out. Most of these steps are moreover difficult to automate. This makes the approach intensive from the human-resources rather than the computational point of view. Finally, we want to point out that the setup to carry out QM/MM calculations is rather involved compared to standard DFT or MD approaches.

Limitations of the matrix chemistry

This is a direct consequence of employing MD in the bulk region. Thus, there must be an interatomic potential available to describe the matrix (MM) region far away from the defect. There is, however, a second issue that needs to be addressed. The interatomic potential should yield the same lattice parameters and if possible also the same elastic constants as obtained from the employed QM method. Both constraints put severe limits on the matrix composition. In Sec. 4.6.2 we explain how to overcome these limitations.

4.6.2 General workflow

System selection

Before starting with calculations, it is important to know the limitations and strengths of the QM/MM approach (see Sec. 4.6.1). Therefore, a good example would be to model solute instance solute segregation to a dislocation. A dislocation usually exhibits a long ranged

elastic stress field, which can be accurately described using QM/MM [178]. To investigate the core structure with purely periodic QM approaches [179, 180], depending on the type of dislocation di- [181] or quadropole [182] arrangements are used such that the stress-fields cancel each other. Furthermore, compared to the Greens function approach (see Sec. 3.3.1), QM/MM can account for non-linear elastic displacements, and more importantly compute total energies for the system, to compare different states. Generally, it is advisable to employ QM/MM if a defect is structurally not accessible by DFT, yet an excellent description is necessary.

Potential rescaling

The empirical potential of the MM region is required to yield similar lattice parameters as the method used in the QM region (usually DFT). If it does not, the used potential needs to be rescaled. This is a common step in QM/MM schemes [1, 153]. To rescale a potential is technically easy for EAM or LJ potentials, but might be highly non-trivial for other potential types. Especially if the matrix contains multiple phases, this has to be done with a great care. We, therefore, demonstrated how to study a multi-phase system with QM/MM in Ref. [177] and summarize it in Chapter 5. Huber *et al.* [1] reported extensively on how the deviations of the lattice parameters and bulk-modulus between the empirical potential and DFT affect the computed energies. A alternative option would be to train a simple ML-FF for the matrix region, as shown by Grigorev *et al.* [178]. Such an approach circumvents potential rescaling, and possible errors arising from a mismatch.

System partitioning

The automatic QM cell construction process in Fig. 4.6 works in practice for a lot of systems. Nevertheless, among the few parameters to choose from are the following:

seed atoms The seed atoms are the starting point for every construction. Usually, only a few are chosen. Seed atoms might be, for instance, be sites directly at a grain boundary or those of a dislocation core.

core shells Starting from the seed atoms, determines how many shells are built around the seed atoms. Note that *seed* and *core* atoms make up the QM region (I), where only QM forces will be used. Its actual number depends on the crystal structure and defect geometry. In general, more *core* shells lead to a larger QM region, however, also increase the number of *buffer* atoms surrounding the *core* region. Nevertheless, at least two *core* shells should be chosen for production calculations.

buffer shells The *buffer* atoms surround the *core* region. It is desirable to keep this number as small as possible, as they are an artifact from the coupling itself. For most

applications, two at most three[1] shells are sufficient. This is, furthermore, confirmed by a convergence test carried out in Ref. [177].

filler width After the *core* + *buffer* cluster is constructed, a bounding box is drawn around it. This box is filled up with *filler* atoms from the initial positions superstructure. The filler width is a padding around the cluster. To make use of our scheme at least one *filler* layer of atoms must be at each face of the simulation box. As those atoms represent overhead, the number should be as small as possible on the other hand. A good starting point would be values in the range from $2 - 3$ Åto pad the cluster with one layer of atoms. Note, that our algorithms allows to specify three different filler widths, one for each spatial direction.

filler vacuum Finally, to avoid that *filler* atoms coming too close to each other due to periodic boundaries a vacuum padding is added along all coordinate axes. A good starting point for the *filler* vacuum padding is the nearest neighbor distance. For an optimal choice a visual inspection of the cell is inevitable.

While we have given some practical advice above, we note that there is no general recipe for how to choose the number of shells. Nevertheless, it is helpful to experiment with the numbers above in combination with a visualization of the resulting QM cell. This can be done effortlessly, when using our implementation through Jupyter Notebooks. Those decisions will greatly affect the computational demand of the study, hence this critical step is best carried out by humans to find a tradeoff between accuracy and computational demand. Upon choosing the filler width and filler vacuum, experimenting with the values is very helpful. To complement this trial and error procedure and to avoid atoms coming too close, observing the pair-distance histogram turned out to be very helpful (see Chapter 6).

[1] private communication with L. Huber

Chapter 5

Interfacial segregation to phase boundaries in TiAl

Parts of this chapter were published within the article "Segregation to α_2/γ interfaces in TiAl alloys: a multiscale QM/MM study" [177]

5.1 Introduction

We have selected the TiAl intermetallic system for this case study. Our motivation is threefold. Firstly, the base TiAl system is simple enough (simple crystallographic structures, non-magnetic, binary, stable,...) to allow for testing new methodological implementations. Specifically, we apply the QM/MM approach to study segregation to Ti_3Al/TiAl $\alpha_2(1000)/\gamma(111)$ phase boundary. Secondly, the TiAl-based alloys have been extensively investigated (primarily experimentally), including numerous contributions from the Leoben group [183, 184], thus guaranteeing sufficient data for validation of our predictions. Lastly, the development of novel TiAl-based alloys is a very vivid research area, both from the fundamental as well as from the applied (industrial) point of view. Therefore, consistent and complete datasets are necessary for the knowledge-based design of new systems.

To properly elucidate the behavior of solutes at a phase boundary, it is necessary to formulate the segregation energetics for a two-component two-phase system carefully. We present such an approach in Sec. 5.2.6. The majority of the available literature deals with segregation in simple metals (e.g., Mg [185], Mo or W [186]).

The chapter is organized as follows: We first introduce structural models for the considered boundaries and the QM/MM methodology. Next, we focus on important aspects of coupled QM and MM calculations. Afterwards, we compare two different QM/MM setups by benchmarking them against pure density functional theory (DFT) calculations. In the next section,

we provide details for the discussion of the site preference and compare our results against literature data. The largest portion of the results focuses on determining the segregation and phase preference for selected $3d$, $4d$, and $5d$ transition metal solutes, and compares the predictions with concentration profiles across phase boundaries determined using the atom probe tomography.

5.2 Computational methods

5.2.1 Structural models

An advantage of the coherent phase boundary is that due to the periodic boundary conditions, the simulation cells can be small in the x and y (in-plane) directions. Our cells are aperiodic out-of-plane. As Kanani, Hartmaier, and Janisch [187, 188] pointed out, there is no unique way to model α_2/γ interfaces, since the constituting half-crystals may be rotated against each other, thus making up different phase-boundaries, yielding different interface energies. Based on their results we chose the energetically most favorable interface configurations [187, 188], which are depicted in Fig. 5.1.

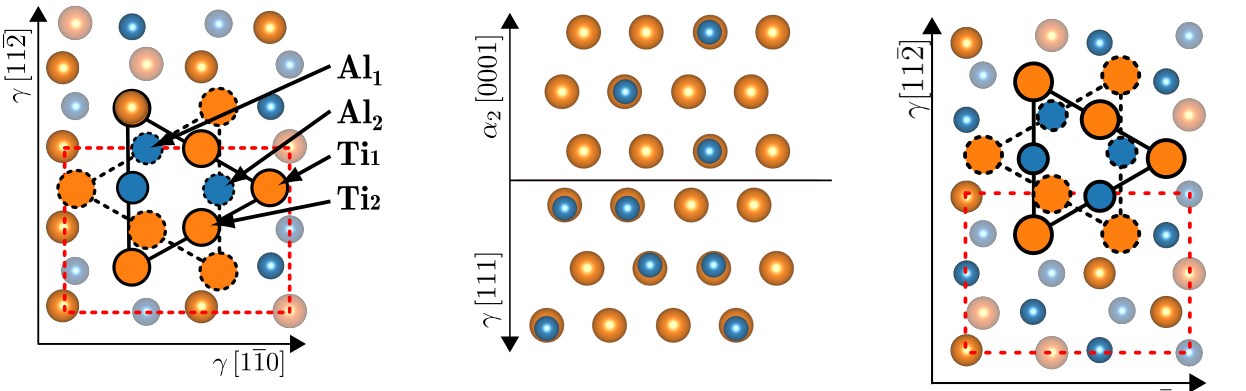

(a) The $\alpha_2(0001)/\gamma(111)$ interface (the γ half-crystal is rotated by 180°).

(b) The γ/γ interface "*true-twin-boundary*" (TT),

Figure 5.1: Atomistic interface models for (a) the α_2/γ phase-boundary and (b) the γ/γ boundary. The orange and blue spheres represent Ti and Al atoms, respectively. The solid border atoms refer to the α_2 or γ-grain sitting above. The γ half-crystals are rotated by 60° with respect to each other. The dashed lines and dashed atom border correspond to the lower grains.

Although the $\alpha_2(0001)/\gamma(111)$ interface yields a near-to-hexagonal cell, we have used orthogonalized cells. This is because the LAMMPS's triclinic crystal symmetry setting cannot handle hcp-like cells. Thereby, the number of atoms is doubled, which is particularly important for the QM region. Moreover, this reduces the relative solute concentration at the interface, which is $1/16 = 6.25\,\text{at.}\%$. Each QM/MM cell consists of 56 layers, where each

of those consists of eight atoms ($56 \times 8 = 448$). The cells ($\alpha_2(0001)/\gamma(111)$) contain 28 layers above and below the interface. The cell dimensions are $5.77 \times 9.90 \times 130.02$ Å. The cells are periodic along a, and b vectors and exhibit no periodicity along the c direction. Similarly, we constructed α_2 and γ-bulk cells to compute bulk formation energies, resulting in the same amount of atoms. We have chosen two QM/MM setups, which drastically differ in their computational demand. In the first (demanding) one, the model sizes were chosen such that the QM region results in similar (same number of atoms) models as used in previous work [189]. In the truly dilute limit, the planar cell dimensions should be much larger, however the above-mentioned in-plane dimensions make parts of the present study comparable with previous work and hence allows for validation of the new implementation. The computational cost of the demanding QM/MM setup is almost equal to the DFT. The overhead introduced in terms of CPU time due to QM/MM is (within this study) compared to the DFT setup on average less than one percent. The second setup is minimalistic and reduces the computational effort for a single-point calculation by roughly one order of magnitude. Finally, we repeat all calculations with DFT and benchmark both QM/MM setups against pure DFT. We show that QM/MM is also applicable to systems that are chemically more complex than simple metals.

5.2.2 QM calculations

All quantum-mechanical calculations were carried out in the framework of Density Functional Theory (DFT) with the Vienna Ab-initio Simulation Package (VASP) [190, 191]. The exchange and correlation functional was treated at a generalized gradient approximation level parametrized by Perdew-Burke-Ernzerhof (PBE-GGA) [15, 17]. For the electronic self-consistent cycle we set a convergence criterion of $\Delta E_{SCF} = 10^{-4}$ eV/cell. The convergence criterion for the ionic loop is discussed in Sec. 5.2.5. All calculations were carried out in non-spin-polarized mode. The projector augmented wave (PAW) method [34, 192] was used to describe the electron-ion interactions. The plane-wave cutoff energy was set to 350 eV. For the k-mesh sampling of the Brillouin zone, a Monkhorst-Pack [193] scheme with $6 \times 3 \times 1$ k-points was chosen. These settings were used for the QM region of the coupled QM/MM calculations (Sec. 5.2.5). In DFT calculations carried out for benchmarking the QM/MM setups, we allow all ions to relax.

5.2.3 MM calculations

MM calculations were performed with the LAMMPS simulator [194, 195] using an embedded-atom-method (EAM) potential for the binary Al-Ti system parameterized by Zope and Mishin [196]. To make it compatible with the QM calculations, it was spatially rescaled to match the DFT computed lattice parameters of both γ-TiAl and α_2-Ti_3Al. This process is

	γ-TiAl		α_2-Ti_3Al	
	a	c	a	c
DFT [Å]	3.993	4.065	5.751	4.655
EAM [Å]	4.037	4.109	5.812	4.706
Deviation [%]	+1.11	+1.08	+1.08	+1.08
Rescaled EAM [Å]	3.995	4.065	5.749	4.654
Deviation [%]	+0.041	+0.011	−0.034	−0.025

Table 5.1: Ground state lattice parameters produced by the rescaled EAM potential compared with DFT with settings described in Sec. 5.2.2.

described in the next section.

5.2.4 EAM potential rescaling

To obtain a force convergence during the coupled QM/MM relaxation, both methods (DFT and MD) should yield the same lattice parameters for the same phases. This rescaling is an important part of any QM/MM [153, 157, 178] scheme and has been extensively discussed by Huber *et al.* [1]. Therefore we calculated the potential energy surfaces (PES) for the unit cells of both phases, γ-TiAl (tetragonal) and α_2-Ti_3Al (hexagonal), as functions of the lattice parameters a and c, $E^{\gamma}_{\mathrm{DFT}}(a,c)$ and $E^{\alpha_2}_{\mathrm{DFT}}(a,c)$. The DFT-optimized lattice parameters corresponding to the global minimum on these PES are displayed in Tab. 5.1. EAM potentials are tabulated on an equidistant mesh of radial points and the spatial distance Δr of the table entries is given in the potential header. We, therefore, computed the Δr value which minimises the objective function

$$\mathcal{O}(\Delta r) = (a^{\gamma}_{\mathrm{DFT}} - a^{\gamma}_{\mathrm{MM}})^2 + (a^{\alpha_2}_{\mathrm{DFT}} - a^{\alpha_2}_{\mathrm{MM}})^2 + (c^{\gamma}_{\mathrm{DFT}} - c^{\gamma}_{\mathrm{MM}})^2 + (c^{\alpha_2}_{\mathrm{DFT}} - c^{\alpha_2}_{\mathrm{MM}})^2 \to \min \quad (5.1)$$

The equilibrium lattice parameters of the re-scaled EAM potential, as well as their deviations from the DFT values, are shown in Tab. 5.1.

Table 5.1 shows that the rescaled EAM potential largely reduces the deviation between DFT and MD. Therefore, the aforementioned Δr was changed by $\approx -0.98\%$, such that the new EAM potential minimizes Eq. (5.1). Huber *et al.* [1] intensively assessed the influence of the lattice mismatch and number of buffer shells on the formation energies of solutes at a grain boundary. They show that a mismatch in bulk moduli between DFT and rescaled EAM potential does not lead to a substantial error [1, 157]. Hence, we focused the re-scaling solely on matching the lattice parameters. Nevertheless, there remains a mismatch, which might cause an error introduced by the presented methodology. We will show in Sec. 5.3.1 that

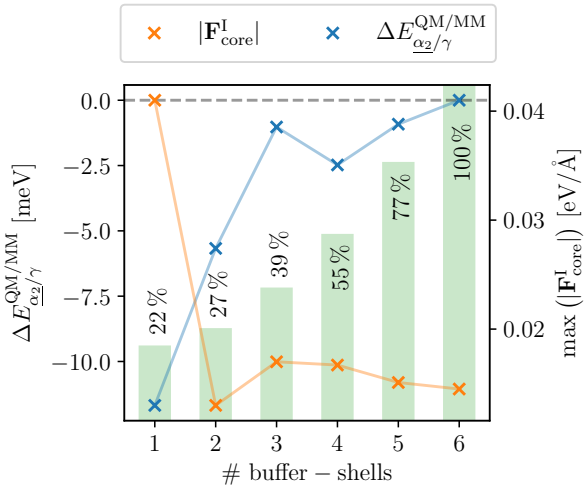

Figure 5.2: Error estimation of the total QM/MM energy, $\Delta E^{\mathrm{QM/MM}}_{\underline{\alpha_2}/\gamma}$, (blue) and the maximum force norm on an atom in the *core* region of the QM cell, $\max(|\mathbf{F}^{\mathrm{I}}_{\mathrm{core}}|)$ (orange) for a Pd decorated $\underline{\alpha_2}/\gamma$ interface as a function of buffer shells. The number of core shells was set to two. The reference line (black dashes) corresponds to $N^{\mathrm{shell}}_{\mathrm{buffer}} = 6$. The green bars represent the relative computational cost.

those differences are small ($|E^{\mathrm{DFT}} - E^{\mathrm{QM/MM}}| < 10$ meV). Finally we note that throughout the study we use only the rescaled EAM potential in the MM region.

5.2.5 The QM/MM coupling

In a hybrid QM/MM approach (cf. Chapter 4) the system is decomposed into two regions (I and II). Region one (I) is treated accurately with QM and is furthermore the domain where the solutes are placed. In the present study, we refer to those layers around the interface as the *core* region. The remaining part of the cell is treated with MM and is usually denoted as region II. In other words region I denote the QM and II the MM part. We have used a QM/MM scheme as proposed by Huber *et al.* [1, 157], to perform DFT/MD coupled relaxations. The algorithm was implemented in the `pyiron_contrib`[158] project within the `pyiron` framework [159]. The QM/MM workflow was implemented as a directed graph. For its visualization, the reader is referred to the Sec. 4.4.1 (Fig. 4.8).

We have chosen two different QM/MM setups. For both setups, the *filler* region was chosen to be a second $\alpha_2(0001)/\gamma(111)$ interface. The reason is that a material-material interface in contrast to a material-vacuum interface introduces only weak electronic perturbations, and therefore leads to accurate forces in the *core* region [1]. The first, accurate, setup (denoted with ↑) uses two atomic layers around the interface planes (the region of interest) for the *core* region. Furthermore, to obtain accurate total QM/MM energies and forces in the core region, we have chosen to construct six *buffer*-layers to shield the *core* region. The convergence of

the total energy as a function of the number of buffer shells, for a Pd decorated $\underline{\alpha_2}/\gamma$-interface is shown in Fig. 5.2. The same number of *core*, *buffer*, and *filler* layers were chosen for both γ and α_2-bulk cells. Using this setup our QM region becomes similar to the cells used to study this system with pure DFT [189]. This setup yields 192 atoms in the QM region.

The second, minimalistic setup, in the following marked with $\downarrow$, uses only one *core*, and one *buffer* shell and results in only 64 atoms in the QM region. This setting lowers the computational effort by roughly one order of magnitude.

All calculations are performed at constant volume obtained by optimizing the pristine cells with the EAM potential. The ionic positions of the coupled QM/MM systems were relaxed with a force convergence criterion $\Delta F \leq 0.015$ eV/Å. To find the equilibrium positions, we used at most $N_{\max} = 200$ coupled steps with a gradient descent minimizer. The initial step size of the minimizer was set to $\Gamma_0 = 0.075$.

5.2.6 Evaluation methods

Site preference

To determine the preferred sublattice Θ, Al or Ti in our case, of a solute X in a bulk phase $\mathbf{P}$, we compare the formation energies of the solute of both sublattices. The formation energy reads

$$E_{\mathbf{P}}^{f,X\to\Theta} = E_{\mathbf{P}}^{X\to\Theta} - E_{\mathbf{P}} + \mu_{\mathbf{P}}^{\Theta} - \mu^{X} \ . \tag{5.2}$$

where $E_{\mathbf{P}}^{X\to\Theta}$ denotes the energy where X replaces a Θ atom. $E_{\mathbf{P}}$ corresponds to the undecorated system. In bulk systems, $\mu_{\mathbf{P}}^{\Theta}$ corresponds to a range of values rather than a single scalar. Taking the difference of Eq. (5.2) for $\Theta = \mathrm{Ti}$ and $\Theta = \mathrm{Al}$, eliminates the dependence of $\mu_{\mathbf{P}}^{X}$ and yields

$$\begin{aligned} \Delta E_{\mathbf{P}}^{f,X} &= E_{\mathbf{P}}^{f,X\to\mathrm{Al}} - E_{\mathbf{P}}^{f,X\to\mathrm{Ti}} \\ &= E_{\mathbf{P}}^{X\to\mathrm{Al}} - E_{\mathbf{P}} + \mu_{\mathbf{P}}^{\mathrm{Al}} - \mu^{X} - \left[E_{\mathbf{P}}^{X\to\mathrm{Ti}} - E_{\mathbf{P}} + \mu_{\mathbf{P}}^{\mathrm{Ti}} - \mu^{X}\right] \\ &= E_{\mathbf{P}}^{X\to\mathrm{Al}} - E_{\mathbf{P}}^{X\to\mathrm{Ti}} + \underbrace{\mu_{\mathbf{P}}^{\mathrm{Al}} - \mu_{\mathbf{P}}^{\mathrm{Ti}}}_{\Delta\mu_{\mathbf{P}}} . \end{aligned} \tag{5.3}$$

which is solely a function of the difference of the chemical potentials $\Delta\mu_{\mathbf{P}}$. Hence, negative values of $\Delta E_{\mathbf{P}}^{f,X}$ denote that X will prefer the Al sublattice. Consequently, the site preference of defects in the bulk system depends on the chemical potential difference $\Delta\mu_{\mathbf{P}}$, which is related to the composition. The range allowed for $\Delta\mu_{\mathbf{P}}$ can be estimated by computing the thermodynamic limits, upon imposing the co-existence conditions with the neighboring

phases. If $\Delta E_{\mathbf{P}}^{f,X}$ does not cross the zero line within the thermodynamically accessible range of $\Delta\mu_{\mathbf{P}}$, we regard the alloying element X to exhibit a "*strong*" site preference in phase $\mathbf{P}$. Otherwise, we call it a "*weak*" or "*compositionally dependent*". The actual values for the range of $\Delta\mu_{\alpha_2}$ and $\Delta\mu_{\gamma}$ are given in the next section, while for the derivation we refer the reader to Appendix .1.1.

Thermodynamic limits of the difference of chemical potentials

As $\Delta\mu_{\mathbf{P}}$ is bounded by thermodynamic limits we have calculated those using Eqs. (38)–(41). For the stochiometric composition, $\Delta\tilde{\mu}_{\mathbf{P}}$ an expression is obtained by requiring the formation energies of the anti-site defects to be identical. Therefore we get

$$E_{\mathbf{P}}^{f,\mathrm{Ti}\to\mathrm{Al}} \approx E_{\mathbf{P}}^{f,\mathrm{Al}\to\mathrm{Ti}} \tag{5.4}$$

$$\Delta\tilde{\mu}_{\mathbf{P}} \equiv (\mu_{\mathbf{P}}^{\mathrm{Ti}} - \mu_{\mathbf{P}}^{\mathrm{Al}}) \approx \frac{E_{\mathbf{P}}^{\mathrm{Al}\to\mathrm{Ti}} - E_{\mathbf{P}}^{\mathrm{Ti}\to\mathrm{Al}}}{2}. \tag{5.5}$$

The α_2 phase ($\mathbf{P} = \alpha_2$) is bordered by the α-Ti with ≈ 6 at.% Al [197] for low and the γ-TiAl phase for high aluminum contents. Hence, we have computed the thermodynamic limits as -2.89 eV $= \Delta\mu_{\alpha/\alpha_2} \geq \Delta\mu_{\alpha_2} \geq \Delta\mu_{\alpha_2/\gamma} = -3.55$ eV. This is in good agreement with Wei *et al.* [189] who obtained -3.52 eV for $\Delta\mu_{\alpha_2/\gamma}$. For the derivation of these limits, the reader is referred to Appendix .1.1. For the difference at the stochiometric composition we obtained $\Delta\tilde{\mu}_{\alpha_2} = -3.30$ eV.

For the γ-TiAl phase, which is bordered h-$TiAl_2$ for high aluminum contents, we obtained for the limits -3.55 eV $= \Delta\mu_{\alpha_2/\gamma} \geq \Delta\mu_{\gamma} \geq \Delta\mu_{\gamma/h} = -3.96$ eV and $\Delta\tilde{\mu}_{\gamma} = -3.71$ eV for the stochiometric composition. The derivation is given in Appendix .1.2.

Segregation and phase-preference energies

Unlike in bulk regions of the γ and α_2 phases, where all Ti or Al sites are equivalent, breaking the translation symmetry at the interface may lead to various Ti or Al sites becoming non-equivalent. At a phase-boundary $\mathbf{B}$, on the atomistic level, each of the sublattices Θ may split into i symmetry non-equivalent sites Θ_i. For each of those sites and for a solute X occupying this site, the energy of formation reads

$$E_{\mathbf{B}}^{f,X\to\Theta_i} = E_{\mathbf{B}}^{X\to\Theta_i} - E_{\mathbf{B}} + \mu_{\mathbf{B}}^{\Theta} - \mu_{\mathbf{B}}^{X}\,. \tag{5.6}$$

Consequently, we refer to the minimum of those formation energies as the formation energy for a specific sublattice Θ of a boundary $\mathbf{B}$

$$E_{\mathbf{B}}^{f,X\to\Theta} = \min_i E_{\mathbf{B}}^{f,X\to\Theta_i}\,. \tag{5.7}$$

Indeed, at the α_2/γ interface, a solute can be placed at two chemically distinct Ti sites on the α_2 side of the interface and at two different Al sites on the γ side. We distinguish those by a subscript index. Hence, similarly to Eq. 5.3, using Eq. 5.7 one can define the difference in the sublattice formation energies, to investigate site preference at the boundary.

Moreover, in the following, we distinguish between two scenarios. $\underline{\alpha_2}/\gamma$ refers to the solute X decorating the α_2 side and, similarly, $\alpha_2/\underline{\gamma}$ represents X sitting on the γ side of the interface. To elucidate the mechanisms at the α_2/γ interface we define three differences of formation energies.

$$\begin{aligned}\Delta E^f_{\alpha_2\to\underline{\alpha_2}/\gamma} &= E^{f,X\to\Theta}_{\underline{\alpha_2}/\gamma} - E^{f,X\to\Theta'}_{\alpha_2} \\ &= \min_{\Theta,\Theta'\in\{\mathrm{Ti,Al}\}} \left(E^{X\to\Theta_i}_{\underline{\alpha_2}/\gamma} + E_{\alpha_2} + \mu^{\Theta}\right) - \left(E^{X\to\Theta'}_{\alpha_2} + E_{\alpha_2/\gamma} + \mu^{\Theta'}\right)\end{aligned} \tag{5.8}$$

and similarly,

$$\Delta E^f_{\gamma\to\alpha_2/\underline{\gamma}} = \min_{\Theta,\Theta'\in\{\mathrm{Ti,Al}\}} E^{f,X\to\Theta}_{\alpha_2/\underline{\gamma}} - E^{f,X\to\Theta'}_{\gamma} \tag{5.9}$$

$$\Delta E^f_{\gamma\to\alpha_2} = \min_{\Theta,\Theta'\in\{\mathrm{Ti,Al}\}} E^{f,X\to\Theta}_{\alpha_2} - E^{f,X\to\Theta'}_{\gamma} \tag{5.10}$$

Note that in the case of $\Theta = \Theta'$ the chemical potential terms vanish, otherwise they equate to $\pm\Delta\mu_{\alpha_2/\gamma}$. In contrast to the pure bulk-setting (Eq. (5.3)), the chemical potential μ^{Θ} in Eqs. (5.8)–(5.10) becomes a scalar value. Due to the co-existence of the α_2 and γ phase, Gibbs' phase rule yields one degree of freedom less. A negative value for Eqs. (5.8) and (5.9) corresponds to segregation to the interface at the corresponding site. In contrast, values for Eq. (5.10) represent a tendency for the solute X to partition into the α_2-bulk phase. Figure 5.3 illustrates a schematic physical interpretation of the energies defined above for the α_2/γ interface.

We note, that it is possible the come up with a single value for the segregation energy by minimizing the energy difference over all boundaries and bulk states simultaneously. Nevertheless, the presented approach helps to elucidate the behavior of the solutes at the interface better, as it allows us to draw a qualitative spatial energy profile (see Fig. 5.3). As this concept, however, introduces some additional complexity, we have visualized Fig. 5.3 for each solute separately (Fig. .15), where we used the γ-bulk as a reference state.

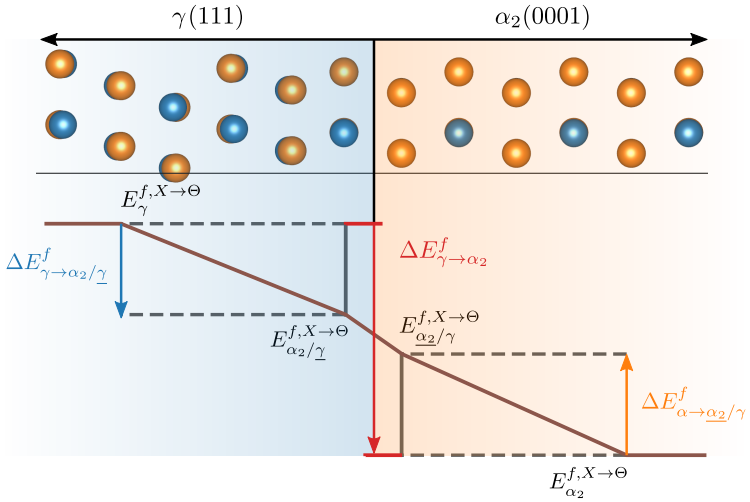

Figure 5.3: Schematic illustration of the energy levels, and meaning of the defined energies at the $\alpha_2(0001)/\gamma(111)$ interface. The brown line represents the spatial energy profile. The colored arrows correspond to the difference in formation energies. Eq. (5.9) – blue, Eq. (5.10) – red and Eq. (5.8) – orange

5.2.7 Interface properties

Cleavage energy and critical interface strength

In order to quantify the impact of solutes on the mechanical properties of the interfaces, we carried out cleavage calculations to estimate the cohesive energy and the critical interface strength. Therefore, the solutes were placed at their preferred sites (Tab. 5.3) and the simulation box is cleaved by inserting vacuum between the atomic layers which form the interface. This method is also referred to in the literature as a rigid displacement method [198] as no relaxations are allowed during separating the two half-crystals. For the α_2/γ interface, the calculations were carried out with the solute sitting on either side of the interface. Twenty discrete separations (vacuum sizes) δ between 0.01 Å and 6 Å were used to fit the universal binding energy relation [199]:

$$\Delta E(\delta) = E_c \left[1 - \left(1 + \frac{\delta}{l_c} \right) e^{-\frac{\delta}{l_c}} \right] , \tag{5.11}$$

$\Delta E(\delta)$ expresses the increase of the total energy (per interface area unit) as a function of the displacement (inserted vacuum thickness) δ. The fitting parameters E_c and l_c are the cleavage energy and the critical length (elongation at which all bonds simultaneously break).

$$\sigma_c = \left. \frac{\mathrm{d}\Delta E(\delta)}{\mathrm{d}\delta} \right|_{\delta = l_c} = \frac{E_c}{e l_c} \tag{5.12}$$

defines critical stress which is the maximum stress the system survives before cleaving. The approach was used to discuss the interface strengths in transition-metal nitrides and carbides [198, 200–203]. The raw data and the corresponding fits are available in the Appendix 7.3 (Fig. .13).

The cleavage energy is often related to the surface energy E_{surf} as $E_c = 2E_{\text{surf}}$. It is worth noting that while no relaxations are allowed during the rigid displacement method, the cleavage energy E_c is overestimated with respect to the corresponding surface energy E_{surf}. Additionally, since structural relaxations were prevented, only the QM region (containing the added vacuum and the alloying species X) and its corresponding energy $\Delta E^{\text{QM}}(\delta)$ were considered for $\Delta E(\delta)$.

Elasticity and fracture toughness

For estimating the fracture toughness we combine the results from Sec. 5.2.7 with the elasticity data using the following formula [204]:

$$K_{IC} \approx \sqrt{4\gamma_d C} \approx \sqrt{4E_c C_{zzzz}}, \tag{5.13}$$

where γ_d is the interfacial debonding energy, which we approximate with the cleavage energy E_c. C refers to the directional Young's modulus of the system, normal to the cleavage plane. Eq. (5.13) was previously successfully used for estimating fracture toughness of thin-film systems [205], including superlattices [206, 207]. The α_2/γ lamellar colonies, which are an important microstructural feature of advanced Ti-Al alloys, can be seen as a pack of alternating α_2 and γ Ti-Al thin layers. In the present work, C is approximated by the interface stiffness C_{zzzz}, calculated using the energy–strain method. The simulations cell is deformed with uniaxial strain in the interface normal direction. We used six discrete loading steps until a maximum deformation of 4 %. Importantly, the whole strain was localised only at the interfacial bond in order to get an interface-relevant material descriptor. The interface stiffness is determined from a quadratic fit of the total energy as function of the strain, $U(\varepsilon_{zz})$:

$$C_{zzzz} = \left.\frac{\partial^2 U}{\partial \varepsilon_{zz}^2}\right|_{\varepsilon_{zz}=0}. \tag{5.14}$$

The fits for the individual solutes are shown separately in the Appendix 7.3 (Fig. .14).

5.3 Results

5.3.1 Benchmark QM/MM against DFT and literature

For 22 alloying elements we have computed the differences in the formation energies for the different sublattices (Eq. (5.3)) with DFT and compared it with our two QM/MM setups.

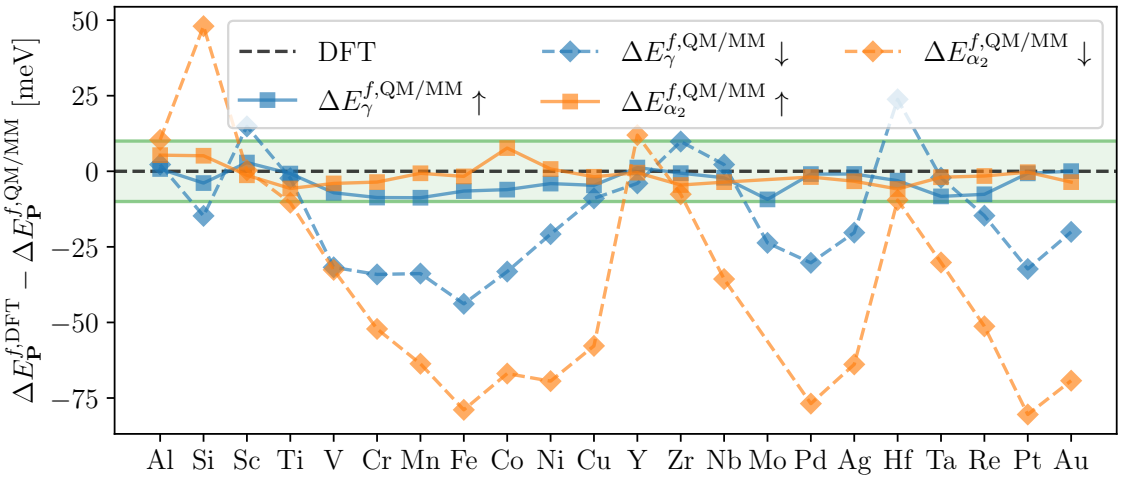

Figure 5.4: Error in QM/MM computed formation energies (Eq. (5.3)) of different solutes in the γ-TiAl and α_2-Ti_3Al bulk, with respect to the full DFT reference. Squares represent the computationally more demanding QM/MM $\uparrow$ and diamonds the minimalistic $\downarrow$ setup. Orange points refer to the α_2 and blue points to the γ phase. The green ribbon represents the target confidence interval of ± 10 meV region around the DFT reference.

Figure 5.4 shows the energy differences between the DFT and the QM/MM values for both setups. The green ribbon represents ± 10 meV and encloses all values of the computationally demanding ($\uparrow$ = squares) QM/MM setup. Thus it proves, that the difference between DFT and QM/MM is vanishing for computationally demanding settings.

For the minimalistic QM/MM setup ($\downarrow$), the differences are much larger, up to ≈ 80 meV for Pt. The deviations are larger in the α_2 phase than in the γ-bulk phase. The difference tends to increase for later transition metals. This can be understood in terms of strain energy errors, which are introduced by the QM/MM methodology in two ways: firstly, relaxations are only accounted for in the positional (and not cell) degrees of freedom, and, secondly, since the *filler* atoms are held fixed, large segregants may induce filler-buffer strain that does not cancel out in other components of the segregation energy calculation. The latter is of particular concern when the number of *core* shells is small. Nevertheless, usually $\Delta E_{\mathbf{P}}^{f}$ is in the range of 1eV, and consequently, even this setup produces very reasonable estimates, as we show later.

Figure 5.5 compares the values computed by Eq. 5.3 for the α_2 (upper panel) and γ-bulk phase (lower panel), for three different setups (DFT, QM/MM $\uparrow$ and $\downarrow$) to literature data. It confirms, in addition to Fig. 5.4, that the presented QM/MM method is able to reproduce DFT extremely accurately. Notably, even for minimalistic QM/MM settings ($\downarrow$), our implementation manages to reproduce DFT values well. Although the differences might seem large in Fig. 5.4 at a first glance, they are small compared to the spread found throughout the presented literature data (see Tab. 5.2).

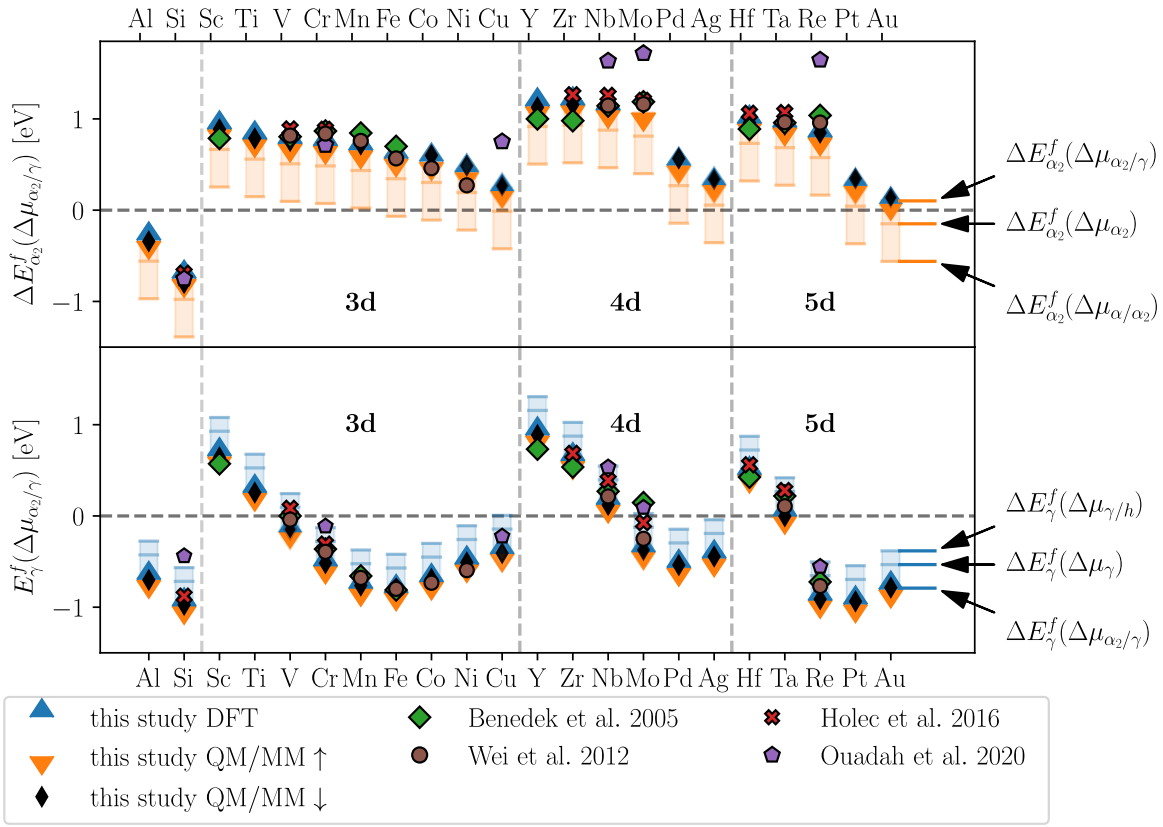

Figure 5.5: Difference of the defect formation energy between the Ti and Al sublattice (Eq. (5.3)) for the α_2-Ti_3Al and the γ-TiAl bulk phases. The shaded regions represent the range of allowed values. The construction and meaning of the thermodynamic limits are defined in Sec. 5.2.6. Points, representing literature data, exhibit a small black border.

Figure 5.5 reveals excellent agreement with the study of Wei *et al.* [189] for both α_2 and γ bulk phases. Comparing our data with Holec *et al.* [208] reveals a good agreement, yet a slight underestimation of $\Delta E^f_{\alpha_2}$ and overestimation of ΔE^f_γ. Furthermore, upon comparison with Benedek *et al.* [209], Fig. 5.5 reveals no systematic trend. Finally, the largest differences are observed, when comparing the present study with Ouadah, Merad, and Abdelkader [210]. Interestingly, for the α_2 phase, there is a good agreement for Si and Cr, while for Cu, Nb, Mo, and Re the differences are more than 100%. ($\Delta E^f_{\alpha_2} = 0.74$ eV compared to 1.58 eV for Re). A more detailed and quantitative analysis is presented in Tab. 5.2.

5.3.2 Site preference

We calculated the site preference energies for a wide range of solutes for the α_2- and γ-bulk phases as well as for the α_2/γ and γ/γ interfaces. For the α_2/γ interface we also have differentiated between the site preference energy at each side of the interface, $\underline{\alpha_2}/\gamma$ and $\alpha_2/\underline{\gamma}$ respectively. For the bulk phases, the $\Delta E^f_{\mathbf{P}}$ is a function of $\Delta\mu_{\mathbf{P}}$, which allows drawing a

Table 5.2: Average, standard and maximum deviation of the $\Delta E^f_{\alpha_2}$ and ΔE^f_{γ} compared to literature data, shown in Fig. 5.5. All values are in eV. The first column corresponds to the brown circles, the second to the red crosses, the third to the green square, and the fourth column to the purple pentagons in Fig. 5.5. The last column corresponds to data points denoted by the black diamonds.

$\lvert\Delta E^{f,\text{lit.}}_{\mathbf{P}} - \Delta E^f_{\mathbf{P}}\rvert$		Wei [189]	Holec [208]	Benedek [209]	Ouadah [210]	QM/MM ↓
$\mathbf{P} = \alpha_2$	average	0.092	0.138	0.127	0.436	0.042
	std	0.048	0.038	0.058	0.323	0.027
	max	0.161	0.178	0.239	0.847	0.080
$\mathbf{P} = \gamma$	average	0.099	0.205	0.160	0.403	0.016
	std	0.045	0.085	0.128	0.111	0.011
	max	0.151	0.314	0.533	0.547	0.037

point-defect phase diagram for each of the solutes. For these diagrams we refer the reader to the Appendix .1 (Fig. .11 shows the diagrams for the α_2 and Fig. .12 for the γ phase). For the interface structure, this degree of freedom is lost due to the requirement of co-existing α_2 and γ phases. Therefore, in Fig. 5.6 ΔE_f is fully defined by a scalar value.

Table 5.3: Summary of the site preference of different solutes, according to Eq. (5.2). Bold sublattice names indicate a strong site preference for the solute. When sublattice splitting occurs due to the broken symmetry at the interface, the preferred sites are indicated with subscript (see Sec. 5.3.2 for an explanation).

	Al	Si	Sc	Ti	V	Cr	Mn	Fe	Co	Ni	Cu	Y	Zr	Nb	Mo	Pd	Ag	Hf	Ta	Re	Pt	Au
α_2	**Al**	**Al**	Ti	Ti	Ti	Ti	Ti	Ti	Ti	Ti	Al	**Ti**	**Ti**	**Ti**	**Ti**	Ti	Ti	**Ti**	**Ti**	Ti	Ti	Al
γ	**Al**	**Al**	**Ti**	**Ti**	Al	**Al**	**Al**	**Al**	**Al**	**Al**	Al	**Ti**	**Ti**	**Ti**	Al	**Al**	**Al**	**Ti**	Ti	**Al**	**Al**	**Al**
$\underline{\alpha_2}/\gamma$	Al	Al	Ti_1	Ti_2	Ti_2	Ti_2	Ti_2	Ti_2	Ti_2	Ti_2	Ti_2	Ti_1	Ti_1	Ti_2	Ti_2	Ti_2	Ti_2	Ti_1	Ti_2	Ti_2	Al	Al
$\alpha_2/\underline{\gamma}$	Al_1	Al_1	Ti	Ti	Al_2	Al_2	Al_2	Al_2	Al_2	Al_2	Al_2	Ti	Ti	Ti	Al_2	Al_2	Al_2	Ti	Ti	Al_2	Al_2	Al_2
γ/γ	Al	**Al**	**Ti**	**Ti**	Ti	Al	**Al**	**Al**	**Al**	Al	Al	**Ti**	**Ti**	Ti	Al	Al	Al	**Ti**	Ti	**Al**	**Al**	**Al**

Site preference at the $\alpha_2(0001)/\gamma(111)$ interface

As mentioned in Sec. 5.3.2, there are two Ti sites at the α_2 side of the interface. The different sites are marked explicitly in Fig. 5.1. The first one (Ti_1) exhibits five Al and seven Ti nearest neighbors. The Ti_2 site is surrounded by four Al and eight Ti atoms. Thus the Ti_1 is slightly Al-rich compared with the Ti_2 site. The γ side of the interface also exhibits a splitting of the Al sublattice into two symmetry in-equivalent sites. Al_1 sites have nine Ti and three Al neighbors (we refer to them as the Ti-rich sites), whereas Al_2 sites are surrounded by four Al and eight Ti atoms.

Focusing on the latter (γ) side, Tab. 5.3 reveals that Si and Al prefer the Ti-rich Al_1 sites while all other solutes with the Al sublattice preference occupy the Al_2 sites. Table 5.3 and

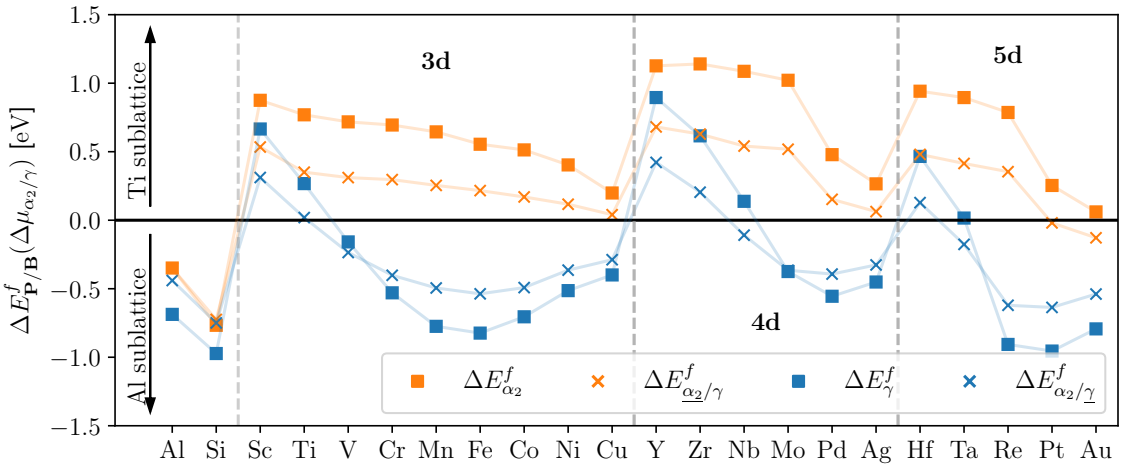

Figure 5.6: Formation energy differences between Ti and Al sublattices. Orange squares represent α_2-bulk (Eq. (5.3)), crosses $\underline{\alpha_2}/\gamma$ boundary (Eq. (5.7)), blue squares γ-bulk (Eq. (5.3)) and crosses $\alpha_2/\underline{\gamma}$ boundary (Eq. (5.7)). All values are calculated at $\Delta\mu_{\alpha_2/\gamma}$ (see Sec. 5.2.6).

Fig. 5.6 (blue) show that most of the solutes considered here prefer the Al site, and only the early $3d$ (Sc and Ti), $4d$ (Y and Zr) and (Hf and Ta) $5d$ elements prefer the Ti sublattice.

Absolute values of $\Delta E^f_{\alpha_2}$ and $\Delta E^f_{\underline{\alpha_2}/\gamma}$ continuously decrease with increasing atomic number throughout the periods for the α_2 side of the interface (Fig. 5.6, orange diamonds). Our calculations predict that almost all transition metals prefer the Ti sites. Moreover, the Ti sublattice preference gets more pronounced with increasing period ($3d < 4d < 5d$). Except for Sc, Zr, and Mn (preferring Ti_1 sites), all elements prefer the Ti_2 sites (Tab. 5.3).

The early transition metals (Sc, Ti, Y, Zr, and Hf) prefer the Ti sublattice independent of the interface side. Except for V (γ side) and Cu and Pt (α_2 side), all elements preserve their bulk site preference, although the absolute values of the site energy at the interface decrease with respect to their bulk states (see arrows in Fig. 5.6). Thus, solutes become more "*indifferent*" about their preferred sublattice, most likely due to a less ordered chemical environment at the interface. This is in good agreement with previous works as mentioned in Sec. 5.3.1.

Site preference at the γ/γ interface

It is noteworthy that the bulk-to-interface changes of the site energy at the γ/γ interface (overlaying diamonds and squares in Fig. 5.7) are much smaller as compared with the α_2/γ interface (Fig. 5.5). We attribute this to the (chemically) coherent nature of the γ/γ interface. Except for Y, the energy differences stay below an absolute value of ≈ 100 meV.

Due to the similarity between bulk and interface site preference, the trends are identical with the γ bulk and also with the γ side of the α_2/γ interface: early transition metals (Sc, Ti, Y, Zr and Hf) strongly prefer Ti sublattice, Al, Si and late transition metals prefer the Al sublattice.

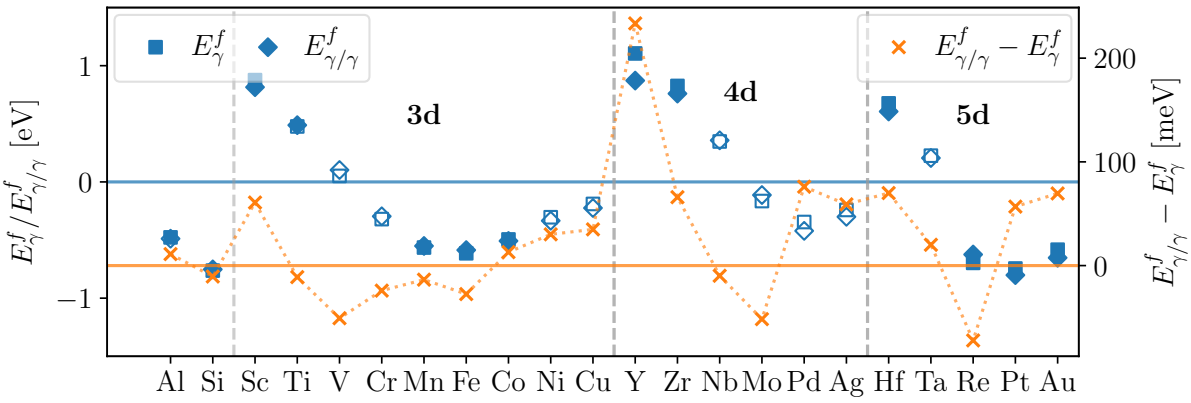

Figure 5.7: Site preference energies at the γ/γ interface (diamonds) and in the γ-bulk (squares). Crosses show the difference of the site energy values (right y-axis). Filled and open symbols represent strong and weak site preference, respectively.

5.3.3 Solute segregation

For a more detailed visualization, we refer the reader to Fig. .15. Following the principle of minimum energy, the following segregation behavior is predicted:

Segregation and phase-partitioning at the α_2/γ phase-boundary

Partitioning into the γ bulk phase Sc prefers both the γ side of the interface and the γ bulk over the α_2 side of the interface and the α_2 bulk phase. The positive values of $E^f_{\gamma\to\underline{\gamma}/\alpha_2}$ further indicate that the bulk state is preferred (although marginally in the case of Sc).

Partitioning into the α_2 bulk phase $3d$ transition metals (Cr, Mn, Fe, Co, Ni), as well as Mo, Pd, Ag, Ta, Au, Cu, and Re, prefer the α_2 phase. All those solutes show substantial positive (orange) $E^f_{\alpha_2\to\underline{\alpha_2}/\gamma}$ values, and thus prefer the α_2 bulk state. Moreover, the elements show a strong phase preference for the α_2 bulk phase ($E^f_{\gamma\to\alpha_2} < 0$).

Elements segregating to the interface Y, V, Zr, and Nb exhibit the minimum energy state at the γ side of the interface. Y, Zr and Nb exhibit similar $E^f_{\gamma\to\alpha_2/\underline{\gamma}}$ between -50 and $-100\,\mathrm{meV/at}$. Consequently, the preference for the interface (with respect to γ bulk) is rather small. Interestingly, the phase preference (and hence the driving force for segregation from the α_2 phase) is largest for Y and almost disappears for Nb. In contrast to those three elements, V shows a strong preference for the γ side of the interface state, although it otherwise prefers the α_2 bulk phase.

Si, Hf, and Pt are predicted to reside on the α_2 side of the interface. In the case of Si, this reflects the overall phase preference for the α_2 phase, and within that a slight preference for the interface position. Similar scenario applies also to Pt, whereby the preference for the

interface is much stronger. Lastly, Hf exhibits a slight phase preference for the γ bulk phase, as well as negative segregation energy from both phases to the interface with the α_2 side being the preferred one.

Comparison with experiments The amounts of alloying elements in experimentally studied alloys refer to the overall compositions and often range values above a few at. %. In multiphase systems, the alloying element is likely preferably present in one of the co-existing phases, whereas other phases are depleted of this element. Consequently, the local compositions may reach above 10 at. % or even more. Enrichment at the phase boundary in the order 1 at. % is therefore difficult to detect, since in the same spacial region happens the transition from e.g. 10 at.% (phase containing the alloying element) to 0 at. % (phase depleted of the element). In other words, a strong phase preference may hinder the experimental observation of phase-boundary segregation (happening on top of the phase segregation). This needs to be kept in mind when discussing the phase boundary segregation in multi-phase alloys, as it is the case of studies where the alloying composition exhibits more than 0.5 at. % of Nb and Cr in Ref. [211] and Mn and Cr for Ref. [212].

Using atom-probe-tomography (APT), Klein *et al.* [211] found Si to strongly partition into the α_2 bulk phase. Although our results suggest Si to segregate to the α_2 side of the interface, the energy gain at the interface itself is rather small, i.e. $|E^f_{\gamma\to\alpha_2}| \gg |E^f_{\alpha_2\to\underline{\alpha_2}/\gamma}|$. Moreover, the segregation to the interface may be soon disadvantaged by a Si accumulation during the initial phase of the partitioning process, which will later lead to a substantial amount of Si in the α_2 grain due to $E^f_{\gamma\to\alpha_2} \ll 0$. Mn and Cr [212] and Mo [211] were also experimentally reported to partition into the α_2 phase, fully in line with our predictions.

Gerstl, Kim, and Seidman [212, 213] reported on a partitioning of Zr and Nb to the γ bulk phase. In our predictions, both of these elements would prefer to occupy sites at the γ side of the interface. Using similar arguments as for Si above, we speculate that the segregation tendency of the γ side of the interface will be saturated and at later stages, which presumably correspond to the experimental conditions, Zr and Nb will occupy γ bulk site (which are preferred over any site in the α_2 phase). Especially for Y and Nb, the scales in Fig. .15 reveal a small difference between the γ-bulk and $\alpha_2/\underline{\gamma}$-state.

Finally, let us recall the APT measurement of Gerstl, Kim, and Seidman [212, 213] proving that Hf favors the α_2 side of the α_2/γ interface, fully in line with our results.

As for most elements, the phase preference ($E^f_{\gamma\to\alpha_2}$) tends to overrule interface segregation, we especially want to highlight Nb, Hf, Zr, and Sc (where $|E^f_{\gamma\to\alpha_2}|$ is small) as promising candidates for tailoring interface properties. Elements such as Mn, Fe, Co, Re, etc. will exhibit a strong thermodynamic force to partition into one phase, which inhibits any potential of using them for grain boundary-based micro-structure design. On the contrary, Nb, Hf,

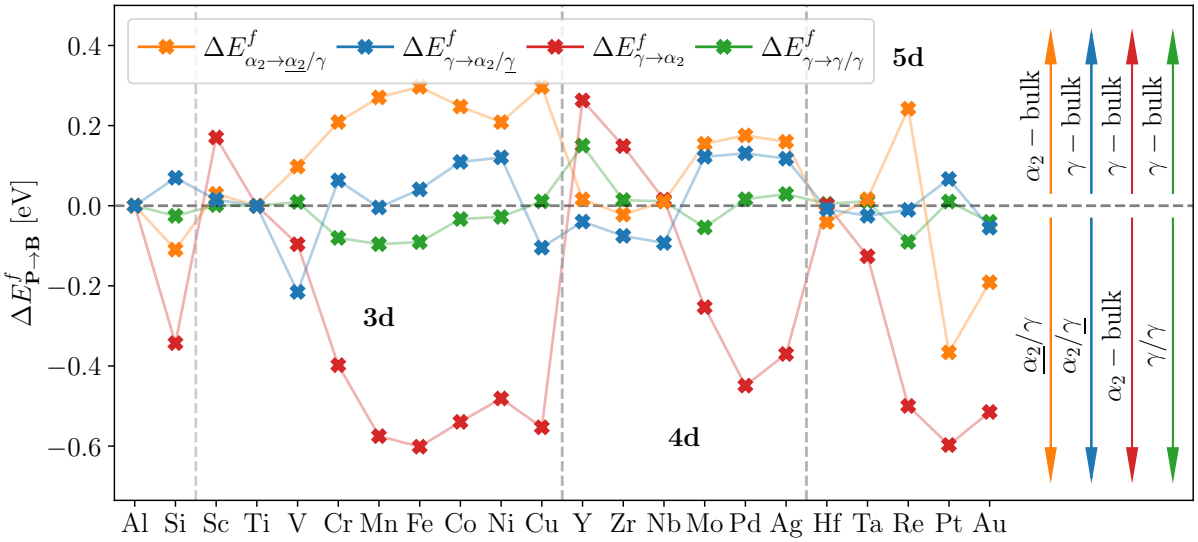

Figure 5.8: Segregation energies for the cases $\gamma \to \gamma/\gamma$ (green), $\alpha_2 \to \underline{\alpha_2}/\gamma$ (orange) and $\gamma \to \alpha_2/\underline{\gamma}$ (blue). $\gamma \to \alpha_2$-bulk Squares indicate a Ti-sublattice-preference, diamonds refer to a preference for the Al sublattice. Stars indicate that the solute changes its preferred sublattice. Filled and drawn symbols distinguish between strong and compositionally dependent site preference. Half-filled points indicate segregation from "*strong*" → "*weak*" if filled on the right side and vice versa in case the left side is filled. If a solute exhibits a box above the plot, it experiences negative segregation energy, while the color intensity represents the strength with respect to the strongest segregating element.

Zr, and Sc could be engineered to stay at the interface, since the phase preference may be overruled by thermal contributions.

In conclusion, although the specimens underwent heat treatments and show complex alloying concepts in the experimental studies [211–213] our predictions show very good qualitative predictive power. Some discrepancies may be related to the actual overall amount of the alloying element—our calculations correspond to a dilute limit—, the overall alloy constitution—we assume ideal compositions of the α_2 and γ phases—and finite temperature heat treatments.

Segregation to the γ/γ interface

Due to the coherent nature of the γ/γ interface, solutes feel only a small thermodynamic force to segregate. This is a similar behaviour due to the almost identical site energies for the γ/γ interface and γ bulk (Fig. 5.7) for nearly all solutes. As both sides of the interface are chemically equivalent the segregation behaviour of the solute is solely defined $E_{\text{seg}}^{\gamma\to\gamma/\gamma}$. The absolute values of the segregation energy are expected to be smaller compared with the α_2/γ interface which is indeed confirmed by our calculations (Fig. 5.8, cf. the green points to all other). Nonetheless, we predict a small segregation tendency for the 3*d* metals, as well

as for Si, Mo and Re.

5.3.4 Interface properties

As with segregation properties presented in Fig. 5.8, the mechanical properties in Fig. 5.9 are only expected to be a qualitative guide, since approximations in the calculations interfere with a direct, quantitative comparison with experiment. To describe the impact of segregating elements, we will focus on the changes in mechanical properties with respect to pristine interfaces (e.g., $\Delta\sigma_c$) rather than on the absolute values (e.g., σ_c).

Cleavage energy, E_c The cleavage energy $E_c = 3.64\,\mathrm{J/m^2}$ for the α_2/γ interface is in excellent agreement with previous study by Wei *et al.* [189] ($E_c = 3.62\,\mathrm{J/m^2}$), wheres the γ/γ interface yields a lower value of $3.47\,\mathrm{J/m^2}$. V, Cr, Nb, Mo, Ta and Re slightly increase E_c value when placed on the α_2 side of the interface, however, most of the remaining studied species decrease E_c with respect to the pristine interface. Majority of elements lead to an increase when placed on the γ side of the interface; the largest enhancement is predicted for Re with over 5% increase. Interestingly, when solutes at the γ side of the α_2/γ interface exhibit a cleavage energy trend almost identical to that of the γ/γ interface. Y and Sc have a detrimental effect on E_c for all interface positions.

Critical stress, σ_c The critical stress values $\sigma_c = 22.4\,\mathrm{GPa}$ is predicted to be higher than tensile strength obtained from tensile tests simulated using molecular dynamics ($\sigma_C^{\alpha_2/\gamma} = 15.6\,\mathrm{GPa}$ Li *et al.* [214]). This is due to the localisation of strain in cleavage calculations. All three configurations show very similar behaviour. Cu, Nb, Pd and Pt do not influence the critical stress; Y, Sc and Zr are major detrimental dopants, similarly to the cleavage energy, while Re yields an increase of $\approx 9\%$. Overall, $3d$ metals improve σ_c.

Interface stiffness, C_{zzzz} Pristine γ/γ and α_2/γ interfaces have interface stiffness of 214 GPa and 157 GPa, respectively, suggesting that the γ/γ interface is significantly stiffer. C_{zzzz} is mostly anti-correlated to the cleavage energy and critical stress. The $3d$ metals (Cr, Mn, Fe, Co and Ni) reduce the absolute values, at both interfaces. On the other hand Y, Zr, Hf and Ta increase C_{zzzz} in considered configurations. The largest enhancement of C_{zzzz} (stiffening) is predicted for Mo at the α_2/γ interface. In general, solutes have a more detrimental effect on the γ/γ interface than on the α_2/γ one; the largest deviation from the pristine values is predicted for Fe ($\delta C_{zzzz}^{\gamma/\gamma}(\mathrm{Fe}) \approx 14\%$); also, the impact of segregating species seem generally larger than in the cases of cleavage energy and critical stress. Nb, Mo and Ta are exceptions from the anti-correlation by simultaneously enhancing both cleavage energy E_c and interface stiffness ($\Delta C_{zzzz} > 0$) at the α_2/γ interface. Finally, in contrast

to the cleavage energy, we obtain similar values for solutes being on either side of the α_2/γ interface.

Fracture toughness K_{IC} We combined cleavage energy, E_c, and interface stiffness, C_{zzzz}, according to Eq. (5.13) to obtain a prediction for K_{IC}. Due to the significantly larger C_{zzzz} for the γ/γ interface as compared with the α_2/γ interface, and comparable values for E_c, more energy is needed to stretch the γ/γ than the α_2/γ interface bonds, resulting in higher fracture toughness values. Regarding the solute impact, since larger relative deviations are obtained in the stiffness values, the trends for the fracture toughness are mostly governed by stiffness trends.

Although $3d$ metals (Cr, Mn, Fe, Co) increase cleavage energy, they reduce the overall fracture toughness of the γ/γ interface. Sc, Zr and Y show no influence at the α_2/γ but a drop at the γ/γ interface. Generally, all solutes except for Hf, Zr and Ta reduce fracture toughness at the γ/γ interface. Regarding the α_2/γ interface, elements that are not subject to the anti-correlation between E_c and ΔC_{zzzz}, namely Nb, Ta and Mo, result in the largest enhancement of fracture toughness. It is worth mentioning also Re, which has a similar impact as Ta, but the enhancement is fully governed by an increase in E_c, unlike the case of Hf and Zr, where an increase in C_{zzzz} overrules a slight decrease in E_c.

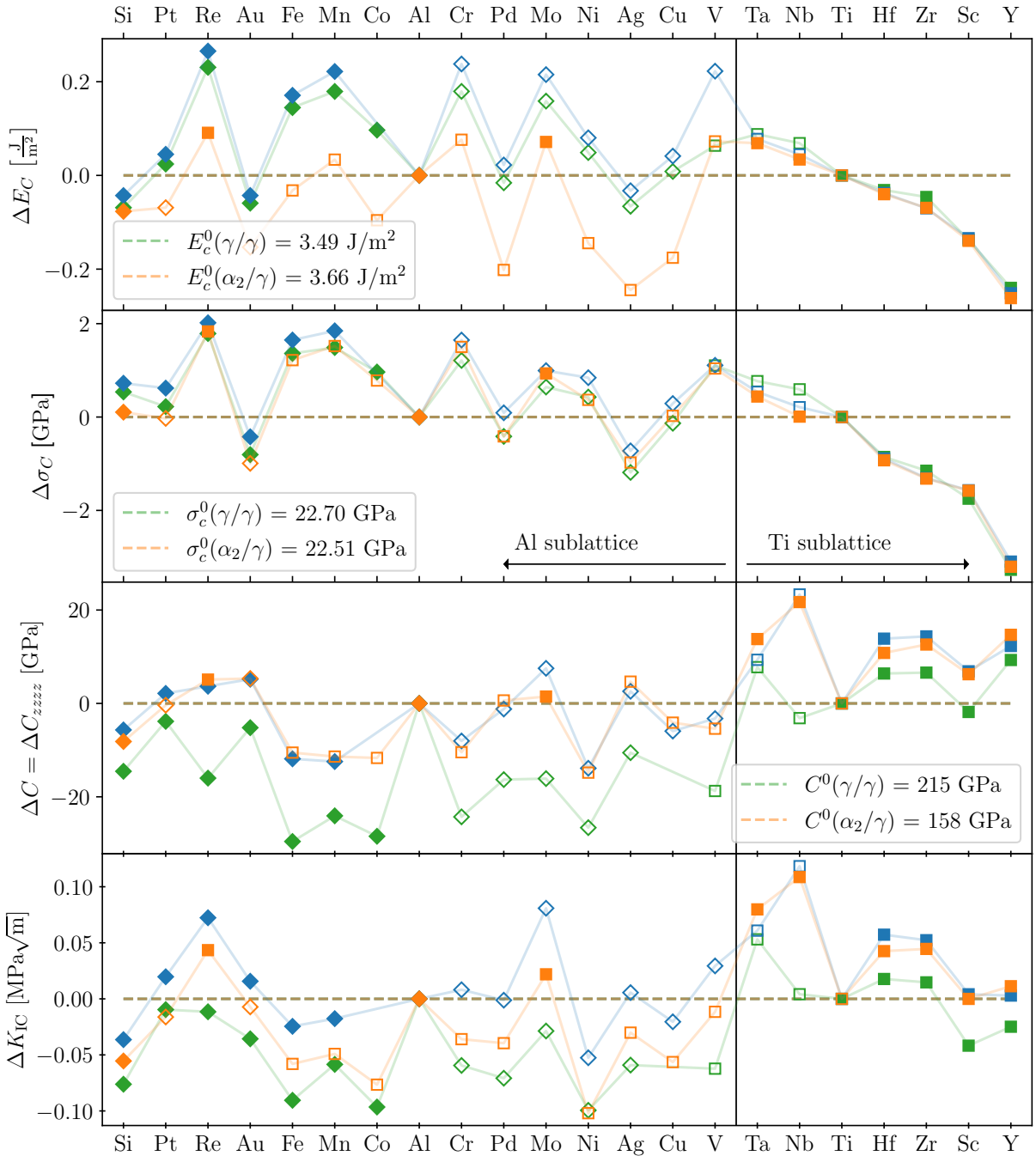

Figure 5.9: Critical interface stress σ_C, interfacial cleavage energy E_C, directional Young's modulus (normal to the interface-plane) C_{zzzz} and estimated fracture-toughness of (α_2/γ, γ/γ) lammellar packet K_{IC}. The orange curve denotes that the solute was placed on the α_2-side of the α_2/γ interface, while the blue curve corresponds to the γ side of the interface. The green curve shows the values for solutes at the γ/γ-TT interface. The elements are sorted in ascending order by $\Delta E^f_{\alpha_2/\underline{\gamma}}$ (c.f. Fig. 5.6).

Chapter 6

Models for configurational complex alloys

Many metals exhibit miscibility over the whole or at least partial composition range. This property is crucial as it allows the creation of alloys with outstanding properties. In such solid solutions, the lattice positions are randomly occupied with several atomic species. This disorder, however, poses a challenge for first-principles modeling. As mentioned many times, in this thesis before, the simulation boxes one can deal with are of finite size and most often rather small (tens to hundreds of atoms). In their ground-breaking work, Wei *et al.* [215] showed, how to arrange small (simulation) cells such that they mimic the properties of real alloys well. Such structures are named special quasirandom structures (SQS). Furthermore, they were the first to come up with an algorithm for finding such SQS [216].

The following chapter is structured as follows: Firstly, we give an introduction to quantifying short-range order in crystalline solids. The notation of this part is borrowed from a publication [217]. In the second part, we describe how Warren-Cowley short-range order (WC-SRO) parameters can be extended to describe triplet correlations. This work was partly carried out together with Ulrich Pototschnig, hence a small part of the second section is based on his bachelor thesis [218] (first paragraph of Sec. 6.2). From there on we make a short detour, and try to link our approach to traditional cluster expansion (CE). Then we briefly introduce, our implementation. Finally, we discuss how triplet parameters might be incorporated into our current structure enumerator based on pair WC-SRO parameters.

6.1 Measuring (dis)order in crystals

To generate crystal structures, that mimic a real solid solution, one has to be able to "*measure*" (dis)order in the simulation cell and compare it with the ideal case. Such a measure, by comparing the number of bond pairs in a finite cell with those of an ideal solution was suggested many decades ago [219–221]. Consider a finite simulation box with N lattice sites, occupied with atoms A and B. We refer to the sequence of A and B atoms,

$\sigma = \langle A, B, A, \ldots, B \rangle$, as the (atomic) configuration or arrangement. To quantify disorder in the cell, corresponding Warren-Cowley short-range order (SRO) parameter reads

$$\alpha_{AB}(\sigma) = 1 - \frac{N_{AB}(\sigma)}{NMx_A x_B}\,. \tag{6.1}$$

Where N_{AB} denotes the number of $A-B$ bonds in the finite cell. The denominator of Eq. (6.1) corresponds to the number of bonds in the ideal solution. Consequently, M is the number of nearest neighbors in the given atomic arrangement. Fig. 6.1 illustrates the possible values the SRO parameter can take. For a clustered (Fig. 6.1a) case the number of bonds in the ideal solutions will outweigh those in the simulations box and lead to negative values for the SRO parameters. The opposite holds for the ordered case (Fig. 6.1c). The cell will mimic the random alloy best once Eq. (6.1) approaches zero (Fig. 6.1b).

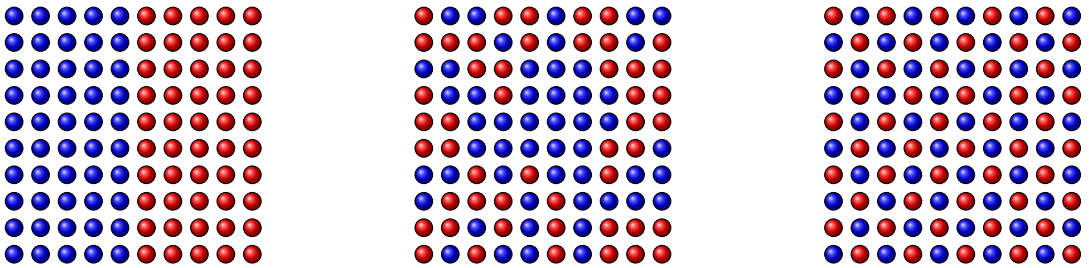

(a) clustering: $\alpha_{AB} > 0$ since $N_{AB} < NMx_a x_b$

(b) random: $\alpha_{AB} \approx 0$ since $N_{AB} \approx NMx_a x_b$

(c) ordered: $\alpha_{AB} < 0$ since $N_{AB} > NMx_a x_b$

Figure 6.1: Visualization on the clustered state (a), disordered state (b), and ordered state (c) together with the corresponding relations between the number of $A-B$ bonds with α_{AB} [222].

6.1.1 Pair correlations

Figure 6.1 illustrates the physical intuition behind Eq. (6.1). Nevertheless, the above equation needs generalization to be applicable to real-world use cases. Before starting to generalize Eq. (6.1), one should clarify the terminology. More precisely, above when speaking of $A-B$ bonds we referred to nearest neighbor $A-B$ pairs. Our simulation box contains $\frac{1}{2}N(N-1)$ pairs, from which the above definition takes into account only a fraction of them. Therefore, from now on we will refer to nearest neighbors, as "*pairs in the first coordination shell*". Consequently, Eq. (6.1) can be generalized to an arbitrary number of coordination shells. The radius and hence, the number of coordination shells available is given by the maximum pair distance of atoms in the simulation box. The WC-SRO describing disorder using pairs of the i^{th} coordination shell therefore reads

$$\alpha_{AB}^{i}(\sigma) = 1 - \frac{N_{AB}^{i}(\sigma)}{NM^{i}x_{A}x_{B}}\,. \tag{6.2}$$

While the above equation looks very similar to Eq. (6.1), the generalization has major implications. Assuming, that C coordination shells fit into the box, many SRO parameters are needed to describe the finite cell. Furthermore, M^i now denotes the number of pairs in the i^{th} coordination shell. Finally, another final step is missing to describe the disorder of real-world composition. Therefore, the above equation needs adaptions such that it is suited to multi-component systems. The corresponding SRO parameters are defined as

$$\alpha_{\xi\eta}^{i}(\sigma) = 1 - \frac{N_{\xi\eta}^{i}(\sigma)}{NM^{i}x_{\xi}x_{\eta}} \tag{6.3}$$

where ξ and η are species occurring in the system. Similarly to Eq. (6.2), more SRO parameters in multi-component cases. Suppose the configuration contains S different atomic species, for each coordination shell $\frac{1}{2}S(S+1)$ parameters are required for a full description. Thus to find an ideal finite cell $\frac{1}{2}C \cdot S \cdot (S+1)$ SRO parameters need to be minimized independently of each other. Note that due to the discrete nature of lattice positions, it is generally not possible to get all SRO parameters to zero for small cells at least.

We note that the $\frac{1}{2}$ prefactor arises because atom pairs are invariant to the exchange of the atoms. Hence, the symmetry condition

$$\alpha_{\xi\eta}^{i} = \alpha_{\eta\xi}^{i} \quad \forall\, \xi \neq \eta \tag{6.4}$$

holds, as we treat $\xi - \eta$ and $\eta - \xi$ pairs equally.

We point out that while developing the theory to describe the disorder, we implicitly assumed that the atoms in the simulation box are arranged on a perfect periodic lattice. Therefore, we compute the number of pairs in a finite box with N lattice positions for a specific coordination shell as follows

$$M^{i} = \frac{|\{r_{jk} \mid R_{i-1} < r_{jk} \leq R_{i}\}|}{N}\,. \tag{6.5}$$

For a perfect lattice, M^i will be an integer number, while otherwise, its meaning changes to an average coordination number within the shell.

6.1.2 Limitations of pair correlations

The applicability of our approach can be judged by looking at the spectrum (histogram) of pair distances. For a perfect lattice in a finite simulation box with coordination shell radii R_i the spectrum proportional to a sum a delta functions

$$|\vec{r}_{ij}|(r) = \sum_{i=1}^{C} f_i \delta(r - R_i) \tag{6.6}$$

where f_i are just arbitrary coefficients depending on the box size and lattice type. In general, when applying relaxations, these delta-peaks begin to smear out. Figure 6.2 illustrates such smearing, happening during an ionic relaxation. As long as the individual distributions do not overlap one might choose artificial coordination shell radii such that $N^i_{\xi\eta}$ remains constant throughout the relaxation process. Nevertheless, we note that this only holds for the first four coordination shells in Fig. 6.2, as the distributions around the sixth and seventh coordination shell overlap. This is, related to the fact, that the difference between coordination shell radii to decrease with increasing shell index.

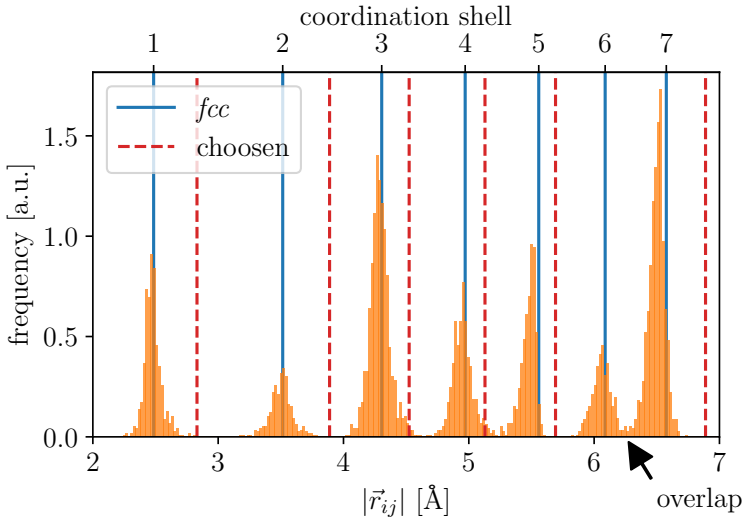

Figure 6.2: Pair distances for a *fcc* lattice (blue) and the histogram for a relaxed $Ni_{60}Cr_{20}Co_{16}Ti_6Al_6$ cell (orange).

Furthermore, in the case of overlapping distributions, Eq. (6.5) becomes a real instead of an integer number. In such a case, minimizing the SRO parameters will still yield a random structure, however, as it is not uniquely determined how to partition the pair distances into coordination shells the results might slightly differ depending on its choice.

6.1.3 Objective function

Minimizing all pair SRO parameters at the same time independently of each other to obtain a disordered model, does not leverage the full power of the WC-SRO parameter quantification. Hence, it restricts an implementation to generating only disordered cells, while the description would allow generating clustered (Fig. 6.1a), partially clustered, partially ordered as well as ordered (Fig. 6.1c) cells. Thus, by combining the WC-SRO parameters into a single scalar using

$$\mathcal{O}^{\alpha}(\sigma) = \sum_{i}^{S} w^{i} \sum_{\xi,\eta}^{C} p_{\xi\eta} \left| \tilde{\alpha}^{i}_{\xi\eta} - \alpha^{i}_{\xi\eta}(\sigma) \right| \tag{6.7}$$

$$= \sum_{i}^{S} \sum_{\xi,\eta}^{C} \tilde{w}^{i}_{\xi\eta} \left| \tilde{\alpha}^{i}_{\xi\eta} - \alpha^{i}_{\xi\eta}(\sigma) \right| \text{ where } \tilde{w}^{i}_{\xi\eta} = w^{i} p_{\xi\eta} \tag{6.8}$$

enables a more flexible optimization process. In Eq. (6.8), w^i is the i^{th} element of a vector of length C containing the weighting factors of the contributions of the individual coordination shells. $p_{\xi\eta}$ is a matrix of size $S \times S$ through which, each bond type may be weighted differently or disabled completely. Finally, $\tilde{\alpha}^{i}_{\xi\eta}$ is a set of "*target*" SRO parameter values allowing to tune each element of Eq. (6.3) towards a desired values. To see for which material systems or cases these parameters may be tuned we refer the reader to Ref. [217].

6.2 Generalization to triplet - correlations

In addition to the generalizations — arbitrary coordination shells and multi-component configurations — one can also include higher-order correlations such as triangles. The motivation to do so is twofold. Firstly, there exist material systems where pair-correlations alone cannot explain all observed phenomena [223]. Secondly, and more importantly, for practical applications there are usually many atomic arrangements σ which minimize a given set of pair SRO parameters or Eq. (6.8). To avoid the degeneracy of solutions, we can further refine our description of randomness. Hence, the next larger cluster of atoms (other than a pair) would be a triplet, made of three atoms and three bonds, between those atoms as depicted in Fig. 6.3b.

Before, generalizing the pair SRO parameter, it is helpful to introduce a notation to describe triplets of atoms. A triplet itself consists of three bonds. We denote a bond between a ξ and an η atom by their distance $c_{\xi\eta}$, which is the corresponding coordination shell and consequently must be an integer number between one and C, the number of coordination shells.

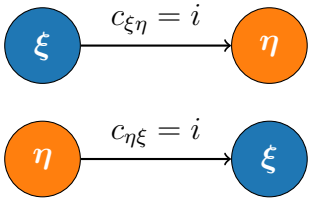

(a) Schematic illustration of an atom pair, described by a (pair) SRO parameter $\alpha^i_{\xi\eta}$. The pairs show the possible construction paths. $c_{\xi\eta}$, $c_{\eta\xi}$ denote the coordination shell of the pair

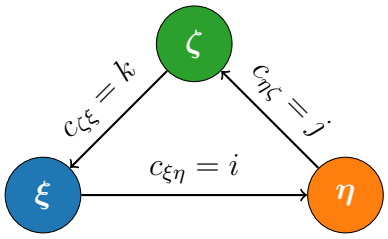

(b) Schematic illustration of a triplet, described by a (triplet) SRO parameter $\beta^{ijk}_{\xi\eta\zeta}$

Figure 6.3: Schematic illustrations of general atom pairs and triplets. ξ, η and ζ refer to atomic species. i, j and k denote coordination shell indices.

Since, we treat $\xi - \eta$ and $\eta - \xi$ bonds equally the symmetry relation

$$c_{\xi\eta} = c_{\eta\xi} \tag{6.9}$$

must hold, which also gives rise to Eq. (6.4). In the most general case a triplet consists of three atoms ξ, η and ζ which are connected by three bonds of length i, j and k, where e.g. i refers to the i^{th} neighbor distance. Therefore, we describe such specific triplet using $T^{ijk}_{\xi\eta\zeta}$. Note that the order of sub- and superscript indices does matter. Hence, $T^{ijk}_{\xi\eta\zeta}$ refers to a triangle made up of a ξ — η bond of length i ($c_{\xi\eta} = i$), an η — ζ bond of length j ($c_{\eta\zeta} = j$) and finally a ζ — ξ bond of length k ($c_{\zeta\xi} = k$). Such a construction is illustrated in Fig. 6.3b. This notation is however, needs some further clarification. Observe, that both both sub- and superscript indices contain three distinct entries, allowing six different arrangements of the indices each. Those again may be combined into 36 constellation of indices. Figure 6.4 visualizes the fact that for $T^{ijk}_{\xi\eta\zeta}$ we can find six different index constellations that describe the same triplet, for which we introduce the notation $T\left\{{ijk \atop \xi\eta\zeta}\right\}$.

The braces denote that the indices may be permuted, yet not arbitrarily the sub- and superscript indices are in a relation to each other. Having 36 constellations at our disposal where always six of them describe the same triangle, reveals it is possible to construct, again six, non-equivalent triangles (see Fig. 6.5a).

Therefore we will denote a triplet SRO parameter comparing the number of $T\left\{{ijk \atop \xi\eta\zeta}\right\}$ triangles in a cell with those of an ideal solution, to as $\beta^{ijk}_{\xi\eta\zeta}$ with. Such a parameter will have the form of

$$\beta^{ijk}_{\xi\eta\zeta} = 1 - \frac{N^{ijk}_{\xi\eta\zeta}(\sigma)}{\#\text{ of triplets in the ideal solution}} \tag{6.10}$$

where $N^{ijk}_{\xi\eta\zeta}(\sigma)$ is the number of $T\left\{{ijk \atop \xi\eta\zeta}\right\}$ triplets in the cell for a given atomic arrangement

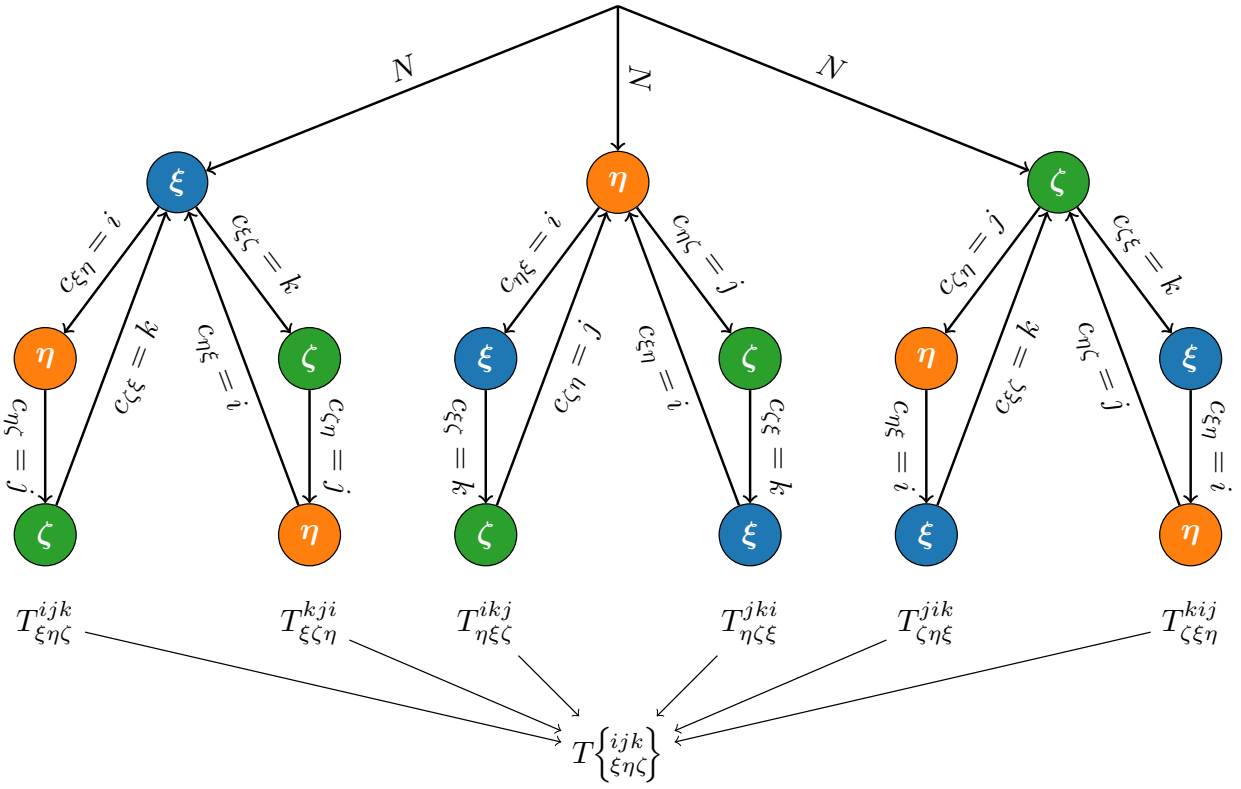

Figure 6.4: Visualisation of the six different construction routes for triplets.

σ. In the next section we will elaborate on how to determine the denominator of Eq. (6.10) and find an expression for the triplet SRO.

6.2.1 Denominator - Number of triplets in an ideal solution

To start with, we forget about the species populating a triplet and focus solely on its lengths. Ignoring the species, we find that we can define a triangle as a multiset[1] of the coordination shells of the constituent pairs. Therefore, denoting a triangle using $\{1, 2, 3\}$ also includes triangles, that would be formed by permutation of the numbers within the braces, e.g., $\{2, 3, 1\}$ or $\{3, 1, 2\}$. This is rather obvious as the order of how the triangle is constructed does not matter. Suppose we want to compute the number triangles $T^{\{ijk\}}$ with length $\{i, j, k\}$ for a general lattice. Therefore, let $\bar{M}$ be the set of all lattice sites within the largest coordination sphere $\max\{i, j, k\}$. Hence, the number of all triplets we can form from the sites in $\bar{M}$, whose constituent pairs form the multiset $\{i, j, k\}$, is defined as $T^{\{ijk\}}$. In more formal notation

$$\tilde{T}^{\{ijk\}} = \frac{1}{6} \sum_{\alpha,\beta,\gamma}^{\bar{M},\bar{M},\bar{M}} \{c_{\alpha\beta}, c_{\beta\gamma}, c_{\gamma\alpha}\} \delta_{\{c_{\alpha\beta},c_{\beta\gamma},c_{\gamma\alpha}\},\{i,j,k\}} \tag{6.11}$$

[1] a multiset is a set can hold each element multiple times

where $c_{\alpha\beta}$ etc. is the coordination shells distance of the pair $\alpha - -\beta$ formed by sites α and β. The Kronecker-delta will yield one in case the multisets are identical, and zero otherwise.

For a finite set of lattice positions, such as our simulation box, we average all lattice positions, and Eq. (6.11) becomes

$$T^{\{ijk\}} = \frac{1}{6N} \sum_{\alpha,\beta,\gamma}^{N,N,N} \{c_{\alpha\beta}, c_{\beta\gamma}, c_{\gamma\alpha}\} \delta_{\{c_{\alpha\beta},c_{\beta\gamma},c_{\gamma\alpha}\},\{i,j,k\}} \tag{6.12}$$

where N is the number of lattice positions. Note, that this definition yields similar properties as Eq. (6.5) as it will give integer numbers for perfect lattices.

Finally, we have to populate all the calculated triangles with species. According to Fig. 6.4, for the first atom we can on average either choose either Nx_ξ — ξ atoms, Nx_η — η atoms or Nx_ζ — ζ atoms. However, no matter which of the paths we take we must be able to construct exactly $T^{\{ijk\}}$. Therefore by averaging over the path from Fig. 6.4 we obtain an expression for the triplet SRO parameter which reads

$$\beta^{ijk}_{\xi\eta\zeta} = 1 - \frac{N^{ijk}_{\xi\eta\zeta}(\sigma)}{NT^{\{ijk\}}x_\xi x_\eta x_\zeta} \tag{6.13}$$

where similarly to Eq. (6.3), $N^{ijk}_{\xi\eta\zeta}$ is the number of triplets found in the cell. We want to note that the super-/subscript notation used in Eq. (6.13) suffers from two shortcomings. Firstly, there exist index permutations that represent the same physical triplet parameter, as shown in Fig. 6.4. Secondly, it is as a consequence not apparent at first sight which sub/superscript index permutations refer to different triplets. For pairs where the pair might be either occupied by one or two different species it is therefore easy to compute how many pair parameters ($\frac{1}{2}C(S^2+S)$, given S different species and C coordination shells) are needed to fully describe the interactions (see the end of Sec. 6.1.1).

6.2.2 Number of triplet parameters

To account for all triplet interactions, in contrast, to pair SRO parameters, many more triplet SROs are needed.

Furthermore, to compute the number of correlation parameters needed, we introduce the index multiplicity $\tilde{c}$ for the coordination shells and the $\tilde{s}$ for the species indices. A pair parameter $\alpha^i_{\xi\eta}$ has one coordination shell index (superscript) and two distinct species indices as a subscript. Hence follows that $\tilde{c} = 1$ and $\tilde{s} = 2$. Analogously, for a triplet correlation parameter $\beta^{ijk}_{\xi\eta\zeta}$ we obtain $\tilde{c} = \tilde{s} = 3$. In contrast we find $\tilde{c} = 2$ and $\tilde{s} = 2$ for a parameter of type $\beta^{iij}_{\xi\xi\eta}$.

Hence, the number of parameters needed to describe all interactions in a system with S species and considering C coordination shells can be written as

$$N^{\text{tuples}} = \sum_{\tilde{c}=1}^{3}\sum_{\tilde{s}=1}^{3} m_{\tilde{c}\tilde{s}} \binom{C}{\tilde{c}} \binom{S}{\tilde{s}} \tag{6.14}$$

where $m_{\tilde{c}\tilde{s}}$ refers to a multiplicity. That is how many distinct tuples can be constructed for a given set of pair distances and species. For example, consider an equilateral triplet ($\{i,i,i\}$, $\tilde{c}=1$) composed by two species ξ and η. In such a case one can only create two distinct triplets (as all other permutations lead to the same physical object). Those are $\beta^{iii}_{\xi\xi\eta}$ and its inversion with respect to the atomic species $\beta^{iii}_{\eta\eta\xi}$, resulting in $m_{12}=2$. All multiplicities for triplet SRO parameters are listed in Tab. 6.1.

		$\tilde{s}$	1	2	3
			$\{\xi,\xi,\xi\}$	$\{\xi,\xi,\eta\}$ $\{\eta,\eta,\xi\}$	$\{\xi,\eta,\zeta\}$
	1	$\{i,i,i\}$	1	2	1
$\tilde{c}$	2	$\{i,i,j\}$ $\{j,j,i\}$	2	8	6
	3	$\{i,j,k\}$	1	6	6

Table 6.1: Multiplicities with respect to the number of distinct species and distinct coordination shells in the indices $m_{\tilde{c}\tilde{s}}$.

To illustrate how we arrive at the number of given numbers in Tab. 6.1, all the possible construction are visualized in Fig. 6.5. Plugging in the values from Tab. 6.1 into Eq. (6.14) ($\tilde{c}=\tilde{s}=3$), leads to an expression for the number of triplets required to describe all possible occurring interaction which reads

$$N^{\beta} = \frac{1}{6} CS\,(CS+1)\,(CS+2) \approx \mathcal{O}(C^3S^3) \tag{6.15}$$

We will discuss the implication of this result later. For now, we want to point out that Eq. (6.14) recovers also our formula for the number required pair SRO parameters by setting $\tilde{c}=m_{cs}=1$ and $\tilde{s}=2$ we obtain

$$N^{\alpha} = \frac{1}{2} CS\,(S+1) \approx \mathcal{O}(S^2) \tag{6.16}$$

Finally, we want briefly discuss the implications of Eq. (6.4). As mentioned earlier (at the end of the last section) due to the different construction paths, leading to different sub- and superscript permutations for β, it is not straightforward to distinguish between β notation

referring to equal or distinct parameters. Therefore we have summarized all the β parameter permutations describing different triplets in Tab. 6.2. Therein, the references to Fig. 6.5 visualize the triplets described by the parameters. Note that the number of entries in each cell in Tab. 6.2 corresponds to the multiplicity number found in Tab. 6.1.

	$\tilde{s}$	1	2	3
		$\{\xi,\xi,\xi\}$	$\{\xi,\xi,\eta\}$ $\{\eta,\eta,\xi\}$	$\{\xi,\eta,\zeta\}$
1	$\{i,i,i\}$	$\beta^{iii}_{\xi\xi\xi}$	$\beta^{iii}_{\xi\xi\eta}$ $\beta^{iii}_{\eta\eta\xi}$	$\beta^{iii}_{\xi\eta\zeta}$
2	$\{i,i,j\}$ $\{j,j,i\}$	$\beta^{iij}_{\xi\xi\xi}$ $\beta^{jji}_{\xi\xi\xi}$	(Fig. 6.5d) $\beta^{iij}_{\xi\eta\xi}$, $\beta^{iij}_{\eta\xi\eta}$, $\beta^{jji}_{\xi\eta\xi}$, $\beta^{jji}_{\eta\xi\eta}$ $\beta^{iij}_{\xi\xi\eta} = \beta^{iij}_{\eta\xi\xi}$ $\beta^{iij}_{\eta\eta\xi} = \beta^{iij}_{\xi\eta\delta}$ $\beta^{jji}_{\xi\xi\eta} = \beta^{jji}_{\eta\xi\xi}$ $\beta^{jji}_{\eta\eta\xi} = \beta^{jji}_{\xi\eta\eta}$	$\beta^{iij}_{\xi\eta\zeta} = \beta^{iij}_{\zeta\eta\xi}$ (Fig. 6.5b) $\beta^{iij}_{\zeta\xi\eta} = \beta^{iij}_{\eta\xi\zeta}$ $\beta^{iij}_{\eta\zeta\xi} = \beta^{iij}_{\xi\zeta\eta}$ $\beta^{jji}_{\eta\zeta\xi} = \beta^{jji}_{\xi\zeta\eta}$ $\beta^{jji}_{\eta\zeta\xi} = \beta^{jji}_{\xi\zeta\eta}$ $\beta^{jji}_{\eta\zeta\xi} = \beta^{jji}_{\xi\zeta\eta}$
3	$\{i,j,k\}$	$\beta^{ijk}_{\xi\xi\xi}$	$\beta^{ijk}_{\xi\xi\eta}$ (Fig. 6.5c) $\beta^{ijk}_{\eta\eta\xi}$ $\beta^{ijk}_{\eta\xi\xi}$ $\beta^{ijk}_{\xi\eta\eta}$ $\beta^{ijk}_{\xi\eta\xi}$ $\beta^{ijk}_{\eta\xi\eta}$	$\beta^{ijk}_{\xi\eta\zeta}$ (Fig. 6.5a) $\beta^{ijk}_{\xi\zeta\eta}$ $\beta^{ijk}_{\zeta\xi\eta}$ $\beta^{ijk}_{\zeta\eta\xi}$ $\beta^{ijk}_{\eta\zeta\xi}$ $\beta^{ijk}_{\eta\xi\zeta}$

Table 6.2: Index symmetries of triplet SRO parameters according to Fig. 6.5.

Geometric constraints in perfect lattices

The above considerations represent the most general case where triangles can be built from any sequence of coordination shell indices. However, since the triangle inequality must hold, not all of them are geometrically possible of view for each lattice. Therefore, Tab. 6.3 compares the theoretical amount of index sequences in a system with $C = 7$ coordination shells, with the geometrically allowed number. Please note, that here we omit the number of species in the system. The actual number of β triplet SRO parameters will also depend on S.

6.2.3 Triplet objective function

Similarly to the pair SRO parameters, one can define a triplet objective function that reads

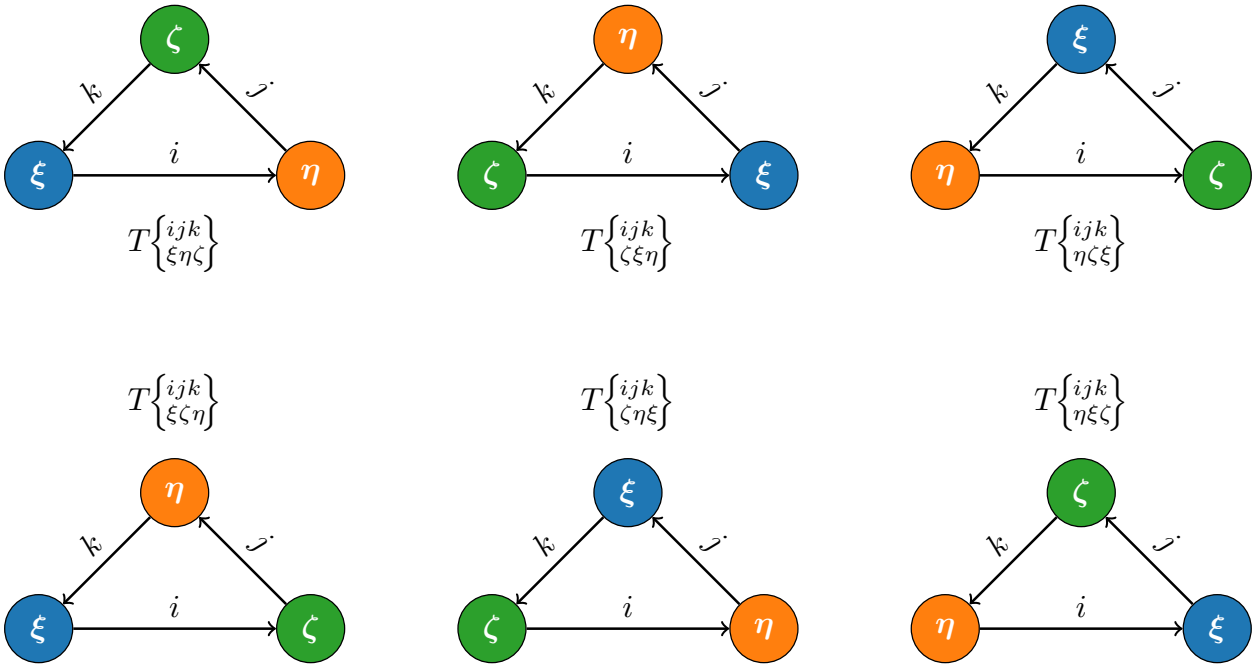

(a) Possible (distinct) triplet constructions for three different species $\{\xi, \eta, \zeta\}$, with three different side lengths $\{i, j, k\}$. ($m_{cs} = m_{33} = 6$),

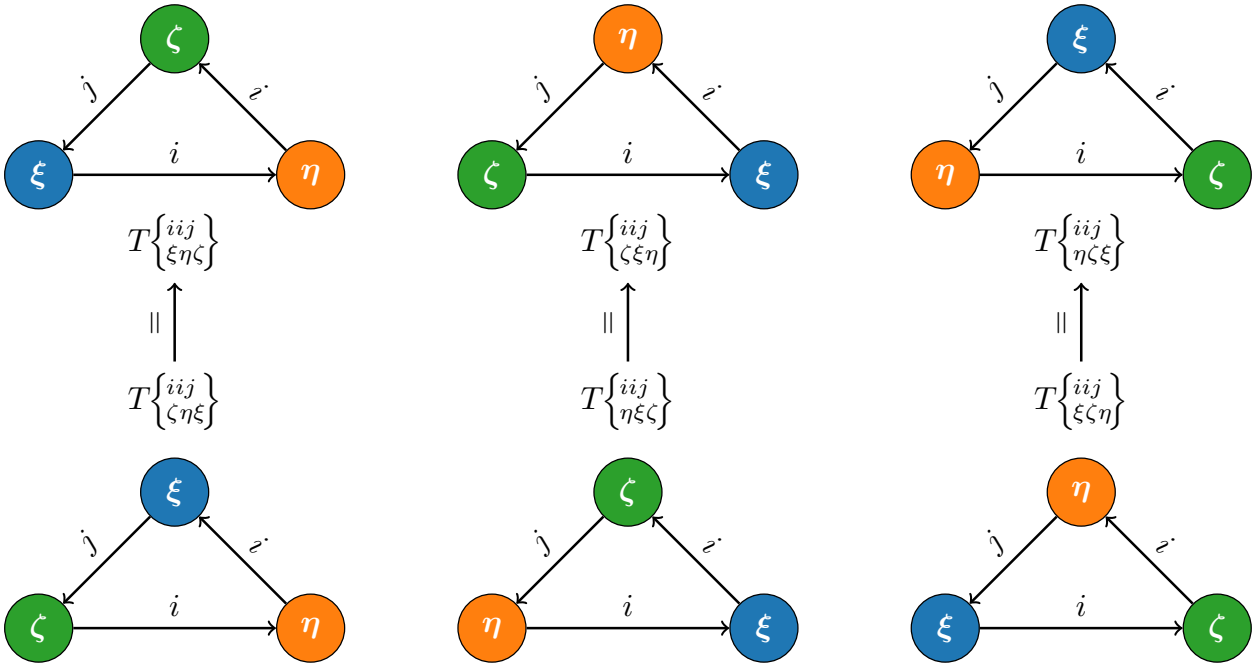

(b) Possible (distinct) triplet constructions for three different species $\{\xi, \eta, \zeta\}$, with two different side lengths $\{i, i, j\}$. Note that of a given index pair i, j one may also construct different triangles using $\{j, j, i\}$ hence the three parameters exhibit a multiplicity of two, totaling in six ($m_{cs} = m_{23} = 6$) different triangles.

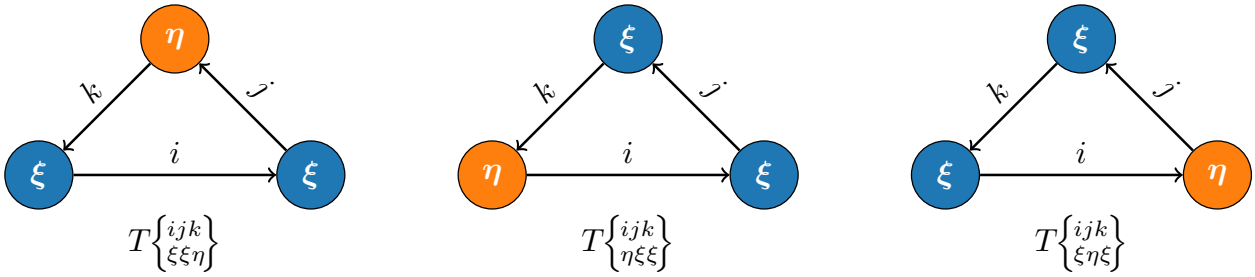

(c) Possible (distinct) triplet constructions for two different species $\{\xi, \xi, \eta\}$, with three different side lengths $\{i, j, k\}$. Similarly to Fig. 6.5b, the above construction exhibits also a multiplicity of two by inverting species to a set $\{\eta, \xi, \xi\}$. Consequently it is possible to construct $m_{cs} = m_{32} = 6$ different triangles.

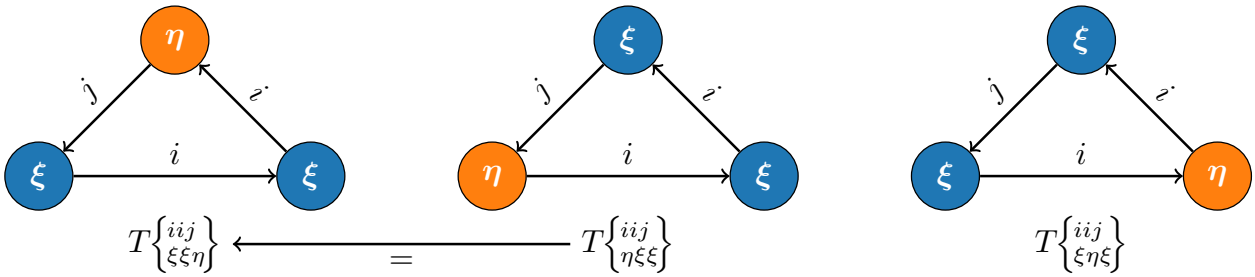

(d) Possible (distinct) triplet constructions for two different species $\{\xi, \xi, \eta\}$, with two different side lengths $\{i, i, j\}$. The number of possible triangles ($m_{cs} = m_{22} = 8$) for this case is eight, two parameters for each of the two shell permutations ($\{i, i, j\}$, $\{j, j, i\}$) and furthermore, two for each of the species permutations ($\{\xi, \xi, \eta\}$, $\{\eta, \xi, \xi\}$).

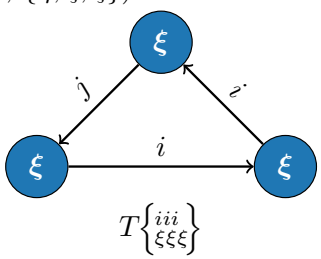

(e) Possible (distinct) triplet constructions for one specie $\{\xi, \xi, \xi\}$, with one side length $\{i, i, i\}$ ($m_{cs} = m_{11} = 1$).

Figure 6.5: Visualization of possible triplets, for different general (Figs. 6.5a & 6.5c), isosceles (Figs. 6.5b & 6.5d) and equilateral (Fig. 6.5e) triangles, formed by atoms of one (Fig. 6.5e)

	$1 = \{i, i, i\}$	$2 = \{i, i, j\}$	$3 = \{i, j, k\}$
theoretical	$\binom{7}{1} = 7$	$2\binom{7}{2} = 42$	$\binom{7}{3} = 35$
fcc	4	19	19
bcc	1	13	11
hcp	2	12	10

Table 6.3: Number of triplet SRO parameters for maximal coordination of $C = 7$, tabulated for equilateral, isosceles, and general triangles for the most important lattices. Note that the above table does not contain any information about the species.

$$\mathcal{O}^{\beta}(\sigma) = \sum_{i,j,k}^{C} \sum_{\xi,\eta,\zeta}^{S} w_{\xi\eta\zeta}^{ijk} |\tilde{\beta}_{\xi\eta\zeta}^{ijk} - \beta_{\xi\eta\zeta}^{ijk}| \tag{6.17}$$

where similar to Eq. (6.8), $w_{\xi,\eta\zeta}^{ijk}$ denote triplet interaction weights. Similarly, $\tilde{\beta}_{\xi\eta\zeta}^{ijk}$ denote the target triplet SRO parameters. To quantify both pair and triplet randomness of the cell, we add Eq. (6.8) and Eq. (6.17) and rewrite the sums to finally obtain

$$\mathcal{O}^{\alpha+\beta}(\sigma) = \sum_{i}^{C} \sum_{\xi,\eta}^{S} \tilde{w}_{\xi\eta}^{i} |\tilde{\alpha}_{\xi\eta}^{i} - \alpha_{\xi\eta}^{i}| + \sum_{j,k}^{C} \sum_{\zeta}^{S} w_{\xi\eta\zeta}^{ijk} |\tilde{\beta}_{\xi\eta\zeta}^{ijk} - \beta_{\xi\eta\zeta}^{ijk}| \,. \tag{6.18}$$

As the pair weights $\tilde{w}_{jk}^{i}$ decrease with increasing coordination shell i, they account for the fact that far distant pairs are less important than nearest neighbors. The number of triplet SRO parameters is huge compared to the number of pair SRO parameters, hence it is impractical to choose a separate interaction weight for each triplet interaction. Therefore, we propose to assemble the triplet interaction weights $w_{\xi\eta\zeta}^{ijk}$ from the weights of the constituent pairs, such that

$$w_{\xi\eta\zeta}^{ijk} = \tilde{w}_{\xi\eta}^{i} \tilde{w}_{\eta\zeta}^{j} \tilde{w}_{\zeta\xi}^{k} = w^{i} w^{j} w^{k} p_{\xi\eta} p_{\eta\zeta} p_{\zeta\xi} \,. \tag{6.19}$$

This way we do reduce the number of parameter while keeping the intuitive relation that "*smaller*" triplets (i.e with shorter sides) have higher importance.

6.3 Relation to cluster expansion

One of the main criticisms of WC-SRO parameters is that they are not physically-informed. Hence, using them to find SQS structures solely considers atom geometry. In this section, we propose a possible way, how to inform pair and triplet parameters about the system's chemistry. We, therefore, start by expanding the total energy of a system with $u = 1, \ldots, N$ atoms into many-atom clusters. Such an expansion reads

$$E = V^{(0)} + \sum_{u}^{N} V^{(1)}(\vec{R}_u) + \overbrace{\frac{1}{2}\sum_{u,v}^{N} V^{(2)}(\vec{R}_u, \vec{R}_v)}^{E^{(2)}} + \frac{1}{6}\sum_{u,v,w}^{N} V^{(3)}(\vec{R}_u, \vec{R}_v, \vec{R}_w) + \dots \tag{6.20}$$

where $\vec{R}_w$ denote the atom positions. $V^{(0)}$ is a constant that is often set to zero. $V^{(2)}, \dots, V^{(M)}$ are the many-body potentials. While these potentials, in reality, may take a complicated form, let us restrict ourselves to systems where the atomic positions are limited to a perfect lattice. The most important consequence is that the input arguments for the many-body potentials become discrete. Hence, instead of a full parameterization, one needs to know the values of many-body potentials only at a few points of the input space. To illustrate this more clearly, we focus on the pair-potential term, $V^{(2)}$. To evaluate the sum, only a few pair-distances, namely the coordination-shell radii (see. Fig. 6.2) are needed. However, $V^{(2)}$ also takes into account the atomic species, making up the pair. In other words, $V^{(2)}$ will yield different values for the same given distance of ξ — η and η — ζ atoms. Consequently, we can rewrite the pair-term of Eq. (6.20) for a lattice to

$$E^{(2)} = \frac{1}{2}\sum_{i}^{C}\sum_{\xi,\eta}^{S,S} V_{\xi\eta}^{i,(2)} N_{\xi\eta}^{i} \quad \text{where} \quad \frac{1}{2}N(N-1) = \frac{1}{2}\sum_{i}^{C}\sum_{\xi,\eta}^{S,S} N_{\xi\eta}^{i} \tag{6.21}$$

C and S represent the coordination shell and species in the system repectively. $N_{\xi\eta}^{i}$ is the number of ξ — η pairs separated by radius of the coordination shell i, similarly as in the definition of the pair SRO in Eq. (6.3). Moreover, the equation reveals that we need to know $\frac{1}{2}CS(S+1)$ values of $V^{(2)}$ to fully describe the pair interactions. Note, that this again corresponds to the number of pair SRO parameters. Analogously, we can rewrite the triplet term of Eq. (6.20) to

$$E^{(3)} = \sum_{i,j,k}^{C}\sum_{\xi,\eta,\zeta}^{S} V_{\xi\eta\zeta}^{ijk,(3)} N_{\xi\eta\zeta}^{ijk}\,. \tag{6.22}$$

Observe the similarity between the interaction of clusters on a lattice and our objective function (Eq. (6.8) and Eq. (6.21)), and thereby the relation between the artificial weights $\tilde{w}_{\xi\eta}^{i}$ and $V_{\xi\eta}^{i,(2)}$ and $w_{\xi\eta\zeta}^{ijk}$ and $V_{\xi\eta\zeta}^{ijk,(3)}$. Hence we can recast the cluster expansion into our notation as follows

$$E = V^{(0)} + \sum_{\xi}^{S} V_{\xi}^{(1)} N_{\xi} + \sum_{i}^{C}\sum_{\xi,\eta}^{S} V_{\xi\eta}^{i,(2)} N_{\xi\eta}^{i} + \sum_{i,j,k}^{C}\sum_{\xi,\eta,\zeta}^{S} V_{\xi\eta\zeta}^{ijk,(3)} N_{\xi\eta\zeta}^{ijk} + \cdots \tag{6.23}$$

Before unifying the purely geometric SRO approach with cluster expansion, we have to rewrite the SRO parameters and plug them into the objective functions (Eqs. (6.8) and (6.17)) to see the relation more clearly

$$\mathcal{O}^{\alpha}(\sigma) = \sum_{i}^{S}\sum_{\xi,\eta}^{C} \tilde{w}^{i}_{\xi\eta} |\tilde{\alpha}^{i}_{\xi\eta} - \overbrace{1 + f^{i}_{\xi\eta} N^{i}_{\xi\eta}(\sigma)}^{\alpha^{i}_{\xi\eta}}| \quad \text{with} \quad f^{i}_{\xi\eta} = (N M^{i} x_{\xi} x_{\eta})^{-1} \tag{6.24}$$

$$\mathcal{O}^{\beta}(\sigma) = \sum_{i,j,k}^{C}\sum_{\xi,\eta,\zeta}^{S} w^{ijk}_{\xi\eta\zeta} |\tilde{\beta}^{ijk}_{\xi\eta\zeta} - \underbrace{1 + f^{ijk}_{\xi\eta\zeta} N^{ijk}_{\xi\eta\zeta}(\sigma)}_{\beta^{ijk}_{\xi\eta\zeta}}| \quad \text{with} \quad f^{ijk}_{\xi\eta\zeta} = (N T^{\{ijk\}} x_{\xi} x_{\eta} x_{\zeta})^{-1} \tag{6.25}$$

All that happened in the above equations is that we have gathered the denominator of the pair and triplet SRO parameters into the variable $f^{i}_{\xi\eta}$ and $f^{ijk}_{\xi\eta\zeta}$ respectively. The motivation for doing so is twofold. Firstly it shows clearly that this part (the denominator) of the SRO parameters does not depend on the atomic configuration σ. Therefore, one can precompute those in advance. Secondly, these prefactors are furthermore subject to performance considerations as in an implementation they avoid floating point division in the inner loops and replace them with multiplications. Our implementation uses Eq. (6.24) for finding optimized structures. Despite, the performance considerations, by choosing $f^{i}_{\xi\eta} = \tilde{\alpha}^{i}_{\xi\eta} = f^{ijk}_{\xi\eta\zeta} = \tilde{\beta}^{ijk}_{\xi\eta\zeta} = 1$, we find that the above equations reduce to

$$\mathcal{O}^{\alpha}(\sigma) = \sum_{i}^{S}\sum_{\xi,\eta}^{C} \tilde{w}^{i}_{\xi\eta} N^{i}_{\xi\eta}(\sigma) \tag{6.26}$$

$$\mathcal{O}^{\beta}(\sigma) = \sum_{i,j,k}^{C}\sum_{\xi,\eta,\zeta}^{S} w^{ijk}_{\xi\eta\zeta} N^{ijk}_{\xi\eta\zeta}(\sigma) \tag{6.27}$$

For fixed compositions furthermore, the first term of our reformulated cluster expansion in Eq. (6.23) become constants. Consequently, the combined objective function in Eq. (6.18) can be interpreted as a cluster expansion, which is truncated at clusters of size three. In other words: by simply changing setting the values for $f^{i}_{\xi\eta}$, $\tilde{\alpha}^{i}_{\xi\eta}$, $f^{ijk}_{\xi\eta\zeta}$ and $\tilde{\beta}^{ijk}_{\xi\eta\zeta}$ to 1, the implementation will — instead of finding optimized SQSs — predict total energies for given atomic arrangements. Furthermore, it becomes obvious to inform your system about the chemistry by choosing physically sensible values for the interaction weights, such that our objective function truly becomes Eq. (6.23).

6.3.1 Determining interaction parameters

To find the minimal energy structure, we have to give physical meaning to the interaction parameters rather than choosing arbitrary numbers. Therefore, we suggest determining the interaction parameters from first-principles methods. In traditional cluster expansion, the interaction parameters are obtained via linear regression from DFT cells. In contrast, to the traditional "*top-down*" approach we propose to compute the interaction energies of the individual occurring clusters directly. Consequently, in such an approach many small clusters have to be computed. The actual number that needs to be carried out is identical to the number of SRO parameters. We note that this might be handled efficiently and accurately using real-space DFT implementations such as, e.g., SIESTA [224]. Let us we denote the total energy of an atom ξ by E_ξ. Consequently, the interaction energy of an ξ — η atom pair, separated by the radius of the i^{th} coordination shell, can be computed as

$$E^{i,\text{int}}_{\xi\eta} = E^{i}_{\xi\eta} - E_\xi - E_\eta \tag{6.28}$$

where $E^i_{\xi\eta}$ the total energy of the system. Similarly, the interactions energy of a triplet can be defined, by subtracting the constituent pair interactions and singlet energies as

$$\begin{aligned} E^{ijk,\text{int}}_{\xi\eta\zeta} &= E^{ijk}_{\xi\eta\zeta} - \underbrace{E^{i,\text{int}}_{\xi\eta} - E^{j,\text{int}}_{\eta\zeta} - E^{k,\text{int}}_{\zeta\xi}}_{\text{pairs}} - \underbrace{E_\xi - E_\eta - E_\zeta}_{\text{single atoms}} \\ &= E^{ijk}_{\xi\eta\zeta} - E^{i}_{\xi\eta} - E^{j}_{\eta\zeta} - E^{k}_{\zeta\xi} + E_\xi + E_\eta + E_\zeta \,. \end{aligned} \tag{6.29}$$

Finally by choosing $\tilde{w}^i_{\xi\eta} = E^{i,\text{int}}_{\xi\eta} = V^{i,(2)}_{\xi\eta}$ and correspondingly in $w^{ijk}_{\xi\eta\zeta} = E^{ijk,\text{int}}_{\xi\eta\zeta} = V^{ijk,(3)}_{\xi\eta\zeta}$, the objective functions (Eqs. (6.24)–(6.25)) yield the physically informed energies for a given configuration σ. Note, that there exist tools to extract the interaction energy already for a long time. In the cluster expansion approach [225, 226] the interaction energies are extracted from a set of DFT calculations. They can be also computed directly using Greens function methods [223, 227, 228]. Both motioned approaches result in more accurate and physically sensible energies compared to interaction energies compute from isolated clusters. However, those interaction parameters have to be computed for each material system separately. In contrast, isolated cluster interactions, although lacking physical insight for a specific system, would be transferable, to physically-informed the generation of an SQS in the first place. Furthermore, it would be easily possible, with modest computational effort, to compute those energies for a large part of the periodic table, and tabulate them. A database might be shipped with our implementation (see next section), that would allow users to choose better values for $\tilde{w}^i_{\xi\eta}$ and $w^{ijk}_{\xi\eta\zeta}$.

6.4 Implementation

Within this thesis, we have implemented a structure enumerator which efficiently computes pair SRO parameters of atomic arrangements σ. The implementation is named *sqsgenerator*. The code is available as a Python package and features a command line interface. The core parts, e.g., to compute the values of Eq. (6.3) are written in C++ to exploit shared memory parallelization using OpenMP. Furthermore, the core routines are MPI (distributed memory) parallelized, such that the code is able to exploit high-performance-computing (HPC) systems. For desktop-scale applications, OpenMP parallelized pre-built binaries are available via Anaconda package repositories. Searching for an optimal atomic arrangement employing the above description is inherently suited to be carried out on a parallel architecture. This is because communication is only needed when a new minimum is found. However, with ongoing execution time, this becomes a rare event in practice. Furthermore, as memory requirements are negligible on a modern system, one can easily afford MPI parallelization, which has the advantage that less synchronization happens. Therefore, our implementation exhibits nearly an ideal speedup for distributed memory parallelization as shown in Fig. 6.6. Implementation details are given in a more extensive way in Ref. [217]

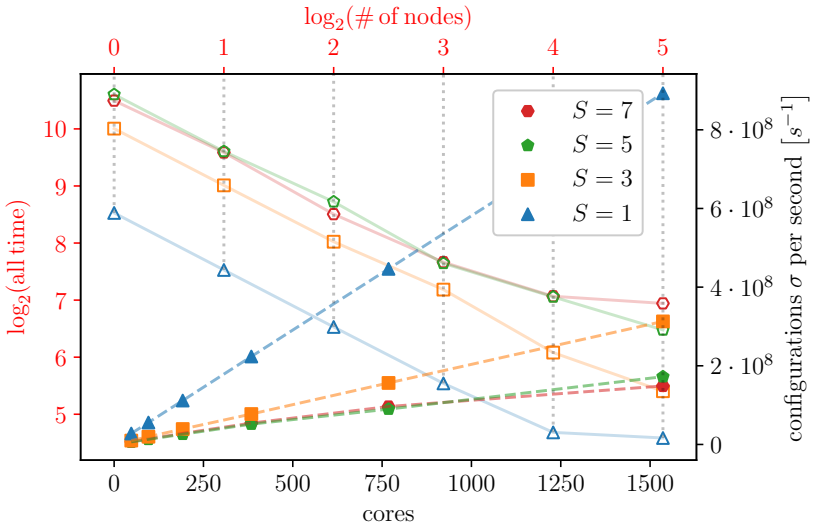

Figure 6.6: Number of analyzed structures (right black y-axis) per second of *sqsgenerator* in MPI mode as a function of the number of the physical cores (lower black x-axis) and coordination shells (full symbols, dashed lines). Open symbols connected by the solid lines show the linear scaling time (left red y-axis) versus the number of nodes (upper red x-axis). The analyzed structures represent a binary $A_{0.5}B_{0.5}$ alloy on a *bcc* lattice with 128 atoms. (Taken from Ref. [217])

6.4.1 Outlook for our implementation

We emphasize that our implementation uses currently only pair SRO parameters to find optimal SQS structures. Hence, expanding it to take into account triplet SRO parameters

is desirable. However, there are a few caveats. Firstly, our implementation is focused on an efficient pair SRO computation, which is necessary due to exponentially growing configurational space (= possible permutations of σ) with the model size. Consequently, as the number of triplets grows with $\mathcal{O}(N^3)$ in combination with the vast amount of triplet SRO parameters, would substantially increase the computational cost per atomic configuration σ. To solve this Pototschnig [218] has suggested to pre-scan the configurational space by computing pair-correlations and determining the triplet SRO parameters only for those arrangements which yield the same value for the pair objective (Eq. (6.8)). He was able to show that atomic arrangements which are equal from a pair perspective, can be further distinguished by accounting for the triplet correlations for selected cases. In contrast, to use the implementation to predict energies and ordering of systems, both (pair and triplet) objective functions need to be calculated. Furthermore, choosing this path would require, from a usability perspective, to couple the code with DFT packages in order to compute the interaction energies in Eqs. (6.28) and (6.29) on the fly.

Chapter 7

Segregation in a disordered Ni-based alloy

Segregation to grain boundaries (GB) in pure metals has been studied extensively [229] using first principles. Also, solute segregation in Ni-base superalloys was subject to many theoretical investigations [230–233], especially by Razumovskiy et al. [234–236] already more than one decade ago. Nevertheless, all of the studies try to guide alloy development of Ni-based super alloys [232, 233, 236], by predicting solute segregation to GB by using pure Ni models. The main motivation of this chapter is to reveal the impact of solute segregation, when accounting for chemical disorder in the atomistic models, and hence employ more "*realistic*" models. Therefore, this chapter is structured as follows. In the beginning, we will give an introduction to solute segregation in simple metals. Then we present the computational setup for treating disordered systems. After pointing out the main differences between segregation energies in a pure and disordered system, we continue by discussing the impact of the spectral properties of the segregation energy on McLean-type isotherms. In the second part of the chapter, we adapt Guttman's model to include solute-matrix interactions in a disordered system. After presenting the adapted model, we propose a simple method to extract the necessary interaction parameters, needed for the (adapted Guttmann) model. Finally we conclude this chapter by presenting further research topics towards a better theoretical description of Ni-based alloys.

7.1 Segregation in simple metals

The tendency of a solute to segregate to a boundary, in the dilute limit, is usually quantified using the segregation energy. In contrast to the two-phase system in Chap. 5, we focus in this chapter on grain boundaries between grains of one phase. We start by considering a grain boundary in a pure metal of species M (matrix). We compare the formation energy of

a solute atom X in the bulk (B) with the formation energy at the grain boundary (GB)

$$\begin{aligned}\Delta E_{\text{seg}}^{X,i} &= \underbrace{\left(E_{\text{GB}}^{X\to M_i} - E_{\text{GB}} + \mu_{\text{GB}}^{M} - \mu_{\text{GB}}^{X}\right)}_{E_{\text{GB}}^{f,X}} - \underbrace{\left(E_{\text{B}}^{X\to M} - E_{\text{B}} + \mu_{\text{B}}^{M} - \mu_{\text{B}}^{X}\right)}_{E_{\text{B}}^{f,X}} \\ &= E_{\text{GB}}^{X\to M_i} - E_{\text{B}}^{X\to M} - E_{\text{GB}} + E_{\text{B}} \quad \text{for} \quad \mu_{\text{GB}}^{M} = \mu_{\text{B}}^{M}, \mu_{\text{GB}}^{X} = \mu_{\text{B}}^{X}\,. \end{aligned} \tag{7.1}$$

E_{GB} and E_{B} refer to the total energies of the undecorated systems with and without GB, respectively. μ^M is the chemical potential of the matrix element M. $E_{\text{B}}^{X\to M}$ and $E_{\text{GB}}^{X\to M_i}$ represent the energies of the decorated system, where one M atom is replaced by an X atom. The i denotes the index of the segregation site. Compared to the bulk, the GB plane breaks the translational symmetry of the lattice, therefore, not all lattice positions at the GB are symmetrically equivalent anymore. Fig. 7.1a illustrates this for a pure Ni $\Sigma5(210)$ for which three sites at the grain boundary are different. Consequently, Eq. (7.1) yields three energies for one solute. If the above definition of the segregation energy exhibits negative values, the solute tends to segregate to the GB, whereas for positive values it stays in the bulk.

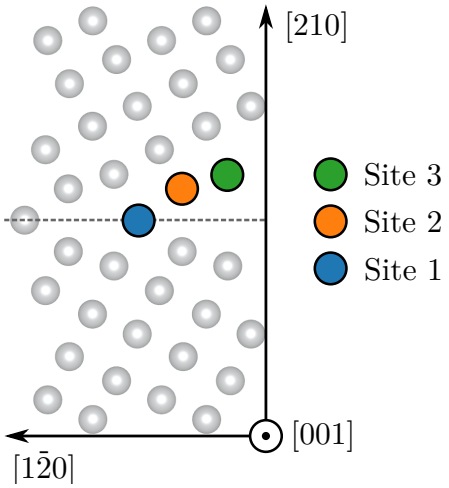

(a) The three different segregation sites at a $\Sigma5(210)$ Ni grain boundary

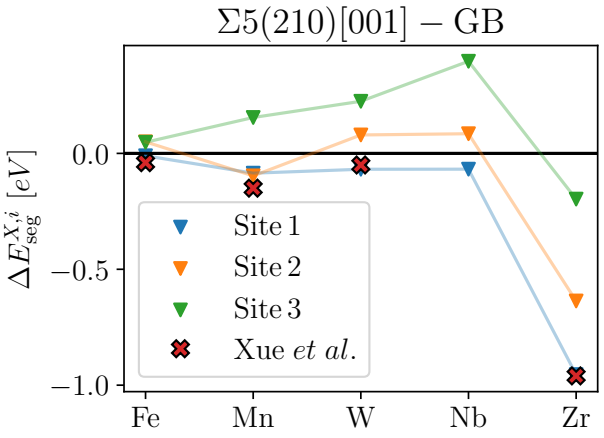

(b) Segregation energies, $E_{\text{seg}}^{X,i}$, for the three segregation sites shown in Fig. 7.1a. The colors of the lines correspond to the sites. The red crosses are values reported by Xue *et al.* [233].

Figure 7.1: Atomistic model of a Ni grain boundary, showing the symmetrically inequivalent segregation sites and corresponding segregation energies.

Often, literature reports a single value for the segregation energy, rather than a set of values. Therefore a common convention is to use the minimum value across all sites $\Delta E_{\text{seg}}^{X} = \min_i \Delta E_{\text{seg}}^{X,i}$. Figure 7.1b shows the segregation energies for five different solutes for the three segregation sites at a $\Sigma5(210)[001]$ Ni symmetric tilt grain boundary. The plot reveals an excellent agreement with literature data reported by Xue *et al.* [233] (red crosses). Nevertheless, those values were obtained using a standard approach, therefore within this section,

we will not discuss the numbers further. We will comment them later in the light of a comparison with a more realistic alloy model.

7.2 Segregation in disordered systems

To best to our knowledge, within first principles approaches, segregation in alloys is always investigated with models of the corresponding pure metal. That is, the calculations for Ni-based superalloys are done in pure Ni systems [232, 233, 235], or similarly, pure iron grain boundaries are used as a surrogate model for steels [237–240]. Therefore, in the following section, we will elucidate the impact of the chemical disorder on solute segregation in a Ni-based alloy.

	x^{Ni} (N^{Ni})	x^{Cr} (N^{Cr})	x^{Co} (N^{Co})	x^{Ti} (N^{Ti})	x^{Al} (N^{Al})
bulk (108)	$0.55\dot{5}$ (60)	$0.\overline{185}$ (20)	$0.\overline{148}$ (16)	$0.0\overline{55}$ (6)	$0.0\overline{55}$ (6)
GB (114)	0.561 (61)	0.184 (21)	0.149 (17)	0.053 (6)	0.053 (6)
$\lvert x_{\mathrm{B}} - x_{\mathrm{GB}}\rvert$	$5.85 \cdot 10^{-3}$	$9.75 \cdot 10^{-4}$	$8.29 \cdot 10^{-3}$	$2.92 \cdot 10^{-3}$	$2.92 \cdot 10^{-3}$

Table 7.1: Compositions of the bulk and GB simulations cells. The number of atoms distributed in the cells is written in parenthesis next to the mole fractions. The difference between the cell compositions for each matrix element is given in the last row.

7.2.1 Computational setup

If not specified otherwise in the following section the term "*literature*" refers to Refs [233, 236]. To compute the bulk energy, in contrast to the literature, we do not place the solute atoms at "*bulk*" like sites of the grain-boundary, but rather use $4 \times 4 \times 4$ supercell of *fcc*-Nickel. The cell with 108 atoms in total, is randomly occupied with the composition shown in Tab. 7.1. To find a good SQS, we use *sqsgenerator* (see Sec. 6.4) with a Monte-Carlo approach, considering the first seven coordination shells with interaction weights $w^i = \frac{1}{i}$. We select the best cell among 10^{10}. In contrast to the pure Ni bulk, where only one bulk state is available, this symmetry is broken in a disordered system. Consequently, the individual lattice positions exhibit different local compositions. Therefore, placing a solute atom at each lattice position allows to sample bulk energies for different local compositions.

To make our results closely comparable with the literature, we have used very similar GB cells as reported by the studies of Razumovskiy, Lozovoi, and Razumovskii [236]. The cell vectors $\vec{a} = [1\bar{2}0]$, $\vec{b} = [001]$ and $\vec{c} = [210]$ refer to the axes in Fig. 7.1a.

We use a vacuum padding of 9.5 Å in $\vec{c}$ direction. In contrast to literature, however, we use a much larger GB-plane area of $A_{\mathrm{GB}} = |\vec{a} \times \vec{b}| = 82.88$ Å^2 (27.75 Å^2 in Ref. [233]), resulting in cells that contain 114 atoms. The motivation for this choice is two-fold. Firstly,

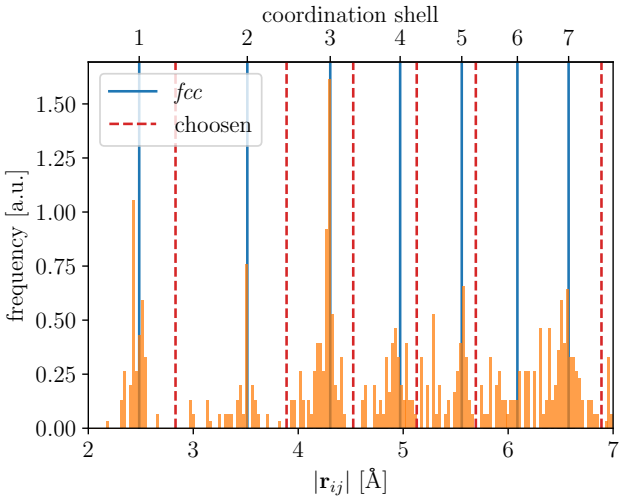

Figure 7.2: Pair distance histogram (orange) of the Ni-Σ5(210)[001] simulation cell with 114 atoms. The red dashed lines are the manually chosen coordination shell radii for the SQS optimization. The blue refers to the distances in a pure *fcc*-Ni crystal.

a larger cell with a solute atom will more accurately model the dilute limit. Secondly, and more importantly, for a model of an alloy with a complex composition as in Tab. 7.1 we want the GB and bulk compositions to be as similar as possible. In an ideal case, the are the same. The reason is that the chemical potential of a species is a function of concentration/composition. More precisely the chemical potential μ^{M^ξ} of a matrix species M^ξ is a function of the composition vector $\mu^{M^\xi} = \mu^{M^\xi}(\mathbf{x})$ where $\mathbf{x} = (x^{\mathrm{Ni}}, x^{\mathrm{Cr}}, x^{\mathrm{Co}}, x^{\mathrm{Ti}}, x^{\mathrm{Al}})$ in the present case. Consequently, to apply Eq. (7.1), we demand chemical potential in the bulk and grain boundary system $\mu_{\mathrm{B}}^{M^\xi}(\mathbf{x}_{\mathrm{B}}) = \mu_{\mathrm{GB}}^{M^\xi}(\mathbf{x}_{\mathrm{GB}})$, and hence $\mathbf{x}_{\mathrm{B}} = \mathbf{x}_{\mathrm{GB}}$ to be the same. As the number of atoms in the bulk and GB cell is not the same, we try to get them as close as possible to minimize the compositional deviations $|\mathbf{x}_{\mathrm{B}} - \mathbf{x}_{\mathrm{GB}}|$. The last row of Tab. 7.1 clearly shows that the maximum deviation is < 0.5 % for our setup. Thus it is reasonable to assume $\mu_{\mathrm{B}}^{M^\xi}(\mathbf{x}_{\mathrm{B}}) \approx \mu_{\mathrm{GB}}^{M^\xi}(\mathbf{x}_{\mathrm{GB}})$ and hence to use a modified (simplified) version of Eq. (7.1).

SQS of grain boundaries

While we have employed our implementation to find a SQS for the bulk system, applying it to the GB structure needs more care. We start with a GB structure without vacuum padding as an input for *sqsgenerator*. Due to the presence of the GB, the pair distances histogram strongly deviates from a perfect *fcc* crystal, as shown in Fig. 7.2.

Therefore, we have manually specified the coordination shell radii (see Sec. 6.1.2) to group the pairs as depicted in Fig. 7.2. Consequently, for the GB cells we omit the distinction between the individual segregation sites (Site 1 – 3 in Fig. 7.1a). Therefore each SQS cell exhibits thirty different segregation sites (Site 1 splits into twelve, 2 into six, and 3 again into twelve). To get proper statistics we generate five different GB-SQS. We find them by

enumerating 10^{11} atomic arrangements in a Monte-Carlo approach using our *sqsgenerator* package. The optimization process yields multiple solutions, from which we select five as follows.

Selecting the five best SQS As each of the thirty GB sites might be coordinated differently, we want to sample as many possible local atomic environments as possible. For each solution of the SQS optimization, we compute the local composition vector for all GB sites by taking into account the nearest neighbors. Therefore we define the set of all composition vectors for the j^{th} solution of the SQS optimization

$$\mathbf{X}_j = \left\{ \mathbf{x}^i_{\text{GB}_j} \right\}_{i=1,\dots,30} . \tag{7.2}$$

We now want to find a combination of five SQS structures from all N solutions, which yield the maximum number of distinct local composition vectors. In other words, we find the solution indices j,k,l,m, and n which we need to combine to maximize the number of local environments

$$N^{\text{env}} = \max \left| \mathbf{X}_j \cup \mathbf{X}_k \cup \mathbf{X}_l \cup \mathbf{X}_m \cup \mathbf{X}_n \right| . \tag{7.3}$$

Although this process of selecting the right SQS structure might look like pettifoggery we point out that the worst combination (from our SQS solutions) yields only 96 different while the optimal choice results in 133 out of 150 theoretically possible environments. In total this results in 253 DFT calculations per solute, 108 for the bulk plus 150 (30 sites $\times$ 5 SQSs) for the GB states. This strongly contrasts with the pure Ni system, where we need only four (one bulk plus three GB sites) calculations.

7.2.2 Segregation energy in a complex matrix

Before we generalize Eq. (7.1), let us clarify the implications of a disordered matrix. Firstly, the formation energy for a point defect in bulk cannot be described by a single value anymore, as it is strongly influenced by the local environment. Therefore, to get a proper description, it is necessary to sample as many local environments as possible. This is why we place the solute at each of the 108 bulk sites. Secondly, the solute can replace not only one species in bulk but rather any of the species present $\widetilde{M} \in \{\text{Ni}, \text{Cr}, \text{Co}, \text{Ti}, \text{Al}\}$. Therefore in the following, we refer to the formation energy of a solute $X \in \{\text{Fe}, \text{Mn}, \text{W}, \text{Nb}, \text{Zr}\}$ replacing an $\widetilde{M}$ atom at the j^{th} site to as $E_{\text{B}}^{f,X_j^{\widetilde{M}}}$. Similarly, if $\widetilde{M}$ is replaced at the i^{th} site at the grain-boundary we refer to it as $E_{\text{GB}}^{f,X_i^{\widetilde{M}}}$. Taking all this into account the segregation energies for multi-component matrix reads

$$\Delta E_{\mathrm{seg}}^{X_{ij}^{\widetilde{M}\widetilde{M}'}} = \overbrace{E_{\mathrm{GB}}^{X\to\widetilde{M}_i} - E_{\mathrm{GB}} + \mu_{\mathrm{GB}}^{\widetilde{M}} - \mu_{\mathrm{GB}}^{X}}^{E_{\mathrm{GB}}^{f,X_i^{\widetilde{M}}}} - \overbrace{E_{\mathrm{B}}^{X\to\widetilde{M}'_j} + E_{\mathrm{B}} - \mu_{\mathrm{B}}^{\widetilde{M}'} + \mu_{\mathrm{GB}}^{X}}^{E_{\mathrm{B}}^{f,X_j^{\widetilde{M}'}}} . \tag{7.4}$$

We will assume the same chemical potential of the matrix spices in bulk and at the GB $\mu_{\mathrm{GB}}^{\widetilde{M}} \approx \mu_{\mathrm{B}}^{\widetilde{M}} = \mu^{\widetilde{M}}$. Furthermore, the solute species X is both the GB and the bulk are in the dilute limit at nearly the same concentrations, therefore $\mu_{\mathrm{GB}}^{X} = \mu_{\mathrm{B}}^{X}$, and they cancel out each other. Finally, by regrouping the chemical potential term to $\Delta\mu^{\widetilde{M}\widetilde{M}'} = \mu^{\widetilde{M}} - \mu^{\widetilde{M}'}$ we can rewrite the above equation to

$$\Delta E_{\mathrm{seg}}^{X_{ij}^{\widetilde{M}\widetilde{M}'}} - E_{\mathrm{GB}}^{X\to\widetilde{M}_i} - E_{\mathrm{GB}} - E_{\mathrm{B}}^{X\to\widetilde{M}'_j} + E_{\mathrm{B}} + \Delta\mu^{\widetilde{M}\widetilde{M}'}\delta_{\widetilde{M}\widetilde{M}'} \tag{7.5}$$

where $\delta_{\widetilde{M}\widetilde{M}'}$ is the Kronecker δ to indicate that the chemical potential term vanishes for equal bulk and GB species. Hence, the chemical potential term only vanishes if the solute replaces the same atom in the bulk and the GB. Therefore, in the following, if not specified otherwise, we will account only for such cases $\widetilde{M} = \widetilde{M}'$ such that the above equation becomes

$$\Delta E_{\mathrm{seg}}^{X_{ij}^{\widetilde{M}}} = E_{\mathrm{GB}}^{X\to\widetilde{M}_i} - E_{\mathrm{GB}} - E_{\mathrm{B}}^{X\to\widetilde{M}'_j} + E_{\mathrm{B}} \tag{7.6}$$

Furthermore, it is noteworthy that when speaking about the segregation of the solute X to the GB cannot be quantified anymore by a single value for the segregation energy, but rather by a whole spectrum. Consequently, when considering N^{B} bulk and N^{GB} GB states, with $\Delta E_{\mathrm{seg}}^{X}$,

$$\Delta E_{\mathrm{seg}}^{X} = \left\{ \Delta E_{\mathrm{seg}}^{X_{ij}^{\widetilde{M}\widetilde{M}'}} \;\middle|\; \widetilde{M} = \widetilde{M}' \right\}_{\forall i=1,\dots,N_{\mathrm{GB}}, j=1,\dots,N_{\mathrm{B}}} \tag{7.7}$$

we refer to the set of all possible combinations of GB sites i and bulk sites j where both are occupied with the same atoms $\widetilde{M}$. In the following, when speaking of the segregation of a solute to the grain boundary we refer to the whole set/spectrum of segregation energies

7.2.3 Segregation in a complex matrix

Energy spectrum of segregation energies

We have concluded the last section, stating that we have to deal with a whole spectrum of segregation energies. Such an approach had been suggested already by White and Coghlan [241] and got attention again more recently. Huber *et al.* [242] sampled the fundamental

zones [243] (orientations of the cutting boundary plane [244, 245]) of a Σ5 grain boundary. Therein, he uses a Gaussian distribution to describe the energy spectra. Scheiber and Romaner [246] discussed the impact of energy spectra more intensively and tried to connect it with the measurable enthalpy and entropy. They found a Gumbel distribution fitting their energy spectra best. Similarly, Wagih and Schuh [247] studied the grain boundary segregation in a polycrystal and investigated the impact of the segregation energy spectra on the stability of noncrystalline materials. We follow the approach from Wagih and Schuh [247] and use a skew-normal distribution to fit the distribution of the segregation energies of Eq. (7.6). We note that this brings an additional degree of freedom as compared to the Gumbel distribution. In contrast to the inherently symmetric Gaussian and the left-skewed Gumbel distribution, the skew-normal distribution exhibits an additional skew parameter allowing for both left and right-hand skewed energy spectra. For a solute X, the skew-normal distribution reads

$$\hat{F}^X(\Delta E^X_{\text{seg}}) = \frac{1}{\sigma\sqrt{2\pi}} \exp\left(-\frac{(\Delta E^X_{\text{seg}} - \mu)^2}{2\sigma^2}\right) \operatorname{erfc}\left(-\frac{\alpha(\Delta E^X_{\text{seg}} - \mu)}{\sqrt{2\sigma^2}}\right) \tag{7.8}$$

where μ and σ are the parameters of a Gaussian distribution, and α the skewness parameter. The sign of α determines the side of the skew; $\alpha = 0$ yields a Gaussian distribution.

If not mentioned otherwise, we employ an "*exact*" normalized discrete distribution (histogram) for further calculations, rather than the skew-normal fit. We denote the frequency of the ξ^{th} bin as $\hat{F}^X_\xi$ where $\xi = 1, \ldots, N$ and N is the number of bins of the histogram. Finally, we define the mean values of the discrete distribution as

$$\left\langle \Delta E^X_{\text{seg}} \right\rangle = \left\langle F^X \right\rangle = \sum_{\xi}^{N} F^X_\xi \Delta E^{X,\xi}_{\text{seg}} \underbrace{\Delta(\Delta E^X_{\text{seg}})}_{\text{bin width}} \tag{7.9}$$

where $\Delta E^X_{\text{seg},\xi}$ is the center of the ξ^{th} histogram bin and $\Delta(\Delta E^X_{\text{seg}})$ is the histogram's bin width. Analogously, by turning the sum into an integral we arrive at the mean value for the continuous representation

$$\left\langle \hat{F}^X \right\rangle = \int_{-\infty}^{\infty} \hat{F}^X(\Delta E^X_{\text{seg}}) \Delta E^X_{\text{seg}} \mathrm{d}\Delta E^X_{\text{seg}} \,. \tag{7.10}$$

Finally, we want to point out the difference between the energy spectra discussed in literature [242, 246, 247] and the present work. All the literature studies obtain the spectra in pure metals by studying a wide variety of structurally different GBs. In contrast, we

focus only on one GB (Σ5(210)[001]). The segregation of energy distribution arises from the chemically different local coordinations of bulk and states. In other words, the distribution in the literature is due to the structural variety of grain boundaries, while in the present study, it is caused by the chemical complexity of the alloy model.

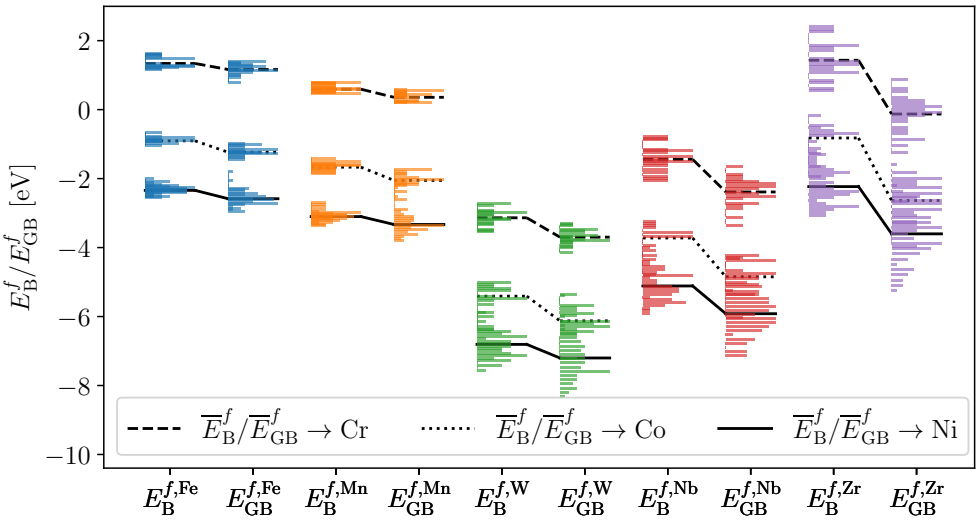

Figure 7.3: Bulk formation ($E^{f,X}_B$) is the left and GB formation energy spectra $E^{f,X}_{GB}$ as the right column for each solute. The spectra for each solute replacing Ni (solid), Co (dotted), and Cr (dashed) sites are plotted individually. For the individual formation energies the chemical potential terms do not cancel out hence the individual spectra are shifted along the y-axis by a constant offset $\mu^X - \mu^{\widetilde{M}}$ with $\widetilde{M} \in \{\mathrm{Ni}, \mathrm{Co}, \mathrm{Cr}\}$.

Figure 7.3 shows that the spectral property of the segregation energy is given by the spectral nature of both $E^{f,X}_B$ and $E^{f,X}_{GB}$ throughout all solutes. Furthermore, we find that the spectral width is similar for both GB and bulk formation energy. In contrast, in the noncrystalline case as investigated in Refs. [246, 247], the left part $E^{f,X}_B$ would collapse into a single energy level. Furthermore, only a single spectrum would be there per solute. The splitting is due to the multi-component nature of the matrix. More precisely there would be five matrix elements and consequently five spectra per solute. Due to the low concentrations of Ti and Al, we have omitted those as the number of computed states is not large enough to generate a sensible histogram.

Comparison with the pure Ni system

Figure 7.4 shows the discrete and fitted (skew-normal) segregation energy spectra for all five solutes. Each of the plots (Figs. 7.4a – 7.4e) shows three spectra, one for each of the three pristine GB sites. All values (mean, fit parameters, and pure segregation energies) for Fig. 7.4 are summarized in Tab. 7.3.

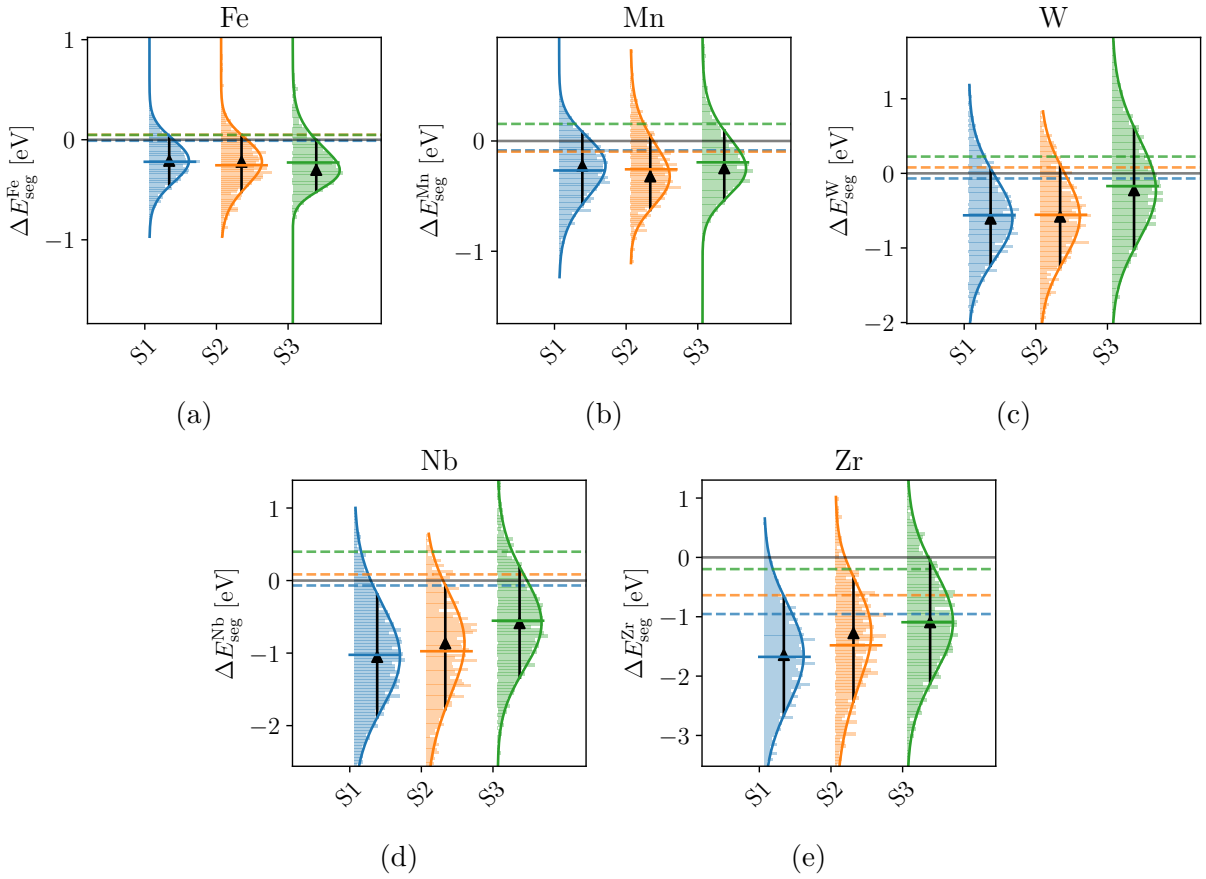

Figure 7.4: Segregation energy spectra $\Delta E_{\text{seg}}^{X}$ for Fe (Fig. 7.4a), Mn (Fig. 7.4b), W (Fig. 7.4c), Nb (Fig. 7.4d) and Zr (Fig. 7.4e). The energies forming the spectra are grouped by their former location of the GB state (site 1 to 3) on the pristine boundary. The solid line around the histogram is a fitted skew-normal distribution. The colored solid horizontal line refers to the distribution's mean value $\langle \Delta E_{\text{seg}} \rangle$ (Eq. (7.9)). The black triangle and bar denote the mode and the FWHM. The dashed colored lines represent the corresponding energy in the pure Ni system.

Analyzing the expectation value $\left\langle \Delta E_{\text{seg}}^{X} \right\rangle$ (solid colored horizontal line) of the distributions in Figs. 7.4a – 7.4e immediately reveals a drastically enhanced segregation (more negative) tendency compared to the pristine system. While for iron the enhancement in Fig. 7.4a is ≈ 0.25 eV for all three segregation spectra we find up to ≈ 1 eV for Nb. Interestingly the relation between the segregation energies of the sites in the pure system corresponds to the relation of the mean values of the distributions, except for Mn. Therefore, for Fe we find S1 $\approx$ S2 $\approx$ S3, and S1 $\approx$ S2 $<$ S3 for Mn, W and Nb. Similarly, the relation S1 $<$ S2 $<$ S3 holds for Zr. To quantify the width of the spectra we employ the FWHM. Therefore, for Fe, Mn, and Zr we find nearly the same FWHM (all three values within 0.1 eV). For W, S3 shows a broadening of ≈ 0.3 eV (compared to S1), and Nb a sharpening of 0.2 eV.

Analyzing, the corresponding skew values in Tab. 7.2 clearly reveals that a Gaussian distribution would not be sufficient to describe the spectra since $|\alpha| > 0$. Similarly, also Gumbel

	Site	Fe	Mn	W	Nb	Zr
$\Delta E_{\text{seg}}^{\text{pure}}$ [eV]	S1	−0.01	−0.09	−0.07	−0.07	−0.95
	S2	0.05	−0.10	0.08	0.08	−0.64
	S3	0.05	0.15	0.22	0.40	−0.20
$\langle \Delta E_{\text{seg}}^{X} \rangle$ [eV]	S1	−0.23	−0.28	−0.59	−1.05	−1.70
	S2	−0.26	−0.28	−0.60	−1.00	−1.46
	S3	−0.24	−0.19	−0.19	−0.56	−1.11
α [-]	S1	-0.86	−1.44	1.06	0.79	−0.78
	S2	−1.40	1.77	0.81	−1.43	−1.81
	S3	2.30	1.66	1.05	0.87	−0.01
FWHM [eV]	S1	0.50	0.66	1.30	1.70	2.00
	S2	0.57	0.67	1.37	1.71	2.10
	S3	0.52	0.63	1.64	1.53	2.06

Table 7.2: Expectation values of the energy spectra $\langle \Delta E_{\text{seg}}^{X} \rangle$ (Eq. (7.9)), skew parameter α and FWHM of the fitted skew-normal distribution. The first three rows show the segregation energy in the pure Ni system $\Delta E_{\text{seg}}^{\text{pure}}$, for each of the pristine GB sites. The columns correspond to Fig. 7.4a – 7.4e.

distribution does not have enough degrees of freedom. This is shown by a sign change of the skew values for Fe of S2 ($\alpha < 0$) and S3 ($\alpha > 0$). Thus, S2 exhibits left- and S3 a right-skewed spectrum. Finally, we find that the FWHM tends to decrease from Fig. 7.4a to Fig. 7.4e.

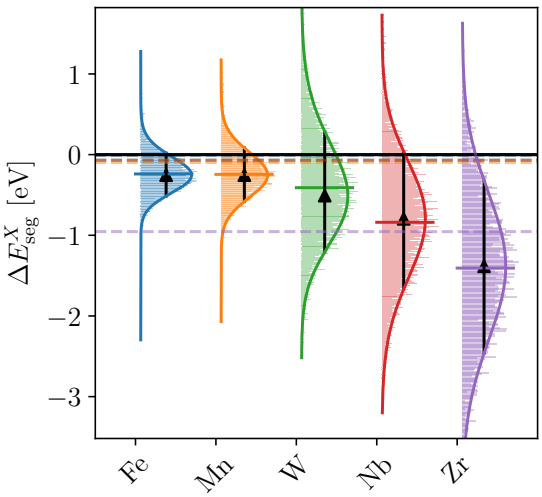

Figure 7.5: Segregation energy spectra $\Delta E_{\text{seg}}^{X}$ for all five solute elements. The solid line around the histogram is a fitted skew-normal distribution. The colored solid horizontal line refers to the mean values $\langle E_{\text{seg}}^{X} \rangle$. The black triangle and bar denote the mode and the FWHM of the skew-normal distribution. The dashed colored lines represent the segregation energy in the pure Ni system.

However, keep in mind that the separation between S1, S2, and S3 in the disordered system is not present any more and is solely for better comparison with the pristine system. Consequently, for each solute, there is only one spectrum in the disordered system rather than three. Those are shown in Fig. 7.5, where each of the spectra corresponds to the union of all three from Fig. 7.4. E.g. the blue spectrum in Fig. 7.5 is computed by unifying all three from Fig. 7.4a. Similarly, as Tab. 7.2 corresponds to Fig. 7.4, Tab. 7.3 summarizes the fitting parameters and the values for the segregation energies in the pristine system.

	Fe	Mn	W	Nb	Zr
$\min \Delta E_{\text{seg}}^{\text{pure}}$ [eV]	−0.01	−0.10	−0.07	−0.07	−0.95
$\langle \Delta E_{\text{seg}}^{X} \rangle$ [eV]	−0.24	−0.24	−0.42	−0.83	−1.41
α [-]	0.97	0.72	1.45	−0.94	−0.66
FWHM [eV]	0.53	0.66	1.49	1.70	2.14

Table 7.3: Fitting parameters of the unified energy spectra (combination of S1, S2, and S3). It shows the same values as Tab. 7.2 but for Fig. 7.5.

Therefore, by looking at the mean values in Fig. 7.5, we observe again a strongly enhance segregation tendency for all of the five elements. Note that the enhancement is up to an order of magnitude larger than the predicted tendency in the pristine system for Fe, Mn, W, and Nb. E.g., for Nb, we find nearly no tendency to segregate to the GB ($\Delta E_{\text{set}}^{\text{pure}} = -0.07$ eV) in the pure system, Tab. 7.3 reports a mean value of the spectrum at $\langle \Delta E_{\text{seg}}^{\text{Nb}} \rangle = -0.83$ eV. In contrast, for Zr we report $\Delta E_{\text{seg}}^{\text{pure}} = -0.95$ eV and hence already a strong segregation tendency in pure Ni, we still find an enhancement to $\langle \Delta E_{\text{seg}}^{\text{Zr}} \rangle = -1.41$ eV for the alloyed system.

7.2.4 Impact on McLean type segregation

To predict the equilibrium concentration at a grain boundary as a function of the segregation energy, we can employ a thermodynamic model. The first, yet still commonly used, is the McLean isotherm [248]. It connects the equilibrium solute concentration for a species X at the GB, X_{GB}^{X} with the the Gibbs free-energy of segregation, $\Delta G_{\text{seg}}^{X}$, and reads

$$\frac{X_{\text{GB}}}{1 - X^{\text{GB}}} = \frac{X^{\text{B}}}{1 - X^{\text{B}}} \exp\left(-\frac{\Delta G_{\text{seg}}^{X}}{k_B T}\right) \tag{7.11}$$

where X_{B} is the bulk concentration. In 0 K first-principles calculation, it is common to substitute $\Delta E_{\text{seg}}^{X}$ for $\Delta G_{\text{seg}}^{X}$ due to the relation

$$\Delta G = \Delta H - T\Delta S = \overbrace{\Delta U}^{\Delta E} + \overbrace{\Delta pV + p\Delta V}^{0} + \overbrace{T\Delta S}^{0 \text{ K=0}} . \tag{7.12}$$

When applying Eq. (7.11) to real material systems one faces several shortcomings. Firstly, most metals and alloys are poly crystalline, hence not only one GB but a huge variety of GBs will be present. Furthermore, even for a single GB in a pure system, it is not sufficient to describe it with a single segregation energy (see Fig. 7.1a). In other words, the McLean-isotherm corresponds to a single site approximation. Therefore, Eq. (7.11) might be generalized to multiple segregation sites i as suggested by [241]. To account for our disordered system, similarly as for a poly crystalline systems we have to average over the whole set of states forming an energy spectrum [247]. To employ a density of states (= spectrum) distribution to obtain an averaged solute concentration $\left\langle X^{\mathrm{GB}}(T)\right\rangle$ was proposed earlier [249–251] and reads according to Ref. [252] for a continuous distribution as

$$\left\langle \hat{X}^{\mathrm{GB}}(T)\right\rangle = \int_{-\infty}^{\infty} X_i^{\mathrm{GB}}(\Delta E_{\mathrm{seg}}^X, T)\hat{F}^X(\Delta E_{\mathrm{seg}}^X)\mathrm{d}\Delta E_{\mathrm{seg}}^X\,. \tag{7.13}$$

Similarly, for a discrete spectrum, the above equation need to be modified to

$$\left\langle X^{\mathrm{GB}}(T)\right\rangle = \sum_u^N X^{\mathrm{GB}}(\Delta E_{\mathrm{seg}}^{X,u}, T)F_u^X \underbrace{\Delta(\Delta E_{\mathrm{seg}}^X)}_{\text{bin width}} \tag{7.14}$$

for the discrete case respectively, where u is the bin index. X_{GB} is obtained by rewriting Eq. (7.11) and reads for the multi-site case as derived by White and Coghlan [241] as

$$X_u^{\mathrm{GB}} = \left[1 + \frac{1 - X^{\mathrm{B}}}{X^{\mathrm{B}}} \exp\left(-\frac{\Delta E_{\mathrm{seg}}^{X,u}}{k_B T}\right)\right]^{-1} \tag{7.15}$$

for the $,\xi^{\mathrm{th}}$ site. At this point, we want to clarify the terminology. Although Eq. (7.13) appears similarly in Ref. [247], the underlying physical meaning is slightly different. In the works [246, 247], the formation of the energy spectrum arises from combining exactly one bulk state (because there is only one nonequivalent site on an *fcc* lattice) with the large variety of GB states (from many different sites at different GBs). In other words, there is a spectrum of GB site formation energies but only one bulk formation energy per solute. Hence, when computing ΔE_{seg} the bulk formation energy stays always the same. Hence each segregation energy corresponds to a state at a GB. Therefore the term "*multi-site*" McLean equation is accurate. In the present case, we deal also with a spectrum of bulk-formation energies (108 distinct energies per solute), which is again combined with a spectrum of GB site formation energies. Consequently, each site i in the "*multi-site*" McLean equation refers to a set of combinations of bulk and GB states that yield the same (continuous) or similar (discrete) segregation energy. Similarly we group (the states) with a certain energy bin width, since we deal with a discrete histogram.

For a good model, it is necessary that the ensemble of local environments sampled for both bulk and GB states is representative of the real alloy.

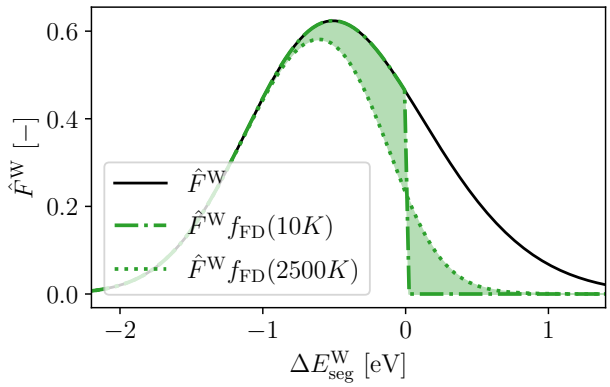

Figure 7.6: Segregation energy spectrum for tungsten. The black line is the spectrum as shown in Fig. 7.5. The dash-dot and dotted lines refer to distributions multiplied with Fermi-Dirac distribution at 10 and 2500 K respectively.

Temperature dependence of the energy spectrum

At 0 K all states with a negative segregation energy will be filled up, in equilibrium. At finite temperatures, also higher states might be filled with solute atoms due to thermal activation. As each site or "trap" can be only filled by a single solute atom, it should be legit to apply Fermi-Dirac statistics [253, 254]. To account for the thermal activation, we multiply the energy spectrum and consequently set the "*Fermi level*" to zero. Segregation energy of zero means that the bulk and grain boundary formation energies for the solute point defect are the same. Hence, it refers analogously to the highest occupied state. Figure 7.6 shows the impact of temperature, due to the FD distribution for tungsten. Consequently to account for this type of temperature dependence, the distribution to average over (Eqs. (7.13) – (7.14)) is different at each temperature T.

Determining the enthalpy and entropy of segregation

The original purpose of the McLean isotherm was to determine the segregation energy from a set of measured concentrations at different temperatures. By rewriting the equation we hence get an expression for an "*effective*" segregation energy which reads

$$\Delta G_{\mathrm{eff}} = -k_B T \ln\left(\frac{\left\langle X^{\mathrm{GB}}\right\rangle \left(1-\left\langle X^{\mathrm{GB}}\right\rangle\right)}{X^{\mathrm{B}}(1-X^{\mathrm{B}})}\right). \tag{7.16}$$

where $\left\langle X^{\mathrm{GB}}\right\rangle$ is the the averaged equilibrium GB concentration from Eq. (7.14). Therein we follow the work by Scheiber and Romaner [246], to obtain a temperature dependence of $\Delta G_{\mathrm{eff}}(T)$. Note that if we would have used Eq. (7.15) instead of $\left\langle X^{\mathrm{GB}}\right\rangle$ the temperature dependence of ΔG would cancel.

Therefore, for a given bulk concentration X^{B} we obtain a temperature dependence for the segregation energy. Furthermore, we exploit the relation from Eq. (7.12). Hence, the slope and intercept from a linear fit will yield an estimate for ΔH and ΔS. Recall that ΔG_{eff} of a single (non averaged) McLean isotherm is a constant, with respect to T . Consequently, a temperature range in which Eq. (7.16) becomes constant indicates that the segregation behavior (determined by the averaged isotherm) can be approximated with a single value. Technical details on how the linear fit is carried out are given in Appendix .3.1. The influence of the parameters of the skew-normal distribution's parameters on $\Delta G_{\mathrm{eff}}(T)$ are summarized in Figs. .16 – .19.

Impact of energy spectra on McLean isotherms

Figures 7.7a – 7.7e compare all the different isotherms discussed so far. Firstly we focus on the upper panels of Fig. 7.7. The difference between the simply averaged isotherm (dashed colored line) according to Eq. (7.14) and the FD-smeared (solid colored lines) is negligible as they overlap. However, a comparison of the averaged (colored dashed line) with the black dashed isotherm computed from $\Delta E_{\mathrm{seg}}^{\mathrm{pure}}$ reveals significantly lower solute concentrations at higher temperatures. In contrast, the single isotherm computed from the mean value spectrum (colored dotted line) overestimates the GB concentration at lower temperatures but drops below the averaged isotherms, as those show a significantly flatter slope. The flattening of the averaged isotherms becomes more pronounced for solutes with an increased segregation tendency (e.g., compare Fe and Mn on the one hand, with W, Nb, and Zr on the other hand) while consequently, the crossover between the mean and the averaged isotherm shifts to higher temperature. Therefore, for Nb and Zr it is not on the shown temperature scale anymore. In summary, all three isotherms are significantly distinct from each other, e.g., for Nb we find at 1500 K concentrations ranging from $X^{\mathrm{GB}}(\Delta E_{\mathrm{seg}}^{\mathrm{pure}}) = 6.9\%$ over $X^{\mathrm{XB}}(\langle\Delta(E_{\mathrm{seg}})\rangle) = 69.4$ % to $\left\langle X^{\mathrm{GB}}(F(\Delta E_{\mathrm{seg}}))\right\rangle = 95.0$ %.

The lower panels show the effective segregation energy according to Eq. (7.16). The dotted line gives a mean value of the distribution as a reference. The black dashed linear fit illustrates how we arrive at ΔH and ΔS. For Fe (Fig. 7.7a) and Mn (Fig. 7.7b), ΔG_{eff} converges to a (nearly) constant value for temperatures > 1500 K. This convergence curvature decreases for W and Nb, whereas for Zr, ΔG_{eff} exhibits nearly linear behavior. Therefore, we focus on Fe and Mn and try to elucidate this deviation. A "*simple*" McLean isotherm (at constant X^{B}) is characterized by a single segregation energy, which is constant throughout a temperature range. The temperature dependence hence arises due to the spectral nature of the segregation energy. We find a strong temperature dependence for ΔG_{eff} for Fe and Mn for up to $T \approx 750$ K. The flattening behaviour to a constant level means that for high T, it is possible to describe the isotherm using a single-site McLean isotherm. In contrast, W, Nb, and Zr show a strong dependency on the effective segregation energy over the whole

temperature range.

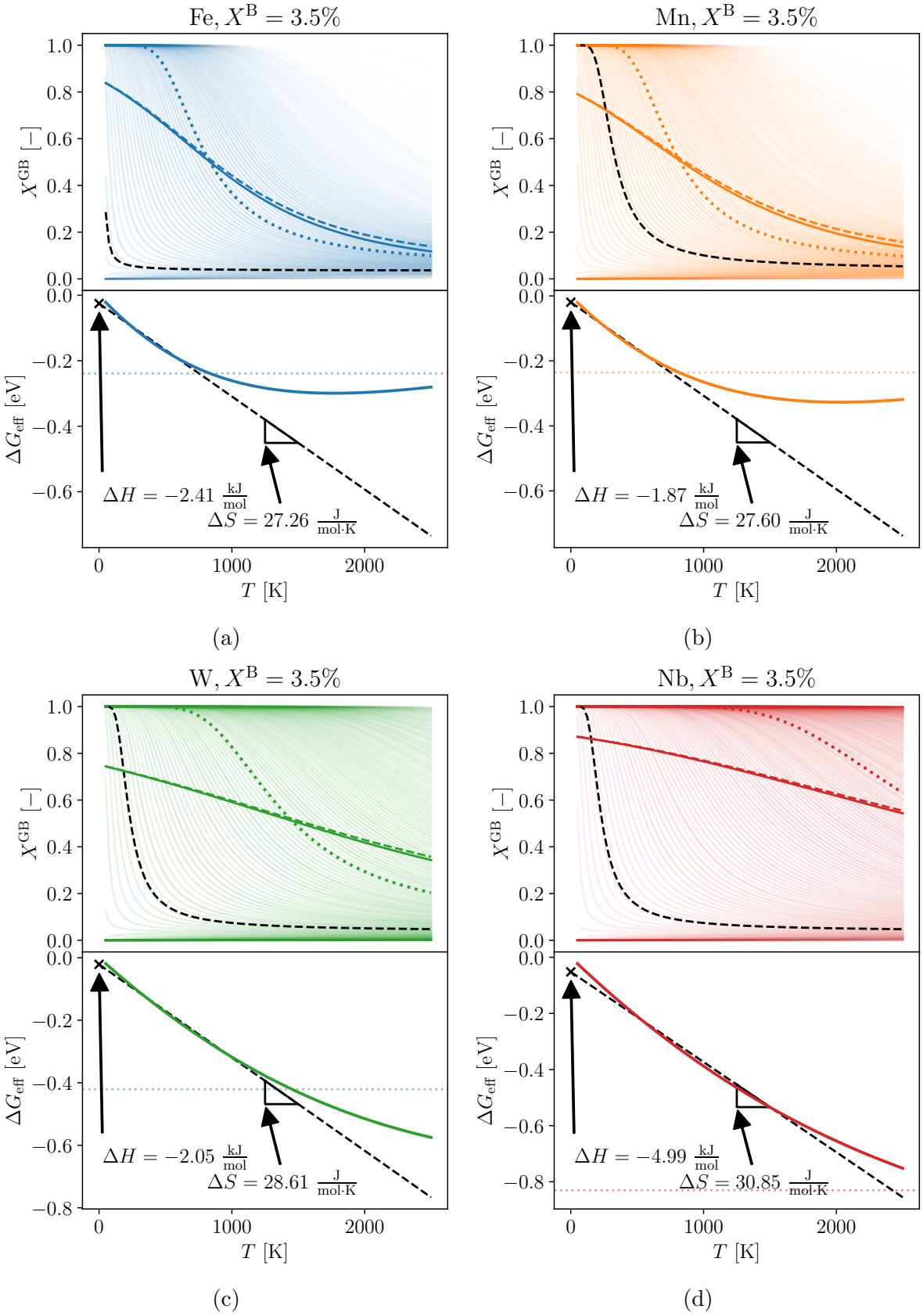

(a) (b) (c) (d)

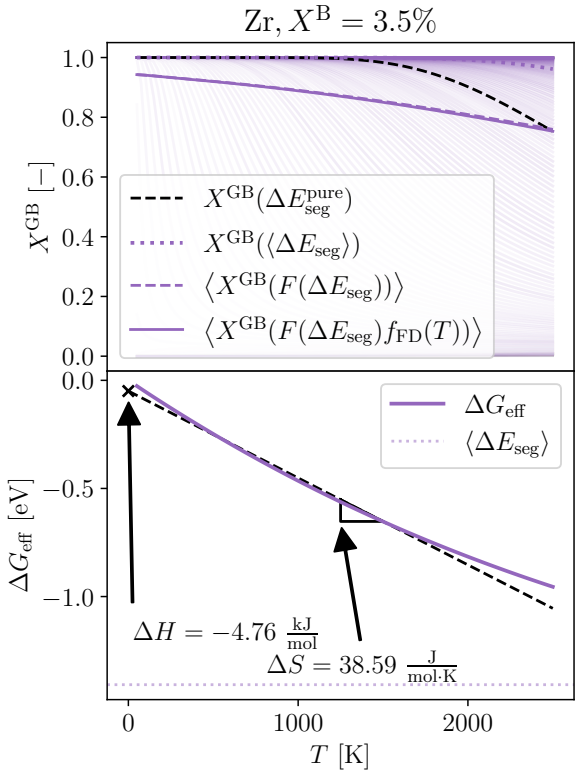

(e)

Figure 7.7: The upper panels show the impact of the energy spectra on McLean-type segregation. The black dashed and the colored dotted line shows the isotherms (Eq. (7.11)) for the pure system and the mean value of the distribution (Eq. (7.9)). The translucent isotherms in the background refer to the different energy states (Eq. (7.15)) of the histogram. The colored dashed line is the average of those isotherms according to Eq. (7.13). The solid colored line represents the average employing FD-smeared energy spectra as described in Sec. 7.2.4. The lower panels show a colored solid line representing the effective segregation energy ΔG_{eff} according to Eq. (7.16). The black dashed line is a linear fit for the low T regime. The colored dotted line is $\langle \Delta E_{\mathrm{seg}}^{X} \rangle$ as a reference. All isotherms in Figs. 7.7a–7.7e are plotted for constant $X^{\mathrm{B}} = 3.5$ at. %.

So far Fig. 7.7 showed the averaged McLean isotherms for a constant bulk solute concentration of $X^{\mathrm{B}} = 0.035$. Nevertheless, one may vary also the X^{B} and study the impact on the isotherms. Furthermore, executing a linear fit to Eq. (7.16) at each bulk concentration allows reporting the dependence of ΔH and ΔS on X^{B}. Fig. 7.8 shows X^{GB} in the first and ΔG_{eff} in the second panel for a bulk solute concentration range of $1.0 \cdot 10^{-5} < X^{\mathrm{B}} < 0.5$. However, note that $X^{\mathrm{B}} = 0.5$ is far beyond the dilute limit, hence, the underlying assumption of non-interacting solutes will not hold anymore. Interestingly, we find that the effective segregation energy changes its curvature in Fig. 7.8a for Fe at ≈ 2000 K and at ≈ 1000 K for Mn. The linear behavior of the effective segregation energy in Fig. 7.7e is preserved throughout the whole concentration range of X^{B} as shown in Fig. 7.8c. For all solutes, we

find (in the third panel) a logarithmic-like shaped dependency of ΔH and ΔS. For Zr, Nb, and W, ΔH and ΔS have nearly overlapping shapes. However, upon comparing the solute with each other, note that each panel for each solute has a different y-axis scale.

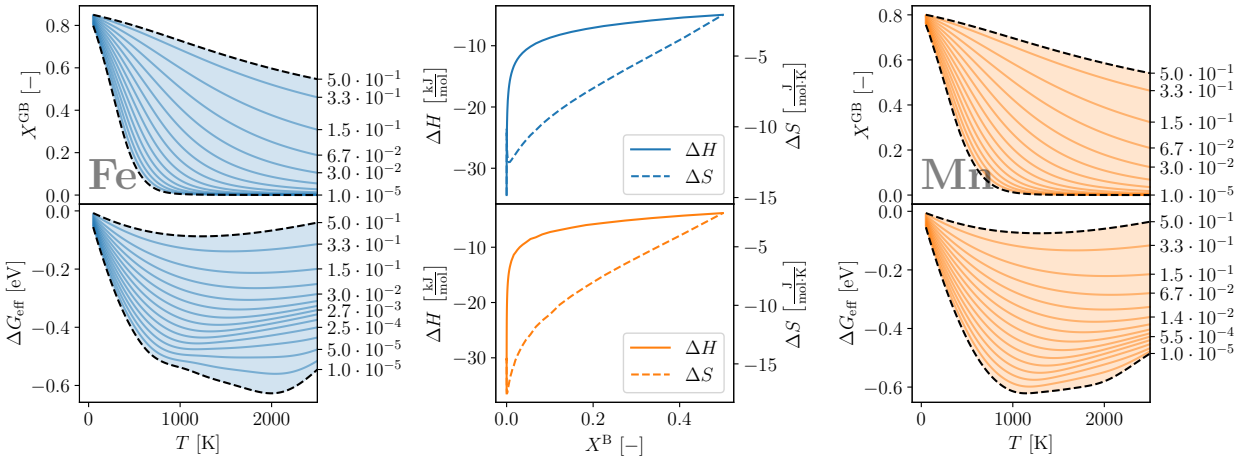

(a)

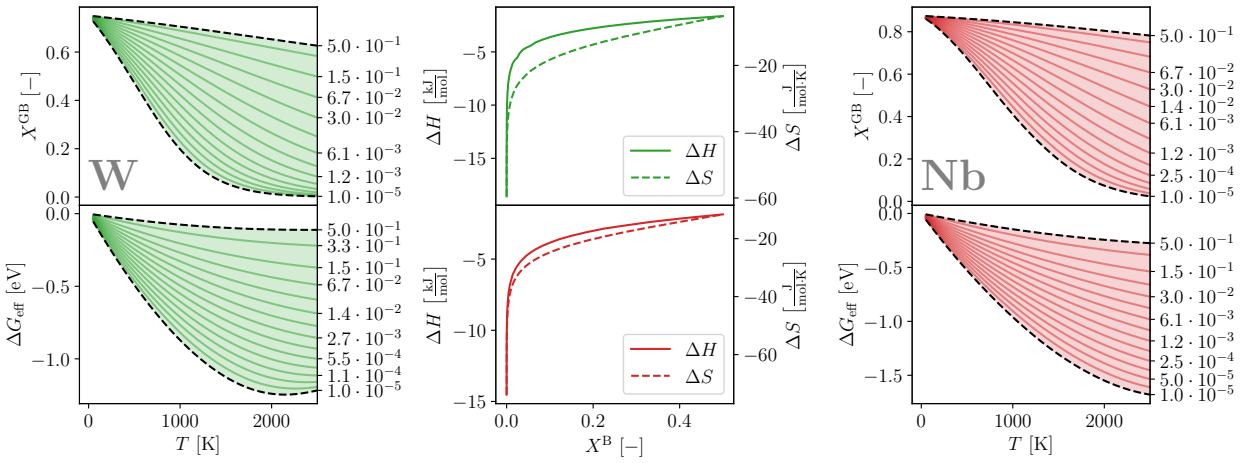

(b)

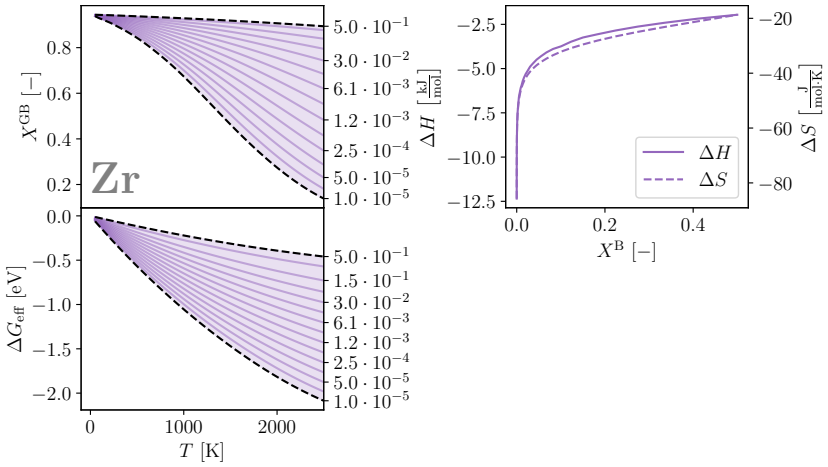

(c)

Figure 7.8: McLean isotherms for all five solutes. For each solute there are three plots, where Fig. 7.8a gathers Fe and Mn, and Fig. 7.8b combines W and Nb. The first panel (with the solute's name in it) shows the McLean isotherms for different bulk concentrations $1.0 \cdot 10^{-5} < X^B < 0.5$. The second panel (below the first) visualizes the corresponding effective segregation energies ΔG_{eff}. The last plot shows ΔH and ΔS as a function of the bulk solute concentration X^B.

7.2.5 Beyond the McLean segregation - An (adapted) Guttmann model

The McLean model has been extended and adapted for various applications. E.g., the Fowler-Guggenheim isotherm [255] adds a concentration-dependent term to ΔG_{seg} to account for solute interactions beyond the dilute limit. The model of Guttmann [256] is an extension to a ternary system within a non-ideal solution. Another prominent example would be the model from Wynblatt and Chatain [257]. For a more extensive review of the thermodynamic model for GB segregation, we refer the reader to the excellent book from Lejček [258].

A modified Guttmann model

As our models depict a multicomponent system, in the following we will adapt Guttmann's model in two ways. Firstly, as atomistic models always replace only one solute atom per cell, they represent a dilute system. Secondly, as pointed out by Wagih and Schuh [247], the Guttmann model was designed to be used with a single segregation energy. Therefore, we will adapt it for application in our disordered system, exhibiting a segregation energy spectrum. Before we start with the modifications, we quickly summarize the basics of the original Guttmann model.

In the above McLean equation, we made a simplification to ΔG_{seg} which we did not speak of yet. As the Gibbs free energy is composed of the standard Gibbs free energy of segregation ΔG^0_{seg} and an excess term ΔG^E_{seg} such that

$$\Delta G_{\text{seg}} = \Delta G^0_{\text{seg}} + \Delta G^E_{\text{seg}} \tag{7.17}$$

we implicitly set $\Delta G^E_{\text{seg}} = 0$ in Eq. 7.11. In a regular solution of randomly distributed solvent and solute atoms, the excess Gibbs energy is equal to the mixing enthalpy and might be expressed by a constant pair interaction energy between nearest neighbors [259–262].

$$\Delta G^E_{\text{seg}} = \Delta H_m = \sum_{\xi \neq \eta} \alpha_{\xi\eta} X_\xi X_\eta \,. \tag{7.18}$$

When ξ and η are species of the system, X_ξ and X_η denote the corresponding site fractions in the bulk. $\alpha_{\xi\eta}$ are the interaction parameters. Within the context of this thesis, note the difference to the pair SRO parameters discussed in Sec. 6.1.1, as those interaction parameters represent an energy. Furthermore, $\alpha_{\xi\eta}$ can be expressed in terms of bonding energies $\varepsilon_{\xi\eta}$ for the corresponding bonds [263] as

$$\alpha_{\xi\eta} = Z\left(\varepsilon_{\xi\eta} - \frac{\varepsilon_{\xi\xi} + \varepsilon_{\eta\eta}}{2}\right) \tag{7.19}$$

where Z is the coordination number in the crystal or at the GB. In the following, M denotes the species of a pure elemental matrix. Then, the excess Gibbs energy for a solute ξ reads in a multi-component setting in a matrix of species M is given [258]

$$\Delta G_{\xi}^{E} = -2\left(\alpha_{\xi M}^{\mathrm{GB}} X_{\xi}^{\mathrm{GB}} - \alpha_{\xi M}^{\mathrm{B}} X_{\xi}^{\mathrm{B}}\right) + \sum_{\eta \neq \xi, M} \left(\alpha_{\xi\eta}^{\prime\mathrm{GB}} X_{\eta}^{\mathrm{GB}} - \alpha_{\xi\eta}^{\prime B} X_{\eta}^{\mathrm{B}}\right) . \tag{7.20}$$

with $\alpha_{\xi\eta}^{'} = \alpha_{\xi\eta} - \alpha_{\xi M} - \alpha_{\eta M}$. Note, that in the above equation, one differentiates between the pair interaction parameters at the GB, $\alpha_{\xi M}^{\mathrm{GB}}$, and in the bulk phase, $\alpha_{\xi M}^{\mathrm{B}}$. Commonly one assumes $\alpha_{\xi M}^{\mathrm{GB}} \simeq \alpha_{\xi M}^{\mathrm{B}}$ for which the equation simplifies to [259]

$$\Delta G_{\xi}^{E} = -2\alpha_{\xi M}^{\mathrm{GB}}\left(X_{\xi}^{\mathrm{GB}} - X_{\xi}^{\mathrm{B}}\right) + \sum_{\eta \neq \xi, M} \alpha_{\xi\eta}^{\prime\mathrm{GB}}\left(X_{\eta}^{\mathrm{GB}} - X_{\eta}^{\mathrm{B}}\right) . \tag{7.21}$$

Adapting the model to our needs

As described through Eqs. (7.20) – (7.21) we cannot use the model yet. Firstly, our setup within this chapter models the dilute limit, hence there are no interactions between the solutes, $\alpha_{\xi\eta} = 0$. Hence, the net interaction parameter becomes $\alpha_{\xi\eta}^{'} = -\alpha_{\xi M} - \alpha_{\eta M}$, and we can rewrite Eq. (7.20) to

$$\Delta G_{\xi}^{E} = -2\left(\alpha_{\xi M}^{\mathrm{GB}} X_{\xi}^{\mathrm{GB}} - \alpha_{\xi M}^{\mathrm{B}} X_{\xi}^{\mathrm{B}}\right) + \sum_{\eta \neq \xi, M} \left[(\alpha_{\xi M}^{\mathrm{B}} + \alpha_{\eta M}^{\mathrm{B}}) X_{\eta}^{\mathrm{B}} - (\alpha_{\xi M}^{\mathrm{GB}} + \alpha_{\eta M}^{\mathrm{GB}}) X_{\eta}^{\mathrm{GB}}\right] . \tag{7.22}$$

This has an important implication: Eq. (7.22) only contains solute-matrix pair interaction parameters of type $\alpha_{\xi M}$. The dilute limit model also affects the definition of the pair interaction parameters $\alpha_{\xi M}$. Eq. (7.19) requires the solute's self pair interaction energy $\varepsilon_{\xi\xi}$, to computer the interaction parameter. Due to the dilute limit models this we cannot extract this value from our calculation (see Sec. 7.2.5, later this chapter). Therefore we assume that the pair interaction energy between two solutes ξ is the equals to the pair interaction energy of the matrix M. Consequently, for $\varepsilon_{\xi\xi} = \varepsilon_{MM}$, Eq. (7.19) becomes

$$\alpha_{\xi M} = Z\left(\varepsilon_{\xi M} - \varepsilon_{MM}\right) . \tag{7.23}$$

The second shortcoming with the model is that it considers only one matrix species M while our composition according to Tab. 7.1 exhibits five matrix elements. To account for that we compute an "*effective*" or "*averaged*" pair interaction parameter modeling the solute matrix interaction, for both the GB and bulk. Therefore, suppose $\widetilde{M}$ is a matrix species (Ni, Co, Cr, Ti, or Al in our case), and ξ is a solute species. Furthermore, let a ξ atom replace the i^{th}

site in a GB structure and the j^{th} site in the bulk. Then we define a "*per-site*" interaction parameter as

$$\bar{\alpha}^{\text{GB},i}_{\xi M} = \sum_{\widetilde{M}} Z^{i}_{\widetilde{M}} \left(\varepsilon^{\text{GB}}_{\xi\widetilde{M}} - \varepsilon^{\text{GB}}_{\widetilde{M}\widetilde{M}} \right) \tag{7.24}$$

$$\bar{\alpha}^{\text{B},j}_{\xi M} = \sum_{\widetilde{M'}} Z^{j}_{\widetilde{M'}} \left(\varepsilon^{\text{B}}_{\xi\widetilde{M}} - \varepsilon^{\text{B}}_{\widetilde{M'}\widetilde{M'}} \right) \tag{7.25}$$

where $Z^{i}_{\widetilde{M}}$ and $Z^{j}_{\widetilde{M'}}$ are the numbers of $\xi - \widetilde{M}$ bonds at the i^{th} GB and j^{th} bulk site respectively. Note that the subscript M is not any more to the matrix species (as our models exhibit five of them) but rather denotes the effctive matrix at the corresponding site. In the above equation, $\widetilde{M'}$ is the host species that is replaced by the solute atom ξ at the site i and j. Still, we find a physical interpretation of the averaged "*per-site*" interaction parameter $\bar{\alpha}^{i}_{\xi M}$: It measures whether the site i is attractive for a solute ξ compared to its original state when occupied with a $\widetilde{M'}$ atom. Substituting the averaged pair interactions (Eqs. (7.24) and (7.25)) back into Eq. (7.22) we obtain an expression for the excess Gibbs free energy for a pair of a GB and bulk sites which reads

$$\Delta G^{E,ij}_{\xi} = -2 \left(\bar{\alpha}^{\text{GB},i}_{\xi M} X^{\text{GB}}_{\xi} - \bar{\alpha}^{\text{B},j}_{\xi M} X^{\text{B}}_{\xi} \right) + \sum_{\eta \neq \xi, M} \left[(\bar{\alpha}^{\text{B},j}_{\xi M} + \bar{\alpha}^{\text{B},j}_{\eta M}) X^{\text{B}}_{\eta} - (\bar{\alpha}^{\text{GB},i}_{\xi M} + \bar{\alpha}^{\text{GB},i}_{\eta M}) X^{\text{GB}}_{\eta} \right] . \tag{7.26}$$

Note, that we have similarly defined a single segregation energy for a combination of a GB site i and a bulk site j in Eq. (7.6). Such a formulation has the advantage, that, similarly to the multi-site McLean formalism, we can group the states such that we arrive at a multi-site multi-component Guttmann isotherm. We do so, however only within a discrete setting by averaging over Eq. (7.26). Therefore let K be the set of all tuples (i, j) within the k^{th} bin of our discrete segregation energy histogram for the solute ξ. We then average over all combination of allowed sites in K as

$$\Delta \bar{G}^{E}_{u} = \frac{1}{|K|} \sum_{(i,j) \in K} G^{E,ij}_{u} . \tag{7.27}$$

Note that if N is the total number of combinations of bulk and GB states, then $F^{X}_{u} = \frac{|K|}{N}$ holds. In other words the number of states in histogram bin must be equal the number of elements in K. Finally we arrive at a multi-state isotherm which reads for the u^{th} segregation energy state when solved for X^{GB}_{u} as

$$X_u^{\mathrm{GB}} = \left[1 + \frac{1 - X^{\mathrm{B}}}{X^{\mathrm{B}}} \exp\left(-\frac{\Delta E_{\mathrm{seg}}^u + \Delta \bar{G}_u^E}{k_b T}\right)\right]^{-1} \tag{7.28}$$

where $\Delta E_{\mathrm{seg}}^{\xi,i}$ is substituted for $\Delta G_{\mathrm{seg}}^{\xi,i}$. Note that although Eq. (7.28) looks similar to the McLean multi-site Eq. (7.15) solving it is much more involved. Since $\Delta \bar{G}_\xi^{E,i}(X_1^{\mathrm{GB}}, \ldots, X_\xi^{\mathrm{GB}}, \ldots, X_N^{\mathrm{GB}})$ is a function of all the N solute site fraction at the GB, the Eq. (7.20) represents a fixed point expression. Furthermore, for each state i one has to solve a system of N coupled fixed point equations simultaneously.

Determining pair interaction energies

One last ingredient is missing, namely the pair interaction energies at the GB $\varepsilon_{\xi\widetilde{M}}^{\mathrm{GB}}$ and in the bulk $\varepsilon_{\xi\widetilde{M}}^{\mathrm{B}}$. While it is possible to estimate them using a pair potential (when available), we describe a different approach here. As mentioned Sec. 7.2.1, we have 258 DFT calculations at our disposal per solute, hence for all five solutes there are 540 bulk and 750 calculation involving GBs. Although this is a large number of calculations, it is not sufficient as it does not allow for extracting solute self-interactions (for segregation of a single solute) and solute-solute interactions (for co-segregation). Nevertheless, in the following we demonstrate, how the pair interactions involving one solute and matrix elements, as well as matrix-matrix interactions, could be extracted from our present data. To get all inputs necessary for using the Guttmann's model, approximately doubled amount of calculations (with more than one solute in the simulation box) would be needed. Such data is not at our disposal at this time. To continue we assume that upon replacing a solute in either the bulk a GB the energy differences can be mostly attributed to the reforming of the bonds (chemical part of the solution energy), while the elastic contribution can be neglected. Furthermore, we assume the atoms in the relaxed cell to occupy a perfect lattice and therefore ignore the local elastic distortions. Using these assumptions, we expand the energy of a system in a cluster-expansion-like manner as in Eq. (6.23) as

$$E = V^{(0)} + \sum_{\xi}^{S} V_\xi^{(1)} N_\xi + \sum_{i}^{C} \sum_{\xi,\eta}^{S,S} V_{\xi\eta}^{i,(2)} N_{\xi\eta}^i + \ldots \tag{7.29}$$

but truncate the series at the level of pair interactions. S and C are, similar as in the previous chapter, the species and the coordination shells in the system. We can neglect $V^{(0)}$ and set $V_\xi^{(1)} = \mu^\xi$ to the chemical potential. Moreover, we only consider nearest-neighbor interactions, which causes the sum over the coordination shells to drop. We rewrite the above equation as

$$E \approx \sum_{\xi}^{S} \mu^{\xi} N_{\xi} + \sum_{\xi,\eta}^{S} V_{\xi\eta}^{1,(2)} N_{\xi\eta}^{1} \,. \tag{7.30}$$

Therefore N_ξ is the number of ξ atoms in the system, and $N^1_{\xi\eta}$ the number of ξ–η bonds (= nearest neighbor pairs) in the system. In that case $V^{1,(2)}_{\xi\eta}$ will correspond to the pair interaction energies $\varepsilon_{\xi\eta}$. We continue by expanding the following expression $E_{\mathrm{B}}^{X\to\widetilde{M}} - E_{\mathrm{B}}$ into such a cluster expansion, where the first term refers to the total energy of the system where a solute atom X replaces a matrix atom of species $\widetilde{M}$. The latter term is the energy of the disordered system without the solute X. Substituting this expression into Eq. (7.30), we obtain

$$E_{\mathrm{B}}^{X\to\widetilde{M}} - E_{\mathrm{B}} \approx \mu^{X} - \mu^{\widetilde{M}} + \sum_{\xi,\eta}^{S,S} \varepsilon_{\xi\eta} \Delta N^{1}_{\xi\eta} \,, \tag{7.31}$$

where $\Delta N^1_{\xi\eta}$ is the difference in numbers of ξ – η bonds between the system with and without the solute atoms. In our system with five solute atoms $\xi \in \{\mathrm{Fe}, \mathrm{Mn}, \mathrm{W}, \mathrm{Nb}, \mathrm{Zr}\}$ and five matrix $\widetilde{M} \in \{\mathrm{Ni}, \mathrm{Cr}, \mathrm{Co}, \mathrm{Ti}, \mathrm{Al}\}$, we need in total fifty parameters to express the energy: Ten chemical potentials, five of type μ^ξ plus five of type $\mu^{\widetilde{M}}$, and 40 pair interaction energies. 25 solute-matrix interactions $\varepsilon_{\xi\widetilde{M}}$, five matrix element self-interactions $\varepsilon_{\widetilde{M}\widetilde{M}}$, and ten matrix-matrix interaction energies $\varepsilon_{\widetilde{M}\widetilde{M}'}$. Note, due to the dilute limit we do not have $\varepsilon_{\xi\xi}$ terms. We define an interaction vector $\mathbf{J}$ with N^{P} (50 in our case) entries where N^{P} is the number of parameters. Similarly, we introduce an energy vector $\mathbf{E}$ with N^{C} ($540 = 5 \times 108$ in our case, for the bulk) entries with N^{C} being the number of calculations available. The matrix $\mathbf{\Pi}$ connecting $\mathbf{J}$ and $\mathbf{E}$ will consequently have dimensions $N^{\mathrm{C}} \times N^{\mathrm{P}}$. For $N^{\mathrm{C}} \geq N^{\mathrm{P}}$ we find the over-determined set of equation

$$\mathbf{E} = \mathbf{\Pi} \cdot \mathbf{J} \,. \tag{7.32}$$

Finally, we can compute the pair interaction energies using

$$\mathbf{J} = \mathbf{\Pi}^{-1} \cdot \mathbf{E} \,. \tag{7.33}$$

Using our (somewhat artificial) splitting of the species of the system into solute (ξ) and matrix species ($\widetilde{M}$), the interaction vector $\mathbf{J}$ is defined as

$$\mathbf{J} = \left[\mu^{\xi_1}, \cdots, \mu^{\xi_N}, \mu^{\widetilde{M}_1}, \cdots, \mu^{\widetilde{M}_{N'}}, \varepsilon_{\xi_1\widetilde{M}_1}, \cdots \varepsilon_{\xi_N\widetilde{M}_{N'}}, \varepsilon_{\widetilde{M}_1\widetilde{M}_1}, \cdots \varepsilon_{\widetilde{M}_N\widetilde{M}_{N'}} \right]^T . \tag{7.34}$$

Consequently, assuming N solute species and N' matrix species, $\mathbf{\Pi}$ reads

$$\mathbf{\Pi} = \tag{7.35}$$
$$\begin{bmatrix} N_{\xi_1}^{(1)} & \cdots & N_{\xi_N}^{(1)} & N_{\widetilde{M}_1}^{(1)} & \cdots & N_{\widetilde{M}_{N'}}^{(1)} & \Delta N_{\xi_1\widetilde{M}_1}^{(1)} & \cdots & \Delta N_{\xi_N\widetilde{M}_{N'}}^{(1)} & \Delta N_{\widetilde{M}_1\widetilde{M}_1}^{(1)} & \cdots & \Delta N_{\widetilde{M}_N\widetilde{M}_{N'}}^{(1)} \\ \vdots & & \vdots & \vdots & & \vdots & \vdots & & \vdots & \vdots & & \vdots \\ N_{\xi_1}^{(i)} & \cdots & N_{\xi_N}^{(i)} & N_{\widetilde{M}_1}^{(i)} & \cdots & N_{\widetilde{M}_{N'}}^{(i)} & \Delta N_{\xi_1\widetilde{M}_1}^{(i)} & \cdots & \Delta N_{\xi_N\widetilde{M}_{N'}}^{(i)} & \Delta N_{\widetilde{M}_1\widetilde{M}_1}^{(i)} & \cdots & \Delta N_{\widetilde{M}_N\widetilde{M}_{N'}}^{(i)} \\ \vdots & & \vdots & \vdots & & \vdots & \vdots & & \vdots & \vdots & & \vdots \\ N_{\xi_1}^{(N^{\mathrm{C}})} & \cdots & N_{\xi_N}^{(N^{\mathrm{C}})} & N_{\widetilde{M}_1}^{(N^{\mathrm{C}})} & \cdots & N_{\widetilde{M}_{N'}}^{(N^{\mathrm{C}})} & \Delta N_{\xi_1\widetilde{M}_1}^{(i)} & \cdots & \Delta N_{\xi_N\widetilde{M}_{N'}}^{(N^{\mathrm{C}})} & \Delta N_{\widetilde{M}_1\widetilde{M}_1}^{(N^{\mathrm{C}})} & \cdots & \Delta N_{\widetilde{M}_N\widetilde{M}_{N'}}^{(N^{\mathrm{C}})} \end{bmatrix}$$

where the superscript indices in parenthesis denote the index of the calculation. By applying the (pseudo)-inverse matrix on the energy vector yield an estimation for ε^{B}. Similarly, we might expand $E_{\mathrm{GB}}^{X\to\widetilde{M}} - E_{\mathrm{GB}}$, for which in our case $N^{\mathrm{C}} = 750$ (five solutes times five SQS times 30 sites per SQS) calculations are available, to arrive at an estimate for $\varepsilon^{\mathrm{GB}}$. As for both the bulk and the GB cases, Eq. (7.33) is over-determined, Eq. (7.32) can be used to inversely predict the energies for the interaction vector $\mathbf{J}$ to verify our assumptions.

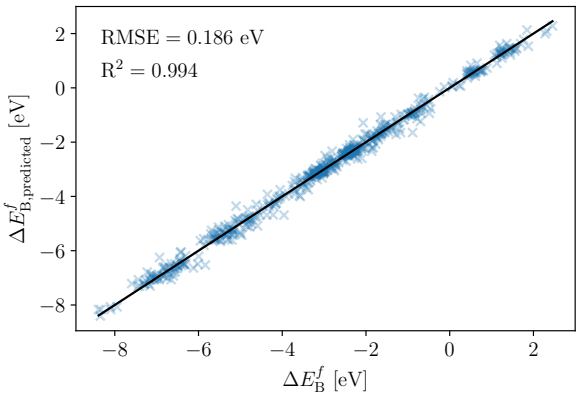

(a) Predicted energy differences $E_{\mathrm{B}}^{X\to\widetilde{M}} - E_{\mathrm{B}}$ for all bulk calculation using $\mathbf{J}_{\mathrm{B}}$

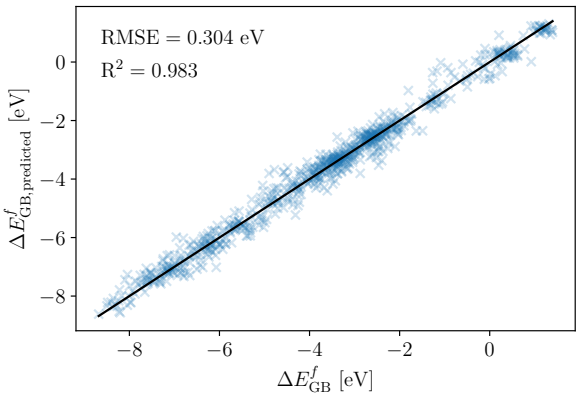

(b) Predicted energy differences $E_{\mathrm{GB}}^{X\to\widetilde{M}} - E_{\mathrm{GB}}$ for all GB calculation using $\mathbf{J}_{\mathrm{GB}}$

Figure 7.9: Actual energy versus the predicted energy using a simple pair-interaction model for bulk and GB calculations.

Figures 7.9a and 7.9b show the deviation of the difference in energies when expanding it as a linear sum of the interaction parameters $\mathbf{J}_{\mathrm{B}}$ and $\mathbf{J}_{\mathrm{GB}}$. The predicted energies are plotted against the calculated ones. The deviations originate of two main reasons. Firstly the pair interaction energy is a function of the distance between two atoms. On a perfect lattice, the nearest neighbor distance is constant for all pairs, which is not the case for our relaxed models, where the pair distances are smeared out (see Fig. 6.2). Secondly, taking into account only nearest neighbor pairs is a simplification that neglects pairs at larger distances as well as multi-body terms. The first shortcoming explains why we find from Fig. 7.9 a smaller

deviation for the bulk case (RMSE = 0.186 eV) than for the GB case (RMSE = 0.304 eV): The distribution of first-neighbor distances is broader in the relaxed GB structures. This is firstly, due to the inherent structural complexity of the GB resulting in a broader distribution of first neighbor distances. Secondly, stronger local relaxations at the disordered GB will broaden the distribution even further.

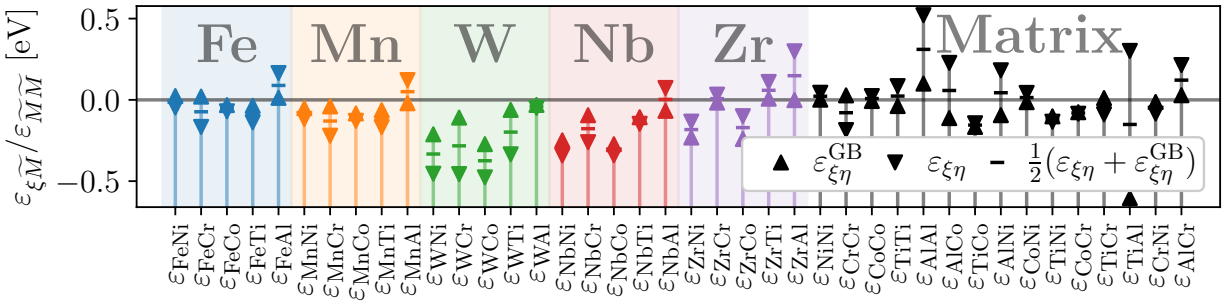

Figure 7.10: Computed pair interaction energies at the GB (upright triangles) and in the bulk (downwards pointing triangle). Colored interaction energies are solute-matrix interaction $\varepsilon_{\xi\widetilde{M}}$, where black symbols represent matrix-matrix type interaction energies $\varepsilon_{\widetilde{MM}}$.

Figure 7.10 shows the values of the pair interaction energies for all occurring interactions in our model system. The values for the bulk and GB interaction are represented by upright and inverted triangles. The horizontal bar refers to the mean value of the interaction. Focusing on the solute atoms (colored blocks) reveals that for across all solutes the interaction with Al is the weakest one (always the last entry in the colored blocks). Additionally, we find weaker solute-matrix interactions for Fe and Mn than for W and Nb. Furthermore, Fig. 7.10 confirms that Guttmann's assumption of $\varepsilon^{\mathrm{GB}} \simeq \varepsilon^{\mathrm{B}}$ is justified, the values are similar for most of the interactions. Except for the solute-matrix interactions of W (green block), we find a larger discrepancy between the bulk and GB interaction parameters. Finally, we observe the largest differences for interaction containing aluminum, e.g., $\varepsilon_{\mathrm{ZrAl}}$, $\varepsilon_{\mathrm{AlAl}}$, $\varepsilon_{\mathrm{AlCo}}$, $\varepsilon_{\mathrm{AlNi}}$ with the largest deviation of ≈ 0.8 eV for $\varepsilon_{\mathrm{TiAl}}$. Due to the low amounts of Ti and Al in our models, it is much more unlikely to (re)form Ti–Al than e. g. Ni–Cr bonds. Consequently the ΔN_{TiAl} term will be nonzero only rarely in $\mathbf{\Pi}$, leading to bad estimates for those interaction parameters.

While we have given the theoretical foundation for our modified Guttmann model in Sec. 7.2.5 and estimated the necessary (interaction) parameters for our multi-component systems in the previous section, we have not implemented a solver for Eq. (7.28). It would be interesting to compare the mod. Guttmann model with the McLean, as it takes into account solute-matrix interactions. As the segregation energy spectrum, therefore, becomes a function of the matrix elements, tungsten would be an interesting candidate for comparison, due to its strong interaction with the matrix.

7.3 Outlook

Besides the fact that the numerical solution of the coupled isotherms of the modified Guttmann model are to be computed, we want to point the reader's attention to several other research topics that will complement the present studies. First of all, one might go beyond the dilute limit in the multi-component system. However, as this is a computationally demanding task already in a pure system, using first-principle methods only a few selected solutes might be studied in a disordered system. Secondly, solute-solute interaction might also impact the segregation behavior, which is also the reason why Guttmann's model exists at all, namely to study the co-segregation of phosphorous in iron. Similarly, exploring such solute-solute interactions in a disordered matrix is highly non-trivial and computationally expensive. Finally, and probably the most important feature of the microstructure of Ni-base alloys is the γ' phase. Hence, to fully understand a solute's behavior it is crucial to know also its phase preferences (matrix of γ'). Interestingly, due to the disorder in the matrix, also the phase preference, needs a spectrum-based treatment in contrast to a pure system where a single scalar value is sufficient. However accessing the thermodynamics of the $L1_0$ γ'-phase is again computationally demanding without prior knowledge from experiments, due to the two different sublattices.

Additional activities

List of publications

First author publications

1. **D. Gehringer** , L. Huber, J. Neugebauer & D. Holec . "Segregation to α_2/γ interfaces in TiAl alloys: A multiscale QM/MM study". *Physical Review Materials*, **7** (6), (2023), DOI: 10.1103/physrevmaterials.7.063604

   Abstract: In this study we present an implementation of a coupled multiscale quantum mechanics/molecular mechanics approach well suited for studying compositionally rich extended defects. Our focus is on interfacial phenomena of α_2/γ phase boundaries in intermetallic TiAl alloys. We prove that our implementation is capable of accurately reproducing site-preference energies of solutes reported by previous density functional theory studies. To properly study segregation phenomena, we developed a formalism for segregation energies in systems with two sublattices (Ti and Al). Our model provides predictions consistent with atom probe tomography measurements reported in literature for a large number of solute atoms

   Parts of Chap. 4 are based on this publication.

2. D. Gehringer, M. Friák, D. Holec: "Models of configurationally-complex alloys made simple". *Comput. Phys. Commun.*, **286**, 108664 (2023). DOI: 10.1016/j.cpc.2023.108664

   Abstract: We present a Python package for the efficient generation of special quasi-random structures (SQS) for atomic-scale calculations of disordered systems. Both, a Monte-Carlo approach or a systematic enumeration of structures can be used to carry out optimizations to ensure the best optimal configuration is found for given cell size and composition. We present a measure of randomness based on Warren-Cowley short-range order parameters allowing for fast analysis of atomic structures. Hence, optimal structures are found in a reasonable time for

several dozens or even hundreds of atoms. Both SQS optimizations and analysis of structures can be carried out via a command-line interface or a Python API. Additional features, such as optimization towards partial ordering or independent sublattices allow the generation of atomistic models of modern complex materials. Moreover, hybrid parallelization, as well as distribution of vacancies, are supported. The output data format is compatible with ase, pymatgen and pyiron packages to be easily embeddable in complex simulation workflows.

Parts of Chap. 5 are based on this publication.

3. **D. Gehringer**, T. Dengg, M. N. Popov, D. Holec: "Interactions between a H_2 Molecule and Carbon Nanostructures: A DFT Study". *C — Journal of Carbon Research*, **6** (1), 16 (2020). DOI: 10.3390/c6010016

Abstract: On a long path of finding appropriate materials to store hydrogen, graphene and carbon nanotubes have drawn a lot of attention as potential storage materials. Their advantages lie at hand since those materials provide a large surface area (which can be used for physisorption), are cheap compared to metal hydrides, are abundant nearly everywhere, and most importantly, can increase safety to existing storage solutions. Therefore, a great variety of theoretical studies were employed to study those materials. After a benchmark study of different van-der-Waals corrections to Generalized Gradient Approximation (GGA), the present Density Functional Theory (DFT) study employs Tkatchenko–Scheffler (TS) correction to study the influence of vacancy and Stone–Wales defects in graphene on the physisorption of the hydrogen molecule. Furthermore, we investigate a large-angle (1,0) grain boundary as well as the adsorption behaviour of Penta-Octa-Penta (POP)-graphene.

Co-authored publications

1. I. Spacil, D. Gehringer, D. Holec, M. Albu, J. Li: "Elucidating effects of Eu and P on solidification and precipitation of Al-7Si-0.3Mg based alloys refined by Ta and stochiometric Al-Ti-B". submitted to *Journal of Alloys and Compounds* – under review

Abstract Effects of Eu (up to 500 ppm) and P (up to 40 ppm) on solidification and precipitation of Al-7Si-0.3Mg based alloys refined by solute Ta (0.12wt.%) and stochiometric Al-2.2Ti-1B grain refiner was investigated using optical microscopy, differential scanning calorimetry (DSC) scanning electron microscopy (SEM) and transmission electron microscopy (TEM) as well as density functional theory (DFT) calculations. It was found that (i) solute Ta can refine α-Al grains and is unaffected by the addition of Eu and/or P. (ii) 200 ppm Eu is enough to

modify eutectic Si although its modification effect can be enhanced with higher Eu additions (up to 500 ppm). (iii) A high P concentration (40 ppm) counteratcs the modification effect in the alloy modified with 200 ppm Eu and therefore unmodified structure is obtained. (iv) Even with the addition of Eu and P, the activation energy of stable β-Mg2Si is calculated to be very low (60-70 kJ/mol), indicating a short time for complete precipitation of β-precipitates. (v) One possible nucleation sequence in Al-Si-Mg based alloys modified with Eu has been proposed to be $Mg_3P_2 \rightarrow$ EuP $\rightarrow$ Al2Si2Eu based on the lattice mismatch calculation and thermodynamic stability. (vi) DFT calculations suggest that Eu is energetically favourable for TPRE growth mechanism, which is also true for other chemical modifiers (Ca, Na, Sr, Y and Yb). The present investigation provides new insights into controlling solidification (mainly for the grain refinement of primary Al and eutectic grains) and precipitation (mainly for β-MgSi precipitate) of Al-7Si-0.3Mg based alloys via the addition of Ta as a refiner of α-Al and Eu as a modifier of eutectic Si.

Contribution: I have contributed, during discussions on how to interpret the calculation results. I helped to design the study of the computational part. Moreover I have carried out parts DFT calculations and supplied the models.

2. Y.W. Sun, D. Holec, D. Gehringer, L. Li, O. Fenwick, D.J. Dunstan, C.J. Humphreys: "Graphene on silicon: Effects of the silicon surface orientation on the work function and carrier density of graphene". *Phys. Rev. B Condens. Matter*, **105** (16), 165416 (2022). DOI: 10.1103/PhysRevB.105.165416

Abstract: Density functional theory has been employed to study graphene on the (111), (100), and (110) surfaces of bare silicon (Si) substrates, which provide three different densities of surface atoms. There are several interesting findings. First, carbon atoms in graphene can form covalent bonds with Si atoms, when placed close enough on Si (111) and (100) surfaces, but not on the (110) surface. The Si (111) surface shifts the Fermi level of graphene into its conduction band, resulting in an increase of the electron density by three orders of magnitude. The work function of graphene is increased by 0.29 eV on the (111) surface, likely due to the surface dipole from the redistribution of π orbitals. The change in the number of available states below the Fermi level of graphene due to its interaction with the Si surface, is the main cause for the unconventional doping reported in this paper. The electron density can also be increased by eighty times on a Si (100) substrate without the shift of Fermi level, which is another clear example of the proposed doping mechanism. These striking effects that different orientations of a silicon substrate can have on the properties of graphene are related to the

surface atom density of the substrate. These results provide valuable guidance to the growth of graphene on Si for various purposes for electronic devices.

Contribution: I have contributed, during discussions on how to interpret the calculation results. Moreover I have carried out the DFT calculations

3. F. Schmid, **D. Gehringer**, T. Kremmer, L. Cattini, P.J. Uggowitzer, D. Holec, S. Pogatscher: "Stabilization of Al_3Zr allotropes in dilute aluminum alloys via the addition of ternary elements". *Materialia*, **21**, 101321 (2022).
DOI: 10.1016/j.mtla.2022.101321

Abstract: The formation of Al_3Zr particles within dilute aluminum alloys can contribute effectively to controlling microstructure evolution and enhancing material properties. However, the possible transformation of Al_3Zr from its initial metastable crystal structure $L1_2$ into its stable, tetragonal structure $D0_{23}$ is associated with faster coherency loss and the coarsening of Al_3Zr particles. In this regard, our study aims at identifying ternary elements that can disrupt this mechanism. For this purpose, nine ternary Al-Zr-X alloys (Er, Sc, Hf, Y, Nb, Mn, Cu, Zn and Si) plus a base alloy (Al-Zr) were produced. Isochronal aging was performed at 475 °C and 550 °C, and an investigation of the particle landscape was carried out by STEM and HR-TEM. In parallel, we conducted ab initio calculations to investigate fundamental properties of ternary AlZrX-particles such as substitution likeliness, heat of formation and transformation mechanisms. The elements investigated show various behaviors. Fewer than half of the elements (Er, Sc, Hf and Si) are found to be incorporated into Zr-rich particles to any large extent; Er and Sc exhibit the well-known core-shell structure. Y and Zn do not interfere at all with the precipitation process. Nb, Mn and Cu form particles on their own, with Zr particles often attached to them. Concerning crystal structures, all element additions except for Y and Si widen the stability regime of $L1_2$.

Contribution: I have contributed, the design of the study for the computational part of the paper. Furthermore, the calculations the evaluations and the plotting of the figures in the respective chapter.

4. Y.W. Sun, **D. Gehringer**, D. Holec, D.G. Papageorgiou, O. Fenwick, S.M. Qureshi, C.J. Humphreys, D.J. Dunstan: "Significant interlayer coupling in bilayer graphene and double-walled carbon nanotubes: A refinement of obtaining strain in low-dimensional materials". *Phys. Rev. B Condens. Matter*, **105** (2), 024103 (2022).
DOI: 10.1103/PhysRevB.105.024103

Abstract: This paper solves a longstanding debate: Raman measurements on double-walled carbon nanotubes appear to show that significantly more pressure than

expected can be transmitted to the inner tube. We reinterpret those Raman spectra consistently reported in the literature, by assigning the Raman peaks to coupled vibrational modes of both walls, instead of individual contributions from the inner and outer tubes. These coupled vibrational modes are important for the correct interpretation of the Raman shift from strained layered 2D materials (we demonstrate it on bilayer graphene as an example), for researching the mechanical properties, thermal expansion, and strain engineering of two-dimensional materials.

Contribution: I have provided the calculations and evaluations for the figures in Sec. B.

5. D. Holec, N. Abdoshahi, **D. Gehringer**, L. Hatzenbichler, A. Sakic, H. Clemens: "Electrons meet alloy development: a γ-TiAl-based alloys showcase". *Adv. Eng. Mater.*, (2021). DOI: 10.1002/adem.202100977

Abstract: Density functional theory is a workhorse of present electronic structure calculations. These are increasingly more applied in materials science as they allow for insight beyond experimental capabilities, testing hypotheses, or isolating various phenomena. Herein, an overview of the applications of the electronic structure calculations applied to extracting alloying trends, which, in turn, leads to refining of alloys, is presented. The topic covers the construction of structural models by properly considering site preference. Next are discussed alloying trends in structural and mechanical properties. The final part deals with microstructure features such as extended defects or multi-phase constitutions. The unifying themes of the presented application are compositional trends in properties of lightweight intermetallic γ-TiAl-based alloys

Contribution: I have provided, the methodology and the data for Sec. 2.1 of the publication

6. Y. W. Sun, D. Holec, D. Gehringer, O. Fenwick, D. J. Dunstan, C. J. Humphreys: "Erratum: Unexpected softness of bilayer graphene and softening of A-A stacked graphene layers [Phys. Rev. B 101, 125421 (2020)]". *Phys. Rev. B Condens. Matter*, **103** (11), 119901 (2021). DOI: 10.1103/PhysRevB.103.119901

Contribution: I have performed the calculations presented in the erratum. Moreover, I have found the error which lead to the publication of this correction. Finally I have also written a small section, explaining the technical details which needed to correct the error.

7. M. N. Popov, T. Dengg, **D. Gehringer**, D. Holec: "Adsorption of H2 on Penta-Octa-Penta Graphene: Grand Canonical Monte Carlo Study". *C — Journal of Carbon Research*, **6** (2), 20 (2020). DOI: 10.3390/c6020020

   Abstract: In this paper, we report the results of hydrogen adsorption properties of a new 2D carbon-based material, consisting of pentagons and octagons (Penta-Octa-Penta-graphene or POP-graphene), based on the Grand-Canonical Monte Carlo simulations. The new material exhibits a moderately higher gravimetric uptake at cryogenic temperatures (77 K), as compared to the regular graphene. We discuss the origin of the enhanced uptake of POP-graphene and offer a consistent explanation.

   Contribution: I have contributed the pair-potential with which the study was conducted.

8. Y. W. Sun, D. Holec, **D. Gehringer**, O. Fenwick, D. J. Dunstan, C. J. Humphreys: "Unexpected softness of bilayer graphene and softening of A-A stacked graphene layers". *Phys. Rev. B Condens. Matter*, **101** (12), 125421 (2020).
   DOI: 10.1103/PhysRevB.101.125421

   Abstract: Density functional theory has been used to investigate the behavior of the π electrons in bilayer graphene and graphite under compression along the c axis. We have studied both conventional Bernal (A-B) and A-A stackings of the graphene layers. In bilayer graphene, only about 0.5 % of the π-electron density is queezed through the sp^2 network for a compression of 20 %, regardless of the stacking order. However, this has a major effect, resulting in bilayer graphene being about six times softer than graphite along the c axis. Under compression along the c axis, the heavily deformed electron orbitals (mainly those of the π electrons) increase the interlayer interaction between the graphene layers as expected, but, surprisingly, to a similar extent for A-A and Bernal stackings. On the other hand, this compression shifts the in-plane phonon frequencies of A-A stacked graphene layers significantly and very differently from the Bernal stacked layers. We attribute these results to some sp^2 electrons in A-A stacking escaping the graphene plane and filling lower charge-density regions when under compression, hence, resulting in a nonmonotonic change in the sp^2-bond stiffness.

   Contribution: I have performed the calculations presented in the paper, performed parts of the evaluation. Furthermore, I tried to help throughout various discussions.

Appendix

.1 Thermodynamic limits of the difference of the chemical potentials

.1.1 for the α_2-bulk phase

The thermodynamic limits for the α_2 phase, which is bordered by the α-Ti with ≈ 6 at %. Al, and the γ-TiAl phase. As the α-Ti with Al is a solid solution we have calculated the energy of five different optimized special quasirandom [215] (SQS) structures. Those (SQS) structures' pair-correlations were optimized by systematically probing all possible ($25.6 \cdot 10^6$) atomic arrangements using the *sqsgenerator* package [217]. Each cell having 81 ($3 \times 3 \times 3$-supercell) atoms from which five were aluminum (6.17 at %. Al). For α-Ti and α_2-Ti_3Al to coexist we require

$$\frac{\bar{E}^{\alpha}_{\mathrm{SQS}}}{9} = \frac{5}{81}\mu^{\mathrm{Al}} + \frac{76}{81}\mu^{\mathrm{Ti}} \tag{36}$$

$$E^{\alpha_2} = 3\mu^{\mathrm{Ti}} + \mu^{\mathrm{Al}}\,. \tag{37}$$

Therefore we obtain the lower limit

$$\Delta\mu_{\alpha/\alpha_2} = \mu^{\mathrm{Ti}}_{\alpha/\alpha_2} - \mu^{\mathrm{Al}}_{\alpha/\alpha_2} = \frac{1}{61}\left(36E_{\alpha} - 81E_{\alpha_2}\right). \tag{38}$$

Similarly for the upper thermodynamic limit (γ-TiAl), from requiring

$$E^{\gamma} = \mu^{\mathrm{Ti}} + \mu^{\mathrm{Al}} \tag{39}$$

$$E^{\alpha_2} = 3\mu^{\mathrm{Ti}} + \mu^{\mathrm{Al}} \tag{40}$$

we get analogously

$$\Delta\mu_{\alpha_2/\gamma} = \mu^{\mathrm{Ti}}_{\alpha_2/\gamma} - \mu^{\mathrm{Al}}_{\alpha_2/\gamma} = E^{\alpha_2} - 2E^{\gamma} \tag{41}$$

.1.2 for the γ-bulk phase

The γ-TiAl phase is, for lower Al contents bordered by the α_2-Ti_3Al phase in is hence given by Eq.41. For higher aluminum contents the γ-phase field borders the h-$TiAl_2$. Again, for both phases to co-exist

$$E^{h} = \mu^{\mathrm{Ti}} + 2\mu^{\mathrm{Al}} \tag{42}$$

$$E^{\gamma} = \mu^{\mathrm{Ti}} + \mu^{\mathrm{Al}} \tag{43}$$

from which we obtain

$$\Delta\mu_{\gamma/h} = \mu^{\mathrm{Ti}}_{\gamma/h} - \mu^{\mathrm{Al}}_{\gamma/h} = 3E^{\gamma} - 2E^{h} \tag{44}$$

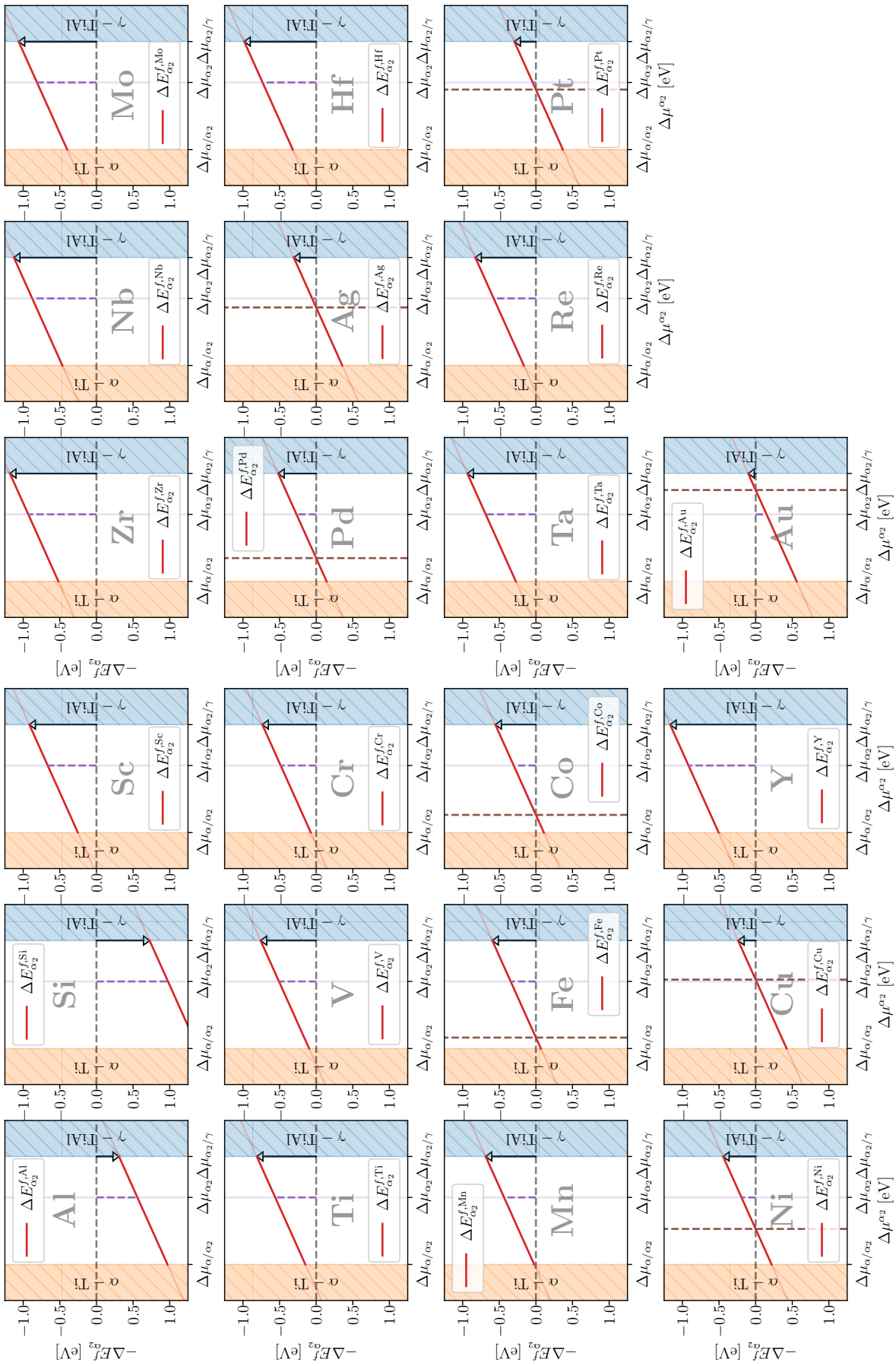

Figure .11: Point defect phase diagram for different solutes in the α_2 phase. The x-axis shows the $\Delta\mu_{\alpha_2}$ as calculated in .1.1

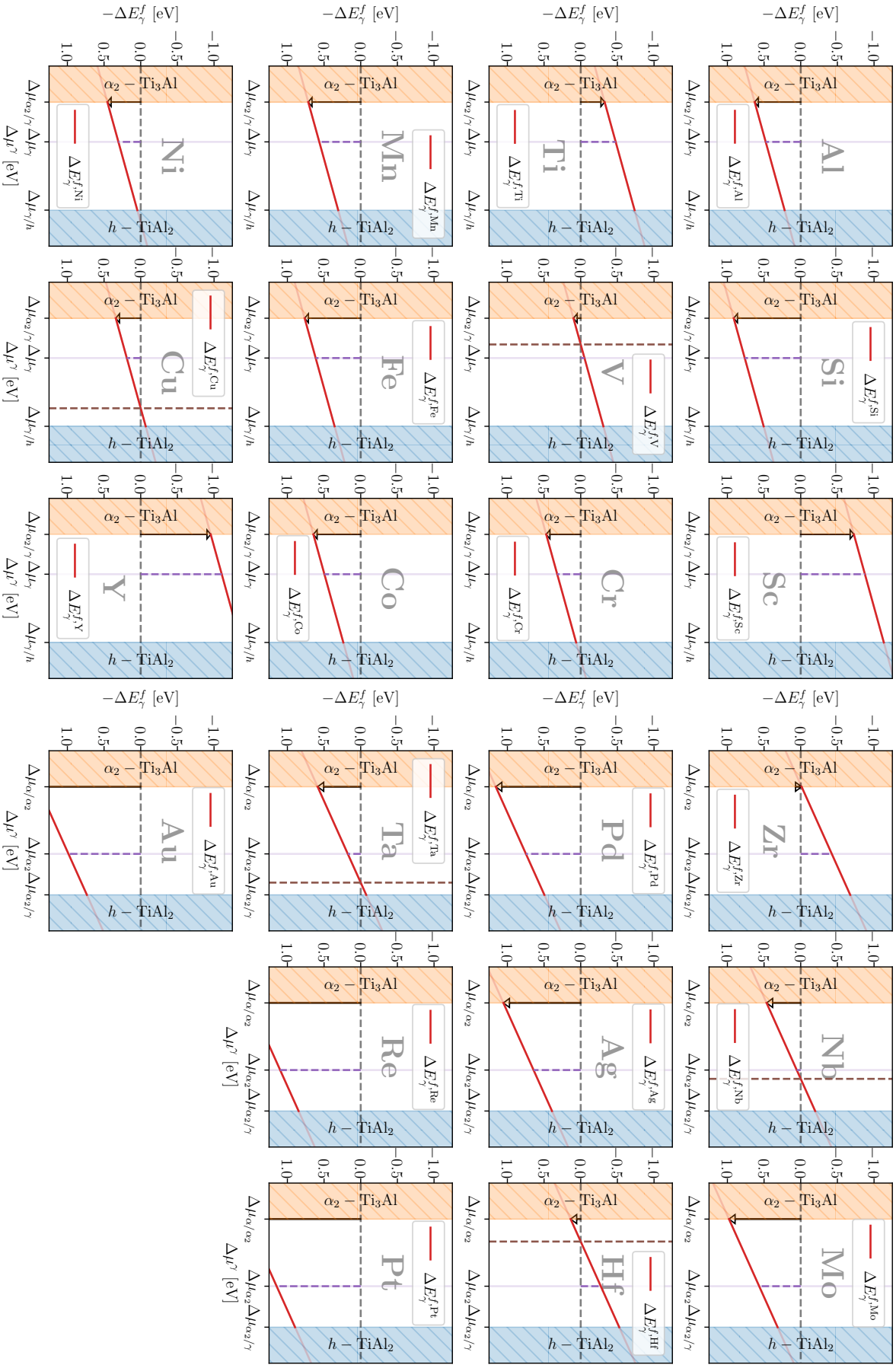

Figure .12: Point defect phase diagram for different solutes in the γ phase. The x-axis shows the $\Delta\mu_\gamma$ as calculated in .1.2

.2 Fits for mechanical properties of TiAl interfaces

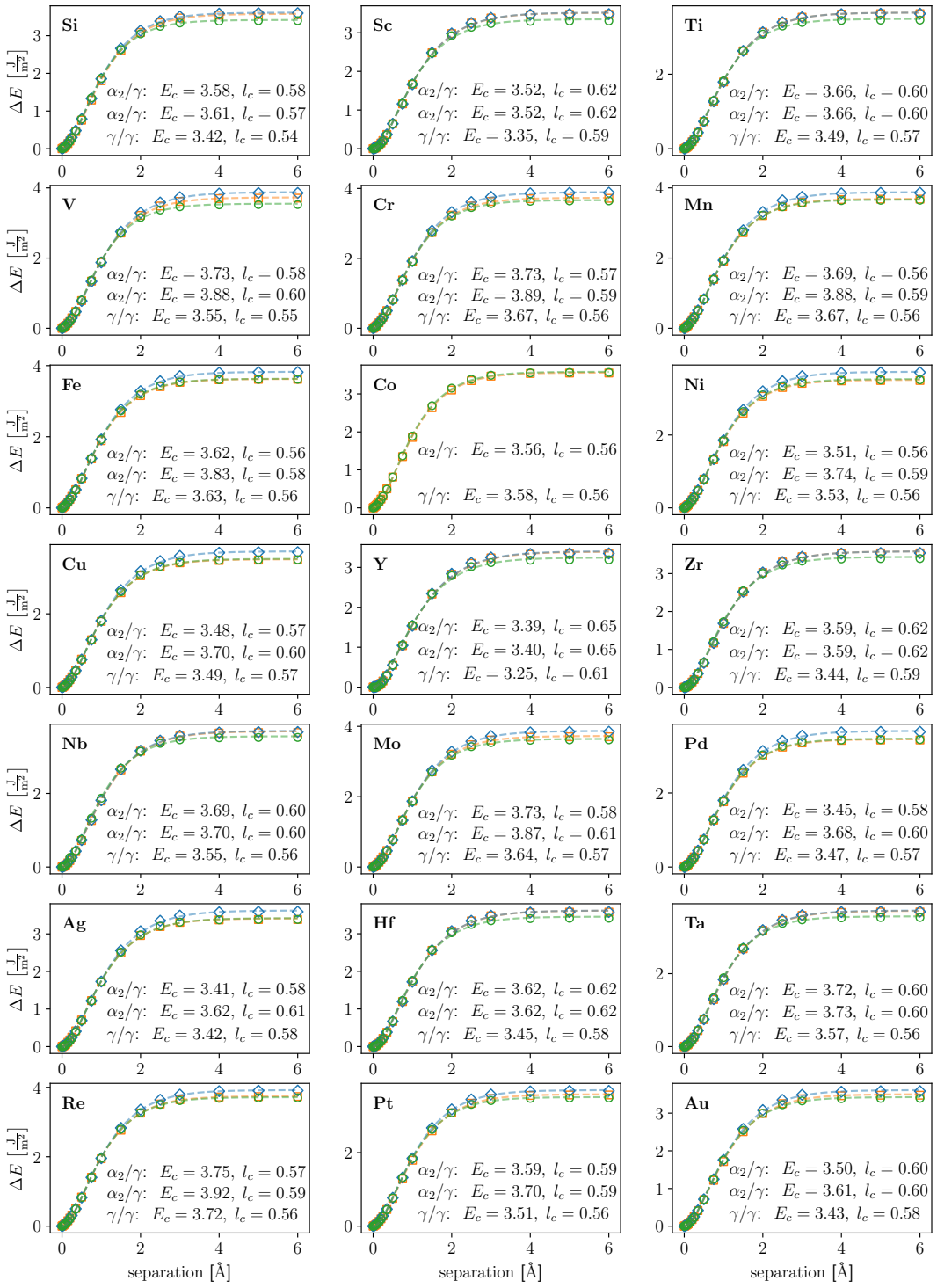

Figure .13: Fit of the universal binding-energy relation [199] for the screened solutes at the γ/γ interface. The x-axis refers to the vacuum-separation.

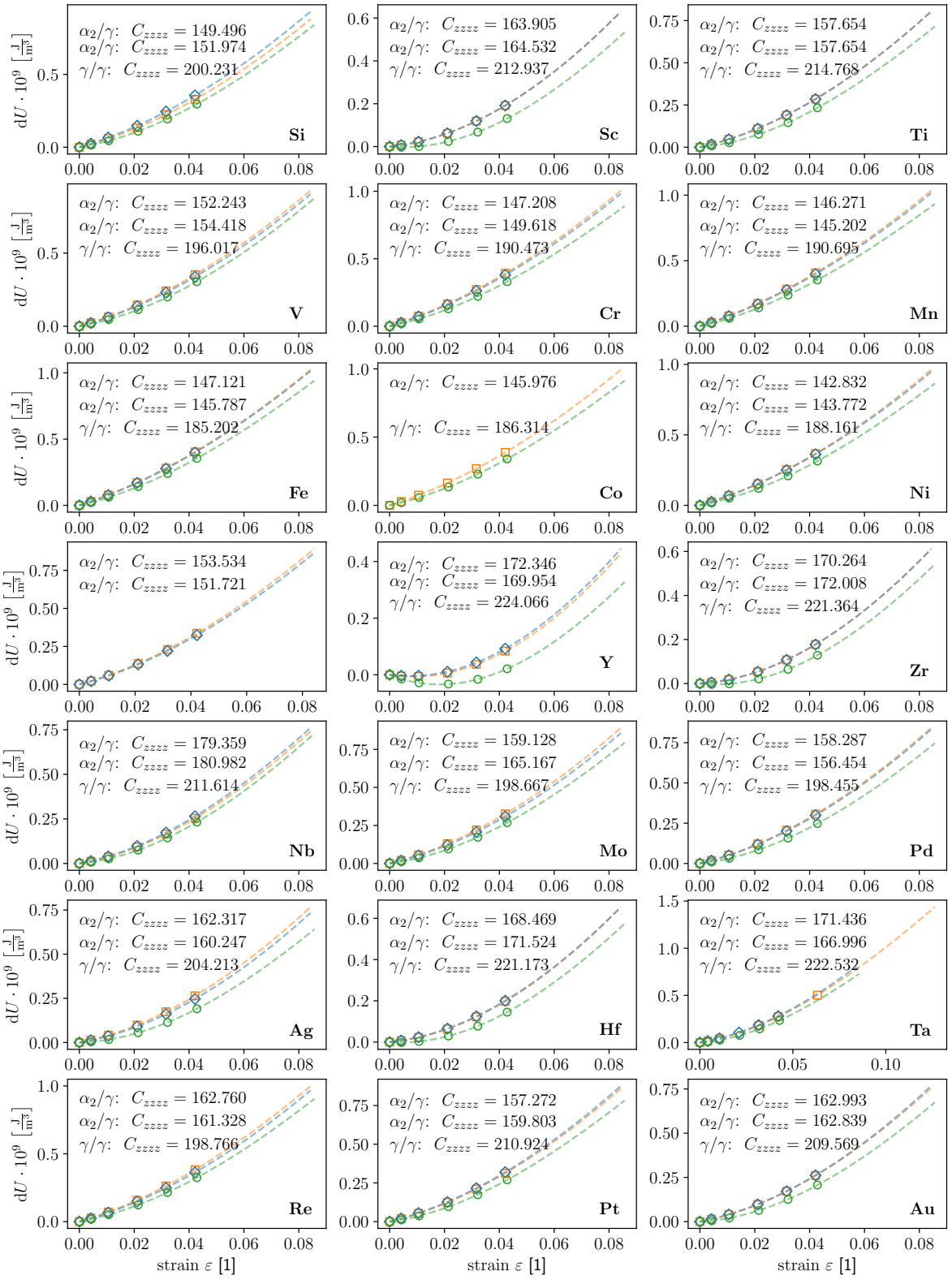

Figure .14: Fits for the estimation of the directional Young's modulus of the $\gamma(111)/\gamma(111)$ interface, into the direction perpendicular to the interface direction. Five discrete datapoints were used to estimate the elastic constants $\frac{U}{V_0} = \frac{1}{2} C_{zzzz} \varepsilon_{zz}^2$.

.3 Amendments to energy of grain boundary spectra

.3.1 Linear fit to extract enthalpy and entropy of segregation

While it may not be visible to the reader, all McLean isotherms (Figs. 7.7, 7.8, .16, .17, .18 and .19) presented exhibit a temperature range from 50 to 2500 K. This is because for very low temperatures finite sized (in terms of bits) floating point arithmetic reaches its accuracy limit. Furthermore, Figs. 7.7 and 7.8 present ΔG_{eff} as a function of temperature accompanied by a linear fit. However, for Fe, Mn and also W we find a strong non-linear behaviour of the effective segregation energy for high temperatures. To tackle this issue we have manually fixed the temperature range for which the linear fit to extract ΔH and ΔS is carried out. For all solutes the lower border is $T_{\text{min}} = 50$ K, while the upper border for Fe and Mn is $T_{\text{max}}^{\text{Fe}} = T_{\text{max}}^{\text{Mn}} = 750$ K. For W we have used $T_{\text{max}}^{\text{Fe}} = 1250$ K. Finally for Nb and Zr the upper limits are $T_{\text{max}}^{\text{Nb}} = T_{\text{max}}^{\text{Zr}} = 2000$ K. We note that for Fig. 7.8 we keep the temperature ranges constant when varying the bulk concentration X^{B}.

Impact of skew-normal distribution parameters on ΔG_{eff}

In the following we want to study the impact of the skew-normal distribution parameters, μ, σ X^{B} and α on the temperature dependence of ΔG_{eff} We begin to obtain an analytic expression for the concentration averaged isotherm $\left\langle \hat{X}^{\text{GB}} \right\rangle$. By substituting Eqs. (7.8) and (7.15) in Eq. (7.13) we obtain

$$\left\langle \hat{X}^{\text{GB}} \right\rangle = \frac{1}{\sigma\sqrt{2\pi}} \int_{-\infty}^{\infty} \frac{\exp\left(-\frac{(u-\mu)^2}{2\sigma^2}\right) \operatorname{erfc}\left(-\frac{\alpha(u-\mu)}{\sqrt{2\sigma^2}}\right)}{1 + \frac{1-X^{\text{B}}}{X^{\text{B}}} \exp\left(-\frac{x}{k_b T}\right)} \mathrm{d}u \,. \tag{45}$$

As best to our knowledge there is no solution in terms of elementary functions when plugging the above averaged isotherm into Eq. (7.16). Therefore, Figs. .16 – .19 show averaged McLean isotherms and effective segregation energies, for hypothetical energy spectra. Each figure presents isotherms are for the variation of a different parameter.

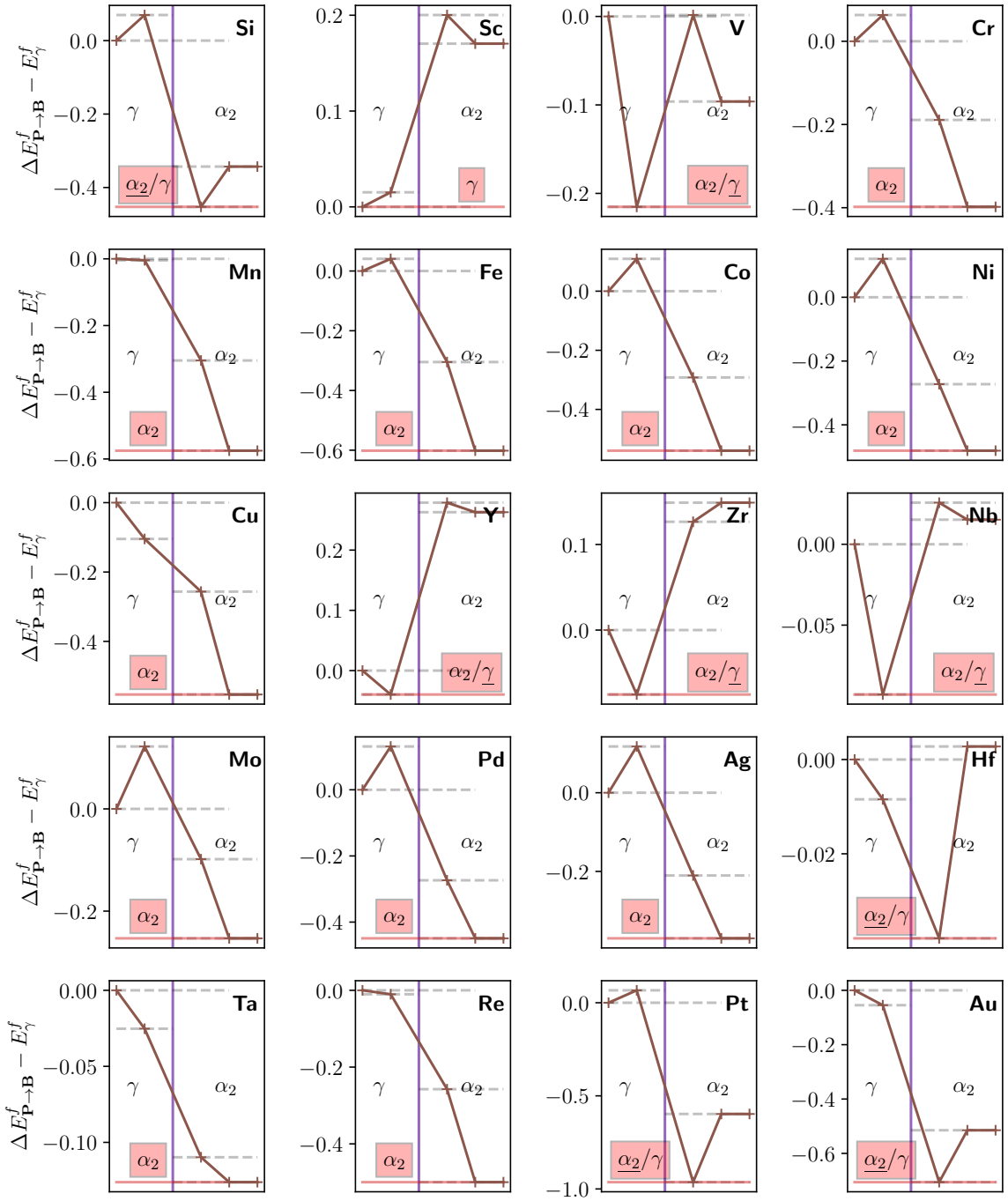

Figure .15: Segregation energies (Eqs. (5.8)-(5.10)) are shown in reference to E^f_γ. The purple line represents the α_2/γ interface. In each plot, the x-axis represents the states of the solute in γ-bulk (very left), at $\alpha_2/\underline{\gamma}$ (left of the purple line), $\underline{\alpha_2}/\gamma$ (right of the purple line) and in the α_2-bulk (very right). The brown line represents the energy difference with respect to E^f_γ.

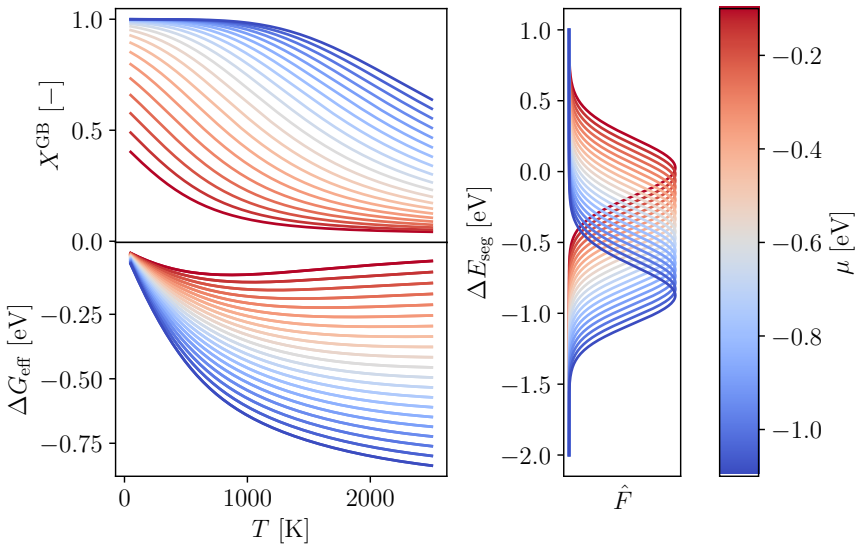

Figure .16: Influence of the variance parameter σ on averaged McLean isotherms (upper panel) and the corresponding effective segregation energy (lower panel). The isotherms are computed for constant $\sigma = 0.25$ eV, $\alpha = 1$, and $X^{\mathrm{B}} = 3.5$ %. μ is varied from -1 to -0.05 eV. The plot on the right shows the corresponding energy spectra.

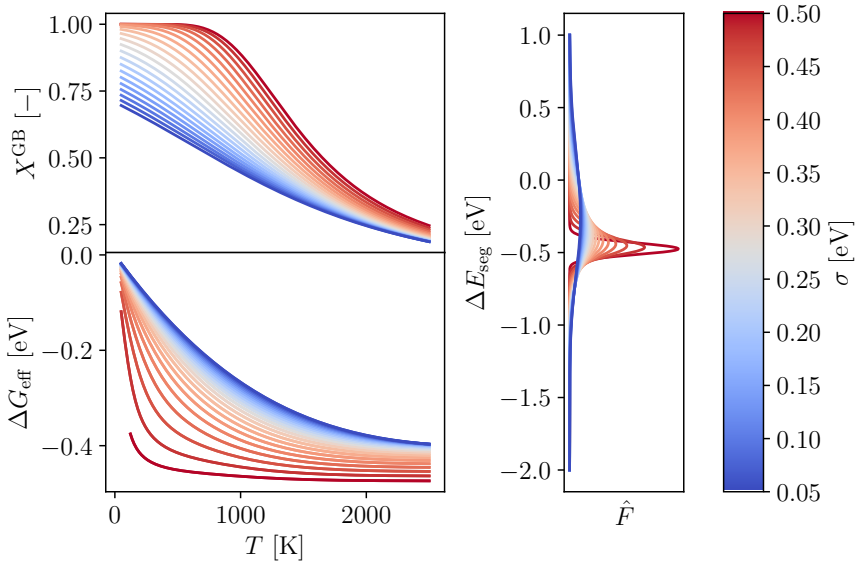

Figure .17: Influence of the skew parameter α on averaged McLean isotherms (upper panel) and the corresponding effective segregation energy (lower panel). The isotherms are computed for constant $\mu = -0.5$ eV, $\alpha = 1$ and $X^{\mathrm{B}} = 3.5$ %. σ is varied from 0.05 to 0.5 eV. The plot on the right shows the corresponding energy spectra.

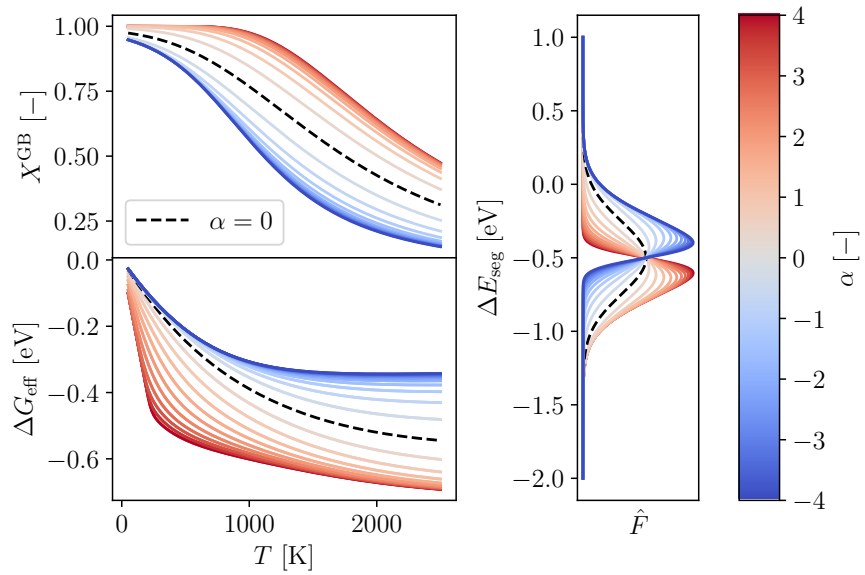

Figure .18: Influence of the variance parameter σ on averaged McLean isotherms (upper panel) and the corresponding effective segregation energy (lower panel). The isotherms are computed for constant $\mu = -0.5$ eV, $\sigma = 0.25$ eV and $X^{B} = 3.5$ %. α is varied from -4 to 4. The plot on the right shows the corresponding energy spectra.

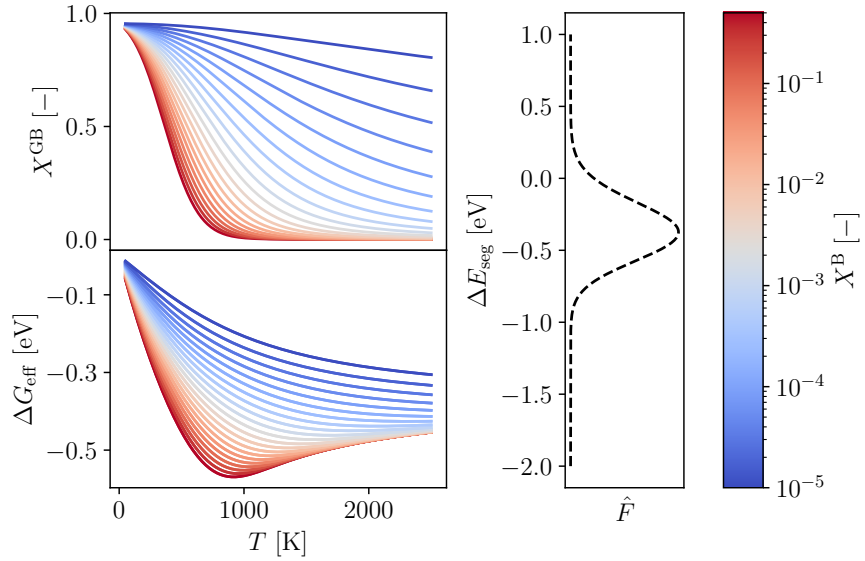

Figure .19: Influence of the bulk solute concentration X^{B} on averaged McLean isotherms (upper panel) and the corresponding effective segregation energy (lower panel). The isotherms are computed for constant $\mu = -0.5$ eV, $\sigma = 0.25$ eV and $\alpha = 1$. X^{B} is varied over several orders of magnitude from $10^{-}5$ to 0.5. The plot on the right shows the corresponding energy spectra.

Bibliography

[1] L. Huber, B. Grabowski, M. Militzer, J. Neugebauer, and J. Rottler, Computational Materials Science **118**, 259 (2016).

[2] M. Born and R. Oppenheimer, Annalen der Physik **389**, 457 (1927).

[3] W. Ritz, Journal für die reine und angewandte Mathematik **135**, 1 (1908).

[4] D. R. Hartree, Mathematical Proceedings of the Cambridge Philosophical Society **24**, 89 (1928).

[5] V. Fock, Zeitschrift für Physik A Hadrons and Nuclei **61**, 126 (1930).

[6] J. C. Slater, Phys. Rev. **81**, 385 (1951).

[7] P. Hohenberg and W. Kohn, Physical Review **136**, B864 (1964).

[8] L. H. Thomas, Mathematical Proceedings of the Cambridge Philosophical Society **23**, 542 (1927).

[9] P. A. M. Dirac, Mathematical Proceedings of the Cambridge Philosophical Society **26**, 376 (1930).

[10] E. Wigner, Physical Review **46**, 1002 (1934).

[11] M. Gell-Mann and K. A. Brueckner, Physical Review **106**, 364 (1957).

[12] J. F. Janak, Physical Review B **18**, 7165 (1978).

[13] R. Stowasser and R. Hoffmann, Journal of the American Chemical Society **121**, 3414 (1999).

[14] A. Savin, C. Umrigar, and X. Gonze, Chemical Physics Letters **288**, 391 (1998).

[15] J. P. Perdew and M. Levy, Physical Review B **56**, 16021 (1997).

[16] J. P. Perdew and A. Zunger, Physical Review B **23**, 5048 (1981), arXiv:0706.3359 .

[17] J. P. Perdew, K. Burke, and M. Ernzerhof, Physical Review Letters **77**, 3865 (1996).

[18] P. J. Stephens, F. J. Devlin, C. F. Chabalowski, and M. J. Frisch, The Journal of Physical Chemistry **98**, 11623 (1994).

[19] J. P. Perdew, J. A. Chevary, S. H. Vosko, K. A. Jackson, M. R. Pederson, D. J. Singh, and C. Fiolhais, Physical Review B **46**, 6671 (1992).

[20] J. Sun, A. Ruzsinszky, and J. Perdew, Physical Review Letters **115** (2015).

[21] D. Mejía-Rodríguez and S. B. Trickey, Physical Review B **102** (2020).

[22] J. Tersoff, Physical Review B **38**, 9902 (1988).

[23] D. W. Brenner, Physical Review B **42**, 9458 (1990).

[24] F. H. Stillinger and T. A. Weber, Physical Review B **31**, 5262 (1985).

[25] M. S. Daw and M. I. Baskes, Physical Review B **29**, 6443 (1984).

[26] M. S. Daw, S. M. Foiles, and M. I. Baskes, Materials Science Reports **9**, 251 (1993).

[27] M. W. Finnis and J. E. Sinclair, Philosophical Magazine A **50**, 45 (1984).

[28] M. I. Baskes, Physical Review B **46**, 2727 (1992).

[29] J. Jung, W. Nishima, M. Daniels, G. Bascom, C. Kobayashi, A. Adedoyin, M. Wall, A. Lappala, D. Phillips, W. Fischer, C.-S. Tung, T. Schlick, Y. Sugita, and K. Y. Sanbonmatsu, Journal of Computational Chemistry **40**, 1919 (2019).

[30] J. R. Chelikowsky and M. L. Cohen, Physical Review B **14**, 556 (1976).

[31] G. B. Bachelet, D. R. Hamann, and M. Schlüter, Physical Review B **26**, 4199 (1982).

[32] D. R. Hamann, M. Schlüter, and C. Chiang, Physical Review Letters **43**, 1494 (1979).

[33] D. Vanderbilt, Physical Review B **41**, 7892 (1990).

[34] P. E. Blöchl, Physical Review B **50**, 17953 (1994).

[35] W. Kohn and L. J. Sham, Phys. Rev. **140**, A1133 (1965).

[36] Y. A. Wang and E. A. Carter, *Theoretical Methods in Condensed Phase Chemistry*, edited by S. D. Schwartz (Springer Netherlands, 2002) pp. 117–184.

[37] G. S. Ho, V. L. Lignères, and E. A. Carter, Computer Physics Communications **179**, 839 (2008).

[38] M. Levy, J. P. Perdew, and V. Sahni, Physical Review A **30**, 2745 (1984).

[39] M. Levy and H. Ou-Yang, Physical Review A **38**, 625 (1988).

[40] B. M. Deb and S. K. Ghosh, International Journal of Quantum Chemistry **23**, 1 (1983).

[41] R. G. Parr and Y. Weitao, *Density-Functional Theory of Atoms and Molecules* (Oxford University Press, 1995).

[42] G. K.-L. Chan, A. J. Cohen, and N. C. Handy, The Journal of Chemical Physics **114**, 631 (2001).

[43] V. Karasiev and S. Trickey, Computer Physics Communications **183**, 2519 (2012).

[44] Y. A. Wang, N. Govind, and E. A. Carter, Physical Review B **60**, 16350 (1999).

[45] C. Huang and E. A. Carter, Physical Review B **81** (2010).

[46] G. S. Ho and E. A. Carter, Journal of Computational and Theoretical Nanoscience **6**, 1236 (2009).

[47] I. Shin and E. A. Carter, Modelling and Simulation in Materials Science and Engineering **20**, 015006 (2011).

[48] M. Chen, L. Hung, C. Huang, J. Xia, and E. A. Carter, Molecular Physics **111**, 3448 (2013).

[49] M. Chen, X.-W. Jiang, H. Zhuang, L.-W. Wang, and E. A. Carter, Journal of Chemical Theory and Computation **12**, 2950 (2016).

[50] J. C. Snyder, M. Rupp, K. Hansen, K.-R. Müller, and K. Burke, Physical Review Letters **108** (2012).

[51] J. Seino, R. Kageyama, M. Fujinami, Y. Ikabata, and H. Nakai, The Journal of Chemical Physics **148**, 241705 (2018).

[52] J. Seino, R. Kageyama, M. Fujinami, Y. Ikabata, and H. Nakai, Chemical Physics Letters **734**, 136732 (2019).

[53] R. Meyer, M. Weichselbaum, and A. W. Hauser, Journal of Chemical Theory and Computation **16**, 5685 (2020).

[54] K. Finzel, The Journal of Chemical Physics **144**, 034108 (2016).

[55] K. Finzel and P. W. Ayers, International Journal of Quantum Chemistry **117**, e25364 (2017).

[56] J. Lehtomäki, I. Makkonen, M. A. Caro, A. Harju, and O. Lopez-Acevedo, The Journal of Chemical Physics **141**, 234102 (2014).

[57] J. J. Mortensen, L. B. Hansen, and K. W. Jacobsen, Physical Review B **71** (2005).

[58] J. Enkovaara, C. Rostgaard, J. J. Mortensen, J. Chen, M. Dułak, L. Ferrighi, J. Gavnholt, C. Glinsvad, V. Haikola, H. A. Hansen, H. H. Kristoffersen, M. Kuisma, A. H. Larsen, L. Lehtovaara, M. Ljungberg, O. Lopez-Acevedo, P. G. Moses, J. Ojanen, T. Olsen, V. Petzold, N. A. Romero, J. Stausholm-Møller, M. Strange, G. A. Tritsaris, M. Vanin, M. Walter, B. Hammer, H. Häkkinen, G. K. H. Madsen, R. M. Nieminen, J. K. Nørskov, M. Puska, T. T. Rantala, J. Schiøtz, K. S. Thygesen, and K. W. Jacobsen, Journal of Physics: Condensed Matter **22**, 253202 (2010).

[59] L. Hung, C. Huang, I. Shin, G. S. Ho, V. L. Lignères, and E. A. Carter, Computer Physics Communications **181**, 2208 (2010).

[60] M. Chen, J. Xia, C. Huang, J. M. Dieterich, L. Hung, I. Shin, and E. A. Carter, Computer Physics Communications **190**, 228 (2015).

[61] W. Mi, X. Shao, C. Su, Y. Zhou, S. Zhang, Q. Li, H. Wang, L. Zhang, M. Miao, Y. Wang, and Y. Ma, Computer Physics Communications **200**, 87 (2016).

[62] P. Golub and S. Manzhos, Computer Physics Communications **256**, 107365 (2020).

[63] X. Shao, K. Jiang, W. Mi, A. Genova, and M. Pavanello, WIREs Computational Molecular Science **11** (2020).

[64] P. Golub, "Conundrum: A program for orbital-free density functional theory calculations," (2020).

[65] P. research group, "Dftpy source code repository," (2022).

[66] S. Boeck, C. Freysoldt, A. Dick, L. Ismer, and J. Neugebauer, Computer Physics Communications **182**, 543 (2011).

[67] E. Hernández and M. J. Gillan, Physical Review B **51**, 10157 (1995).

[68] E. Hernández, M. J. Gillan, and C. M. Goringe, Physical Review B **53**, 7147 (1996).

[69] W. Kohn, Physical Review Letters **76**, 3168 (1996).

[70] S. Ismail-Beigi and T. A. Arias, Physical Review Letters **82**, 2127 (1999).

[71] R. McWeeny, Reviews of Modern Physics **32**, 335 (1960).

[72] D. R. Bowler and T. Miyazaki, Reports on Progress in Physics **75**, 036503 (2012).

[73] S. Goedecker, Reviews of Modern Physics **71**, 1085 (1999).

[74] D. R. Bowler and T. Miyazaki, Journal of Physics: Condensed Matter **22**, 074207 (2010).

[75] J. Aarons, M. Sarwar, D. Thompsett, and C.-K. Skylaris, The Journal of Chemical Physics **145**, 220901 (2016).

[76] L. E. Ratcliff, S. Mohr, G. Huhs, T. Deutsch, M. Masella, and L. Genovese, WIREs Computational Molecular Science **7** (2016).

[77] T. Ozaki, Physical Review B **74** (2006).

[78] Á. Ruiz-Serrano and C.-K. Skylaris, The Journal of Chemical Physics **139**, 054107 (2013).

[79] L. Genovese, A. Neelov, S. Goedecker, T. Deutsch, S. A. Ghasemi, A. Willand, D. Caliste, O. Zilberberg, M. Rayson, A. Bergman, and R. Schneider, The Journal of Chemical Physics **129**, 014109 (2008).

[80] S. Mohr, L. E. Ratcliff, P. Boulanger, L. Genovese, D. Caliste, T. Deutsch, and S. Goedecker, The Journal of Chemical Physics **140**, 204110 (2014).

[81] S. Mohr, M. Eixarch, M. Amsler, M. J. Mantsinen, and L. Genovese, Nuclear Materials and Energy **15**, 64 (2018).

[82] M. Seidl, J. P. Perdew, and S. Kurth, Physical Review Letters **84**, 5070 (2000).

[83] W. A. Hofer, Foundations of Physics **41**, 754 (2010).

[84] T. Pope and W. Hofer, Frontiers of Physics **12** (2017).

[85] S. Gull, A. Lasenby, and C. Doran, Foundations of Physics **23**, 1175 (1993).

[86] C. Doran, A. Lasenby, and S. Gull, Foundations of Physics **23**, 1239 (1993).

[87] W. Gerlach and O. Stern, Zeitschrift für Physik **9**, 349 (1922).

[88] A. Aspect, Nature **398**, 189 (1999).

[89] W. A. Hofer, Frontiers of Physics **7**, 504 (2012).

[90] T. Pope and W. Hofer, Frontiers of Physics **14** (2018).

[91] H. E. Sauceda, S. Chmiela, I. Poltavsky, K.-R. Müller, and A. Tkatchenko, The Journal of Chemical Physics **150**, 114102 (2019).

[92] H. E. Sauceda, M. Gastegger, S. Chmiela, K.-R. Müller, and A. Tkatchenko, The Journal of Chemical Physics **153**, 124109 (2020).

[93] S. Chmiela, H. E. Sauceda, K.-R. Müller, and A. Tkatchenko, Nature Communications **9** (2018).

[94] D. Lu, J. Li, and H. Guo, CCS Chemistry **2**, 882 (2020).

[95] B. C. Sweeny, H. Pan, A. Kassem, J. C. Sawyer, S. G. Ard, N. S. Shuman, A. A. Viggiano, S. Brickel, O. T. Unke, M. Upadhyay, and M. Meuwly, Physical Chemistry Chemical Physics **22**, 8913 (2020).

[96] S. Käser, O. T. Unke, and M. Meuwly, The Journal of Chemical Physics **152**, 214304 (2020).

[97] O. T. Unke, S. Chmiela, H. E. Sauceda, M. Gastegger, I. Poltavsky, K. T. Schütt, A. Tkatchenko, and K.-R. Müller, Chemical Reviews **121**, 10142 (2021).

[98] V. L. Deringer, A. P. Bartók, N. Bernstein, D. M. Wilkins, M. Ceriotti, and G. Csányi, Chemical Reviews **121**, 10073 (2021).

[99] A. V. Shapeev, Multiscale Modeling & Simulation **14**, 1153 (2016).

[100] A. P. Bartók, R. Kondor, and G. Csányi, Physical Review B **87** (2013).

[101] R. Drautz, Physical Review B **99** (2019).

[102] F. Musil, A. Grisafi, A. P. Bartók, C. Ortner, G. Csányi, and M. Ceriotti, Chemical Reviews **121**, 9759 (2021).

[103] C. van der Oord, G. Dusson, G. Csányi, and C. Ortner, Machine Learning: Science and Technology **1**, 015004 (2020).

[104] J. Nigam, S. Pozdnyakov, and M. Ceriotti, The Journal of Chemical Physics **153**, 121101 (2020).

[105] P. J. Steinhardt, D. R. Nelson, and M. Ronchetti, Physical Review B **28**, 784 (1983).

[106] W. Mickel, S. C. Kapfer, G. E. Schröder-Turk, and K. Mecke, The Journal of Chemical Physics **138**, 044501 (2013).

[107] R. Biswas and D. R. Hamann, Physical Review B **36**, 6434 (1987).

[108] R. Kondor, "A novel set of rotationally and translationally invariant features for images based on the non-commutative bispectrum," (2007).

[109] J. Behler, The Journal of Chemical Physics **134**, 074106 (2011).

[110] J. Tersoff, Physical Review B **39**, 5566 (1989).

[111] A. P. Bartók, M. C. Payne, R. Kondor, and G. Csányi, Physical Review Letters **104** (2010).

[112] R. M. Rao, Optical Engineering **29**, 504 (1990).

[113] A. Thompson, L. Swiler, C. Trott, S. Foiles, and G. Tucker, Journal of Computational Physics **285**, 316 (2015).

[114] M. A. Wood and A. P. Thompson, The Journal of Chemical Physics **148**, 241721 (2018).

[115] I. S. Novikov, K. Gubaev, E. V. Podryabinkin, and A. V. Shapeev, Machine Learning: Science and Technology **2**, 025002 (2021).

[116] R. Drautz, M. Fähnle, and J. M. Sanchez, Journal of Physics: Condensed Matter **16**, 3843 (2004).

[117] Y. Lysogorskiy, C. van der Oord, A. Bochkarev, S. Menon, M. Rinaldi, T. Hammerschmidt, M. Mrovec, A. Thompson, G. Csányi, C. Ortner, and R. Drautz, npj Computational Materials **7** (2021).

[118] O. T. Unke and M. Meuwly, Journal of Chemical Theory and Computation **15**, 3678 (2019).

[119] J. Behler and M. Parrinello, Physical Review Letters **98** (2007).

[120] A. Singraber, J. Behler, and C. Dellago, Journal of Chemical Theory and Computation **15**, 1827 (2019).

[121] N. Artrith and A. Urban, Computational Materials Science **114**, 135 (2016).

[122] A. Khorshidi and A. A. Peterson, Computer Physics Communications **207**, 310 (2016).

[123] S. Chmiela, A. Tkatchenko, H. E. Sauceda, I. Poltavsky, K. T. Schütt, and K.-R. Müller, Science Advances **3** (2017).

[124] S. Chmiela, H. E. Sauceda, I. Poltavsky, K.-R. Müller, and A. Tkatchenko, Computer Physics Communications **240**, 38 (2019).

[125] V. Botu and R. Ramprasad, Physical Review B **92** (2015).

[126] V. Botu, R. Batra, J. Chapman, and R. Ramprasad, The Journal of Physical Chemistry C **121**, 511 (2016).

[127] T. D. Huan, R. Batra, J. Chapman, S. Krishnan, L. Chen, and R. Ramprasad, npj Computational Materials **3** (2017).

[128] A. P. Bartók and G. Csányi, International Journal of Quantum Chemistry **115**, 1051 (2015).

[129] R. Jinnouchi, F. Karsai, and G. Kresse, Physical Review B **100** (2019).

[130] R. Jinnouchi, J. Lahnsteiner, F. Karsai, G. Kresse, and M. Bokdam, Physical Review Letters **122** (2019).

[131] R. Jinnouchi, F. Karsai, C. Verdi, R. Asahi, and G. Kresse, The Journal of Chemical Physics **152**, 234102 (2020).

[132] C. R. Trott, S. D. Hammond, and A. P. Thompson, in *Lecture Notes in Computer Science* (Springer International Publishing, 2014) pp. 19–34.

[133] J. E. Sinclair, P. C. Gehlen, R. G. Hoagland, and J. P. Hirth, Journal of Applied Physics **49**, 3890 (1978).

[134] C. Woodward and S. I. Rao, Physical Review Letters **88** (2002).

[135] C. Woodward, D. R. Trinkle, L. G. Hector, and D. L. Olmsted, Physical Review Letters **100** (2008).

[136] S. Rao, C. Hernandez, J. P. Simmons, T. A. Parthasarathy, and C. Woodward, Philosophical Magazine A **77**, 231 (1998).

[137] I. R. MacGillivray and C. A. Sholl, Journal of Physics F: Metal Physics **13**, 23 (1983).

[138] V. K. Tewary, Physical Review B **69** (2004).

[139] M. Ghazisaeidi and D. R. Trinkle, Physical Review E **79** (2009).

[140] J. A. Yasi and D. R. Trinkle, Physical Review E **85** (2012).

[141] M. Ghazisaeidi and D. R. Trinkle, Physical Review B **82** (2010).

[142] X. Zhang, G. Lu, and W. A. Curtin, Physical Review B **87** (2013).

[143] Q. Zhao and R. G. Parr, The Journal of Chemical Physics **98**, 543 (1993).

[144] N. Choly, G. Lu, W. E, and E. Kaxiras, Physical Review B **71** (2005).

[145] P. Grigorev, T. D. Swinburne, and J. R. Kermode, Physical Review Materials **4** (2020).

[146] J. Q. Broughton, F. F. Abraham, N. Bernstein, and E. Kaxiras, Physical Review B **60**, 2391 (1999).

[147] N. Govind, Y. Wang, A. da Silva, and E. Carter, Chemical Physics Letters **295**, 129 (1998).

[148] S. Dapprich, I. Komáromi, K. Byun, K. Morokuma, and M. J. Frisch, Journal of Molecular Structure: THEOCHEM **461-462**, 1 (1999).

[149] T. Vreven, K. Morokuma, Ödön Farkas, H. B. Schlegel, and M. J. Frisch, Journal of Computational Chemistry **24**, 760 (2003).

[150] T. Vreven, K. S. Byun, I. Komáromi, S. Dapprich, J. A. Montgomery, K. Morokuma, and M. J. Frisch, Journal of Chemical Theory and Computation **2**, 815 (2006).

[151] J. Li, J. Wang, Q. Sun, and Y. Jia, Physica B: Condensed Matter **406**, 2767 (2011).

[152] E. Lidorikis, M. E. Bachlechner, R. K. Kalia, A. Nakano, P. Vashishta, and G. Z. Voyiadjis, Physical Review Letters **87** (2001).

[153] Y. Liu, G. Lu, Z. Chen, and N. Kioussis, Modelling and Simulation in Materials Science and Engineering **15**, 275 (2007).

[154] C. Woodward, Materials Science and Engineering: A **400-401**, 59 (2005).

[155] A. Nair, D. Warner, R. Hennig, and W. Curtin, Scripta Materialia **63**, 1212 (2010).

[156] M. Ghazisaeidi and D. Trinkle, Acta Materialia **60**, 1287 (2012).

[157] L. Huber, B. Grabowski, M. Militzer, J. Neugebauer, and J. Rottler, Acta Materialia **132**, 138 (2017).

[158] *pyiron* development team, "pyiron_contrib," `https://github.com/pyiron/pyiron_contrib` (2020).

[159] J. Janssen, S. Surendralal, Y. Lysogorskiy, M. Todorova, T. Hickel, R. Drautz, and J. Neugebauer, Computational Materials Science **163**, 24 (2019).

[160] H. JÓNSSON, G. MILLS, and K. W. JACOBSEN, in *Classical and Quantum Dynamics in Condensed Phase Simulations* (WORLD SCIENTIFIC, 1998).

[161] W. E, W. Ren, and E. Vanden-Eijnden, The Journal of Physical Chemistry B **109**, 6688 (2005).

[162] D. C. Liu and J. Nocedal, Mathematical Programming **45**, 503 (1989).

[163] D. F. Shanno, Mathematics of Computation **24**, 647 (1970).

[164] D. Goldfarb, Mathematics of Computation **24**, 23 (1970).

[165] R. Fletcher, The Computer Journal **13**, 317 (1970).

[166] C. G. Broyden, IMA Journal of Applied Mathematics **6**, 76 (1970).

[167] J. F. Lutsko, Journal of Applied Physics **64**, 1152 (1988).

[168] P. Lucjan, *Ideas of Quantum Chemistry* (Elsevier Science, 2008) p. 620.

[169] F. L. Hirshfeld, Theoretica Chimica Acta **44**, 129 (1977).

[170] R. Bader and T. Nguyen-Dang, in *Advances in Quantum Chemistry* (Elsevier, 1981) pp. 63–124.

[171] W. Tang, E. Sanville, and G. Henkelman, Journal of Physics: Condensed Matter **21**, 084204 (2009).

[172] G. Henkelman, A. Arnaldsson, and H. Jónsson, Computational Materials Science **36**, 354 (2006).

[173] M. Yu and D. R. Trinkle, The Journal of Chemical Physics **134**, 064111 (2011).

[174] N. Koutná, L. Löfler, D. Holec, Z. Chen, Z. Zhang, L. Hultman, P. H. Mayrhofer, and D. G. Sangiovanni, Acta Materialia **229**, 117809 (2022).

[175] L. Löfler, *Defects and their influence on mechanical properties in nitrides: an atomistic study*, Ph.D. thesis, Montanuniversitaet Leoben (2022).

[176] Y. Cui and H. B. Chew, The Journal of Chemical Physics **150**, 144702 (2019).

[177] D. Gehringer, L. Huber, J. Neugebauer, and D. Holec, Physical Review Materials **7** (2023).

[178] P. Grigorev, A. M. Goryaeva, M.-C. Marinica, J. R. Kermode, and T. D. Swinburne, Acta Materialia **247**, 118734 (2023).

[179] H. Li, S. Wurster, C. Motz, L. Romaner, C. Ambrosch-Draxl, and R. Pippan, Acta Materialia **60**, 748 (2012).

[180] L. Romaner, C. Ambrosch-Draxl, and R. Pippan, Physical Review Letters **104** (2010).

[181] W. Cai, V. V. Bulatob, J. Chang, J. Li, and S. Yip, Philosophical Magazine **83**, 539 (2003).

[182] L. Ventelon and F. Willaime, Journal of Computer-Aided Materials Design **14**, 85 (2007).

[183] H. Clemens and S. Mayer, Advanced Engineering Materials **15**, 191 (2012).

[184] D. Holec, N. Abdoshahi, D. Gehringer, L. Hatzenbichler, A. Sakic, and H. Clemens, Advanced Engineering Materials (2021).

[185] L. Huber, J. Rottler, and M. Militzer, Acta Mater. **80**, 194 (2014).

[186] D. Scheiber, R. Pippan, P. Puschnig, A. Ruban, and L. Romaner, International Journal of Refractory Metals and Hard Materials **60**, 75 (2016).

[187] M. Kanani, A. Hartmaier, and R. Janisch, Acta Mater. **106**, 208 (2016).

[188] M. Kanani, A. Hartmaier, and R. Janisch, Intermetallics **54**, 154 (2014).

[189] Y. Wei, Y. Zhang, G.-H. Lu, and H. Xu, Intermetallics **31**, 105 (2012).

[190] G. Kresse and J. Hafner, Phys. Rev. B **47**, 558 (1993).

[191] G. Kresse and J. Furthmüller, Phys. Rev. B **54**, 11169 (1996).

[192] G. Kresse and D. Joubert, Phys. Rev. B **59**, 1758 (1999).

[193] H. J. Monkhorst and J. D. Pack, Phys. Rev. B **13**, 5188 (1976).

[194] S. Plimpton, Journal of Computational Physics **117**, 1 (1995).

[195] "LAMMPS lammps molecular dynamics simulator," `https://lammps.sandia.gov` (2022), accessed: 2020-08-06.

[196] R. R. Zope and Y. Mishin, Phys. Rev. B **68** (2003).

[197] V. Witusiewicz, A. Bondar, U. Hecht, S. Rex, and T. Velikanova, Journal of Alloys and Compounds **465**, 64 (2008).

[198] P. Lazar, J. Redinger, and R. Podloucky, Phys. Rev. B **76** (2007).

[199] J. H. Rose, J. R. Smith, and J. Ferrante, Phys. Rev. B **28**, 1835 (1983).

[200] P. Řehák, M. Černý, and D. Holec, Surface and Coatings Technology **325**, 410 (2017).

[201] N. Koutná, P. Řehák, Z. Chen, M. Bartosik, M. Fallmann, M. Černý, Z. Zhang, M. Friák, M. Šob, P. H. Mayrhofer, and D. Holec, Scr. Mater. **165**, 159 (2019).

[202] N. Koutná, A. Brenner, D. Holec, and P. H. Mayrhofer, Acta Mater. **206**, 116615 (2021).

[203] L. Löfler, R. Hahn, P. H. Mayrhofer, M. Bartosik, and D. Holec, Acta Mater. , 117095 (2021).

[204] M. Ohring, *Materials Science of Thin Films* (Elsevier, 2002) p. 568.

[205] K. Chen and M. Bielawski, Surface and Coatings Technology **203**, 598 (2008).

[206] J. Buchinger, L. Löfler, J. Ast, J. Michler, P. Mayrhofer, D. Holec, and M. Bartosik, SSRN Electronic Journal (2019).

[207] J. Buchinger, A. Wagner, Z. Chen, Z. L. Zhang, D. Holec, P. H. Mayrhofer, and M. Bartosik, Acta Mater. **202**, 376 (2021).

[208] D. Holec, R. K. Reddy, T. Klein, and H. Clemens, Journal of Applied Physics **119**, 205104 (2016).

[209] R. Benedek, A. van de Walle, S. S. Gerstl, M. Asta, D. N. Seidman, and C. Woodward, Phys. Rev. B **71** (2005).

[210] O. Ouadah, G. Merad, and H. S. Abdelkader, Materials Chemistry and Physics **257**, 123434 (2021).

[211] T. Klein, B. Rashkova, D. Holec, H. Clemens, and S. Mayer, Acta Mater. **110**, 236 (2016).

[212] S. S. Gerstl, Y.-W. Kim, and D. N. Seidman, Interface Science **12**, 303 (2004).

[213] S. Gerstl, Y. Kim, and D. Seidman, Microscopy and Microanalysis **8**, 1096 (2002).

[214] W. Li, Y. Yin, Q. Xu, J. Zhou, H. Nan, X. Ji, X. Shen, X. Feng, W. Yu, Z. Tu, and N. Pang, Computational Materials Science **159**, 397 (2019).

[215] S.-H. Wei, L. G. Ferreira, J. E. Bernard, and A. Zunger, Phys. Rev. B **42**, 9622 (1990).

[216] L. Ferreira, S.-H. Wei, and A. Zunger, The International Journal of Supercomputing Applications **5**, 34 (1991).

[217] D. Gehringer, M. Friák, and D. Holec, Computer Physics Communications **286**, 108664 (2023).

[218] U. Pototschnig, *Describing random alloys through triplets: An extension of the Warren-Cowley short-range order parameter*, Master's thesis, Montanuniversität Leoben, Franz-Joßef Straße 12, 8700 Leoben, Austria (2021).

[219] J. M. Cowley, Phys. Rev. **77**, 669 (1950).

[220] J. M. Cowley, Physical Review **120**, 1648 (1960).

[221] J. M. Cowley, Phys. Rev. **138**, A1384 (1965).

[222] D. Nöger, *Optimised structural models of solid solutions for tensorial properties*, Master's thesis, Montanuniversität Leoben, Franz-Joßef Straße 12, 8700 Leoben, Austria (2017).

[223] M. Dehghani, A. V. Ruban, N. Abdoshahi, D. Holec, and J. Spitaler, Computational Materials Science **205**, 111163 (2022).

[224] J. M. Soler, E. Artacho, J. D. Gale, A. García, J. Junquera, P. Ordejón, and D. Sánchez-Portal, Journal of Physics: Condensed Matter **14**, 2745 (2002).

[225] A. van de Walle, Calphad **33**, 266 (2009).

[226] A. Walle and G. Ceder, Journal of Phase Equilibria **23**, 348 (2002).

[227] A. V. Ruban and H. L. Skriver, Physical Review B **66** (2002).

[228] A. V. Ruban, S. Shallcross, S. I. Simak, and H. L. Skriver, Physical Review B **70** (2004).

[229] M. A. Gibson and C. A. Schuh, Data in Brief **6**, 143 (2016).

[230] M. Všianská and M. Šob, Progress in Materials Science **56**, 817 (2011).

[231] M. Černý, P. Šesták, P. Řehák, M. Všianská, and M. Šob, Materials Science and Engineering: A **669**, 218 (2016).

[232] H. Xue, Y. Luo, F. Tang, X. Yu, X. Lu, and J. Ren, Journal of Materials Research and Technology **11**, 1281 (2021).

[233] H. Xue, Y. Luo, F. Tang, X. Lu, and J. Ren, Materials Chemistry and Physics **258**, 123977 (2021).

[234] V. I. Razumovskiy, A. Ruban, I. Razumovskii, A. Lozovoi, V. Butrim, and Y. Vekilov, Scripta Materialia **65**, 926 (2011).

[235] V. I. Razumovskiy, A. Lozovoi, I. M. Razumovskii, and A. V. Ruban, Advanced Materials Research **278**, 192 (2011).

[236] V. Razumovskiy, A. Lozovoi, and I. Razumovskii, Acta Materialia **82**, 369 (2015).

[237] K. Ito, H. Sawada, S. Tanaka, S. Ogata, and M. Kohyama, Modelling and Simulation in Materials Science and Engineering **29**, 015001 (2020).

[238] H. Peng, W. Huo, W. Zhang, Y. Tang, S. Zhang, L. Huang, H. Hou, Z. Ding, and F. Liu, Acta Materialia **251**, 118899 (2023).

[239] Y.-J. Hu, Y. Wang, W. Y. Wang, K. A. Darling, L. J. Kecskes, and Z.-K. Liu, Computational Materials Science **171**, 109271 (2020).

[240] H. L. Mai, X.-Y. Cui, D. Scheiber, L. Romaner, and S. P. Ringer, Acta Materialia **231**, 117902 (2022).

[241] C. L. White and W. A. Coghlan, Metallurgical Transactions A **8**, 1403 (1977).

[242] L. Huber, R. Hadian, B. Grabowski, and J. Neugebauer, npj Computational Materials **4** (2018).

[243] E. R. Homer, S. Patala, and J. L. Priedeman, Scientific Reports **5** (2015).

[244] S. Patala and C. Schuh, Philosophical Magazine **91**, 1489 (2011).

[245] S. Patala and C. A. Schuh, Philosophical Magazine **93**, 524 (2013).

[246] D. Scheiber and L. Romaner, Acta Materialia **221**, 117393 (2021).

[247] M. Wagih and C. A. Schuh, Acta Materialia **181**, 228 (2019).

[248] D. McLean, *Grain Boundaries in Metals* (Clarendon Press, Oxford, 1957) pp. 116–150.

[249] C. L. White and D. F. Stein, Metallurgical and Materials Transactions A **9**, 13 (1978).

[250] T. Mütschele and R. Kirchheim, Scripta Metallurgica **21**, 135 (1987).

[251] R. Kirchheim, Progress in Materials Science **32**, 261 (1988).

[252] S. Suzuki, ISIJ International **30**, 1000 (1990).

[253] N. Louat, Proceedings of the Physical Society. Section B **69**, 459 (1956).

[254] D. Beshers, Acta Metallurgica **6**, 521 (1958).

[255] R. Fowler and E. Guggenheim, *Statistical thermodynamics: a version of statistical mechanics for students of physics and chemistry* (Cambridge University Press, Cambridge, 1939).

[256] M. Guttmann, Surface Science **53**, 213 (1975).

[257] P. Wynblatt and D. Chatain, Metallurgical and Materials Transactions A **37**, 2595 (2006).

[258] P. Lejček, *Grain Boundary Segregation in Metals* (Springer Berlin Heidelberg, 2010) pp. 82 – 86.

[259] P. Lejček and S. Hofmann, Critical Reviews in Solid State and Materials Sciences **20**, 1 (1995).

[260] M. Guttmann, Metal Science **10**, 337 (1976).

[261] J. du Plessis and G. van Wyk, Journal of Physics and Chemistry of Solids **49**, 1441 (1988).

[262] C. J. McMahon and L. Marchut, Journal of Vacuum Science and Technology **15**, 450 (1978).

[263] D. McLean and M. Guttmann, *Interfacial Segregation* (Springer US, 1979) Chap. Grain boundary segregation in multicomponent systems, pp. 261–348.